THÈSE

En vue de l'obtention du

DOCTORAT DE L'UNIVERSITÉ DE TOULOUSE

Délivré par :

Institut National Polytechnique de Toulouse (INP Toulouse)

Discipline ou spécialité :

Génie Électrique

Présentée et soutenue par :

M. DAVID MAGIN FLOREZ RUBIO

le lundi 20 janvier 2014

Titre :

SOURCES D'ALIMENTATION ELECTRIQUE POUR L'ETUDE ET
L'UTILISATION EFFICACE DES LAMPES EXCIMER DBD

Ecole doctorale :

Génie Electrique, Electronique, Télécommunications (GEET)

Unité de recherche :

Laboratoire Plasma et conversion d'Energie (LAPLACE)

Directeur(s) de Thèse :

M. HUBERT PIQUET

M. RAFAEL DIEZ

Rapporteurs :

M. DIEGO ECHEVERRY, UNIVERSIDAD DEL VALLE

M. MARCOS ALONSO, UNIVERSIDAD DE OVIEDO

Membre(s) du jury :

M. FREDY RUIZ, PONTIFICIA UNIVERSIDAD JAVERIANA BOGOTA, Président

M. GEORGES ZISSIS, UNIVERSITE TOULOUSE 3, Membre

M. HUBERT PIQUET, INP TOULOUSE, Membre

M. RAFAEL DIEZ, PONTIFICIA UNIVERSIDAD JAVERIANA BOGOTA, Membre

Acknowledgements

pendant mon séjour en France; ce remerciement est extensive bien sur á Virginie, Yann et Cassandre pour leur aimable accueil chez eux.

Alaric et Priscilla Montenon pour leur amitié, les gentilles invitations et les délicieux repas.

Djibrillah pour sa visite en Colombie et son aide lors de mes premiers jours au LAPLACE.

Agradezco a Diego Botero por su generosidad, simpatía y ayuda incondicional durante mis estadías en Toulouse sin las cuales no me habría divertido tanto, también le quiero agradecer por habernos esperado estóicamente en medio de la nieve.

A mi familia entera, quienes me han alentado y apoyado en todo sentido durante los momentos difíciles de esta aventura. Estoy seguro que no habría logrado llegar a realizar este doctorado sin los valores y enseñanzas que Stella y Aroldo nos inculcaron.

Finalmente a mi amada Malu, por tantos años, tantos viajes y tantos paisajes. A ella corresponde gran parte del buen término de esta tesis.

Résumé: Avec l'objectif d'améliorer le rendement des lampes à excimères (Excil-ampe) à décharge à barrière diélectrique (DBD), un convertisseur en mode de courant, qui permet un ajustement précis de la puissance électrique injectée dans ce type des lampes, à été conçu et mis en œuvre. Ce convertisseur fournit à la lampe un courant de forme d'onde carrée contrôlé au moyen de trois paramètres: l'amplitude, la fréquence et le rapport cyclique, pour obtenir un contrôle total de l'énergie électrique transmise à l'excilampe DBD. La mise en œuvre intègre un transformateur élévateur comme in-terface entre la lampe et un commutateur. Les expériences démontrent le principe de fonctionnement de ce convertisseur, y compris les mesures de puissance du rayonnement UV. Les degrés de liberté du convertisseur sont utilisées pour analyser le comportement de la lampe sous différentes combinaisons de ces trois paramètres, et sont utilisés pour déterminer le point de fonctionnement optimal de la lampe. Ensuite, un convertisseur à résonance du type onduleur série, est proposé pour alimenter la lampe avec une grande efficacité électrique. Afin de contrôler effectivement la puissance de la lampe, le mode de fonctionnement de ce convertisseur utilise le mode de conduction discontinue et la commutation douce (ZCS), avec lequel on obtient aussi de faibles émissions électromag-nétiques et l'on réduit les pertes de commutation. Les relations mathématiques obtenus à partir de l'analyse du diagramme de phase, ont été validées par des simulations et avec des résultats expérimentaux. Enfin, différentes topologies d'alimentations pour DBD sont comparées analytiquement et expérimentalement pour évaluer objectivement les avantages de chaque approche. Une des perspectives de ce travail est l'application de l'alimentation en créneaux pour l'étude de la performance d'autres types de réacteurs et d'excilampes DBD.

Mots clef: *DBD, lampe à excimères, source de courant, convertisseur à résonance, UV.*

Abstract: With the aim to provide a scientific tool for the enhancement of the Dielec-tric Barrier Discharge (DBD) Excimer Lamps (Excilamp) performance, a current-mode converter that allows an accurate adjustment of the electrical power injected into one of those lamps, is designed and implemented. With the proposed converter, the cur-rent supplied to the lamp has a square shape, controlled by means of three parameters: amplitude, duty cycle and frequency, which provides full control of the lamp electri-cal power. Implementation is made considering a step-up transformer interfacing the high-voltage lamp with the converter. Experiments demonstrate the operating principle of this converter, including UV power measurements for a DBD XeCl Excilamp. The capabilities of the converter are used to analyze the lamp behavior under different com-binations of these three parameters, illustrating its capabilities for finding the optimal operating point. Then a series-resonant inverter for the supply of DBD) excilamp is proposed. In order to effectively control the lamp power, the operating mode of this converter combines discontinuous current-mode and soft-commutation (ZCS), obtaining as well low electromagnetic emissions, and reduced switching losses. The mathemati-cal relationships obtained from state plane analysis, are validated with simulations and experimental results. Finally, several topologies of DBDs power supplies are compared analytical and experimentally to elucidate the advantages of each approach. After this

work, one of the perspectives is the application of the square-shape supply in the performance study of other types of DBD excilamps and DBD reactors.

Keywords: *DBD, excilamp, current source, resonant converter, UV.*

Contents

List of Figures

List of Tables

Introduction

As reported by the United Nations "in the year 2011, 768 million people were still without access to improved sources of drinking water while 2.5 billion people did not use improved sanitation" [0.1]. In the particular case of Colombia, the quality of the drinking water provided at the 35% of rural areas does not meet the required standards [0.2] and most of the superficial water sources are not ready for human consumption [0.3]. This harmful situation for many communities, is at the origin of this doctorate work.

This thesis is developed in the context of a research project that aims for the design and implementation of a water disinfection system prototype, based on UV radiation generated by a Dielectric Barrier Discharge excimer lamp. This project is supported by COLCIENCIAS, ICETEX, and the ECOS-NORD program.

The Dielectric Barrier Discharge excimer lamps (DBD excilamps) is an emerging and competitive technology for the efficient production of Ultra-Violet radiation (UV). The UV has well known germicidal properties and the use of UV in disinfection brings several advantages when compared with chemical based methods. The benefits of the DBD excimer lamps (presented later in this Section) together with the advantages of the UV radiation to decontaminate, have motivated the proposal of a water decontamination system based on this technology.

The development of the proposed water decontamination system, implies the concurrence of diverse areas of knowledge like bacteriology, hydrology, mechanics, plasma science and electronics. In this doctoral thesis, we are focused in a particular aspect of the decontamination system: the challenge of enhancing the performance of the DBD excilamp as UV source and the development of a high efficiency power supply for this lamp technology. Although, given the context of this research, the DBD UV excilamps is the focus of our interest, it is important to note that the developments proposed in this thesis can be pertinent for other type of DBD reactors.

What is the Ultra-Violet (UV) Radiation Useful for? The sun is the only natural source of UV radiation found in earth and its UV radiation plays an important role in natural processes, for example for the human beings synthesis of vitamin D and the natural control of microorganisms concentrations due to the UV germicidal property. The germicidal property of the UV is caused in part by the damage that the UV radiation can produce to the cells Nucleic Acids. The DNA absorption at different wavelengths of UV is shown in Fig.0.1, which gives the radiation wavelengths that causes more damages to cells.

For years the germicidal property of the UV radiation has been exploited in decontamination systems employing artificial UV sources [0.5] and nowadays a wide range of
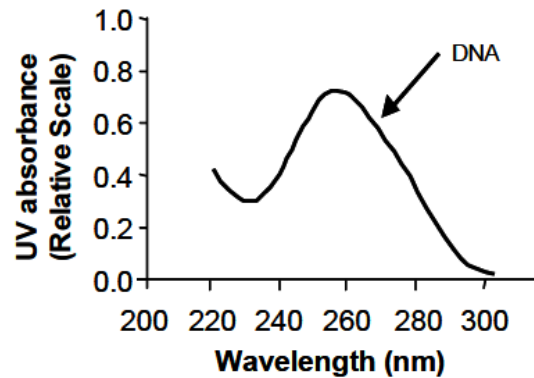
Figure 0.1.: UV absorbance of the DNA [0.4, p. 2-7]

industry and medical processes implement the photo-chemical reactions generated by the UV, among them the micro-lithography [0.6], skin treatment, light production and resin curing [0.7].

Particularly on the field of the water treatment, the UV based systems are advantageous when compared with classical Chlorine, Ozone and Peroxide based methods: the UV does not affect the physic-chemical properties of the water nor produce harmful sub-products and avoid the need for stock of reactive chemicals [0.5], making the UV a good option for their use in isolated rural areas. To generate UV radiation several technologies are available.

Artificial UV Sources   The main artificial sources of UV radiation are presented in Fig. 0.2. The UV LED radiates typically in wavelengths (385 nm) that are not very effective to decontaminate as shown in Fig.0.1.

For germicidal systems, the High Intensity Discharge (HID) Mercury-vapor based lamp is widely used. Its radiation spectra changes depending on the gas mixture pressure. In low-pressure lamps the radiation presents two main peaks, in 185 and 254 nm, in contrast, in medium-pressure lamps a polychromatic spectrum is observed with approximately only the 30% corresponding to UV. The Mercury content of this type of lamps can be dangerous for the environment and is strictly regulated. However not only the Mercury-vapor is used in HID lamps to produce UV; the HID Xenon lamps provides high intensity UV radiation flashes with an almost continuous spectra from the UV up to the Infrared radiation, useful e.g. to simulate the sun light. Thus, if a specific wavelength is required, a large amount of its radiated power becomes useless.

Another type of Mercury free UV sources are the DBD excilamps. This type of lamp is made from a sealed crystal bulb filled with an halogen gas, or halogen-rare gas mixture. Differing from the HID lamps, the metallic electrodes are placed outside of the crystal bulb. Its radiation wavelength depends on the gas mixture used and is quasi mono-chromatic. Compared with the other UV sources, the DBD excilamp technology

Figure 0.2.: Main UV artificial sources. From left to right: LED [0.8], HID Mercury-vapor lamp [0.9], HID Xenon lamp [0.10] and DBD excimer lamp

present special features well adapted for the requirements of several applications. Next, we describe these characteristics.

Main Advantages of the DBD Excilamps   Compared with the other UV artificial sources, the DBD excilamp presents the following distinctive features:

- It is mercury free. Consequently can be used in environments where the mercury content is hazardous, e.g. in the food and medicament industry.

- The electrodes are not in contact with the gas. Consequently, differing from the conventional discharge lamps, the electrodes are not deteriorated by the discharge.

- Instantaneous ignition. This implies no need for warm up time and immediate availability.

- Offers a wide radiation surface due to its geometry.

- The radiation wavelength is very precise and depends mainly on the gas composition, which can be selected according to the microorganism to be treated or the particularities of the application.

The DBD excilamps are nowadays focus of active research and the lamp performances continues to be improved. However, many years of research and developments are behind this technology.

DBD Excilamps Technology Landmarks   The origin of the DBD excilamps technology can be traced back to the first dielectric-barrier discharges investigations (1865) [0.11]. Since 1955 earlier reports on the Vacuum UV and UV radiation emission from rare gases were published [0.12,0.13,0.14,0.15,0.16,0.17] and an extensive review discussing the formation of excimers and its properties dates from 1975 [0.18]. A pioneer work integrating the excimer UV production and DBD, appears in 1988 [0.19], followed by many original works reporting the enhancement of the excilamps efficiency [0.20,0.21] and power [0.22], proposing excilamp models [0.23] and patenting excilamp devices [0.24, 0.25]. Authors in [0.26] proposed the first experiments with pulsed power supplies enhancing the excilamp efficiency (previously supplied with sinusoidal voltage generators). Later in [0.27]

the current mode power supply for this application, was proposed. One of the first reported works of decontamination using UV from DBD excilamps is [0.28], published in 2001. The research in excilamps for UV production continues and extensive reviews of the excilamps technology and their applications can be found in [0.11, p. 27], [0.12], [0.29]-[0.30].

Thanks to this long history of investigations on the DBD, their operating fundamentals and physical understanding are well known today. Additionally, different types of power supplies have been evaluated and implemented for many different industrial and medical applications. Nevertheless, we have found that there are still possibilities to improve the efficiency and performance of the power supplies for DBD excilamps. Particularly, the following improvement opportunities have been detected.

Improvement Opportunities   Nowadays, the mechanisms and phenomena behind the DBD excilamps technology are not totally explained and understood, for example:

- The correlation between the lamp radiative efficiency and the lamp operating point has not been clearly established.

- A deeper insight about the impact of the operating conditions (current intensity, operating voltage, frequency, etc.) in the existing excilamp electrical models, is needed.

- The efficiency of the DBD power supplies can be enhanced through the optimization of a power supply that assures the power delivered to the lamp and the operating point, taking into account the DBD excilamp model and the parasitic elements of the system.

If these topics of the excilamps technology are developed:

- More UV could be obtained with less energy, which is particularly important for decontamination applications because that makes easier the connection to a low power renewable source of energy.

- The UV power per lamp unit area could be increased, reducing the size of the DBD excilamp.

- A more fitted lamp equivalent model could be used to design more reliable and efficient power supplies.

- A better understanding of the physic-chemical mechanisms of the excimers could be elucidated.

Objectives   According to the research project context and based on the ideas exposed before concerning the DBD excilamps technology, this doctoral research has been oriented to the enhancement of the DBD excilamp performance as UV source, through the

study of the lamp intrinsic performance, the supply-lamp interactions and the development of a high efficiency power supply for this lamp technology.

In this sense, the first objective of this thesis is:

- The development of a power supply adapted to the DBD excimer UV lamp under study, capable of controlling the lamp power and the operating point by means of three degrees of freedom of the lamp current: operating frequency, amplitude and duty cycle.

The subsequent objective is:

- To determine the optimal operating point of the lamp, from the point of view of the conversion from electrical power to UV radiation power, within the power supply operating range.

And finally,

- The development, implementation and validation of a power supply to operate at the lamp optimal operating point, and maximizing the supply performance in terms of:
    - Electrical efficiency.
    - Coupling to the electrical network or to a renewable source of energy (photovoltaic, micro-hydroelectric).

This thesis is organized as follows. In Chapter 1, a literature review of the DBD excilamps technology is presented. Based on this information, the basic concepts behind the conception of a DBD power supply are explained, complemented by a general review of the power supplies already divulged in the literature.

Then, according to the first objective of this thesis, the development and validation of an innovative power supply that allows the adjustment of the DBD lamp electrical power with three Degrees Of Freedom (D.O.F), is presented. Exploiting this new capability of lamp power and operating point adjustment, a parametric study of the operating point impact over the lamp UV production is performed (Chapter 3), finding the optimal operating conditions for the lamp under study: On the basis of the parametric study results and with the aim of increasing the lamp-supply performance, a converter conceived with a high-efficiency criteria and to work at the optimal lamp operating point, is proposed in Chapter 4.

Finally, an analytical and experimental comparison of the proposed supplies and other high-efficiency topologies, working at the DBD excilamp optimal operating point, is presented and analyzed.

Bibliography

[0.1] United Nations, "Drinking water, sanitation & hygiene. statistics, graphs and maps." `http://www.unwater.org/statistics_san.html`, Nov. 2013.

[0.2] Defensoria del Pueblo - Colombia, *DIAGNOSTICO DE LA CALIDAD DEL AGUA PARA CONSUMO HUMANO ANO 2010*. Defensoria del Pueblo de Colombia, Nov. 2011.

[0.3] Instituto de Hidrologia, Meteorologia y Estudios Ambientales, *Estudio Nacional del Agua 2010*. Bogota D.C.: IDEAM, 2010.

[0.4] United States Environmental Protection Agency, *ULTRAVIOLET DISINFECTION GUIDANCE MANUAL FOR THE FINAL LONG TERM 2 ENHANCED SURFACE WATER TREATMENT RULE*. EPA, Nov. 2006.

[0.5] I. Soloshenko, V. Y. Bazhenov, V. A. Khomich, V. V. Tsiolko, and N. G. Potapchenko, "Comparative research of efficiency of water decontamination by UV radiation of cold hollow cathode discharge plasma versus that of low- and medium-pressure mercury lamps," *IEEE Transactions on Plasma Science*, vol. 34, no. 4, pp. 1365–1369, 2006.

[0.6] C. Dorval Dion and J. Tavares, "Photo-initiated chemical vapor deposition as a scalable particle functionalization technology (a practical review)," *Powder Technology*, vol. 239, pp. 484–491, May 2013.

[0.7] M. Wertheimer, A. Fozza, and A. Holländer, "Industrial processing of polymers by low-pressure plasmas: the role of VUV radiation," *Nuclear Instruments and Methods in Physics Research Section B: Beam Interactions with Materials and Atoms*, vol. 151, pp. 65–75, May 1999.

[0.8] NICHIA CORPORATION, "UV-LED." `http://www.nichia.co.jp/en/product/uvled.html`, 2013.

[0.9] OSRAM GmbH, "PURITEC HNS germicidal ultraviolet lamps." `http://www.osram.com/osram_com/products/lamps/specialty-lamps/ultraviolet-lamps/puritec-hns/index.jsp?productId=ZMP_86446`.

[0.10] Xenon corporation, "About xenon flashlamps." `http://www.xenoncorp.com/lamps.html`, 2013.

[0.11] U. Kogelschatz, "Dielectric-barrier discharges: Their history, discharge physics, and industrial applications," *Plasma Chemistry and Plasma Processing*, vol. 23, no. 1, pp. 1–46, 2003.

[0.12] M. Lomaev, E. Sosnin, and V. Tarasenko, "Excilamps and their applications," *Progress in Quantum Electronics*, vol. 36, pp. 51–97, Jan. 2012.

[0.13] P. G. WILKINSON and Y. TANAKA, "New xenon-light source for the vacuum ultraviolet," *Journal of the Optical Society of America*, vol. 45, pp. 344–349, May 1955.

[0.14] Y. TANAKA, "Continuous emission spectra of rare gases in the vacuum ultraviolet region," *Journal of the Optical Society of America*, vol. 45, pp. 710–713, Sept. 1955.

[0.15] B. Stevens and E. Hutton, "Radiative life-time of the pyrene dimer and the possible role of excited dimers in energy transfer processes," *Nature*, vol. 186, pp. 1045–1046, June 1960.

[0.16] W. C. Ermler, Y. S. Lee, K. S. Pitzer, and N. W. Winter, "Ab initio effective core potentials including relativistic effects. II. potential energy curves for xe2," *The Journal of Chemical Physics*, vol. 69, pp. 976–983, Aug. 1978.

[0.17] R. J. DeYoung and W. R. Weaver, "Spectra from nuclear-excited plasmas," *Journal of the Optical Society of America*, vol. 70, pp. 500–506, May 1980.

[0.18] J. B. Birks, "Excimers," *Reports on Progress in Physics*, vol. 38, p. 903, Aug. 1975.

[0.19] B. Eliasson and U. Kogelschatz, "UV excimer radiation from dielectric-barrier discharges," *Applied Physics B Photophysics and Laser Chemistry*, vol. 46, pp. 299–303, Aug. 1988.

[0.20] J.-Y. Zhang and I. W. Boyd, "Efficient excimer ultraviolet sources from a dielectric barrier discharge in rare-gas/halogen mixtures," *Journal of Applied Physics*, vol. 80, no. 2, p. 633, 1996.

[0.21] E. A. Sosnin, M. I. Lomaev, A. N. Panchenko, V. S. Skakun, and V. F. Tarasenko, "Glow and barrier discharge efficient excilamps," in *Proc. SPIE* (V. F. Tarasenko, G. V. Mayer, and G. G. Petrash, eds.), vol. 3403, pp. 308–313, June 1998.

[0.22] V. Tarasenko, M. Lomaev, A. Panchenko, V. Skakun, E. Sosnin, and A. Fedenev, "High-energy lasers and high-power excilamps," in *, Summaries of papers presented at the Conference on Lasers and Electro-Optics, 1996. CLEO '96*, pp. 375–, 1996.

[0.23] B. Eliasson and U. Kogelschatz, "Modeling and applications of silent discharge plasmas," *IEEE Transactions on Plasma Science*, vol. 19, pp. 309–323, Apr. 1991.

[0.24] B. Turner and J. T. Dolan, "Excimer lamp with high pressure fill," Nov. 1997. U.S. Classification: 313/570; 313/568; 313/571; 313/572; 315/39; 315/246; 315/248; 315/344 International Classification: H01J 6112; H01J 6120.

[0.25] Zoran Falkenstein, USHIO America Inc., "Development of an excimer UV light source system for water treatment." `http://www.revistavirtualpro.com/files/TIE04_200701.pdf`.

[0.26] V. F. Tarasenko, A. V. Krivonosenko, M. I. Lomaev, V. S. Skakun, E. A. Sosnin, and D. V. Shitz, "High-power excilamps with short-pulse duration," in *Proc. SPIE*, vol. 4065, pp. 826–835, 2000.

[0.27] R. Diez-Medina, *Alimentation de puissance d'une lampe exciplexe à décharge à barrière diélectrique, en vue du contrôle du rayonnement.* PhD thesis, INPT, Toulouse, 2008.

[0.28] A. Laroussi, F. C. Dobbs, Z. Wei, A. Doblin, L. Ball, K. Moreira, F. Dyer, and J. Richardson, "Effects of excimer UV radiation on microorganisms," in *Pulsed Power Plasma Science, 2001. IEEE Conference Record - Abstracts*, pp. 321–, 2001.

[0.29] M. I. Lomaev, V. S. Skakun, E. A. Sosnin, V. F. Tarasenko, D. V. Shitts, and M. V. Erofeev, "Excilamps efficient sources of spontaneous UV and VUV radiation," *Physics-Uspekhi*, vol. 46, pp. 193–209, Feb. 2003.

[0.30] Thomas Openlander, "Mercury-free sources of VUV/UV radiation: application of modern excimer lamps (excilamps) for water and air treatment1," *Journal of Environmental Engineering and Science*, vol. 6, pp. 253–264, May 2007.

1. Literature review

The conception and analysis of power supplies for DBD excilamps, as for any other type of supply, requires a model of the load. The different DBD excilamp models found in the literature, are constructed from the theory and phenomena involved in the operation of this lamp technology. Accordingly, first in this Chapter, the DBD UV excilamps operating theory is described. On the basis of these operating fundamentals, an electrical model of the DBD excilamp, necessary for the power supplies design, is selected. Then, using the lamp model as starting point, the power supply characteristics to achieve the control of the lamp power, are determined. On this scope, some excilamp power supplies proposed prior to this thesis, are studied and finally, some examples of commercially available DBD excilamp based systems and their typical performances are mentioned.

1.1. DBD Excimer UV lamps

The production of UV radiation in an excimer lamp is explained from the mechanisms involved in the creation of excited unstable molecules called excited dimmers (excimers) or excited complex (exciplexes); to simplify the terms we will refer to both of them as excimers. These excimers are created by means of an electric discharge that can be generated by different means. One of the techniques to produce this discharge is the Dielectric Barrier Discharge (DBD). In particular, the DBD is well adapted for the excitation of an excilamp because it benefits the homogeneity of the discharges and consequently produces a more uniform radiation along the lamp surface.

   Therefore, two main phenomena involved in the DBD excilamp operation can be highlighted: The production of a Dielectric Barrier Discharge and the creation of excimers. Accordingly, in this Section first the mechanisms involved in the operation of a DBD and its role on the UV production, are described. Then, using some results from previous works, the influence of the power supply in the UV radiation of an excimer lamp is explained. On the basis of this theory, the modeling of DBD excilamps is introduced and an electrical model of the lamp, suitable for the power supplies design, is selected.

1.1.1. Operating Principle

A DBD is produced when an electric discharge occurs between two electrodes which are separated at least with one dielectric layer, as shown in Fig.1.1. The DBD creation is initiated by an avalanche of electrons, produced by an electric field applied between the lamp electrodes (1.2-A). After [1.1], following the avalanche, occurs the transition to a self-sustained current, which flows through the "channel" formed by the ionized
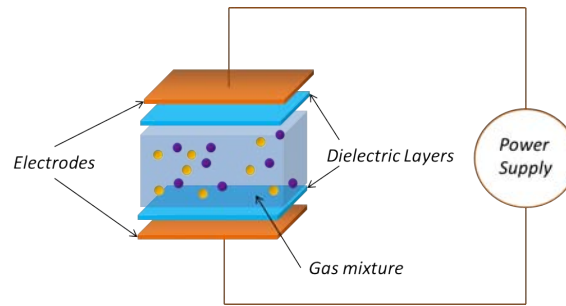
Figure 1.1.: Structure of a DBD lamp with planar geometry

gas (weakly ionized plasma), this conduction channel is known as a streamer (1.2-B). When the streamer connects both dielectric layers, the difference of potential is locally compensated by a region of high electrical density which electric field is close to zero, and the streamer is self-extinguished.

Several micro-discharges as the one described before occur along the dielectric surface in a non-uniform distribution and at different instants of time. The spatial distribution of the streamers across the lamp is influenced mainly by the micro-discharge interactions from one streamer to another. This distribution can be studied using a probability function that uses "memor" property in the streamers creation and with the *Voronoi Polyhedron approach* [1.2, p. 40].

Some of the properties that describe a micro-discharge are: the streamer filament diameter, electron density, propagation time, lifetime, peak current, the current density and charge remnant, among others. At atmospheric pressure, these micro-discharges have lifetimes in the order of nanoseconds, current densities around $100 \ \text{A/cm}^2$ with diameters of about $100 \ \mu m$ [1.1, p. 443].

According to the plasma-physics theory, those properties are determined by the gas composition, the gas pressure and the electrodes configuration. However, the power supply also has an impact in the characteristics of the discharge. Some of the effects of
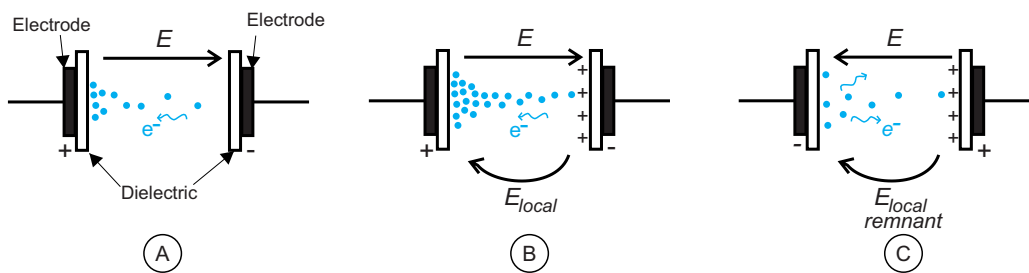
Figure 1.2.: Illustration of the electrons (e^-) avalanche and the produced local electric field E_{local}. Once the direction of the external electric field has changed, the local field remnant helps to the production of the next streamer.

increasing the power supplied to the DBD are the production of more micro-discharges per unit time [1.2, p. 30–49] and the change in the discharge regime. The establishment of an homogeneous instead of a filamentary discharge, has been achieved thanks to the use of special electrodes and power supply operating conditions [1.3].

UV Production The DBD is produced in a volume containing a gas. The collisions of the emitted electrons with the gas atoms (or molecules) produce the atom transition from a ground state to an excited electronic state (ions). The gas atoms or molecules contained in a DBD excilamp are associated among them only in the excited state of energy. When this association is produced, a new excited specie is created.

If this gas is composed by only one element, the created specie is called an excited dimmer or an excimer. If the gas is composed by two different elements, e.g. Xe and Cl, the excited molecule is called an exciplex. This dimmer or exciplex dissociates spontaneously and returns to its ground state releasing energy in the form of a UV photon. In Fig.1.3 the creation of a XeCl exciplex, is represented as described on [1.1].
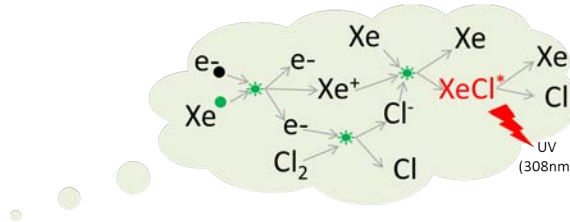
Figure 1.3.: Collisions in a DBD excimer lamp filled with XeCl gas

From the excimer production process described in [1.4], dimmers in the upper excited states descend to the lower excited states shown in Fig.1.4 (conventionally called the B, C and D energy levels) without producing radiation. The UV is only emitted in the ion transition from the B, C, D levels to the ground state (conventionally named A and X), therefore the UV radiation intensity is proportional to the quantity of excimer species produced at these named low levels of energy. In this sense an over-excitation of the ions can reduce the efficiency of the UV radiation production.

The UV radiation of a DBD excimer lamp can be described by different parameters, as average and peak intensity, waveform, frequency, wavelength, discharge regime and efficiency (UV power/electrical power). Several of these parameters, can be controlled by means of the electrical signal supplied to the lamp to produce the discharge [1.1, p. 445], [1.5], [1.6]. Next, some previous works revealing the influence of the lamp operating point on the UV radiation are mentioned.

1.1.2. Operating Conditions

Changes in some of the UV radiation parameters mentioned before, have been already related to variations in the excilamp supply mode. Lomaev [1.4, p. 203] accounts for
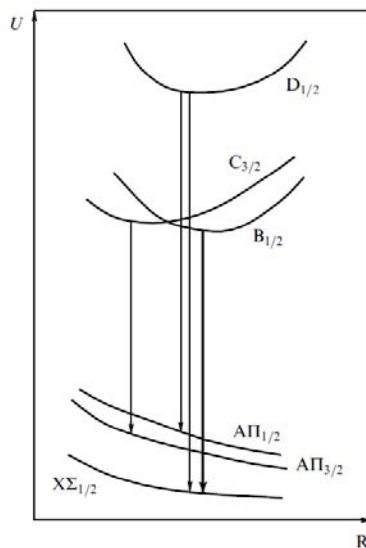
Figure 1.4.: Lower excited states of energy (B, C, D) of an exciplex and the radiative transitions to the ground state (A, X). As appears in [1.4, p. 194]

changes in the streamers visual aspect (density, distribution, filament diameter and filament intensity) due to the variation in the DBD operating frequency. The power injected into the lamp is different for each frequency, hence it cannot be well explained if the changes in the streamers are due to the power or the frequency or both. It has also been demonstrated that the streamer lifetime can be controlled with the duration of current pulses injected to the DBD lamp [1.7].

From these results, the changes in the streamer diameter and intensity are influenced by the type of electrical supply used, and not only by the lamp intrinsic characteristics. However, we point out that from the theory in [1.2, p. 34], some of the properties associated to the streamer micro-discharges, like the duration time and charge transferred, does not depend on the characteristics of the excitation signal.

On the basis of these results, more experiments should be performed in order to study the influence of the power supply in other aspects of the streamer characteristics and the relation of these characteristics with the lamp radiative efficiency. From the physical phenomena involved in the discharge, it can be inferred that the streamer lifetime is dependent on the availability of non-excited species to feed the discharge. In this sense, a study of the streamers lifetime correlated to the production of more streamers in the lamp, has not been found in the literature.

The influence of the power supply in the excimer lamp UV radiation can be studied in two perspectives:

1. From the point of view of the internal mechanisms involved in the production of one streamer.

2. And from the production of all the excimers in the whole ensemble of the lamp.

Production of one streamer From the point of view of a single streamer there exists two main phases: the current propagation and the dissipation [1.2]. The current propagation and the related avalanche of excimers production occurs when the critical gas voltage V_{th} is reached, in consequence, the faster V_{th} is reached the faster the UV radiation starts. Given the capacitive behavior of the lamp, the time to produce the gas breakdown can be controlled by means of injecting a controlled current into the gas capacitance. As higher this current, shorter is the necessary time to produce the gas breakdown.

From the DBD theory in [1.2], after the streamer occurs, its lifetime, dissipation time, among other properties, are inherent to the gas composition, pressure and electrodes configuration. To produce a second streamer in the same place *without* inverting the polarity of the external electric field, requires more energy that the one necessary to produce the precedent streamer, due to the remnant local electric field. Hence, if more charges are transferred in the same direction to the dielectric, is more probable to produce a new streamer in another place. Additionally, as exposed in [1.4], exciting the gas species to the upper energy levels will not produce additional UV radiation, in consequence it should be more UV-efficient to stop the supply immediately after the streamer dies-out and to wait until the ionized channel dissipates to invert the voltage and produce a new streamer in the opposite direction.

The lamp ensemble From the point of view of the whole lamp, each streamer along the lamp surface starts at a different instant of time and influences the production of other streamers by means of the micro-discharge interactions.

The quantity of streamers per unit time depends on the electrical power injected into the gas [1.2, p. 34]. Given a streamer diameter and current density that depends mainly on the gas properties, it could be possible to calculate how much charge must be transferred to the dielectric in a single pulse of current to produce the necessary streamer quantity that fills the lamp area. Taking into account the streamer lifetime and the relaxation time of electrons (e.g. in the order of 40 ns at atmospheric pressure) and of ions (in the order of few µs) an approximation of the optimal frequency of the current could be calculated. For example, from the DBD streamer parameters reported in [1.2, p. 33], with a streamer diameter about 200 µm and a current density of $0.1\,A/cm^2$ per streamer, to fill a 10x10 cm surface area of a dielectric barrier, 50 streamers should be necessary, which corresponds to 315 mA of total conducted current. Suppose that the drifting ions remain in the discharge gap for 10 µs, in this case an excitation repetition rate of 100 kHz allows the ions to dissipate from the discharge volume.

However, in contrast to the fixed streamer lifetime predicted by the theory, authors in [1.7,1.8] have clearly established a tight correlation between the current pulse duration and the discharge streamer existence. Also, the temporal response of the UV radiation produced by the streamer is governed by the current pulse span.

Now that the operating principle of the DBD excilamps has been explained, the electrical modeling of the lamp is reviewed with the aim to establish a useful model to conceive and design its power supply.

1.1.3. Modeling

Different approximations have been already used to develop DBD excilamp models; DBD reactors models oriented to a spatio-temporal description of the plasma, are constructed on the basis of the dynamic of particles and the Maxwell's equations. Those physics-based models are useful for accurate simulation of the discharge creation and distributions [1.9]. The DBD behavior can be described by a set of partial differential equations used for finite element models [1.10], [1.11] and in the estimation of the excilamps UV output [1.12]. Equivalent electrical models, developed on the basis of the differential equations representation, have been built, providing fast identification and validation of the equivalent parameters [1.13, 1.14], [1.15, p. 22].
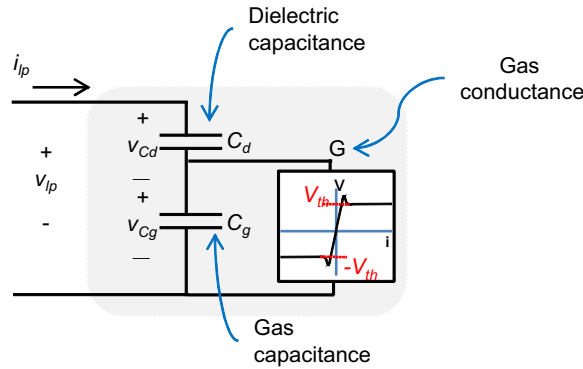
Figure 1.5.: Electrical model of the DBD lamp

The simplified model presented in Fig.1.5 has proven to be appropiate enough for the analytical dimensioning of DBD power supplies [1.16], [1.17], [1.14], consequently this model is used in this thesis for the DBD excilamp converters design. Here, the most important elements of this model are reminded: a coaxial DBD excimer lamp, as the one depicted in Fig.1.6, confines a gas mixture between two silica walls. This lamp geometry can be modeled with the electrical equivalent circuit in Fig.1.5. The lamp silica walls, acting as dielectric barriers, are modeled as the equivalent capacitance C_d.

These barriers are in series with the gas. The electrical model of the gas behavior is given by a gas capacitance in parallel with a gas conductance [1.10], C_g and G respectively. The gas conductance is very small when the absolute value of the gas voltage is smaller than the gas breakdown voltage, V_{th}: the equivalent model of the DBD is thus the series association of C_d and C_g, C_{eq}. When the gas voltage reaches V_{th} by effect of the connected power supply, the gas acquires the behavior of an almost constant voltage source of value V_{th} which remains in series with C_d and which polarity changes according
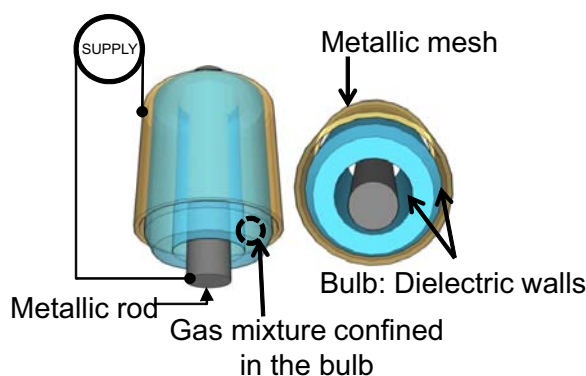
Figure 1.6.: Structure of a coaxial DBD lamp

to the current sense [1.8].

To experimentally determine the values of these three equivalent parameters (C_d, C_g, V_{th}) of a DBD reactor, the use of the Charge-Voltage Lissajous figures is common [1.18, p. 12], [1.19]. In Fig.1.7 the Charge-Voltage plot of a DBD reactor is shown.

To illustrate the parameters computation method let's assume that this figure corresponds to a DBD excimer lamp. In this figure, the change of the lamp voltage v_{lp}, follows a counter-clock wise trajectory as a function of the injected charge, q_{lp}. Starting from the upper-right peak value $\hat{V}_{lp}$, the voltage decreases linearly with the charge according to the capacitor voltage change equation (1.1.1). Therefore, the value of the equivalent capacitor is calculated from the parallelogram slope. Prior to the gas breakdown the charge is transferred to C_d in series with C_g, thus the slope of this first section of the trajectory corresponds to C_{eq}.

$$v_{lp} = \frac{1}{C_{eq}} q_{lp} \tag{1.1.1}$$

Once the gas reaches the breakdown voltage, the slope becomes equal to C_d, and the voltage continues to decrease almost linearly until reaching the lamp negative peak voltage $-\hat{V}_{lp}$. Now knowing C_d, the value of V_{th} is computed according to the lamp model, using (1.1.2), with $\hat{Q}_{lp}$ equal to the absolute value of the maximum charge injected into the lamp.

$$V_{th} = \hat{V}_{lp} - \frac{\hat{Q}_{lp}}{C_d} \tag{1.1.2}$$

As will be explained in the next Section 1.2, the constant voltage of the gas after discharge and the capacitive nature of the lamp, are determinant characteristics for the conception of power supplies for this lamp technology.
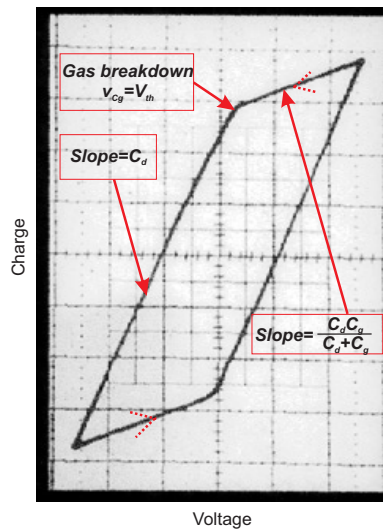
Figure 1.7.: Charge-Voltage Lissajous figure of an ozone reactor [1.18, p. 13]

1.2. Power supplies for DBDs

At the beginnings of the DBD excilamp technology, and still now, voltage mode supplies were used because of their simplicity and low cost. However, on the basis of the DBD excilamp model presented before in Section 1.1 it can be demonstrated that the logical way to control the lamp power is by means of its current, and accordingly, that a current-mode power supply is the right option to determine the DBD excilamp power. For this reason during the last five years more researches have been focused in current-mode supplies.

In this section, using causality analysis the use of current mode supplies as the mean to control the electrical power of a DBD is justified. Next, the need for a step-up transformer in most of the existent supplies is explained. Then, some topologies of already proposed current-mode supplies for DBDs are analyzed. Also a general review of the voltage mode supplies is presented, since they are still used.

1.2.1. Controlling the DBD excilamp power

A DBD excilamp normally operates in the discharge regime known as normal-glow regime, where the gas has an almost constant gas voltage for a large interval of current values [1.14]. Under this assumption and according to the lamp model explained in 1.1.3, the lamp voltage v_{lp} can be computed using the capacitor voltage equation, as a function of the injected current i_{lp}. The value of the equivalent capacitance, before and after ignition, is different. Before ignition, the lamp equivalent capacitance is the series of C_d and C_g, C_{eq}, and v_{lp} is determined by (1.2.1):

$$v_{lp}(t < t_{br}) = v_{lp}(t_o) + \frac{1}{C_g} \int_{t_o}^{t} i_{lp}(\tau) \, \mathrm{d}\tau + \frac{1}{C_d} \int_{t_o}^{t} i_{lp}(\tau) \, \mathrm{d}\tau = v_{lp}(t_o) + \frac{1}{C_{eq}} \int_{t_o}^{t} i_{lp}(\tau) \, \mathrm{d}\tau$$
(1.2.1)

With t_{br} equal to the time instant at which the gas voltage reaches V_{th} due to i_{lp}, producing the gas breakdown.
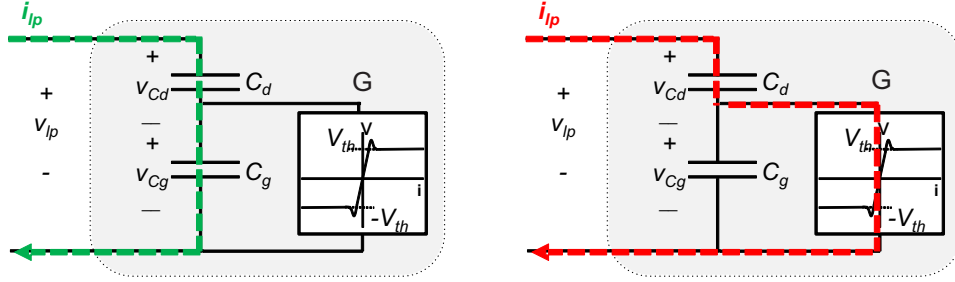
Figure 1.8.: Lamp current path before (left) and after (right) gas breakdown

Before the gas breakdown, i_{lp} flows trough C_d and C_g (Fig.1.8-left), but no current goes into the gas conductance G; during this stage all the lamp power is reactive. If enough current is injected into the lamp, the gas voltage increases until reaching the gas breakdown voltage V_{th}; at that instant (t_{br}) the lamp current path changes, as presented in Fig.1.8, and all the lamp current flows through G; consequently, for $t > t_{br}$, v_{Cg} remains constant at V_{th} and the lamp voltage is now calculated with (1.2.2):

$$v_{lp}(t > t_{br}) = v_{lp}(t_o) + V_{th} + v_{C_d}(t_{br}) + \frac{1}{C_d} \int_{t_{br}}^{t} i_{lp}(\tau) \, \mathrm{d}\tau$$
(1.2.2)

Accounting the DBD lamp capacitive behavior, the supply mode of the lamp must enable a bidirectional current (AC) into the lamp with zero average value, otherwise the magnitude of the lamp voltage v_{lp} would grow uncontrollably (1.2.1).

An important property to observe is that after breakdown the lamp current is equal to the gas conductance current. Given that the gas conductance voltage v_{Cg} remains constant (at V_{th}), the power transferred to the lamp P_{lp} is equal to the power dissipated by G during one period of i_{lp}, T_{lp}. According to the lamp model, the polarity of the gas breakdown voltage changes according to the direction of the current, thus the same energy is dissipated during the positive and negative current semi-cycles. In this sense P_{lp} is calculated here as twice the power dissipated by G from t_{br} until $T_{lp}/2$ (1.2.3):

$$P_{lp} = \frac{2}{T_{lp}} V_{th} \int_{t_{br}}^{T_{lp}/2} i_{lp}(t) \, \mathrm{d}t$$
(1.2.3)

As can be seen on (1.2.3), a current mode supply determining i_{lp} offers two means for the control of the lamp power: the current waveform (i_{lp}) and the current frequency

$(1/T_{lp})$. This property leads to the choice of a current-mode power supply to assure the control of the power injected into the lamp. This fact has been validated experimentally, using a current-mode semi-resonant converter [1.6, 1.7].

Additionally, another interesting property of the DBD power, demonstrated by T.C. Manley [1.19], is that the DBD reactor power depends on the reactor peak voltage ($\hat{V}_{lp}$) and not on the voltage waveform [1.18, p. 11]. In his work, Manley has found a DBD power formula which is expressed here in function of the DBD lamp parameters (1.2.4).

$$P_{lp} = 4f_{lp}V_{th}C_d \left(\hat{V}_{lp} - \frac{V_{th}C_g}{C_{eq}} \right) \qquad (1.2.4)$$

In this formula the lamp power depends on the three parameters of the DBD model, the lamp voltage frequency (f_{lp}) and the lamp peak voltage ($\hat{V}_{lp}$). However, it is important to note that the fact that P_{lp} depends on $\hat{V}_{lp}$ do not means that by using a voltage source, the DBD reactor voltage can be easily controlled. When using a current-mode supply, $\hat{V}_{lp}$ is calculated according to (1.2.1) and (1.2.2).

The Manley's equation is useful for the power supply dimensioning. It allows to compute for example the lamp peak voltage for a given lamp power and operating frequency and accordingly to determine the DBD supply operating voltage.

Now that the lamp power control by means of the lamp current has been demonstrated, next some current mode DBD power supplies already found in the literature are presented.

1.2.2. Current Mode Supplies for DBDs

As explained in the precedent Section 1.2.1, to precisely determine the DBD power, the control of its current is necessary, an this current must be alternating with zero average value to avoid uncontrolled growing of the lamp voltage and damage in the converter. The control of the DBDs current has been already achieved with different approaches. For a better understanding of these topologies, first is explained why a step-up transformer is incorporated in most of the already proposed DBD supplies and then some of these current mode converters are described.

The need for a transformer

For a proper operation of the supply, a zero average value of the lamp current is not enough; the maximum lamp voltage must be determined. From the Manley's equation, the lamp peak voltage is function of the desired lamp power and the lamp equivalent parameters. Typically in DBD excilamps C_g is smaller than C_d and are in the order of pF, V_{th} is of some kV and the operating frequency is about tens to hundreds of kHz. Accordingly, for lamp powers in the order of some tens of Watts, $\hat{V}_{lp}$ values up to 10kV are commonly found.

This level of $\hat{V}_{lp}$ is hardly tolerated by currently available high speed switches. One of the most cost-effective ways to reduce the voltage in the electronic devices of the

converter, is by connecting a step-up transformer between the supply and the DBD lamp.

The main drawback of using the step-up transformer, is the impact of its parasitic elements on the supply; they affect the efficiency and are also a source of limitations on the lamp operating range [1.17, Chap.3]. In Section 2.3.3, the impact of the transformer parasitic elements on the supply operation is studied in detail.

Despite the transformer use implications, in most of the power supplies for DBDs already proposed a step-up high voltage transformer is found. What is more, the transformer parasitic elements such as the magnetizing inductance are used in some DBD supplies as part of the converter design. With descriptive purposes the step-up transformer is not always included in the schematics of the converters explained next.

Proposed Converters

Some of the first proposed current-mode supplies for DBD excilamps are found in [1.20, 1.21]. Their operating principle is the use of an inductance (that shapes the current) and the equivalent capacitance of the DBD, to produce a resonant circuit. The main characteristic of these converters is the use of Discontinuous Conduction Mode (DCM). Thanks to this operating mode, the DBD lamp current all along the converter operating sequence is determined analytically and on this basis the power injected into the DBD is predicted.

To employ a resonant converter as a power supply for the DBD lamp has sense because this type of converter profits the capacitive nature of the DBD load, and also can provide an inherent current source behavior, while reducing the switching losses in the power semiconductors. This feature is especially important in this application due to the high operating frequencies of the DBDs (tens to hundreds of kHz).

One of the proposals found in [1.21] is a Boost-based resonant converter topology. Its schematic is shown in Fig.1.9 as presented in [1.22]. This current-mode converter operates in discontinuous conduction mode thanks to the use of specially designed SCR thyristor switches. The inductance L is charged linearly using the DC input voltage, then
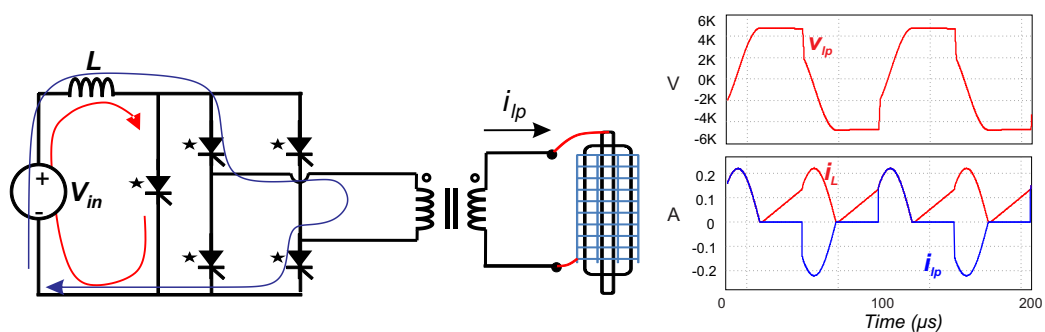
Figure 1.9.: Left: Boost-based DBD power supply designed to operate in DCM [1.22]. Right: the corresponding lamp voltage and current waveforms obtained from simulation.

when the desired value of current is reached, the inductance in series with the voltage source are connected to the DBD lamp, starting the resonance and the current injection into the lamp. The resonance finishes when the current is equal to zero thanks to the thyristor-like switches. For the next half cycle the other bridge diagonal is turned-on, injecting a negative current pulse into the DBD and a symmetrical bipolar voltage in the DBD is obtained as shown in 1.9-right. In this converter the DBD lamp power can be controlled by means of the DC input voltage, the charge time of the inductance and/or by the bridge switching frequency.

Another Boost-based power supply for DBD, shown in Fig.1.10-left, has been proposed in [1.23, p. 85]. In this converter, first the inductance is charged through the switches *Q1* and *Q2*, then *Q2* is turned-off and a resonance is produced; thanks to this resonance the inductance current flows through the decoupling capacitor C and through the DBD lamp via the transformer. Once the inductance current becomes negative, the diode D1 spontaneously turns-on allowing the current returns to the DC voltage source. As observed in the waveforms of Fig.1.10-right, during the resonance this converter produces a positive voltage pulse across the lamp.

However, to avoid the transformer core saturation the lamp average voltage must be zero, accordingly, the area of the negative lamp voltage must be equal to the area of the positive pulse produced during the resonance. For the particular case of the experimental waveform observed in Fig.1.10-right, the area of the DBD positive pulse voltage (Vlp) is around 1 mV.s and the operating frequency is 30 kHz, this implies a constant lamp voltage of -39 V when no current is being injected into the DBD, in order to avoid transformer saturation. One of the main drawback of this non-symmetrical voltage converters is that higher output voltage than those supplies with symmetrical operation is required to obtain the same DBD power.

Differing from the converter in Fig.1.9, this topology allows a continuous oscillation (one period) of the current by the use of bidirectional switches. When the continuous conduction mode is used, high-frequency oscillations can be obtained. However, the decay in the oscillation amplitude makes difficult to ensure the lamp ignition in every oscillation cycle and thus to predict the lamp power and the shape of the UV radiation.
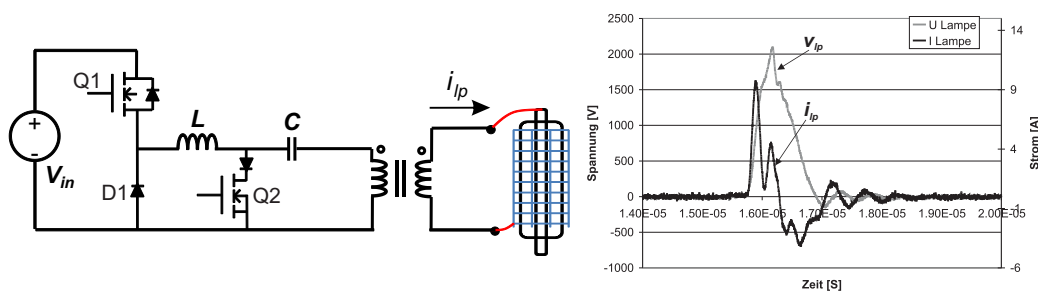
Figure 1.10.: Left: The Adaptive Pulse topology proposed in [1.23, p. 85,144] Right: the corresponding lamp voltage and current waveforms obtained experimentally.

Also, the attenuated DBD lamp current oscillations, observed in Fig.1.10-right, are responsible for conduction losses and delays the possible injection of the next current pulse without achieving a gas breakdown (lamp ignition).

The Flyback topology based converter shown in Fig.1.11 [1.20, p. 1383] operates in two main stages. First the magnetizing inductance L_m is charged by V_{in} producing a linear increase of the transformer magnetizing current. Then, the single switch is opened generating a parallel resonance between L_m and the DBD lamp capacitance. During the charge of L_m, the DC input voltage is seen in the secondary side multiplied by the transformation ratio, imposing a voltage to the equivalent DBD capacitance. In order to obtain the necessary L_m value, the transformer performance is often compromised, therefore this topology is commonly highly affected by the transformer parasitic elements. An improved version of this Flyback based converter can be found in [1.24]. Observe that the obtained lamp voltage waveform is very similar to the Adaptive Pulse topology output .

The second topology found in [1.21] is based on the Buck-Boost converter. The operating principle of this resonant converter relies on the storage of a fixed amount of energy in an inductance for the subsequent transference of this energy, to the DBD lamp, again in DCM. In Fig.1.12 a schematic of this topology is shown.

In the Buck-Boost-based converter the energy injected in each semi-cycle is defined by the duration of the ON sequence of the switch *To*, thus the power injected into the DBD is determined only by the inductance stored energy multiplied by the frequency. The obtained lamp voltage and current are symmetrical as shown in Fig.1.12-right. In Fig.1.13 the experimental waveforms obtained for this type of converter are shown. A computation of the gas conductance current is presented in Fig.1.13-right (i_{gas}) and it is compared with the waveform of the UV radiation to demonstrate the capability of controlling the UV shape. Power supplies working on this basis are found in [1.6, 1.7, 1.15, 1.25]. A benefit of the Buck-Boost supply type is its high stability [1.6].
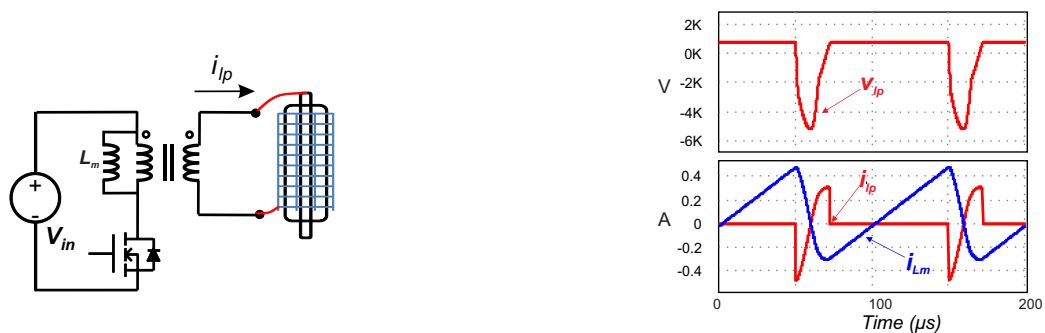
Figure 1.11.: Left: Flyback topology based DBD power supply designed to operate in current-mode. Right: the corresponding lamp voltage and current waveforms obtained from simulation.
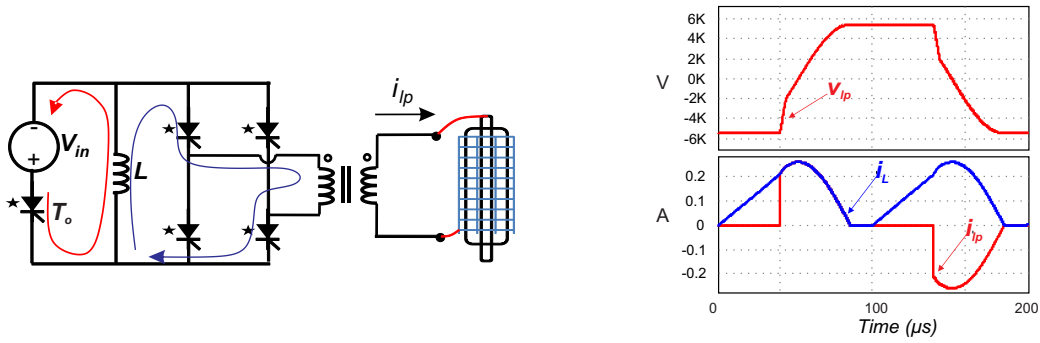
Figure 1.12.: Left: Buck-Boost topology based DBD power supply designed to operate in current-mode. Right: the corresponding lamp voltage and current waveforms obtained from simulation.
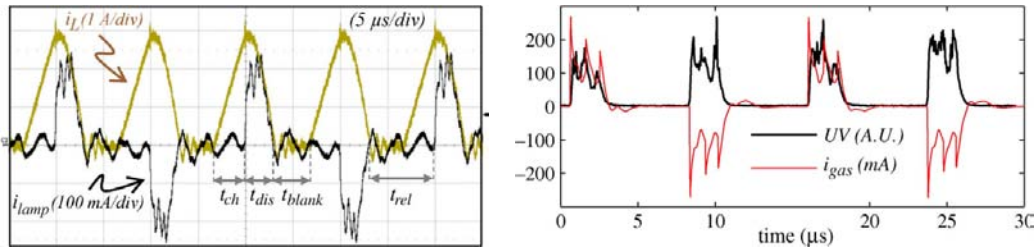
Figure 1.13.: Experimental waveforms of the Buck-Boost-based converter operating in DCM. Left: Inductance current i_L and lamp current i_{lamp} Right: Computed conductance current i_{gas} and measured UV instantaneous response UV. [1.6]

In Fig.1.14 the schematic of a topology called Sinusoidal Pulse [1.26] is presented. This is a resonant converter that combines an inductor (L) pre-charge through the switches *Q1* and *Q2*; followed by a partial discharge of the inductance sustained by the DC input voltage like the Boost-based converter, the discharge starts at the turn-off of switch *Q2*; when the inductance current changes of direction, *Q1* is turned -off allowing a free-wheel oscillation through *Q3*, as done in the Buck-Boost based converter, operating in continuous conduction mode. In this manner a high-frequency current burst is injected into the lamp until the oscillation dies out when all the switches are turned-off. As previously mentioned for the Adaptive Pulse topology, the CCM in the current oscillation can produce very high frequency current pulses, however not in all of these pulses the lamp ignition is achieved or can not be assured, reducing the converter efficiency. Additionally, to implement a soft switching in this CCM topology, a repetition rate between the current bursts that allows a noticeable attenuation of the current and voltage must be used, thus reducing the maximum operating frequency range of the converter and according to (1.2.4) leading to the increase of the output voltage to obtain a required lamp power. Another option to achieve soft switching is the use of a
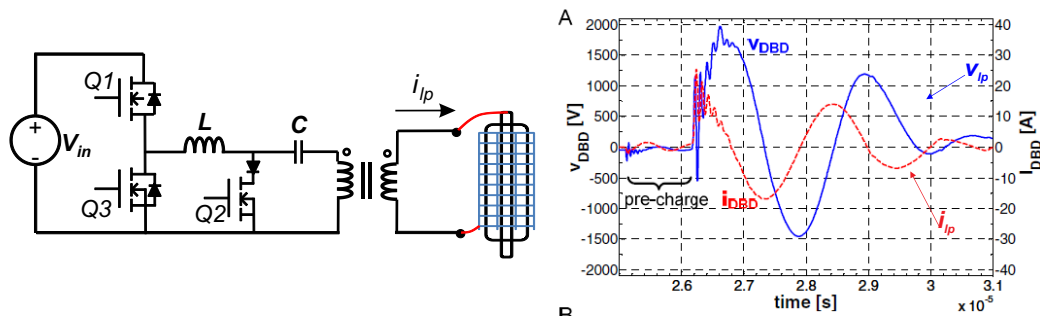
Figure 1.14.: Left: Universal-sinusoidal topology based on the Buck-Boost topology, proposed in [1.27]. Right: The experimental DBD voltage and current burst.

ZVS/ZCS controller, increasing the complexity of the drivers when compared with the DCM topologies. A new version of this topology is proposed in [1.27], where a limit in the number of resonance cycles is implemented.

Motivated by the inconvenient implications of the step-up transformer use mentioned in Section 1.2.2, authors in [1.26] and [1.28] propose transformer-less converter topologies, using high voltage switches; however these proposals have not been yet verified experimentally. The recent availability of High Voltage MOSFETs and diodes based on the SiC technology, could allow the development of transformer-less power supplies for DBDs. As reported by [1.29, 1.30], soon the production of up to 10 kV MOSFETs should be expected. In another approach, piezoelectric transformers have been used for the supply of a DBD reactor, this proposal is intended for low power applications [1.31].

1.2.3. Voltage Mode Supplies for DBD

Because of their simplicity and low cost, power supplies operating in voltage mode have been used since the beginnings of the DBD technology and are used in practical realizations. Following, different voltage mode power supplies for DBDs proposed in the literature are presented and the implications of using a voltage mode supply are analyzed.

Development

The first power sources used to produce the DBD, were sinusoidal high-voltage generators. To produce the sinusoidal high-voltage output, a voltage oscillator connected in cascade to a power amplifier and a step-up transformer was typically used [1.32, p. 54].

The sinusoidal voltage source was followed by unipolar and bipolar pulsed voltage supplies [1.33] obtaining higher power-to-optical lamp efficiencies when employed for DBD exciplex lamps [1.34, p. 56]. Voltage pulses generators have been used with DBD lamps in a pulse frequency range from 100 Hz up to hundred of kHz, reaching output

voltages of 12 kV and high electrical efficiencies of about 90% [1.35, p. 600]. An example of a high-voltage pulse supply schema, is presented in Fig.1.15-A.

In this topology the capacitor C is charged to the input voltage value through the high-side MOSFET and then its energy is released through the low-side MOSFET, the inductance and the Semiconductor Opening Switch (SOS) Diode. When the Diode turns-off and its recover ends up, interrupts the current discharge generating a nano-second voltage pulse of several times the DC input voltage at the output [1.35, p. 601]. According to this operating principle, the rise and fall times of the output voltage and consequently the current injected into the DBD, is determined by semiconductor switching times characteristics. Pulsed power supplies have been used in several applications of DBD [1.36–1.38].

Some of the first resonant converters operating in voltage mode for DBDs are reported in [1.20]. Among them, it can be highlighted the forward topology based converters, used in the industry for low power DBDs of about 20 W. A converter like the one in Fig.1.15-B make use of a series resonance to produce a continuous sinusoidal voltage excitation of the discharge. This continuous excitation impacts negatively the system performance as reported by [1.20, p. 1381], and the obtained lamp current is mainly a displacement current. Another resonant converter operating as a voltage-mode supply for a DBD reactor is found in [1.39].

Implications

Despite the characteristics of simplicity and low cost, the voltage-mode supply does not allow to make an analytical prediction and control of the DBD lamp power and its UV radiation. In order to elucidate this fact, the simplified DBD model is used here; before ignition the DBD excilamp is seen as a capacitor equal to C_{eq}, when this capacitor is connected to a voltage source its current is given by (1.2.5):
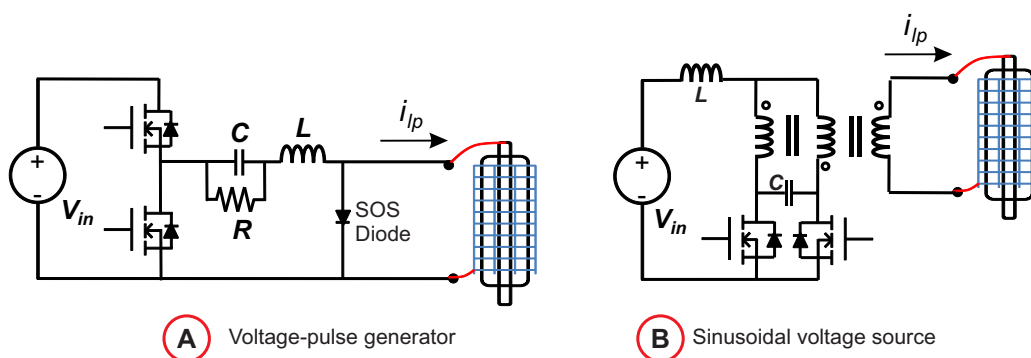
Figure 1.15.: Schematic of a voltage-pulse generator [1.35, p. 601] (A) and a Forward based sinusoidal voltage source [1.20] (B)

$$i_{lp} = C_{eq} \frac{\mathrm{d}v_{lp}}{\mathrm{d}t} \tag{1.2.5}$$

If the injected current is enough to produce the gas breakdown, the current injected into the discharge after breakdown, is calculated with (1.2.6):

$$i_{lp} = C_d \frac{\mathrm{d}\left(v_{lp} - V_{th}\right)}{\mathrm{d}t} \tag{1.2.6}$$

According to (1.2.6) the amplitude and duration of the current injected into the DBD, are highly dependent on the oscillations and on the rise and fall times of the lamp voltage waveform. In order to illustrate this fact, in Fig.1.16 simulation of a voltage source connected to the DBD equivalent circuit through a step-up transformer is shown. A parasitic inductance L_{lk} and a series resistance have been included, and the simulated DBD voltage and current are shown for two different values of L_{lk} with a sinusoidal voltage at v_{in}. For both values of L_{lk} the lamp voltage v_{lp} is very similar, however the current injected into the gas discharge, i_G, can not be controlled. In the case of a square-shape voltage source (Fig.1.16-right), the lamp peak current increases considerably compared to the sinusoidal voltage of the same amplitude and frequency, as expected from (1.2.6) due to the higher derivative values.

As can be observed in these simulated waveforms shown in Fig.1.16-bottom, when a voltage source is used to supply the DBD, the oscillations and slopes of the lamp voltage
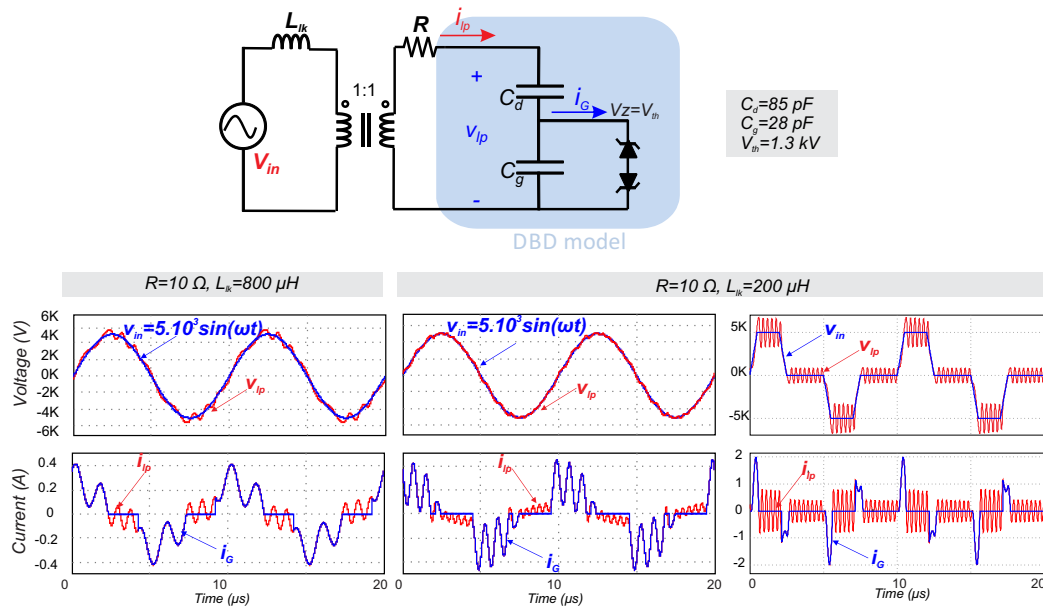
Figure 1.16.: Top: Schematic used for simulation of a voltage source connected to the DBD excilamp. Bottom: The DBD lamp voltage and current simulated waveforms, obtained for an imposed voltage are shown.

are very sensitive to the commutation times of the switches in the case of square-shape or pulsed waveforms, and to the parasitic elements of the converter, e.g. the switching times of the MOSFETs or the SOS Diode, the voltage source output impedance and the leakage inductance L_{lk}. These parameters are different from one device to another and change with the temperature, thus to determine the characteristics of the discharge and an analytical prediction of the gas breakdown and lamp power is not practical. In contrast, when the DBD current is controlled by means of a current-mode supply, the injected power does not depend on the hardly controlled changes of the lamp voltage waveform. Accordingly, the use of a current mode supply is the best choice to control the DBD excilamp power and to assure the repeatability of the converter operating point.

From the outlook presented in this Section, an evolution of the DBD power supplies, since the beginnings of this technology is evidenced. These developments have made of the DBD UV excilamps a commercially viable technology and nowadays this technology is found in industrial products. Next, the performance of some available DBD based commercial systems are presented.

1.3. Characteristics of Commercial DBD Excilamp Based Systems

Currently, commercial systems incorporating both DBD excilamps and its power supplies are available. Since 2001, *Ushio America Inc.* has proposed the development of excimer based UV systems for water treatment [1.40, 1.41]. *Heraeus* provides water treatment systems based on high power (3 kW) excimer UV systems [1.42, 1.43], which are water-cooled. They offer 172, 222, 282 and 308 nm radiation wavelenghts. The 222 nm and 282 nm systems are suggested for inactivation of microorganisms.

Another case is the *DBD ECG* power supply designed for the *Xeradex* excimer lamp by the enterprise *Osram Gmbh* which allows, as reported by the company, an irradiation efficiency of 40%. This level of efficiency is achieved thanks to the pulsed operating mode [1.44]. The circuit topology of this supply is not of public domain. Also for the *Xeradex* lamp, a converter based on the Forward topology, similar to the one presented in Fig.1.15-B and called *Single Switch Resonant Inverter with Energy Feedback* has been patented [1.20]. This resonant inverter is intended for lamp powers around 20 Watt.

In the side of the DBD excilamps performance, the typical efficiency of DBD-Excimer lamps is about 15% for lamps containing halogens (e.g. XeCl) and up to 40% for lamps containing only rare gases (e.g. Xe2) [1.4, 1.45]. The lifetimes are between 1000-5000 hours [1.4]. Typically the gas breakdown voltage is less than 10 kV, but depends on the gas pressure and the gap between electrodes; for lamps with large gap between electrodes, the breakdown voltage can be reduced by placing a metal wire inside the gas discharge region, this wire works as a guide for the first gas ignition [1.45].

Currently, the DBD excimer lamps perform levels of efficiency and lifetimes lower than those of commercial Mercury Low Pressure and Medium Pressure lamps. However its performances are acceptable by the industry for particular applications where the Mercury vapor content is not allowed, or where an specific radiation wavelength is

Figure 1.17.: Xeradex lamp by Osram

required. [1.46–1.48].

The commercial availability of DBD-Excimer lamps is mainly in the 172 nm radiation wavelength, which is recommended for industrial treatments. *Quark technology* sells excimer lamps in 172 and 222 nm, offering a lifetime of 2500 hours and an irradiation power up to 100 mW/cm2 [1.49]. *Ushio* produces excimer lamps and irradiation units in 126, 146, 172, 222 and 308 nm. They report an energy conversion efficiency of 10% [1.50]. The enterprise *Resonance Ltd.* offers an excimer lamp based reactor intended for wafer and LCD panel cleaning.This system radiates from 150 nm to 195 nm, with fluxes above 10 mW/cm2 [1.51].

Osram Gmbh also produces an excimer lamp called *Xeradex* (Fig.1.17) which is designed to radiate at 172 nm. The lamp specification predicts an irradiation efficiency of up to 40% thanks to the use of a pulsed mode power supply; instead of the 10% of radiation efficiency achieved with sinusoidal power supplies [1.44].

1.4. Summary

In this Chapter, the DBD excimer UV lamps and their power supplies have been described. From the works reviewed here it has been found that there is a need for a deeper research of the power supply impact over the DBD excilamp performance. On the basis of a DBD excilamp model, selected due to its usability for the power supply analytical design, the convenience of controlling the power injected into a DBD by means of its current was demonstrated and accordingly, some of the current mode supplies for DBDs already found in the literature were described. As a result is found that the use of the DCM brings the possibility to control the lamp power and to determine the current injected into the discharge and at the same time to control the UV radiation. Also the implications of using a voltage source to supply a DBD were explained. Finally, to highlight the relevance for industrial applications of the DBD UV excilamps, some commercial systems using this technology have been summarized.

Bibliography

[1.1] R. Hippler, H. Kersten, M. Schmidt, and K. H. Schoenbach, eds., *Low Temperature Plasmas: Fundamentals, Technologies and Techniques*. Wiley-VCH, 2 ed., Mar. 2008.

[1.2] Hartnett, James, *Transport Phenomena in Plasma*. Academic Press, Oct. 2007.

[1.3] X. Bonnin, H. Piquet, N. Naude, C. Bouzidi, N. Gherardi, and J.-M. Blaquiere, "Design of a current converter to maximize the power into homogeneous dielectric barrier discharge (DBD) devices," *The European Physical Journal Applied Physics*, July 2013.

[1.4] M. I. Lomaev, V. S. Skakun, E. A. Sosnin, V. F. Tarasenko, D. V. Shitts, and M. V. Erofeev, "Excilamps efficient sources of spontaneous UV and VUV radiation," *Physics-Uspekhi*, vol. 46, pp. 193–209, Feb. 2003.

[1.5] H. Piquet, S. Bhosle, R. Diez, M. Cousineau, M. Djibrillah, D. Le Thanh, A. N. Dagang, and G. Zissis, "Control of the UV flux of a XeCl dielectric barrier discharge excilamp through its current variation," *Quantum Electronics*, vol. 42, pp. 157–164, Feb. 2012.

[1.6] R. Diez, H. Piquet, M. Cousineau, and S. Bhosle, "Current-mode power converter for radiation control in DBD excimer lamps," *IEEE Transactions on Industrial Electronics*, vol. 59, no. 4, pp. 1912–1919, 2012.

[1.7] H. Piquet, S. Bhosle, R. Diez, and M. V. Erofeev, "Pulsed current-mode supply of dielectric barrier discharge excilamps for the control of the radiated ultraviolet power," *IEEE Transactions on Plasma Science*, vol. 38, pp. 2531–2538, Oct. 2010.

[1.8] R. Diez, H. Piquet, and S. Bhosle, "Control of the UV emission of an excimer lamp by means of a current-mode power supply," in *Industrial Electronics, 2009. IECON '09. 35th Annual Conference of IEEE*, pp. 3500–3505, IEEE, Nov. 2009.

[1.9] J. P. Verboncoeur, "Particle simulation of plasmas: review and advances," *Plasma Physics and Controlled Fusion*, vol. 47, p. A231, May 2005.

[1.10] A. Oda, Y. Sakai, H. Akashi, and H. Sugawara, "One-dimensional modelling of low-frequency and high-pressure xe barrier discharges for the design of excimer lamps," *Journal of Physics D: Applied Physics*, vol. 32, p. 2726, Nov. 1999.

[1.11] S. Bhosle, G. Zissis, J.-J. Damelincourt, A. Capdevila, K. Gupta, F. Dawson, and V. Tarasenko, "Implementation of an efficiency indicator in an electrical modeling of a dielectric barrier discharge lamp," in *Conference Record of the 2006 IEEE Industry Applications Conference, 2006. 41st IAS Annual Meeting*, vol. 4, pp. 1784–1790, 2006.

[1.12] L. T. Doanh, S. Bhosle, G. Zissis, and H. Piquet, "Estimation of the light output power and efficiency of a XeCl dielectric barrier discharge exciplex lamp using one-dimensional drift-diffusion model for various voltage waveforms," *IEEE Transactions on Industry Applications*, vol. 49, no. 1, pp. 331–340, 2013.

[1.13] S. Bhosle, G. Zissis, J. Damelincourt, A. Capdevila, K. Gupta, F. Dawson, and V. Tarasenko, "Electrical modeling of an homogeneous dielectric barrier discharge (DBD)," in *Fourtieth IAS Annual Meeting. Conference Record of the 2005*, vol. 4, pp. 2315–2319, IEEE, Oct. 2005.

[1.14] R. Díez, J.-P. Salanne, H. Piquet, S. Bhosle, and G. Zissis, "Predictive model of a DBD lamp for power supply design and method for the automatic identification of its parameters," *The European Physical Journal - Applied Physics*, vol. 37, no. 03, pp. 307–313, 2007.

[1.15] A. El-Deib, *Modeling of and Driver Design for a Dielectric Barrier Discharge Lamp*. Thesis, University of Toronto, Aug. 2010. PhD.

[1.16] A. Flores-Fuentes, R. Pena-Eguiluz, R. Lopez-Callejas, A. Mercado-Cabrera, R. Valencia-Alvarado, S. Barocio-Delgado, and A. de la Piedad-Beneitez, "Electrical model of an atmospheric pressure dielectric barrier discharge cell," *IEEE Transactions on Plasma Science*, vol. 37, pp. 128–134, Jan. 2009.

[1.17] M. A. Djibrillah, *Éléments de conception d'un générateur électrique pour l'alimentation d'un dispositif à décharge à barrière diélectrique (DBD)*. INPT, Apr. 2011.

[1.18] U. Kogelschatz, "Dielectric-barrier discharges: Their history, discharge physics, and industrial applications," *Plasma Chemistry and Plasma Processing*, vol. 23, no. 1, pp. 1–46, 2003.

[1.19] T. C. Manley, "The electric characteristics of the ozonator discharge," *Transactions of The Electrochemical Society*, vol. 84, pp. 83–96, Oct. 1943.

[1.20] W. Sowa and R. Lecheler, "Lamp driver concepts for dielectric barrier discharge lamps and evaluation of a 110 w ballast," in *Industry Applications Conference, 2004. 39th IAS Annual Meeting. Conference Record of the 2004 IEEE*, vol. 2, pp. 1379–1385, IEEE, 2004.

[1.21] R. Diez-Medina, *Alimentation de puissance d'une lampe exciplexe à décharge à barrière diélectrique, en vue du contrôle du rayonnement*. PhD thesis, INPT, Toulouse, 2008.

[1.22] R. Diez, H. Piquet, S. Bhosle, J.-M. Blaquiere, and N. Roux, "Design of a current converter for the study of the UV emission in DBD excilamps," in *IEEE International Symposium on Industrial Electronics, 2008. ISIE 2008*, pp. 62–67, 2008.

[1.23] H.-P. Daub, *Ein adaptives Impuls-EVG zum Betrieb von dielektrisch behinderten Gasentladungslampen.* PhD thesis, KIT Scientific Publishing, Karlsruhe, 2010.

[1.24] A. El-Deib, F. Dawson, G. van Eerden, S. Bhosle, G. Zissis, and T. D. Le, "Analysis and experimental validation of a new current-controlled driver for a dielectric barrier discharge lamp," *IEEE Transactions on Industry Applications*, vol. 47, no. 4, pp. 1971–1982, 2011.

[1.25] M. Cousineau, R. Diez, H. Piquet, and O. Durrieu, "Synthesized high-frequency thyristor for dielectric barrier discharge excimer lamps," *IEEE Transactions on Industrial Electronics*, vol. 59, no. 4, pp. 1920–1928, 2012.

[1.26] M. Meisser, R. Kling, and W. Heering, "Universal resonant topology for high frequency pulsed operation of dielectric barrier discharge light sources," in *2011 Twenty-Sixth Annual IEEE Applied Power Electronics Conference and Exposition (APEC)*, pp. 1180–1187, 2011.

[1.27] M. Meißer, *Resonant Behaviour of Pulse Generators for the Efficient Drive of Optical Radiation Sources Based on Dielectric Barrier Discharges.* PhD thesis, KIT Scientific Publishing, Karlsruhe, 2013.

[1.28] A. El-Deib, F. Dawson, and G. Zissis, "Transformer-less current controlled driver for a dielectric barrier discharge lamp using HV silicon carbide (SiC) switching devices," in *Energy Conversion Congress and Exposition (ECCE), 2011 IEEE*, pp. 1124–1131, IEEE, Sept. 2011.

[1.29] W.-S. Lee, K.-W. Chu, C.-F. Huang, L.-S. Lee, M.-J. Tsai, K.-Y. Lee, and F. Zhao, "Design and fabrication of 4h-sic lateral high-voltage devices on a semi-insulating substrate," *IEEE Transactions on Electron Devices*, vol. 59, no. 3, pp. 754–760, 2012.

[1.30] A. Bolotnikov, P. Losee, K. Matocha, J. Glaser, J. Nasadoski, L. Wang, A. Elasser, S. Arthur, Z. Stum, P. Sandvik, Y. Sui, T. Johnson, J. Sabate, and L. Stevanovic, "3.3kV SiC MOSFETs designed for low on-resistance and fast switching," in *2012 24th International Symposium on Power Semiconductor Devices and ICs (ISPSD)*, pp. 389–392, 2012.

[1.31] J. Alonso, C. Ordiz, M. Dalla-Costa, J. Ribas, and J. Cardesin, "High voltage power supply for ozone generation based on piezoelectric transformer," in *Conference Record of the 2007 IEEE Industry Applications Conference, 2007. 42nd IAS Annual Meeting*, pp. 1901–1908, 2007.

[1.32] M. I. Lomaev, V. S. Skakun, V. F. Tarasenko, and D. V. Shitts, "Excilamps based on xenon dimers excited by a barrier discharge," *Journal of Optical Technology*, vol. 79, no. 8, pp. 498–502, 2012.

[1.33] V. F. Tarasenko, A. V. Krivonosenko, M. I. Lomaev, V. S. Skakun, E. A. Sosnin, and D. V. Shitz, "High-power excilamps with short-pulse duration," in *Proc. SPIE*, vol. 4065, pp. 826–835, 2000.

[1.34] M. Lomaev, E. Sosnin, and V. Tarasenko, "Excilamps and their applications," *Progress in Quantum Electronics*, vol. 36, pp. 51–97, Jan. 2012.

[1.35] M. I. Lomaev, E. A. Sosnin, V. F. Tarasenko, D. V. Shits, V. S. Skakun, M. V. Erofeev, and A. A. Lisenko, "Capacitive and barrier discharge excilamps and their applications (review)," *Instruments and Experimental Techniques*, vol. 49, pp. 595–616, Oct. 2006.

[1.36] A. Shams Taleghani, A. Shadaram, and M. Mirzaei, "Effects of duty cycles of the plasma actuators on improvement of pressure distribution above a NLF0414 airfoil," *IEEE Transactions on Plasma Science*, vol. 40, pp. 1434–1440, May 2012.

[1.37] S. Zhang, W. Wang, L. Jia, Z. Liu, Y. Yang, and L. Dai, "Rotational, vibrational, and excitation temperatures in bipolar nanosecond-pulsed diffuse dielectric-barrier-discharge plasma at atmospheric pressure," *IEEE Transactions on Plasma Science*, vol. 41, pp. 350–354, Feb. 2013.

[1.38] T. Kuroki, T. Oishi, T. Yamamoto, and M. Okubo, "Bromomethane decomposition using a pulsed dielectric barrier discharge," *IEEE Transactions on Industry Applications*, vol. 49, pp. 293–297, Jan. 2013.

[1.39] S. Kalisiak, M. Holub, and T. Jakubowski, "Resonant inverter with output voltage pulse-phase-shift control for DBD plasma reactor supply," in *13th European Conference on Power Electronics and Applications, 2009. EPE '09*, pp. 1–9, 2009.

[1.40] Zoran Falkenstein, USHIO America Inc., "Development of an excimer UV light source system for water treatment." `http://www.revistavirtualpro.com/files/TIE04_200701.pdf`.

[1.41] Z. Falkenstein, "Dielectric barrier discharge-driven (V)UV light source for fluid treatment," July 2002.

[1.42] Heraeus Noblelight LLC., "High power excimer UV system." `http://www.heraeus-noblelight.com/media/webmedia_local/media/pdf/uv/UVP16E_high_power_excimer_system.pdf`.

[1.43] Heraeus Noblelight LLC., "Ultraviolet light for water treatment." `http://www.heraeus-noblelight.com/media/webmedia_local/media/pdf/uv/UVP06_EN_Wasser.pdf`.

[1.44] OSRAM GmbH, "Xeradex excimer lamps." `http://www.osram.com/osram_com/applications/industrial-applications/ozone-production/index.jsp`.

[1.45] A. Voronov, "Mercury free UV-light sources based on excimer lamps," in *17th International Conference on Gas Discharges and Their Applications, 2008. GD 2008*, pp. 501–504, 2008.

[1.46] I. Soloshenko, V. Y. Bazhenov, V. A. Khomich, V. V. Tsiolko, and N. G. Potapchenko, "Comparative research of efficiency of water decontamination by UV radiation of cold hollow cathode discharge plasma versus that of low- and medium-pressure mercury lamps," *IEEE Transactions on Plasma Science*, vol. 34, no. 4, pp. 1365–1369, 2006.

[1.47] WOLFGANG HEERING, "UV SOURCES – basics, properties and applications," *IUVA NEWS*, vol. 6, pp. 7–13, Dec. 2004.

[1.48] S. Schalk, V. Adam, E. Arnold, K. Brieden, A. Voronov, and H. D. Witzke, "UV-lamps for disinfection and advanced oxidation–Lamp types, technologies and applications," *IUVA news*, vol. 8, no. 1, p. 32–37, 2006.

[1.49] Quark Technology Co. Ltd., "Products information - excimer VUV lamp." `http://www.quark-tec.com/english/product/5.html`.

[1.50] USHIO Inc., "Excimer lamps and excimer irradiation unit." `http://www.ushio.co.jp/en/products/list/lamp/lamp_10.html`.

[1.51] Resonance Ltd., "REX4 excimer lamp." `http://www.resonance.on.ca/rex4.htm`.

2. Parametric Control of the DBD Excilamp Electrical Power

In accordance with the objectives proposed for this doctoral study, the first work is focused on the theoretical development and implementation of a square-shape current mode power supply capable of controlling the power injected into a DBD excimer lamp.

In the proposed converter the current supplied to the lamp has a square-shape controlled by means of three Degrees Of Freedom (DOF): amplitude, duty cycle and frequency, parameters that provide full control of the DBD excilamp electrical power. The design and application of this converter to supply DBD excilamps is a novelty and provides a scientific tool for the study of this type of lamps.

This Chapter is organized as follows: firstly, the possibility of adjusting the lamp power by means of a square-shape lamp current control is demonstrated based on the equivalent electrical model of the DBDs. Then, we explain the design and implementation of a converter that controls the lamp current and finally measurements of the obtained operating range are presented. As a consequent study, in Chapter 3, the exploitation of this converter for the study of a DBD excilamp, is demonstrated.

In the context of this research, the converter presented here was published in [2.1], [2.2] exposing the first results of the UV radiation study of a XeCl lamp using the square-shape converter.

2.1. Control of Lamp Power with Three Degrees of Freedom

Here, using the equivalent electrical model for the DBD excilamp and results from previous research works, the feasibility and convenience of a power controller based on a square-shape current mode supply, for this lamp technology, are demonstrated.

The DBD excilamp model used for the converter design is the simplified equivalent electrical circuit described in Section 1.1.3 (Fig.1.5). This model has been chosen from the different approximations reviewed in Section 1.1.3, because it is well adapted for theoretical calculations (analytical converter design) and also for circuit simulation. From this model, a current-waveform suitable for a versatile control of the DBD power is suggested.

2.1.1. Choice of the Current Waveform

In previous works a great similarity between the lamp current and the instantaneous UV radiation waveforms has been shown [2.3], [2.4], where the UV amplitude depends directly on the lamp current intensity. Also, the lamp conversion efficiency (electrical

to UV) has been shown to depend on the lamp current frequency. In order to extent the previous study and to analyze the relationship between the current injected to the lamp and its UV radiation, we propose to supply the DBD lamp with a square-waveform current defined by three DOF: amplitude (J), frequency (f_{lp}) and duty cycle (D_{lp}), as presented in Fig.2.1. This current has zero average value in order to avoid indeterminate growing of the lamp voltage.
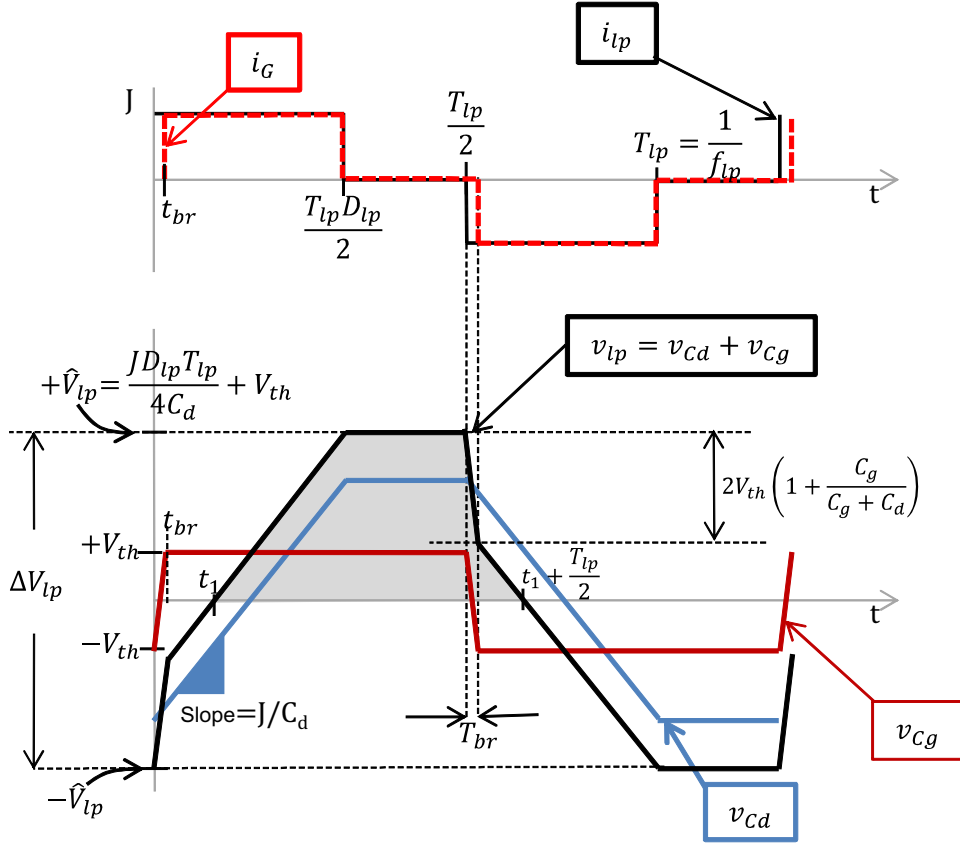
Figure 2.1.: Square-waveform current applied to the lamp i_{lp}, the gas conductance current i_G (top) and voltages calculated using the lamp model (bottom).

In the same Fig.2.1, voltages for the lamp (v_{lp}), the dielectric barriers (v_{Cd}) and the gas (v_{Cg}) are calculated using the model of Fig.1.5. Note that a time T_{br} is required to invert the current direction in the gas conductance.

2.1.2. Lamp Power Computation

Assuming the square-waveform in the lamp current and using the lamp model of Fig.1.5, an expression for the electrical power supplied to the lamp (P_{lp}) is deduced hereafter.

In the equivalent electrical model of the lamp, all the energy transferred from the

supply to C_d and to C_g produce reactive power; the only element that dissipates power is the gas conductance (G) after gas breakdown. According to this model, when the lamp is ignited the gas voltage remains constant; in consequence, the active lamp power depends solely on the current injected into G. The amplitude of this conductance current (i_G) is the same as for the lamp current (J) once breakdown has been obtained, as shown in Fig. 2.1.

To find an expression for the lamp power, the first step is to calculate T_{br}, the breakdown time, necessary to charge C_g from $-V_{th}$ to V_{th}, when J is applied (2.1.1). In this time interval, G is equal to zero and no power is dissipated.

$$T_{br} = \frac{2V_{th}C_g}{J} \qquad\qquad (2.1.1)$$

After breakdown, the current J will flow through the gas conductance. As the gas voltage is assumed constant, the average lamp power, P_{lp}, is computed using (2.1.2):

$$P_{lp} = \frac{2}{T_{lp}} \int_{T_{br}}^{D_{lp}T_{lp}/2} V_{th}J \, \mathrm{d}t \qquad\qquad (2.1.2)$$

By replacing (2.1.1) in (2.1.2), P_{lp} is obtained (2.1.3) as a function of the current parameters. This equation demonstrates that the electrical power of the lamp can be effectively adjusted by means of the three DOF: J, f_{lp} and D_{lp}.

$$P_{lp} = JD_{lp}V_{th} - 4f_{lp}C_gV_{th}^2 \qquad\qquad (2.1.3)$$

This expression can be verified with the Manley's power equation (1.2.4), which depends on $\hat{V}_{lp}$. In this case $\hat{V}_{lp}$ is computed by superposition of the v_{Cd} and v_{Cg}. The total voltage change in the lamp during the injection of each pulse current, ΔV_{lp} in Fig.2.1, is expressed as the sum of the net voltage change in the equivalent capacitors (2.1.4):

$$\Delta V_{lp} = 2\hat{V}_{lp} = \Delta V_{Cd} + \Delta V_{Cg} \qquad\qquad (2.1.4)$$

The net voltage change in C_d during each current pulse is determined by the capacitor voltage equation (2.1.5):

$$\Delta V_{Cd} = \frac{1}{C_d} \int_0^{D_{lp}T_{lp}/2} J \, \mathrm{d}t = \frac{JD_{lp}T_{lp}}{2C_d} \qquad\qquad (2.1.5)$$

And during the same time interval the voltage change in C_g is always equal to $2V_{th}$. Solving (2.1.4), $\hat{V}_{lp}$ is found (2.1.6):

$$\hat{V}_{lp} = V_{th} + \frac{JD_{lp}T_{lp}}{4C_d} \qquad\qquad (2.1.6)$$

Replacing (2.1.6) in the Manley's equation (1.2.4), expression (2.1.3) is found and consequently the two different approaches are validated.

2.2. Square-shape Current Supply Design

To generate the current proposed in Section 2.1, a converter composed of two main blocks connected in cascade is used: a constant current source and a full-bridge current inverter with the lamp as load (Fig.2.2). This structure was previously used in [2.2] and is similar to the classical single-phase current-source inverter [2.5, p.142]. Comparable solutions have been proposed before for ozone generators [2.6] and for the dimming of HID lamps [2.7–2.9]. In the converter proposed here, the control signals for the current source and for the inverter are independent. Hence, the current amplitude is only controlled by the current source; the frequency and the duty cycle are only governed by the current inverter operation, which is described as follows.
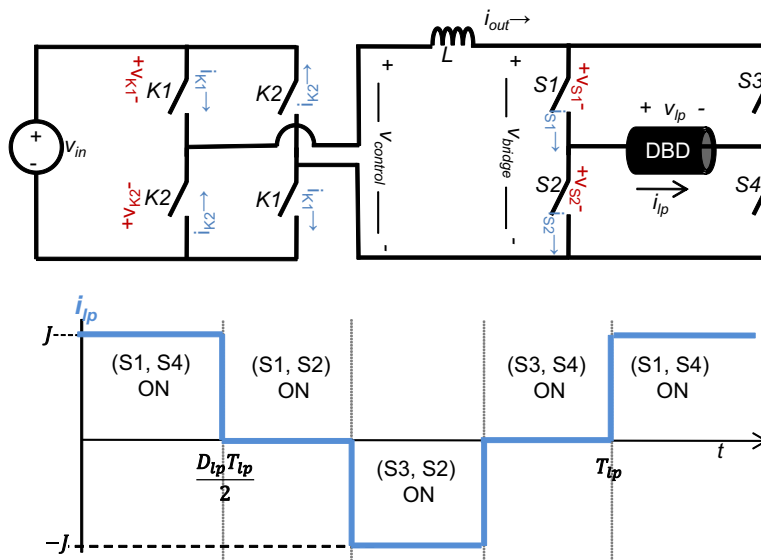
Figure 2.2.: Topology of the two-quadrant chopper based DBD Power Supply

2.2.1. Current Inverter Operation

The output of the DC current source, i_{out}, is connected directly to this inverter (Fig.2.2) and the direction of the lamp current, i_{lp}, is determined by the switching sequence of the full-bridge as shown in Fig.2.3. With only the switches (S1, S4) turned-on, the lamp current will flow in the positive sense; turning ON the pair (S3, S2) the current will have the opposite direction. In order to have zero current in the lamp, without interruption of the i_{out} current path, one of the inverter legs is closed, (S1, S2) or (S3, S4). In this way, the bridge operating frequency is equal to f_{lp}. Next, according to this operating sequence the inverter switches are synthesized.
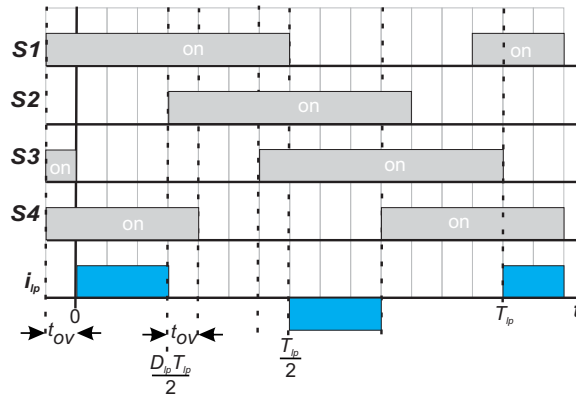
Figure 2.3.: Example sequence of the inverter switches control signals

Inverter Switches Synthesis

To find the inverter switches characteristics, their voltages and currents waveforms are found. When (S1,S4) are ON, their current is positive (i_{s1}) and the voltage across S2 (v_{s2}) and S3 is the same and equal to v_{lp}; when (S2,S3) are ON also with positive current (i_{s2}), the voltage across S1 (v_{s1}) and S4 is also the same and equal to $-v_{lp}$. The voltage and current waveforms for the switches S1 and S2 are shown in Fig.2.4-top for a particular operating case. Accordingly, the characteristic of the inverter switches is determined, as shown in Fig.2.4-bottom.
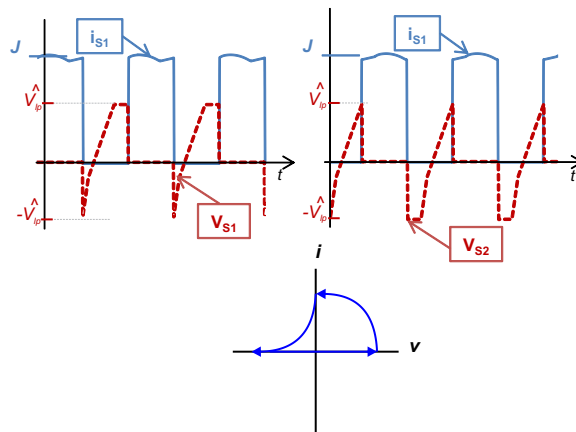
Figure 2.4.: Inverter switches characteristic.

This characteristic corresponds to:

- Bipolar voltage blocking.

- Unidirectional current conduction.

Analyzing the switching conditions which appear in Fig.2.4, the switch presents controlled turn-on under positive voltage and spontaneous turn-off. These properties define a thyristor-like device [2.10]. To implement this two-quadrant switch, a MOSFET device in series with a Diode is used. The MOSFET can be turned-on in the presence of positive voltages and its commutation times are appropriate for the typical operating range of the DBD excilamps. The Diode provides the negative voltage blocking characteristic. The gate signal of each MOSFET is enabled with a duty cycle of almost 50%, according to the time diagram of the control signals presented in Fig.2.3. In this sequence an overlapping time, t_{ov}, between the signals is observed. This overlapping is necessary in practice to avoid an open circuit event, which is non-compatible with the current source output.

As the current source is assumed to be constant during each inverter period, the positive and negative pulses of the lamp current have the same amplitude. In consequence, the zero current average condition is guaranteed by the control of the inverter, injecting the positive and the negative current during the same time.

2.2.2. Constant Current Source

In the topology presented above, the H-bridge is supplied with a constant current. Given the cascade connection between the current source and the inverter, the voltage seen at the current source output is equal to v_{bridge}. According to the inverter operation sequence, v_{bridge} is given by (2.2.1):

$$v_{bridge} = \begin{cases} v_{lp}, & \text{if (S1,S4) are ON} \\ -v_{lp}, & \text{if (S2,S3) are ON} \\ 0, & \text{if (S1,S2) or (S3,S4) are ON} \end{cases} \qquad (2.2.1)$$
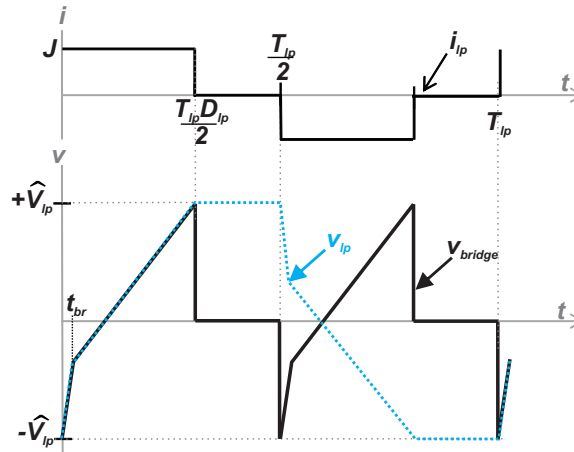
Figure 2.5.: Theoretical waveform of v_{bridge} according to (2.2.1)

In Fig.2.5 the v_{bridge} waveform is shown for a particular operating case. Considering that v_{bridge} is a bipolar voltage, a convenient configuration to implement this DC current source is the two-quadrant chopper topology [2.11] (Fig.2.2) because this topology allows to produce also a bipolar voltage ($v_{control}$) to control the current even in the presence of a negative voltage at the converter output (v_{bridge}).

Other current source topologies, as the one proposed in [2.6] and [2.12] are configurations adapted to drive fast output voltage dynamics. However, because of their simplicity and robustness to drive a bipolar voltage output, the two-quadrant chopper has been chosen. To guarantee a proper operation of the chopper, a right choice of its controller must be done. Next, the characteristics of the controller for this 2-quadrant chopper are analyzed.

2-Quadrant Chopper Controller

To define the type of controller for the current source, the properties of the supplied load are determinant. In the proposed topology, the current source output supplies the full-bridge inverter which is connected itself to the DBD. This type of load is affected by fast voltage transitions, produced by:

- The switching nature of the bridge.

- The non-linear behavior of the DBD.

- The lamp dynamic response that is not considered in the DBD model used; in the practice and differing from the simplified DBD model, the gas breakdown is not instantaneous and produce voltage oscillations at the breakdown instant. In this sense, a more accurate representation of the gas conductance is found in [2.13].

Moreover, the lamp electrical model used for the design of this converter has been identified in steady-state conditions. For these reasons, and because of its well-known robustness and fast response, a hysteresis law is a good choice to implement the current controller.

The operation of this hysteretic controller is described as follows. An hysteresis gap, $\Delta hyst$, determines the upper and lower limits for the current ripple, i_{max} and i_{min} respectively. When i_{out} reaches i_{max}, K2 (in Fig.2.2) is turned-on (K1 turned-off) thus $v_{control}$ is equal to $-V_{in}$ decreasing i_{out} even in the presence of a negative voltage in the current source output (v_{bridge}). Then when i_{out} becomes equal to i_{min}, K1 is turned-on and K2 turned-off, consequently $v_{control}$ is equal to V_{in} and i_{out} increases. According to this operating principle, this controller works at variable frequency.

Controller Operating Frequency

The operating frequency f_c of this hysteretic controller depends on the hysteresis gap, the inductance value of L, the input (V_{in}) and the output voltage (v_{bridge}). Depending on the values of these parameters, two operating cases are possible: $f_c > f_{lp}$ and $f_c <$

f_{lp}. Taking into account that the typical operating frequency of the excilamps is in the range of hundreds of kHz, the case where f_c is higher than f_{lp} implies the use of devices for the current control loop with switching capabilities in the order of MHz and also high switching losses. For example, currently available Hall-effect AC-DC current sensors, necessaries to implement the controller have bandwidths of maximum 150 kHz. Therefore, the operation of the hysteretic control at $f_c < f_{lp}$ is chosen. Next, the necessary conditions to ensure this operating case are deduced.

The value of f_c is smaller than f_{lp} if the variation of i_{out} during one period of v_{bridge} ($T_{lp}/2$ in Fig.2.5), defined here as Δi_{out}, is equal or less than the hysteresis window $\Delta hyst$, as illustrated in Fig.2.6.
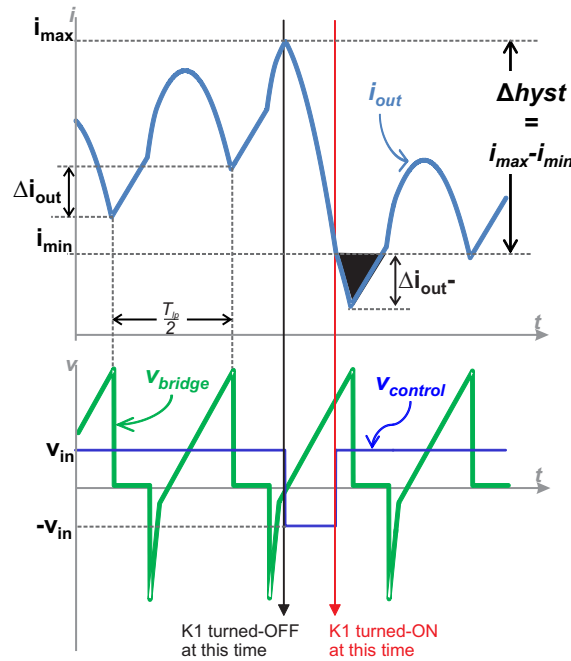
Figure 2.6.: Output current ripple with $f_c < f_{lp}$ (top) with the corresponding inverter and control voltage (bottom). A current spike exceeding the hysteresis limits is observed, this spike occurs because $V_{in} < \hat{V}_{lp}$.

The net change of i_{out} during $T_{lp}/2$, Δi_{out}, is calculated with the inductance current equation in terms of the inductance voltage. We define the variable $k1 = -1$ for K1 OFF and $k1 = 1$ otherwise, to provide an expression for Δi_{out}, in terms of the switch state (2.2.2):

$$\Delta i_{out}(k1) = \frac{1}{L} abs\left(\int_0^{T_{lp}/2} (V_{in}k1 - v_{bridge}) \, \mathrm{d}t \right) \tag{2.2.2}$$

Solving the integral for V_{in}, (2.2.3) is expressed as (2.2.3):

$$\Delta i_{out}(k1) = \frac{1}{L}.abs\left(\frac{k1.V_{in}T_{lp}}{2} - \int_0^{T_{lp}/2} v_{bridge}\,\mathrm{d}t\right) \tag{2.2.3}$$

Given that v_{bridge} is equal to v_{lp} during the duty cycle and zero in the rest of the time interval (2.2.1), we can write (2.2.4):

$$\int_0^{T_{lp}/2} v_{bridge}\,\mathrm{d}t = \int_0^{T_{lp}D_{lp}/2} v_{lp}\,\mathrm{d}t \tag{2.2.4}$$

v_{lp} is equal to the sum of v_{Cd} and v_{Cg}, and as can be inferred from Fig.2.1, the integral of v_{Cd} is equal to zero for the same time span. Consequently (2.2.5):

$$\int_0^{T_{lp}/2} v_{bridge}\,\mathrm{d}t = \int_0^{T_{lp}D_{lp}/2} v_{Cg}\,\mathrm{d}t \tag{2.2.5}$$

Solving (2.2.5) and replacing in (2.2.3) is found (2.2.6):

$$\Delta i_{out}(k1) = \frac{1}{L}.abs\left(\frac{k1.V_{in}T_{lp}}{2} + V_{th}\left(\frac{T_{lp}D_{lp}}{2} - T_{br}\right)\right) \tag{2.2.6}$$

For $k1 = 1$, we obtain the i_{out} increment during $T_{lp}/2$ and for $k1 = -1$, the decrement for the same time span. And now the period of the controller T_c, is calculated as a function of T_{lp}, with the necessary number of i_{out} increments and decrements to cover the hysteresis window ($\Delta hyst$ in Fig.2.6) and multiplying by the v_{bridge} period (2.2.7):

$$T_c = \left(\frac{\Delta hyst}{\Delta i_{out}(1)} + \frac{\Delta hyst}{\Delta i_{out}(-1)}\right)\frac{T_{lp}}{2} \tag{2.2.7}$$

With (2.2.8),

$$\Delta hyst = i_{max} - i_{min} \tag{2.2.8}$$

Solving, we obtain the switching frequency of the hysteretic controller (2.2.9):

$$f_c = \frac{2\left(\left(\frac{V_{in}T_{lp}}{2}\right)^2 - V_{th}^2\left(\frac{T_{lp}D_{lp}}{2} - T_{br}\right)^2\right)}{L\Delta hyst V_{in}T_{lp}^2} \tag{2.2.9}$$

Maximizing (2.2.9) with $D_{lp} = 0$ and T_{br} small enough to be neglected, we obtain the minimum value of L (2.2.10), in order to assure an f_c always below the maximum desired frequency of the hysteretic controller, f_{cmax}:

$$L = \frac{V_{in}}{2f_{cmax}(\Delta hyst)} \tag{2.2.10}$$

In the other controller operating case, with f_c higher than f_{lp}, (2.2.6) is no more valid. In this case f_c changes with the instantaneous value of v_{bridge} and is calculated based on the time it takes i_{out} to go over the hysteresis gap, T_{gap}, (2.2.11), with $T_{gap} < T_{lp}/2$:

$$\Delta hyst = \frac{1}{L} \int_{t_o}^{t_o + T_{gap}} (k1 V_{in} - v_{bridge}) \, \mathrm{d}t \qquad (2.2.11)$$

Additionally, as can be observed in (2.2.6), the increment and decrement of i_{out} depends on the value of V_{in} and also V_{in} allows to limit the controller frequency (2.2.9). Following, the impact of the V_{in} value on the chopper operation is analyzed.

Main DC Input Voltage of the 2-Quadrant Chopper

According to the hysteretic controller operation described in Section 2.2.2, the inductance input port ($V_{control}$) is connected to V_{in} or $-V_{in}$ in order to increase or decrease i_{out}, respectively. Therefore, to assure an instantaneous control of i_{out} independently of the inverter and the controller operating frequencies (f_{lp} and f_c respectively), V_{in} must be greater than the positive peak value of v_{bridge}, and $-V_{in}$ smaller than the negative peak value of v_{bridge}, which are $\hat{V}_{lp}$ and $-\hat{V}_{lp}$ in that order (Fig.2.1).

However, a lower value of V_{in} can be used. If V_{in} is smaller than $\hat{V}_{lp}$ but greater than the average value of v_{bridge}, the instantaneous control characteristic is lost but, as demonstrated below, control of the average of i_{out} is still possible and accurate. This property is useful if a voltage source greater than $\hat{V}_{lp}$ is not available, if the cost of the system should be reduced or to reduce f_c (2.2.9).

To compute the average value of v_{bridge} (2.2.12) we consider half the lamp period (2.2.12):

$$\bar{v}_{bridge} = \frac{2}{T_{lp}} \int_0^{T_{lp}/2} v_{bridge} \, \mathrm{d}t \qquad (2.2.12)$$

Using the expression previously deduced in (2.2.5) and replacing in (2.2.12), $\bar{v}_{bridge}$ is found (2.2.13):

$$\bar{v}_{bridge} = \frac{V_{th} (D_{lp} T_{lp} - 2 T_{br})}{T_{lp}} \qquad (2.2.13)$$

To find the minimum necessary V_{in}, we take the maximum value for the average of v_{bridge}. The worst case is obtained for D_{lp}=1 and T_{br} much smaller compared to T_{lp}; in this case $\bar{v}_{bridge} = V_{th}$. Then V_{in} should be selected greater than V_{th} to control i_{out} in average. If this condition is fulfilled, as can be deduced from (2.2.6), an increment and decrement of i_{out} can be always accomplished. Nevertheless in this case instantaneous control of i_{out} is not possible because the current can exceed the hysteresis limits, as explained below.

When K2 is turned-on (K1 turned-off) in order to decrease i_{out} and this commutation instant coincides with a value of v_{bridge} more negative than -V_{in}, i_{out} will continue to increase until $v_{bridge} > -V_{in}$. In a similar manner, when K1 is turned-on (K2 turned-off) to rise the current value, i_{out} will continue to fall if the v_{bridge} instantaneous value is higher than V_{in} ($\Delta i_{out}(k1 = -1)$ in Fig.2.6). In consequence, in some cases i_{out} can present spikes exceeding the hysteretic limit points (i_{max}, i_{min} in Fig.2.6), however the

maximum value of these spikes can be determined.

With the aim to compute the maximum current value beyond the hysteresis limits (and on this basis choose the value of the inductance L), we use (2.2.2). Given the fact that there is no synchronization between the controllers of the current source and of the inverter, the maximum possible value for the inductance current is computed for the worst cases.

The first case happens when the control circuit turns K1 on, exactly when v_{bridge} is rising and equal to V_{in} (2.2.14):

$$\Delta i_{out-} = \frac{(JD_{lp}T_{lp} + 4C_d(V_{th} - V_{in}))^2}{32JLC_d} \tag{2.2.14}$$

The second case appears if K1 is turned-off when v_{bridge} has reached its most negative value (2.2.15):

$$\Delta i_{out+} = \frac{C_{eq}(-4C_{eq}V_{th} + JD_{lp}T_{lp} + 4C_d(V_{th} - V_{in}))^2}{32JLC_d^2} \tag{2.2.15}$$

This over current spike above i_{max} or below i_{min} cannot be governed by the hysteretic control law ($V_{in} < \hat{V}_{lp}$, $f_c < f_{lp}$), instead, it must be limited using the appropriate value of L. From expressions (2.2.14) and (2.2.15), observe that always $\Delta i_{out-} > \Delta i_{out+}$, hence the worst case for the current spike is given by Δi_{out-} (2.2.14). Accordingly, from (2.2.14) the value of L is calculated in (2.2.16) to obtain the maximum tolerated amplitude for Δi_{out-}, defined here as Δi_{out_x} :

$$L = \frac{(JD_{lp}T_{lp} + 4C_d(V_{th} - V_{in}))^2}{32JC_d\Delta i_{out_x}} \tag{2.2.16}$$

The excess of current beyond the hysteresis limits, computed in (2.2.14) and (2.2.15), is considered as an error on the current control law. As explained before, this error could be avoided using a value of V_{in} higher than $\hat{V}_{lp}$. Nevertheless, an appropriate selection of L reduces this error to a negligible level for $V_{th} < V_{in} < \left|\hat{V}_{lp}\right|$.

The minimum value of L to obtain a maximum error Δi_{out_x} equal to 5 % of J has been plotted as a function of V_{in} in Fig.2.7 (dashed line). This value of L is smaller as V_{in} increases. In contrast, the required L to obtain $f_{cmax} \leq 40\ kHz$, also plotted in Fig.2.7 (solid line), increases linearly with V_{in} (2.2.10). Accordingly, both equations (2.2.10) and (2.2.16), must be evaluated to determine which one defines the minimum value of L.

DC Current Source Switches Synthesis

The Voltage-Current characteristic for K1 and K2 switches is plotted in Fig.2.8. Obtaining for K1 positive voltage blocking and uni-directional current conduction, with controlled turn-off and turn-on. For K2, negative voltage blocking and unidirectional current conduction, with spontaneous turn-off and turn-on under negative voltage. Accordingly the classical MOSFET and diode switching cells are selected.
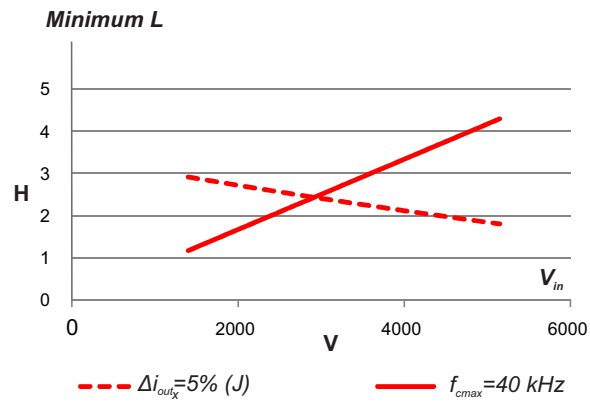
Figure 2.7.: Minimum value of L as a function of V_{in} to obtain: a controller operating frequency below 40 kHz (solid line) and a maximum controller error equal to 5% of J (dashed line). Values calculated using (2.2.10) and (2.2.16) respectively, with the following parameters: $\Delta hyst = 5\%(J)$, V_{th}=1.3 kV, C_d=85 pF, D_{lp}=1, f_{lp}=50 kHz, J=300 mA.
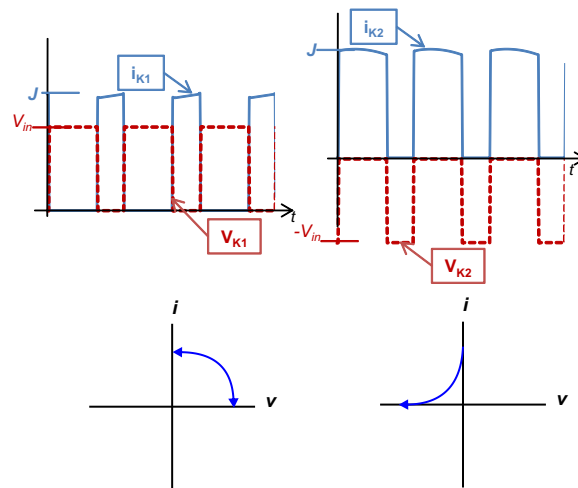
Figure 2.8.: Current source switches characteristic.

At this point, the design of the inverter and two-quadrant chopper has been completed. In order to implement this converter, the characteristics of the lamp to be supplied and the desired operating range must be established.

2.3. Considerations for implementation

The equivalent electrical parameters of the DBD excilamp to be supplied are presented in Table 2.1. These values are used to dimension the converter components, and to establish the acceptable range of the three D.O.F. (J, f_{lp}, D_{lp}).

V_{th}	C_d	C_g	P_{lp}
1310 V	85 pF	27 pF	100 W

Table 2.1.: Equivalent electrical parameters of a XeCl DBD Excilamp

2.3.1. Frequency of the Lamp Current

f_{lp} will be varied from 50 kHz up to 200 kHz; this range has been selected on the basis of previous results presented in [2.14, p. 203], [2.4, p. 1917] and [2.15, p. 1980], concerning the discharge regime and the lamp efficiency.

2.3.2. Output Current and Voltage

The aim of the following calculations is to find the value of the power that can be transferred to the lamp as a function of the lamp peak voltage (or vice versa).

During one current pulse, positive or negative, the lamp voltage changes according to (2.3.1), as depicted on Fig.2.1:

$$\Delta v_{lp} = 2V_{th} + \frac{2V_{th}C_g}{C_d} + \frac{1}{C_d}\int_{t_{br}}^{t_{off}} i_{lp}\,\mathrm{d}t = 2\hat{V}_{lp} \tag{2.3.1}$$

The first and second term of (2.3.1) correspond to the voltage change in the [0-t_{br}] time interval for C_g and C_d respectively. The third term is the voltage change of C_d from t_{br} until the discharge dies out at t_{off}.

Reorganizing (2.3.1), an expression, which corresponds to the electrical charge transferred to the lamp capacitance after gas breakdown (C_d), is obtained for the positive current sequence (2.3.2):

$$\int_{t_{br}}^{t_{off}} i_{lp}\,\mathrm{d}t = Q_{Cd}(t_{br} \rightarrow t_{off}) = 2C_d\left(\hat{V}_{lp} - \frac{V_{th}C_g}{C_{eq}}\right) \tag{2.3.2}$$

The same Q_{Cd} is transferred during the negative current pulse because it is symmetrical to the positive one. During each lamp current cycle, two current symmetrical pulses are injected into the lamp, thus the power is calculated as twice f_{lp} multiplied by the energy injected into the discharge by each current pulse (2.3.3):

$$P_{lp} = 2f_{lp}V_{th} \int_{t_{br}}^{t_{off}} i_{lp} \, \mathrm{d}t \tag{2.3.3}$$

Replacing (2.3.2) in (2.3.3) and solving to find $\hat{V}_{lp}$, we obtain (2.3.4):

$$\hat{V}_{lp} = \frac{P_{lp}}{4f_{lp}V_{th}C_d} + \frac{V_{th}C_g}{C_{eq}} \tag{2.3.4}$$

This equation, which is a form of the Manley's DBD power formula (1.2.3) ([2.16]), has been validated, during the work development, using simulation of the converter with the PSIM® software. Here it is possible to see that for a given lamp operating frequency, the peak voltage across the lamp is a function only of the power injected into the lamp.

According to the characteristics of the DBD excilamp provided in Table 2.1, to provide 100 W of electrical power at $f_{lp} = 50kHz$ and $D_{lp} = 90\%$, a maximum $\hat{V}_{lp}$ of 6.2 kV and J of 92 mA are calculated using (2.3.4) and (2.1.3) respectively. Fig.2.9 presents the obtained P_{lp} for different values of $\hat{V}_{lp}$ as a function of the current frequency, calculated using the Manley's equation (1.2.4) and the DBD excilamp equivalent parameters in Table 2.1.
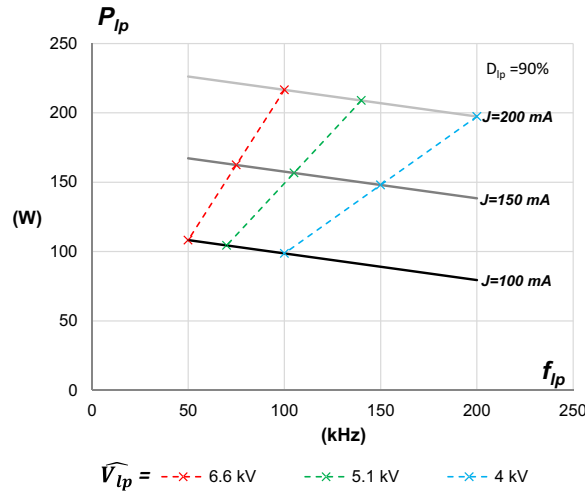
Figure 2.9.: Lamp power as a function of the lamp current frequency, for different values of $\hat{V}_{lp}$.

2.3.3. The Step-up Transformer

Currently available commercial MOSFET technology cannot drive the lamp peak voltage of 6 kV required for the supply of this lamp, leading to the use of a step-up high voltage transformer between the full bridge inverter and the excilamp. After an evaluation of their availability, price, ON resistance, power capability and the operating frequency range, the MOSFETs rated up to 1 kV of Drain-Source voltage, are considered for the

converter implementation. As a reference, some high-voltage MOSFET devices specifications are compared in Table 2.2. Accordingly, with a maximum peak voltage about 6kV in the secondary winding and a safety margin of approximately 40% the MOSFET voltage rating, a minimum transformation ratio of 10 is determined.

$Reference$	$V_{dss}(kV)$	$R_{DS-ON}(\Omega)$	$P(W)$	$Price(USD\$)$
IXTF02N450	4.5	750 @ 10mA	78	32.4
IXTT1N450HV	4.5	85 @ 50mA	520	37
IXTX5N250	2.5	8.8 @ 2.5A	960	80.36
GA04JT17-247	1.7	0.5 @ 4A	91	31
TSTP4N150	1.5	7 @ 2A	160	6.47
IXTA3N120TRL	1.2	4.5 @ 500mA	200	3.405
STP8NK100Z	1	1.85 @ 3.15A	160	3.97
IPI90R500C3	0.9	0.5 @ 6.6A	156	4.1
STW11NM80	0.8	0.4 @ 5.5A	150	3.9

Table 2.2.: Comparison of some High-Voltage MOSFET devices specifications (Source: *www.digikey.com*)

As mentioned in Section 1.2.2, the transformer, with its parasitic components, introduces new elements in the converter circuit; the impact of the transformer on DBD supplies has been previously studied in [2.17, p.106-112], [2.18, Chap.3], [2.11, 2.19]. The aim of this section is to analyze the impact of these parasitic elements in the operation of this specific current mode power supply intended for DBD excilamps, including the effect of grounding the transformer. This analysis was published in [2.20] as part of this doctorate research.

For the analysis to be done in this work, a classical transformer equivalent circuit model, shown in Fig.2.10 is used. It takes into account two main parasitic elements found in the literature: the leakage inductance L_{lk} and the magnetizing inductance L_m [2.5] and due to the capacitive nature of a DBD excilamp, the transformer total self-capacitance C_p [2.21] is also included.
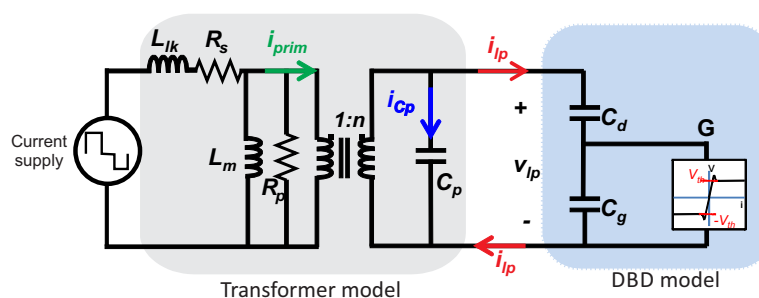
Figure 2.10.: Transformer model with the parasitic elements

Here, each one of the transformer parasitic elements effects are explained and mathe-

matical expression to evaluate their impact are deduced.

Influence of the Parasitic Capacitance

This parasitic capacitance C_p appears in parallel to the lamp (Fig.2.10). Given the capacitive nature of the excilamp, if C_p is comparable to the lamp equivalent capacitance, an important amount of the supply output current i_{prim} injected into the primary winding will flow through C_p, thus affecting the waveform and amplitude of i_{lp} and even forbidding the lamp ignition. The equivalent lamp capacitance is defined as:

- Before gas ignition, the dielectric capacitance C_d in series with C_g.

- Once the gas voltage v_{Cg} reaches V_{th}, the lamp ignition occurs and the gas voltage v_{Cg} remains almost constant, consequently the equivalent capacitance of the lamp is only C_d.

Before the gas ignition, the current divider between C_p and C_{eq} defines how much current is available to produce the gas breakdown (2.3.5):

$$i_{lp} = \frac{i_{prim} C_p}{n\left(C_p + C_{eq}\right)} \qquad (2.3.5)$$

And after breakdown the current divider between C_p and C_d determines how much current is available to hold up the discharge and to transfer power into the gas (2.3.6). In order to reduce this effect, the smallest possible value for C_p is needed.

$$i_{lp} = \frac{i_{prim} C_p}{n\left(C_p + C_d\right)} \qquad (2.3.6)$$

Influence of the Leakage Inductance

By reflecting v_{lp} to the primary side and assuming a constant lamp voltage V_{lp} during the overlap time interval in which S1, S4 and S2 are in ON state, the time it takes for i_{out} to change its value from I_{dc} to zero is T_{lk}, n being the transformer turn ratio (2.3.7):

$$T_{lk} = \frac{n I_{out} L_{lk}}{\hat{V}_{lp}} \qquad (2.3.7)$$

Transferring L_{lk} to the secondary, a resonant circuit is formed with C_p and with the lamp equivalent capacitance. This resonant circuit is responsible for high frequency oscillations observed in i_{lp} (Fig.2.11).

Influence of the Magnetizing Inductance

As shown in Fig.2.10, the magnetizing inductance also appears as a parallel branch which derives a part of the current that should be injected into the lamp. Thus, the current transferred to the primary winding of the ideal transformer is equal to the current inverter output i_{out}, minus the magnetizing current i_m (Fig.2.11). Similar conclusions
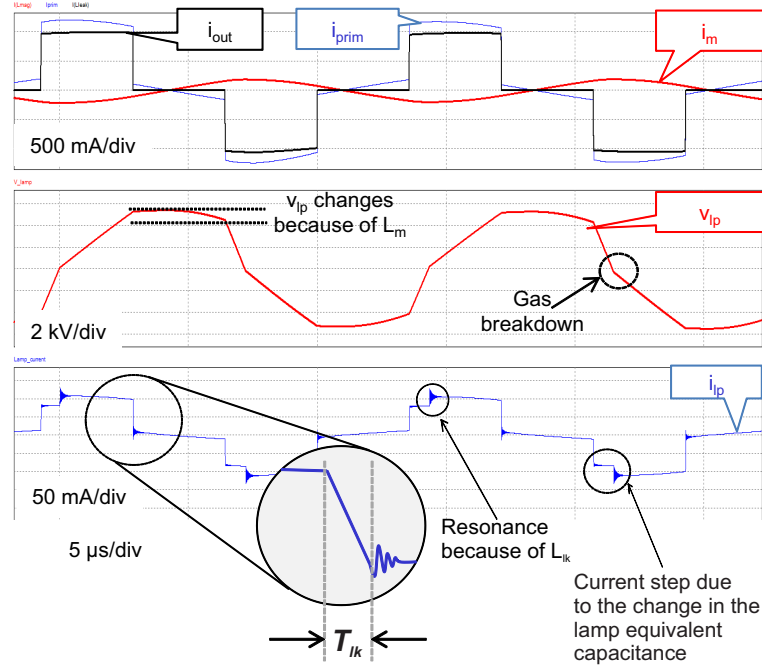
Figure 2.11.: Simulation waveforms illustrating the impact of the transformer parasitic elements

and simulations of the L_m impact are found in [2.17, p. 110]. This current waveform can be strongly affected if L_m presents a low value; as (2.3.8) shows.

$$i_m = \frac{1}{L_m} \int v_{prim} \, \mathrm{d}t \tag{2.3.8}$$

Where v_{prim} is the transformer primary side voltage equal to v_{lp}/n. .

Accordingly, the amplitude of i_m is computed as half the integral of v_{lp}/n (2.3.8) evaluated in the time interval while v_{lp} is positive. This is from the time instant $[t = t_1]$ to $[t = t_1 + T_{lp}/2]$, shown as the shaded area of v_{lp} in Fig.2.1). Assuming that the gas breakdown happens very quickly compared with the duration of the current pulse (Fig.2.11-bottom) we obtain the amplitude of i_m (2.3.9):

$$\hat{i}_m = \frac{n}{2L_m} \left[\hat{V}_{lp} \left(\frac{2 - D_{lp}}{f_{lp}} - \frac{C_d V_{th}}{J} \right) + \frac{2V_{th}^2 C_d}{J} \right] \tag{2.3.9}$$

This equation can be used to define the minimal value of L_m, which causes an acceptable deviation of the current injected into the lamp (ideally the square waveform of Fig.2.1). Additionally, during the relaxation time, when no current is injected in the transformer, i_m continues to flow in lamp, via the resonant circuit formed by L_m and the equivalent lamp capacitance. Consequently v_{lp} does not remain constant, as observed in simulation (Fig.2.11-middle). The variation of v_{lp} occurs at a frequency of f_m given by

(2.3.10) with a maximum decay calculated in expression (2.3.11). Using these equations, the impact of L_m in the current waveform can be calculated.

$$f_m = \frac{1}{2\pi\sqrt{L_m \left(C_p + C_{eq}\right)n^2}} \qquad (2.3.10)$$

$$\Delta v_m = \frac{\hat{i}_m}{4\pi f_m \left(C_p + C_{eq}\right)n^2} \qquad (2.3.11)$$

From the ideas exposed before and as should be expected from the ideal transformer model, L_m must be maximized and C_p minimized to reduce their impact in the supply operation. In order to obtain higher values of L_m the number of transformer turns must be high and in contrast, as demonstrated in [2.22, 2.23], a high number of turns increase the value of C_p. To obtain a balance between these opposite criteria, the minimum possible transformer turns ratio, 10 in this case, should be selected. Next, the transformer design to accomplish the required characteristics is presented, together with the choice of the other converter components.

2.4. Components selection

On the basis of the considerations presented in Section 2.3, the design of the high-voltage transformer and its characterization is presented first. Then, the choice of the current source inductance value and the references of the converter switches, are justified.

2.4.1. Transformer

According to the lamp specifications, power supply operating range and considering the impact of the parasitic elements described in the precedent Section 2.3.3, a transformer has been designed, manufactured and tested for this converter. With the aim to evaluate the transformer performance, an experimental measurement of the obtained parasitic elements values and experimental waveforms of interest are presented.

Electrical Requirements

In Section 2.3.2 was determined a maximum $\hat{V}_{lp}$ of about 6 kV ($P_{lp} = 100\,W, f_{lp} = 50\,kHz$). Accordingly, in Section 2.3.3 a 1:10 transformation ratio is selected, in order to obtain a peak voltage of 600 V in the primary side and across the inverter semiconductors. In the other hand, using (2.1.3) and (2.1.6) a maximum lamp peak current of about 150 mA is calculated to supply 100 W at 200 kHz with $D_{lp} = 80\,\%$. With 1:10 as transformation ratio, 1.5 A peak current is driven by the primary winding. With this current intensity and a maximum operating frequency of 200 kHz, skin and proximity effects become important and the use of Litz wire is necessary. On the basis of these operating conditions, a transformer construction is proposed.

Transformer Construction

To determine the number of turns in the primary and consequently the value of L_m, the first consideration is based on the fact that the fewer the quantity of winding layers, the smaller C_p [2.22]. In this sense, the primary and the secondary windings are constrained to only one layer, consequently the number of turns is restricted by the length of the transformer core.

Imposed a single layer winding, the available length for winding the transformer core and the wire diameter are the parameters that determine the maximum number of turns that can be fitted. One of the core materials that offer a good permeability and low power losses, for a maximum operating frequency of 200 kHz, is the 3F3 from Ferroxcube. Due to its long effective length, the E80/38/20 geometry is chosen. That makes approximately 300 turns to be fitted using only one layer in the secondary winding which implies nearly 30 turns in the primary side.

The transformer has been assembled starting with the secondary high voltage winding installed around the central leg of the core, filling completely the coil surface, obtaining 280 turns. This winding is isolated from the core by a 2 mm acrylic layer. Then an outside 0.5 mm insulation layer is used between the windings, and 28 turns are done for the primary winding. The transformer structure is illustrated in Fig.2.12 and its characteristics are summarized in Table 2.3.

Primary turns	Primary wire	Secondary turns	Secondary wire	Core
28	LITZ 81 strands x 38 AWG 0.00797 mm2	280	Single copper 33 AWG 0.0254 mm2	Material: 3F3 Size: E80-38-20 (Ferroxcube)

Table 2.3.: Transformer materials and construction characteristics

Characterization of the Transformer

With the aim to obtain the equivalent values of the transformer parasitic elements, the measurement of the transformer primary winding impedance in the frequency domain, with the secondary in open circuit, is proposed. This measurement is done using a
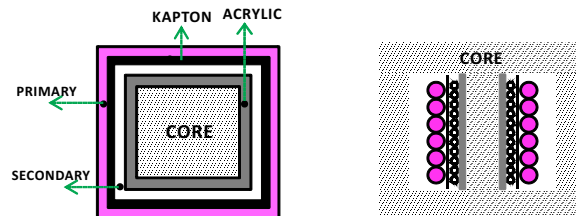
Figure 2.12.: Transversal view of the transformer coils arrangement

frequency response analyzer connected to the transformer primary side. This impedance measurement allows to obtain a voltage-current characteristic of the transformer that contains the effect of L_m, L_{lk}, C_p and the losses. Using the transformer model in Fig.2.10 an analytical expression of this transformer impedance in the frequency domain is deduced. This expression (2.4.3) together with an experimental Bode plot of the transformer impedance is used to find the values of L_m, L_{lk} and C_p.

The transformer impedance Z to be measured at the primary winding with the secondary in open circuit, can be expressed as (2.4.1) according to the transformer model shown in Fig.2.10:

$$Z = (R_s + L_{lk}S) + \frac{1}{Y_p} \tag{2.4.1}$$

With,

$$Y_p = n^2 C_p S + \frac{1}{R_p} + \frac{1}{L_m S} \tag{2.4.2}$$

Replacing (2.4.2) in (2.4.1), it is obtained (2.4.3):

$$Z = R_s \left[\frac{1 + \frac{L_m}{R_{eq}}S + \left(L_m n^2 C_p + \frac{L_{lk} L_m}{R_p R_s}\right) S^2 + \frac{L_{lk} L_m n^2 C_p}{R_s} S^3}{1 + \frac{L_m}{R_p}S + L_m n^2 C_p S^2} \right] \tag{2.4.3}$$

With,

$$R_{eq} = \frac{R_s R_p}{R_s + R_p} \approx R_s \tag{2.4.4}$$

Starting from the experimental Bode plot of the transformer impedance (shown in Fig.2.13) obtained with the frequency response analyzer, a numerical regression is performed, in order to compute the values of the transformer parasitic elements. The regression minimize the quadratic error between the theoretical frequency response of (2.4.3) and the experimental plot. This curve fitting is performed using the function *minerror2* of the Matlab® software.
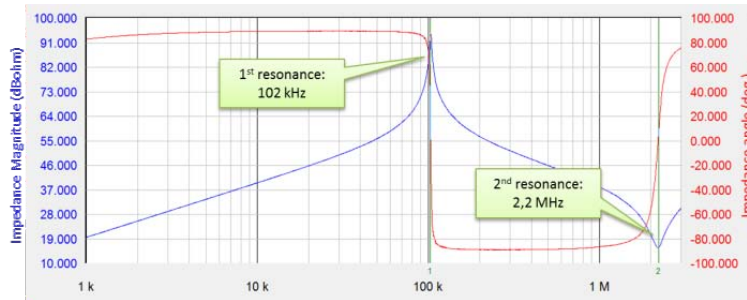
Figure 2.13.: Low-capacitance transformer Bode plot

The experimental impedance plot shown in Fig.2.13 has been obtained for a frequency range from 1 kHz up to 2.5 MHz. The experimental data of impedance and voltage-current phase are used to perform a curve fitting with the theoretical expression given in (2.4.3). The obtained transformer equivalent circuit is $L_m = 4.4mH$, $L_{lk} = 8.2\mu H$, $C_p = 26pF$, $R_p = 105k\Omega$, $R_s = 0.5\Omega$, with a mean square error value of 0.038Ω in the impedance magnitude. In Fig.2.14 the experimental Bode plot of the transformer impedance and the theoretical Bode plot obtained with the computed parasitic elements, are compared.
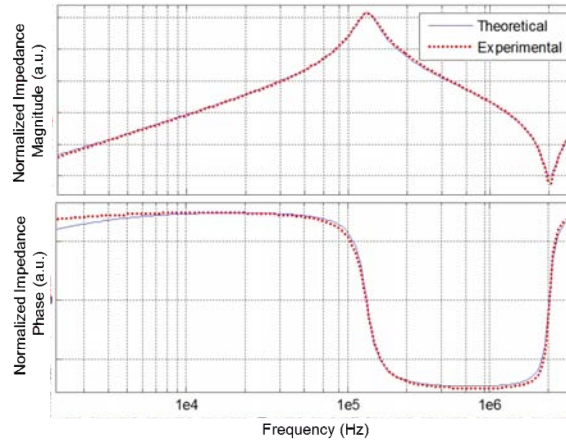
Figure 2.14.: Comparison of the experimental and calculated Bode plots.

The good fitting between the two curves demonstrates that the obtained values of the parasitic elements provide a good representation of the transformer behavior, to be used e.g. for the entire circuit simulation, including the lamp model.

Performance Test

For the experimental essay, the primary side is supplied with a square waveform of 1 A peak current at 70 kHz and 50% duty cycle. Fig.2.15-left presents the current measured at the primary side; a high frequency component (around 1.2 MHz) overlapped to the current pulses, is observed. The lamp current i_{lp} presents high frequency oscillations too. These oscillations are due to the resonance between L_{lk} reflected to the secondary and the equivalent capacitance seen in the secondary side. The magnetizing current is not negligible, and one can notice that the lamp voltage decays 800 V (Fig.2.15) although it is supposed to remains constant.

Because the excilamp under test is intended for water decontamination appliances, the connection of one lamp electrode to the ground is necessary to ensure a good level of safety. This transformer has been tested with satisfactory results prior to the grounding of the excilamp. However, the connection of one lamp electrode to ground has severely affected the transformer performance, even forbidding the lamp ignition for some oper-
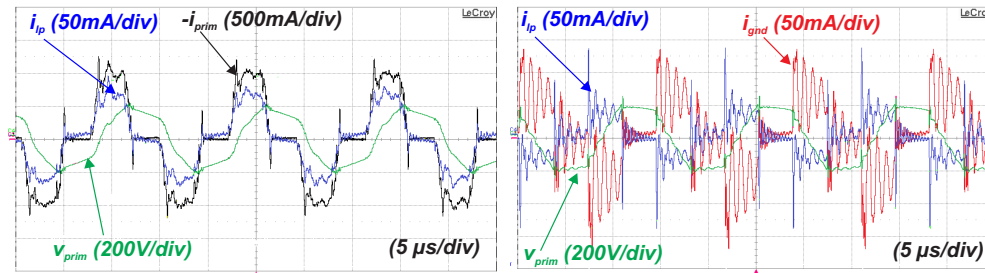
Figure 2.15.: Waveforms obtained using the low-capacitance transformer without connection to ground (left) and with connection of one terminal to ground (right)

ating conditions, that were previously successfully tested without grounding.

Fig.2.15-right presents the lamp current i_{lp} and the current going to the ground i_{gnd}; in this case an important amount of the current transferred from the primary winding is going to ground affecting severely the transformer current transfer to the lamp. Next, the causes of this detriment in the transformer operation when grounding, are analyzed.

Tranformer Grounding   To explain the flow of the transformer current to ground, the existence of a capacitance between the primary and the secondary winding is considered as well as the connection of the converter to ground.

In Fig.2.16 one of the converter terminals is connected to ground directly to simplify the model, however this could be a capacitive path. Due to the connection of one terminal of the secondary winding to ground, the voltage difference between the secondary and the primary winding produces a current flow through C_1.

An equivalent capacitance C_{1p} (2.4.5), which appears in parallel with C_p, is calculated based on the Miller effect. Thus, when the secondary side is connected to ground, the current of C_{1p} produces an additional reduction in the magnitude of i_{lp}. Consequently, a capacitance C_{1p} much smaller than C_{eq} must be achieved: under this condition, the
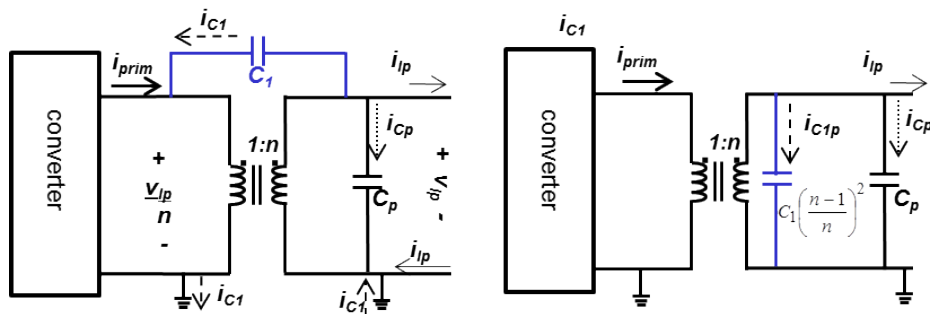
Figure 2.16.: Transformer model to explain the grounding effect

lamp electrode can be connected to ground without prohibiting the lamp ignition.

$$C_{1p} = C_1 \left(\frac{n-1}{n} \right)^2 \tag{2.4.5}$$

With the aim to reduce the value of the equivalent capacitance C_{1p}, an alternative transformer structure is proposed.

Alternative Transformer

In order to reduce the impact of grounding one of the secondary winding terminals, the parasitic capacitance between the windings, C_1, and the stray capacitance C_p must be reduced. In this way, the current divider composed by C_{1p} and C_p deviates less current, and the lamp ignition can be achieved. This is accomplished by increasing the insulation distance between the primary and secondary winding and increasing the distance from the high voltage coil (the secondary) to the core, on the basis of the works presented in [2.19]. Accordingly, the primary side coil is wound first, over a 2 mm acrylic isolation layer disposed between the coils and the core. The next layer is a 3 mm acrylic shield (ϵ=2.7 @ 1MHz). Around this layer, the secondary side coil is wound (Fig.2.17).
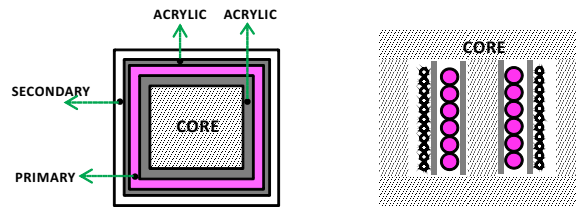
Figure 2.17.:

As previously done for the first transformer, the Bode plot from the primary winding is traced (Fig.2.18) and the values of the parasitic elements are found: $L_m = 3.55mH$, $L_{lk} = 10.9\mu H$, C_p=12.1 pF, $R_p = 112k\Omega$, $R_s = 0.38\Omega$, with a mean square error value
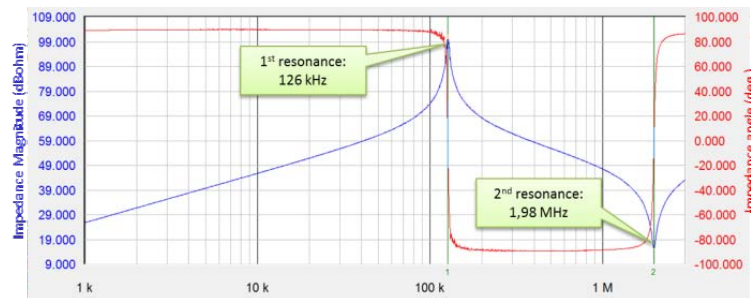
Figure 2.18.: Alternative transformer Bode plot
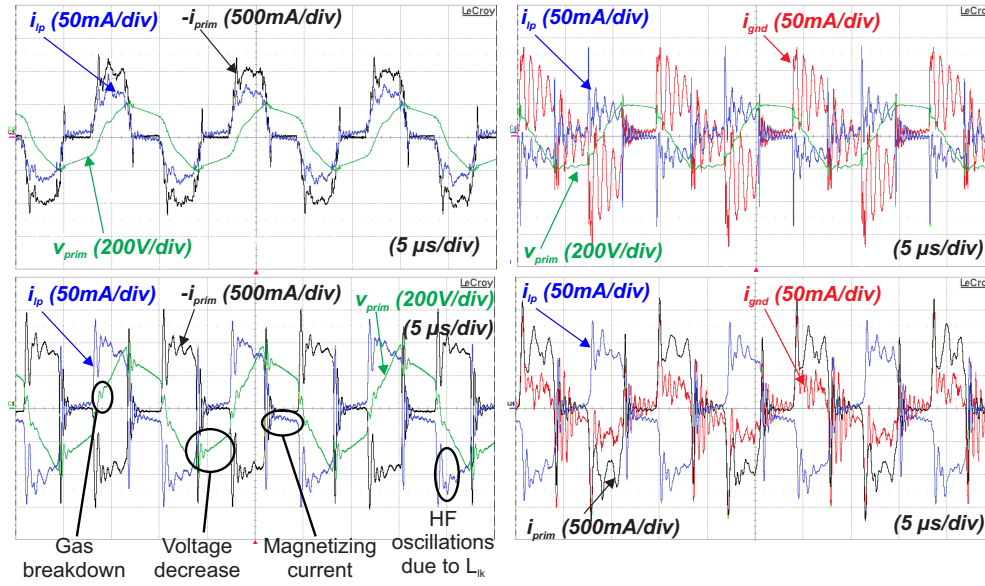
Figure 2.19.: Waveforms obtained using the first (top) and the new transformer (bottom) without connection to ground (left) and with connection of one terminal to ground (right). For the second transformer, i_{gnd} is substantially reduced and the lamp ignition is achieved.

of 0.047Ω in the impedance magnitude. The obtained equivalent capacitance (C_p) has been reduced 46% compared with the first transformer capacitance.

When the excilamp is not connected to ground the ratio between i_{out} and i_{lp} is 10, equal to the turns ratio, instead of 8 obtained for the first transformer (Fig.2.15-top), and the current waveforms are according to the expected results; the decrease in the lamp voltage (seen on the primary side) due to the magnetizing current is observed again (Fig.2.19-top) without substantial changes. Fig.2.19-bottom presents i_{lp} and i_{gnd} for this new transformer, with one lamp electrode connected to the ground. In this case i_{gnd} has been substantially reduced in comparison with the first transformer results and the lamp ignition is achieved while an electrode is grounded.

Even if i_{gnd} is not negligible and a reduction of i_{lp} is seen when compared with the not grounded connection (Fig.2.19-top), the current waveform is respected. From these results, a construction methodology to reduce the impact of grounding the transformer, has been proven.

The square-shape current supply and transformer efficiencies (η) are presented in Table 2.4 for a particular operating point.

f_{lp}	D_{lp}	J	P_{lp}	η transformer not grounded	η transformer grounded	η converter (transf. not included)
70 kHz	50%	90 mA	90 W	87%	81%	65%

Table 2.4.: Alternative transformer and converter efficiencies

2.4.2. Inductance

The current ripple of i_{out} will be limited to 5 % of the maximum current output. This ripple is determined by means of the hysteresis limits of the current source. Accordingly, for a maximum output current of 3 A, the hysteresis limits are i_{max}=3.105 A and i_{min}=2.895 A. Given a minimum f_{lp} of 50 kHz, the controller maximum desired operating frequency is chosen as f_c=40 kHz in order to assure $f_c < f_{lp}$. Now, to compute L it is necessary to determine the DC input voltage V_{in} of the chopper. With 10 as the transformer turns ratio and $V_{th} = 1.3\,kV$, V_{in} must be higher than 130 V. For example, to supply the two-quadrant chopper, the rectified line (120 Vrms) can be used to produce a DC input voltage of approximately 170 V. With $V_{in} = 170\,V$ and using (2.2.10), the minimum value that L must have to operate at $f_c \leq 40kHz$ is computed, obtaining L=15 mH, .

Additionally, given that $V_{in} < \hat{V}_{lp}/n$, (2.2.16) is used to limit the error of the hysteretic control. The maximum value of the i_{out} current spikes is limited to 5% of the i_{out} mean value, that is a maximum overshoot of 150 mA above or below the hysteresis limits. Using (2.2.16), with $\Delta i_{out_x} = 150\,mA$ and $f_{lp} = 50\,kHz$ the minimum value that L must have is found: 28 mH. With this value of L, the maximum f_c is reduced to about 30 kHz.

An inductance of 30 mH was built using two U ferrite cores reference U93/76/30 material 3C90 from Ferroxcube, with a gap length of 1mm and 540 turns.

2.4.3. Switches

The switches K1 are implemented with high power MOSFETS (P8NK100Z, VDSS 1kV, ID=6.5A) and the switches K2 with fast recovery diodes (STTH512D, VRRM=1.2kV, IF=5A) The thyristor-like switches of the inverter are implemented connecting a diode in series with each MOSFET. Switches references are the same as for the two-quadrant chopper used for the constant current source.

2.5. Implementation Results

Next, the operability and electrical efficiency of the converter at its maximum output power is presented for different values of the three D.O.F.. The experimental results concerning the excilamp UV radiation measurements will be presented in Chapter 3.

2.5.1. User Interface for the Operating Point Adjustment

To define the desired operating point (J, f_{lp}, D_{lp}), a PC-based user interface has been developed (Fig.2.20).
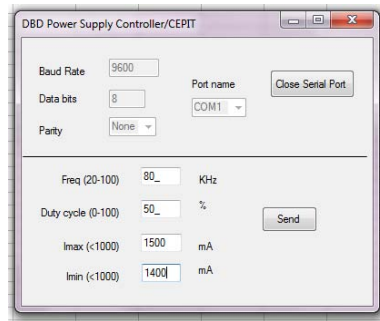
Figure 2.20.: Screen-shot of the software interface used to define the converter operating point

From the PC, the three parameters of the desired operating point are communicated to a Digital Signal Processor (DSP, Fig.2.21). This DSP generates the control signals of the inverter switches and the hysteresis limits of the current source controller. The control signals are produced using four independent PWM modules, consequently the user can vary the operating point of the converter without interruption of the lamp operation. The hysteretic control for the current source is implemented with analog devices, therefore, to allow an adjustment of the current intensity from the PC interface, the two limits of the hysteresis are generated by the DSP using two DAC.
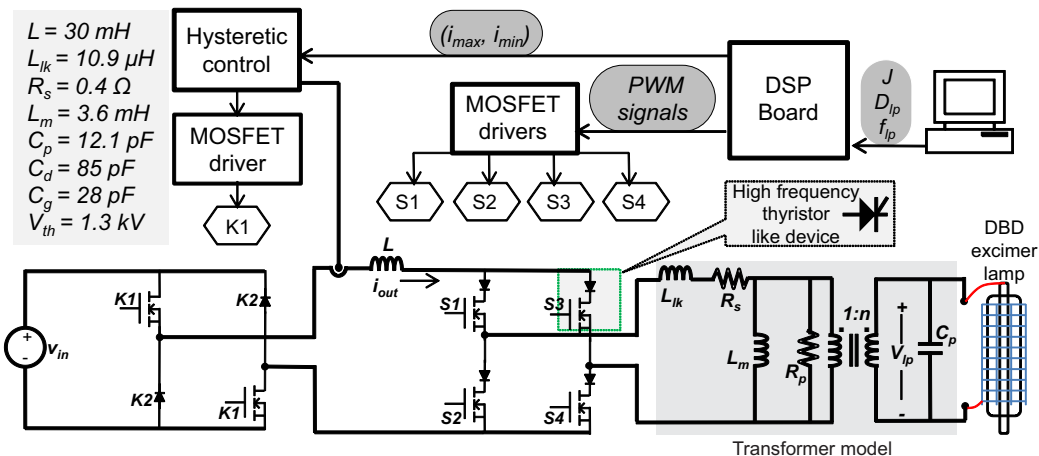
Figure 2.21.: Square-shape DBD Power supply blocks diagram.

2.5.2. Experimental Bench

In order to measure the converter and DBD electrical signals in real time, high speed current probes (Lecroy AP015) and a high voltage floating probe (Agilent N2891A) are used; the phase difference between the voltage and current signals is compensated in the oscilloscope, then both signals are multiplied and averaged to obtain a power measurement (averaging time 1ms).

The voltage probe is connected to the primary side of the transformer in order to diminish the impact of the probe input capacitance (12pF) in the converter behavior, accordingly the lamp voltage is calculated taking into account the transformation ratio. The lamp current is measured directly in the lamp electrodes.

2.5.3. Lamp Power Adjustment

The shape of the lamp current pulses and the lamp voltage is presented in Fig.2.22 for $J = 120mA$, demonstrating the possibility to keep constant the lamp current amplitude while f_{lp} is varied. The decrease in the lamp voltage while no current is injected into the lamp, is a consequence of L_m.
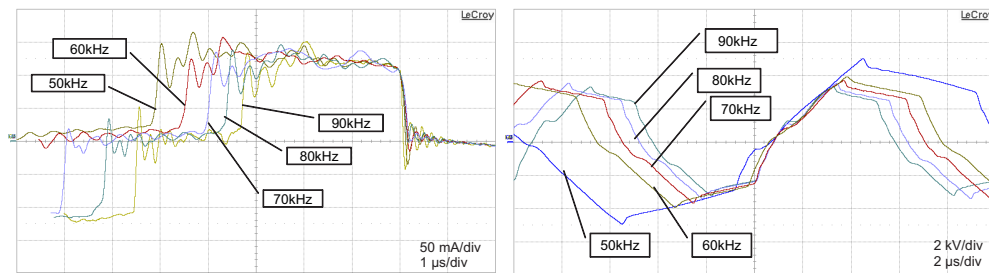
Figure 2.22.: Constant amplitude current pulses injected into the lamp for different f_{lp} values (left) and the corresponding v_{lp} waveform (right)

In Fig.2.23, f_{lp} is preserved constant and different combinations of the other two D.O.F, J, D_{lp}, are used to keep constant P_{lp} at different operating points. In this way is demonstrated that the desired lamp current waveform is preserved while the lamp power is adjusted with the three D.O.F. of the converter. The high frequency oscillations (2.5 MHz) are explained by the resonance between L_{lk} and the equivalent capacitances. Next, in order to demonstrate how the converter allows to adjust the lamp electrical power, each one of the converter D.O.F. are used to determine P_{lp}. For the following demonstration, the voltage probe was connected directly to the lamp to obtain a real-time measurement of the lamp power.
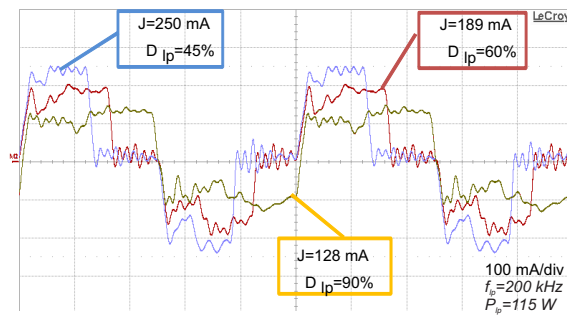
Figure 2.23.: For a given frequency, the same lamp power can be obtained for different combinations of J and D_{lp}

Power Adjustment with D_{lp}

In Fig.2.24, P_{lp} is plotted as a function of J. For this experiment f_{lp} is configured to 80 kHz, then J is fixed to 128 mA and D_{lp} is adjusted to obtain different values of P_{lp}. The same procedure is repeated for J=189 mA and 250 mA. Using the values of the D.O.F. for each one of the obtained operating points and the lamp equivalent parameters of 2.1, with (2.1.3) the theoretical values of P_{lp} are calculated. Comparing the experimental and the theoretical points in Fig.2.24, it can be observed that the experimental power is in general higher than the theoretical one. According to (2.1.3), the reason can be that in the practice the lamp presents a higher V_{th} and/or a smaller C_g values, than the ones used to compute P_{lp} (Table 2.1).
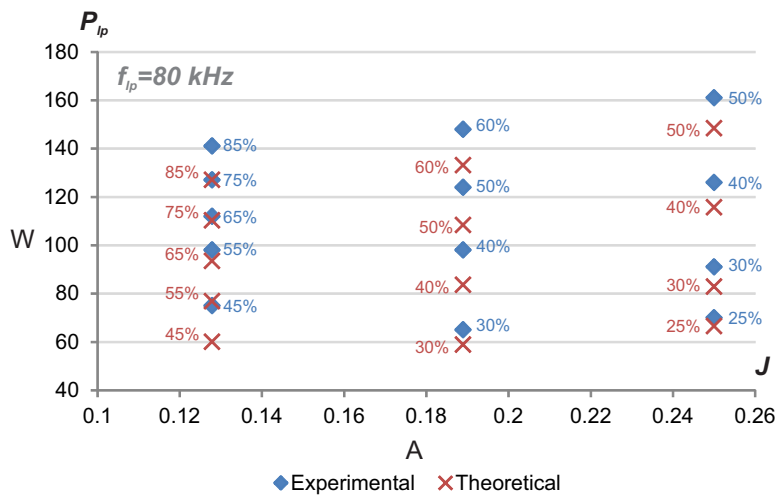
Figure 2.24.: Lamp power as a function of the lamp current amplitude, for $f_{lp} = 80\,kHz$. The duty cycles are placed next to data points.

Power Adjustment with *J*

In Fig.2.25 the obtained values of P_{lp} are plotted for three different values of f_{lp}, with the duty cycle fixed to 50%. f_{lp} is configured first at 50 kHz and the current intensity is used to obtain different values of P_{lp}. The process is repeated for f_{lp}=80 kHz and f_{lp}=110 kHz. Observe that for a given value of J, the power decreases linearly with f_{lp} as predicted by (2.1.3).
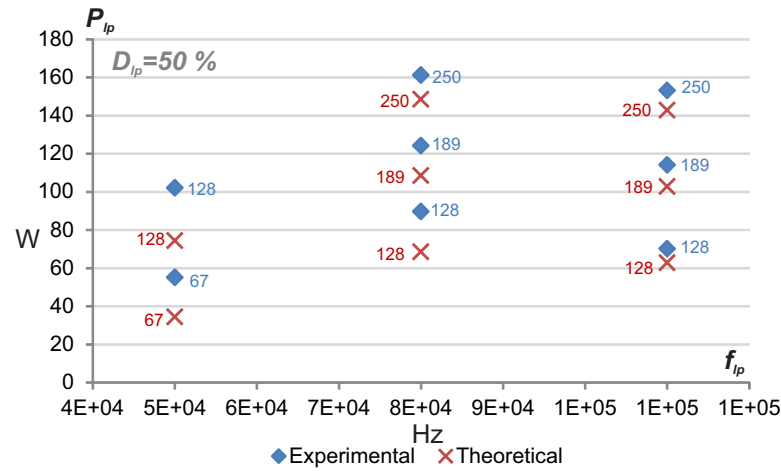
Figure 2.25.: Lamp power as a function of the lamp current frequency, for $D_{lp} = 50\%$. The J values (in mA) are placed next to data points.

Power Adjustment with f_{lp}

Now P_{lp} is plotted as a function of D_{lp}, for a constant value of J as shown in Fig.2.26. To obtain this graphic D_{lp} is configured to 40, 50, 60, 70, 80 and 90%. For each value of D_{lp}, the lamp power is increased by reducing f_{lp} up to levels of $\hat{V}_{lp}$ close to the maximum tolerated. Only three values of f_{lp} are used in order to simplify the graphic interpretation. Observe that for a given frequency, the lamp power increases linearly with D_{lp}. As can be observed in Fig.2.26 the lamp is not operated at all the three frequencies for every value of D_{lp}. The reason is that, according to (2.1.6), as D_{lp} increases, the maximum lamp peak voltage (6 kV) is reached for a lower value of f_{lp}.
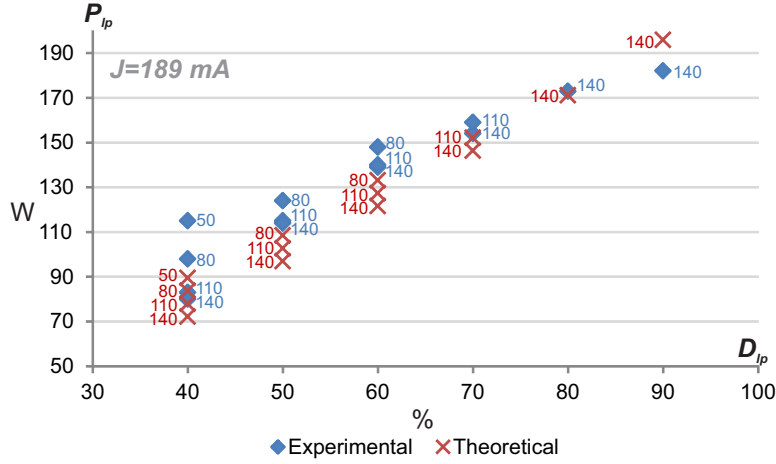
Figure 2.26.: Lamp power as a function of the lamp current duty cycle, for $J = 189\,mA$. The lamp operating frequencies (in kHz) are placed next to data points.

On the Limits of the Converter Operating Range

To verify the output current waveform near to the operating limits of the converter, in Fig.2.27 i_{out} is maintained constant at its maximum value (3A) and the current duty cycle is adjusted to attain a lamp peak voltage of 5 kV for three different values of f_{lp}. The maximum electrical power achieved is 237 W, at the operating conditions shown in Table 2.5. For the three operating points, the desired lamp current waveform is preserved, as shown in Fig2.27. Observe in Fig.2.27 that, as expected according to (2.3.4), by increasing the operating frequency more power can be injected into the lamp for the same output voltage.

2.5.4. Efficiency

The converter efficiency (η) for three operating points near to the maximum converter output voltage, is presented in Table 2.5. The η is mainly affected by the hard switching, the non-negligible ON resistance of the MOSFET switches (1.85Ω) and the efficiency of the step-up transformer. Note that the proposed converter is intended to be used as an equipment for the study of DBD reactors and not as a standalone permanent supply,

$f_{lp}(kHz)$	$D_{lp}(\%)$	$P_{UV}(mW/cm^2)$	$P_{lp}(W)$	$P_{in}(W)$	$\eta(\%)$
50	27	32.3	97	215	45
100	60	54.6	180	310	58
150	87	58.6	237	350	68

Table 2.5.: Converter efficiency for different inverter frequencies, with $\hat{V}_{lp}$=5 kV and J=250 mA
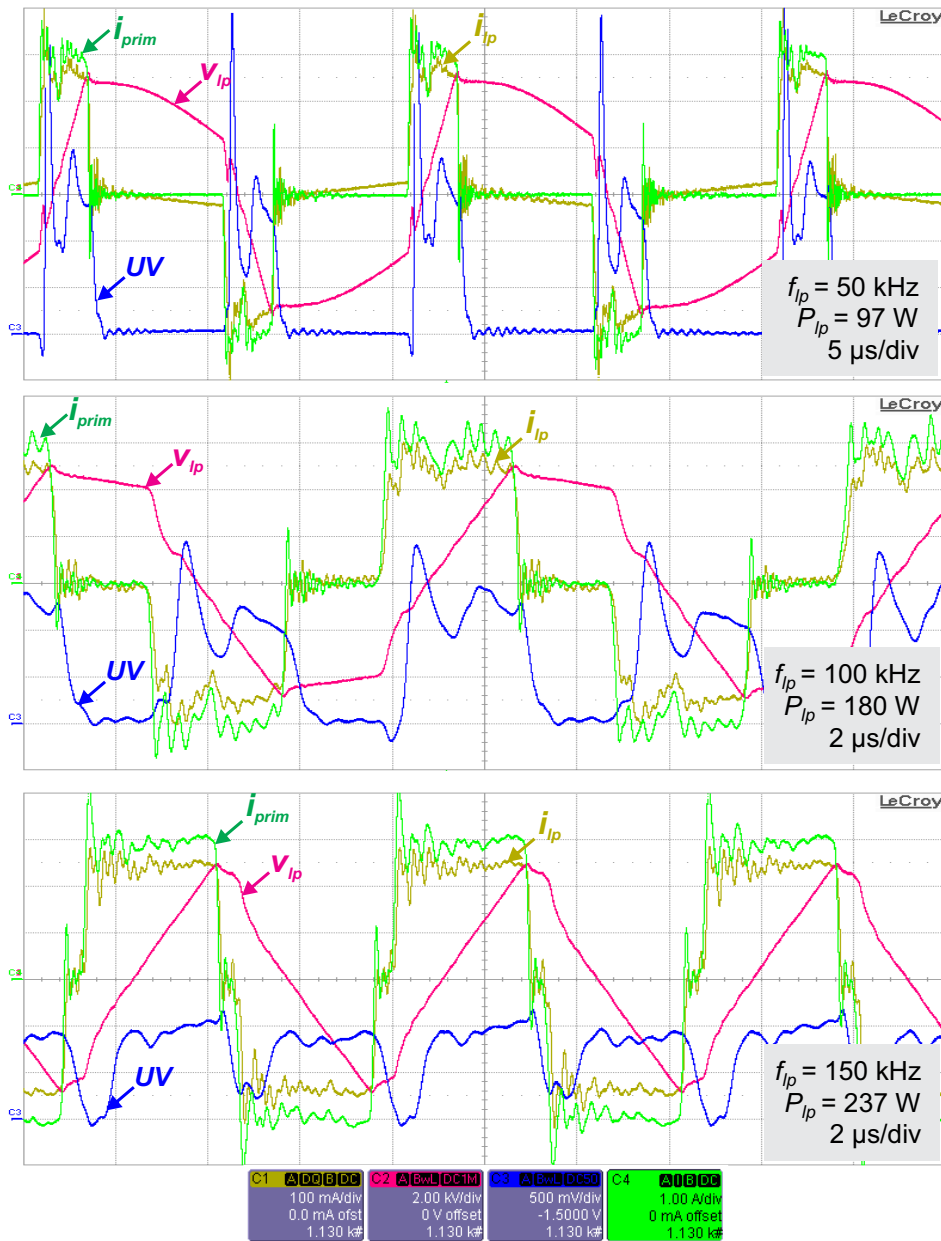
Figure 2.27.: Lamp voltage, current and UV instantaneous response, for three operating points near to the maximum output voltage and current of the converter.

consequently its design criteria has been focused in the respect of the proposed current waveform and not in reduction of the power losses for a particular operating point.

2.5.5. UV radiation

The UV radiation instantaneous response, obtained in the limits of the converter operating range, is presented in Fig.2.27. This UV waveform was acquired using a photo-detector THORLABS PDA-25K, configured in the 20dB gain setting. It is possible to see that the instantaneous UV radiation follows the absolute value of the lamp current, except during the T_{br} time. Also from Fig.2.27, a reduction in the UV pulse intensity when the frequency increases, for the same injected current amplitude, is observed. Hence, an impact of the operating on the UV radiation characteristics is deduced. On the basis of this experimental test, is demonstrated that the average power, intensity, duration and frequency of the UV radiation pulses can be controlled with the D.O.F. of proposed converter. As a subsequent research work, a comprehensive study of the operating point impact over the UV radiation production and over the DBD excimer lamp performance, is presented in Chapter 3.

2.6. Conclusions

With the proposed current-mode power supply, the electrical power and the UV radiation of a DBD Excimer lamp can be effectively adjusted by means of controlling the lamp current using three D.O.F.: amplitude, frequency and duty cycle.

Through the use of this converter a suitable method to study the UV radiation of DBD excimer lamps, is demonstrated. The experimental operating test of this converter performed with a XeCl DBD excilamp, has demonstrated that the lamp model used for the converter design is appropriate.

Bibliography

[2.1] D. Flórez, R. Díez, A. Hay, G. Perilla, F. Ruiz, and H. Piquet, "Programmable current converter synthesis for the evaluation of UV radiation of excimer lamps," in *2010 IEEE ANDESCON*, pp. 1–6, 2010.

[2.2] D. Florez, R. Diez, K. Hay, and H. Piquet, "DBD excimer lamp power supply with fully controlled operating conditions," in *2012 13th International Conference on Optimization of Electrical and Electronic Equipment (OPTIM)*, pp. 1346–1352, 2012.

[2.3] H. Piquet, S. Bhosle, R. Diez, M. Cousineau, M. Djibrillah, D. Le Thanh, A. N. Dagang, and G. Zissis, "Control of the UV flux of a XeCl dielectric barrier discharge excilamp through its current variation," *Quantum Electronics*, vol. 42, pp. 157–164, Feb. 2012.

[2.4] R. Diez, H. Piquet, M. Cousineau, and S. Bhosle, "Current-mode power converter for radiation control in DBD excimer lamps," *IEEE Transactions on Industrial Electronics*, vol. 59, no. 4, pp. 1912–1919, 2012.

[2.5] R. W. Erickson and D. Maksimovic, *Fundamentals of Power Electronics*. Springer, Jan. 2001.

[2.6] J. M. Alonso, C. Ordiz, D. Gacio, J. Ribas, and A. J. Calleja, "Closed-loop regulated power supply for ozone generation based on buck converter and current-fed push-pull resonant inverter," Sept. 2009.

[2.7] F. Diaz, F. Azcondo, C. Brañas, R. Casanueva, and R. Zane, "Digitally controlled low-frequency square-wave electronic ballast with resonant ignition and power loop," *IEEE Transactions on Industry Applications*, vol. 46, no. 6, pp. 2222–2232, 2010.

[2.8] A. V. Stankovic, L. Nerone, and P. Kulkarni, "Modified synchronous-buck converter for a dimmable HID electronic ballast," *IEEE Transactions on Industrial Electronics*, vol. 59, pp. 1815–1824, Apr. 2012.

[2.9] A. L. Kirsten, M. A. Dalla Costa, C. Rech, R. N. do Prado, and T. B. Marchesan, "Digital control strategy for HID lamp electronic ballasts," *IEEE Transactions on Industrial Electronics*, vol. 60, pp. 608–618, Feb. 2013.

[2.10] M. Cousineau, R. Diez, H. Piquet, and O. Durrieu, "Synthesized high-frequency thyristor for dielectric barrier discharge excimer lamps," *IEEE Transactions on Industrial Electronics*, vol. 59, no. 4, pp. 1920–1928, 2012.

[2.11] X. Bonnin, H. Piquet, N. Naude, C. Bouzidi, N. Gherardi, and J.-M. Blaquiere, "Design of a current converter to maximize the power into homogeneous dielectric barrier discharge (DBD) devices," *The European Physical Journal Applied Physics*, July 2013.

[2.12] D. Gacio, J. Alonso, A. Calleja, J. Garcia, and M. Rico-Secades, "A universal-input single-stag2e high-power-factor power supply for HB-LEDs based on integrated buck-flyback converter," *IEEE Transactions on Industrial Electronics*, vol. 58, no. 2, pp. 589–599, 2011.

[2.13] R. Díez, J.-P. Salanne, H. Piquet, S. Bhosle, and G. Zissis, "Predictive model of a DBD lamp for power supply design and method for the automatic identification of its parameters," *The European Physical Journal - Applied Physics*, vol. 37, no. 03, pp. 307–313, 2007.

[2.14] M. I. Lomaev, V. S. Skakun, E. A. Sosnin, V. F. Tarasenko, D. V. Shitts, and M. V. Erofeev, "Excilamps efficient sources of spontaneous UV and VUV radiation," *Physics-Uspekhi*, vol. 46, pp. 193–209, Feb. 2003.

[2.15] A. El-Deib, F. Dawson, G. van Eerden, S. Bhosle, G. Zissis, and T. D. Le, "Analysis and experimental validation of a new current-controlled driver for a dielectric barrier discharge lamp," *IEEE Transactions on Industry Applications*, vol. 47, no. 4, pp. 1971–1982, 2011.

[2.16] T. C. Manley, "The electric characteristics of the ozonator discharge," *Transactions of The Electrochemical Society*, vol. 84, pp. 83–96, Oct. 1943.

[2.17] R. Diez-Medina, *Alimentation de puissance d'une lampe exciplexe à décharge à barrière diélectrique, en vue du contrôle du rayonnement.* PhD thesis, INPT, Toulouse, 2008.

[2.18] M. A. Djibrillah, *Éléments de conception d'un générateur électrique pour l'alimentation d'un dispositif à décharge à barrière diélectrique (DBD).* INPT, Apr. 2011.

[2.19] X. Bonnin, H. Piquet, D. Florez, R. Diez, and X. Bonnin, "Designing the high voltage transformer of power supplies for dbd: windings arrangment to reduce the parasitic capacitive effects," in *Power Electronics and Applications (EPE), 2013 15th European Conference on*, Sept. 2013.

[2.20] D. Florez, X. Bonnin, H. Piquet, and R. Diez, "Impact of the transformer in the current mode supply of dielectric barrier discharge excimer lamps," (Brazilian Power Electronics Conference (COBEP 2013), Gramaos, Brasil), Oct. 2013.

[2.21] L. Dalessandro, F. da Silveira Cavalcante, and J. W. Kolar, "Self-capacitance of high-voltage transformers," *IEEE Transactions on Power Electronics*, vol. 22, pp. 2081–2092, Sept. 2007.

[2.22] F. Blache, J. P. Keradec, and B. Cogitore, "Stray capacitances of two winding transformers: equivalent circuit, measurements, calculation and lowering," in *, Conference Record of the 1994 IEEE Industry Applications Society Annual Meeting, 1994*, pp. 1211–1217 vol.2, 1994.

[2.23] J. Biela and J. Kolar, "Using transformer parasitics for resonant converters - a review of the calculation of the stray capacitance of transformers," in *Industry Applications Conference, 2005. Fourtieth IAS Annual Meeting. Conference Record of the 2005*, vol. 3, pp. 1868–1875 Vol. 3, 2005.

3. Parametric Study of the Operating Point Influence on the DBD Excilamp Performance

In the precedent Chapter, a power supply useful for the study of DBD excilamps has been presented. The exploitation of this converter with a XeCl DBD excilamp is covered here. For this study, the lamp is supplied varying each one of the operating point parameters (D.O.F. of the converter) and the impact of each parameter on the following excilamp characteristics are presented and discussed:

- The UV power: together with P_{lp}, gives a measurement of the excilamp efficiency.

- The UV waveform: allows to understand the effect of the operating point in the instantaneous response of the UV production and to correlate it with the lamp current waveform.

- The lamp electrical model: provides information about the lamp electrical behavior at different operating conditions.

- Pictures of the discharge: to detect a change in the discharge regime.

Explained in the first part of this Chapter is the experimental bench used for the UV radiation measurements. Using this experimental set-up a first study is developed. For the first experiment the current frequency f_{lp} is held constant, the intensity J is configured at a first set-point value, and then, using the current duty cycle D_{lp}, different values of lamp electrical power P_{lp} are obtained. The process is repeated for other values of J, and for each operating point the lamp operation is analyzed, showing the effect of this parameter over the lamp performance. For a second experiment, f_{lp} is the parameter to be evaluated. To do that, J is fixed, f_{lp} is configured at the first operating frequency and using D_{lp}, the lamp power is increased. Again, the process is repeated for several values of f_{lp} and pertinent results regarding the impact of f_{lp} over the lamp performance, are provided. From these results the UV power obtained at similar levels of excitation power can be compared for different operating conditions. We conclude the Chapter with an analysis of all the tested operating points from the point of view of the lamp efficiency, to find the lamp operating conditions with the best electrical-to-UV conversion ratio and also the operating points that maximize the UV output power.

3.1. Experimental Set-up

The DBD UV excilamp under test is filled with a XeCl gas mixture at approximately 160mbar of pressure. The physical dimensions and geometry of the lamp are described in Fig.3.1. In this lamp the external electrode is a metallic mesh and the inner electrode is a metallic pipe in contact with the lamp surface. In this configuration, the external metallic mesh partially obstructs the lamp UV radiation; in this particular lamp, the mesh covers an area that corresponds to approximately 15 % of the whole lamp external surface.
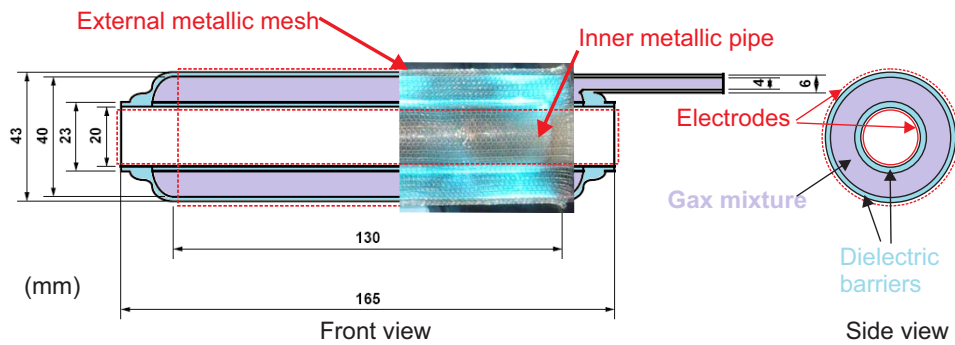
Figure 3.1.: DBD excilamp dimensions. A picture of the actual lamp is superposed to the lamp drawing in order to show the aspect of the electrodes

The UV radiation emitted by this DBD excilamp is measured using the experimental bench illustrated in Fig.3.2, described as follows. The radiation instantaneous response is acquired with a photo-detector THORLABS PDA-25K, configured in the 20dB gain setting. The detector is oriented perpendicular to the lamp, placing its active area at 25mm of the lamp surface. The UV power is measured with the optometer GIGAHERTZ-OPTIK P-9710 using the UV detector SN5816, configured with an integration time of
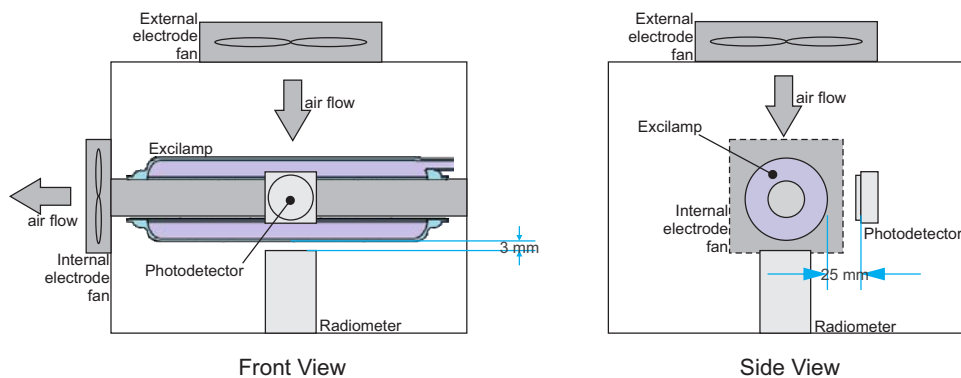
Figure 3.2.: Experimental bench.

0.5s and a dose time of 5s, installed at 3 mm of the lamp surface.

In [3.1] and [3.2] a negative impact of the gas heating over the excilamps UV production is reported. With the aim to evaluate the impact of the lamp heating in our specific experimental bench, the variation of the lamp electrodes temperature and the UV power have been simultaneously measured in the time for a constant value of P_{lp}. In Fig.3.3-left a temperature stabilization time around 10 min. is found, with a decrease of 14% in the UV power (Fig.3.3-right) when compared with the obtained at the lamp ignition instant.
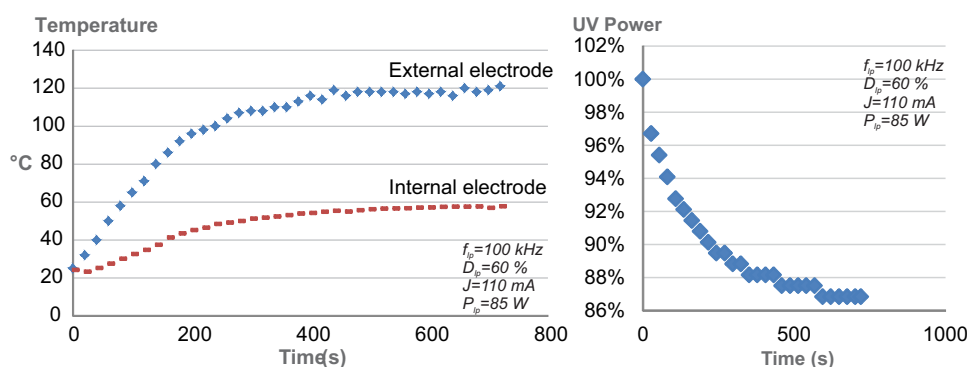
Figure 3.3.: Left: Change in the temperature of the excilamp electrodes for a particular operating point. Right: Excilamp UV power variation in the time due to heating, for a particular operating point.

This result shows the relevance of performing all the UV measurements at the same lamp temperature. Naturally, the lamp temperature and the UV stabilization time is not constant. These parameters change depending on the electrical power injected into the lamp, the cooling system and the ambient temperature. Accordingly, to ensure a constant lamp temperature in steady state for all the operating points to be evaluated, a lamp temperature control loop would be necessary. However, in order to make faster the acquisition of the measurements and to avoid the use of a temperature control loop, we have chosen to carry out the UV measurements for a cold lamp instead of a hot lamp in thermal steady state. In our experiments the external lamp temperature is always the same at the ignition instant. This condition is assured using the following protocol:

1. The cooling system is turned-on prior to the measurements. For the cooling of the two lamp electrodes, forced air coming from two fans is used as depicted in Fig.3.2.

2. The lamp is turned-on at the desired operating point (J, D_{lp}, f_{lp}).

3. Immediately, the radiometer measurement is started, integrating the UV radiation power during 5s.

4. The lamp is turned-off

5. The cooling system keeps running, cooling down the lamp to 40^oC or less.

6. A new UV measurement can be performed.

In this way the increase of the lamp temperature is controlled even if P_{lp} is different. In the next Sections, the experiences obtained using this experimental bench are presented.

3.2. Impact of the Lamp Current Intensity

To evaluate the impact of the lamp current intensity, the value of J is adjusted at 250, 189, 128 and 67 mA, for a constant value of f_{lp}. For each J value, the lamp electrical power is gradually increased with D_{lp}. First the UV power output as a function of J is analyzed. After that, the obtained electrical and UV waveforms are interpreted. In order to evaluate the impact of J over the lamp equivalent model, the Charge-Voltage Lissajous figures (as previously explained in Section 1.1.3) are built and from there, the changes on the lamp equivalent parameters are evaluated. Finally the visual aspect of the discharges for the different values of J is presented.

3.2.1. Impact of J Over the UV Production

In Fig.3.4-3.6, the DBD excilamp UV radiation power as a function of the injected electrical power, is shown. Each trend line corresponds to a different lamp current amplitude J: 67, 128, 189 and 250 mA, where the power is adjusted by mean of the D_{lp} ratio. Each figure shows the plots for a different operating frequency.
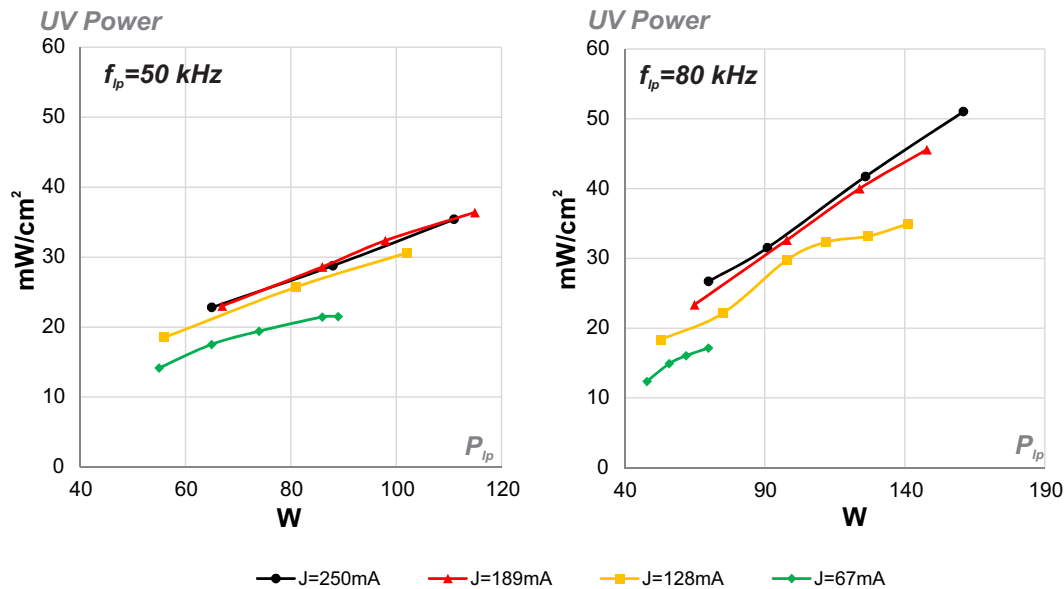
Figure 3.4.: Impact of the excilamp current intensity in the UV output for f_{lp}=50 kHz (left) and f_{lp}=80 kHz (right)

In Fig.3.4-left the UV power obtained for the test performed at f_{lp}=50 kHz is shown. From this result, an increment in the lamp UV production for the same electrical power injected into the lamp, is obtained by increasing J from 67 mA to 128 mA. This increment corresponds to a gain of up to 25% in the UV radiation output obtained for the same values of P_{lp}. When the current pulse intensity is increased from 129 mA to 189 mA, the upward trend in the lamp performance is still advised, but for J above 189 mA a significant gain is not observed.

For higher values of f_{lp} (Fig.3.5-3.6) this positive impact of the current intensity in the UV production is verified too. The maximum value of P_{lp} attained for each operating point is limited by the maximum output voltage, the switches commutation time and T_{br} (2.1.1).

Another characteristic to be noted is an abrupt change in the UV-P_{lp} function slope for $f_{lp} \geq 140\,kHz$. Observe in Fig.3.5-right, with $f_{lp} = 140\,kHz$, that the slope of the $J = 128mA$ trend, changes at P_{lp} around 100 W. For the same frequency at higher values of J, the change is less pronounced but appears around 130 W and 150 W.

As the frequency increases (Fig.3.6) the slope change becomes more evident at all the J values, appearing for lower values of P_{lp} as the current intensity decreases. This result suggest that the excitation power at which the lamp can be supplied with maximum efficiency, can be increased with the augmentation of the current intensity.This change in the UV-P_{lp} ratio corresponds to a reduction in the lamp efficiency with the increase of the injected power, attributed to overexcitation [3.3] or to gas heating [3.4, p. 56].
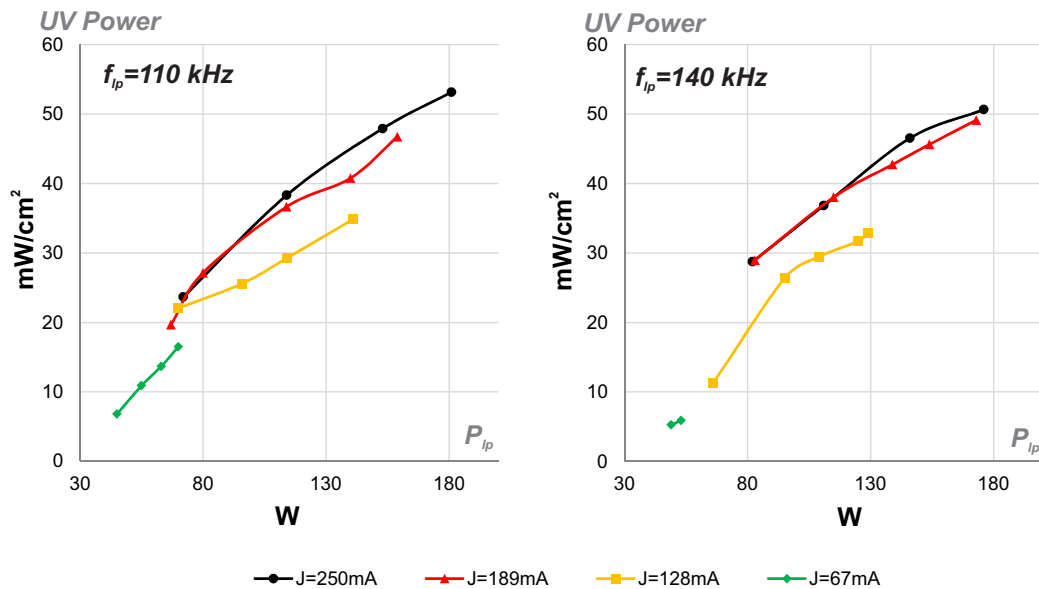
Figure 3.5.: Impact of the excilamp current intensity in the UV output for f_{lp}=110 kHz (left) and f_{lp}=140 kHz (right)
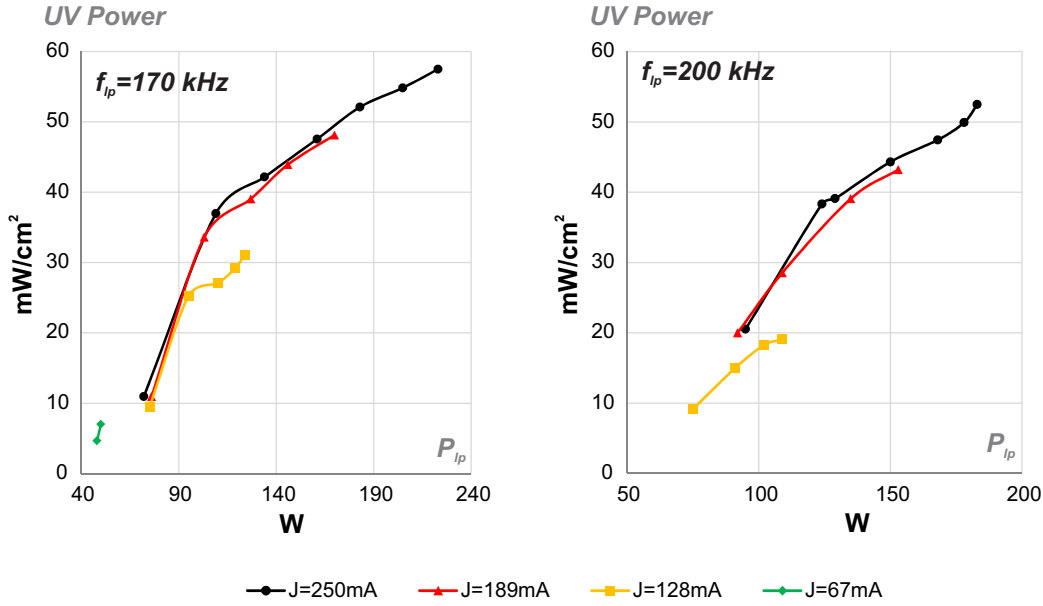
Figure 3.6.: Impact of the excilamp current intensity in the UV output for f_{lp}=170 kHz (left) and f_{lp}=200 kHz (right)

3.2.2. Impact of *J* Over the Electrical and UV Waveforms

In Fig.3.7 the instantaneous response of the excilamp UV output is compared with the lamp current waveform, for operating points of same frequency and electrical power. A reduction in the UV peak value with the increase of the frequency is found when comparing the UV for $f_{lp} = 50\,kHz$ (Fig.3.7-a) with the other UV waveforms in Fig.3.7-b-d. This can be explained by a reduction in the peak current transient injected into the lamp on the rising edge of each current pulse.

In general, a tightly correlation of the lamp current intensity and the UV pulse amplitude is observed. For the operating range of the test, once the lamp ignition is produced the UV radiation is emitted without interruption, as long as the current continue to be injected into the lamp. In Fig.3.8 the experimental lamp current and the UV waveform are plotted together to demonstrate this similitude. In this figure is observed the T_{br} time required to produce the gas breakdown after the beginning of the current pulse injection. Once the gas breakdown is produced the UV pulse starts and its amplitude follows the absolute value of i_{lp} as long as current continues to be injected into the lamp. However, the initial overshoot in the UV pulse and subsequent oscillations, are not observed in the lamp current. In fact, the gas conductance current i_G is the responsible for the UV production [3.5] and in an actual lamp, after gas breakdown i_G is not exactly equal to i_{lp}, however, i_G can not be experimentally measured. With the aim to provide an accurate estimation of i_G and by this mean, an estimation of the UV production, an identification and estimation algorithm is proposed in [3.6].

a. f_{lp}=50 kHz - 2μs/div

b. f_{lp}=80 kHz - 2μs/div

c. f_{lp}=110 kHz - 1μs/div

d. f_{lp}=200 kHz - 1μs/div
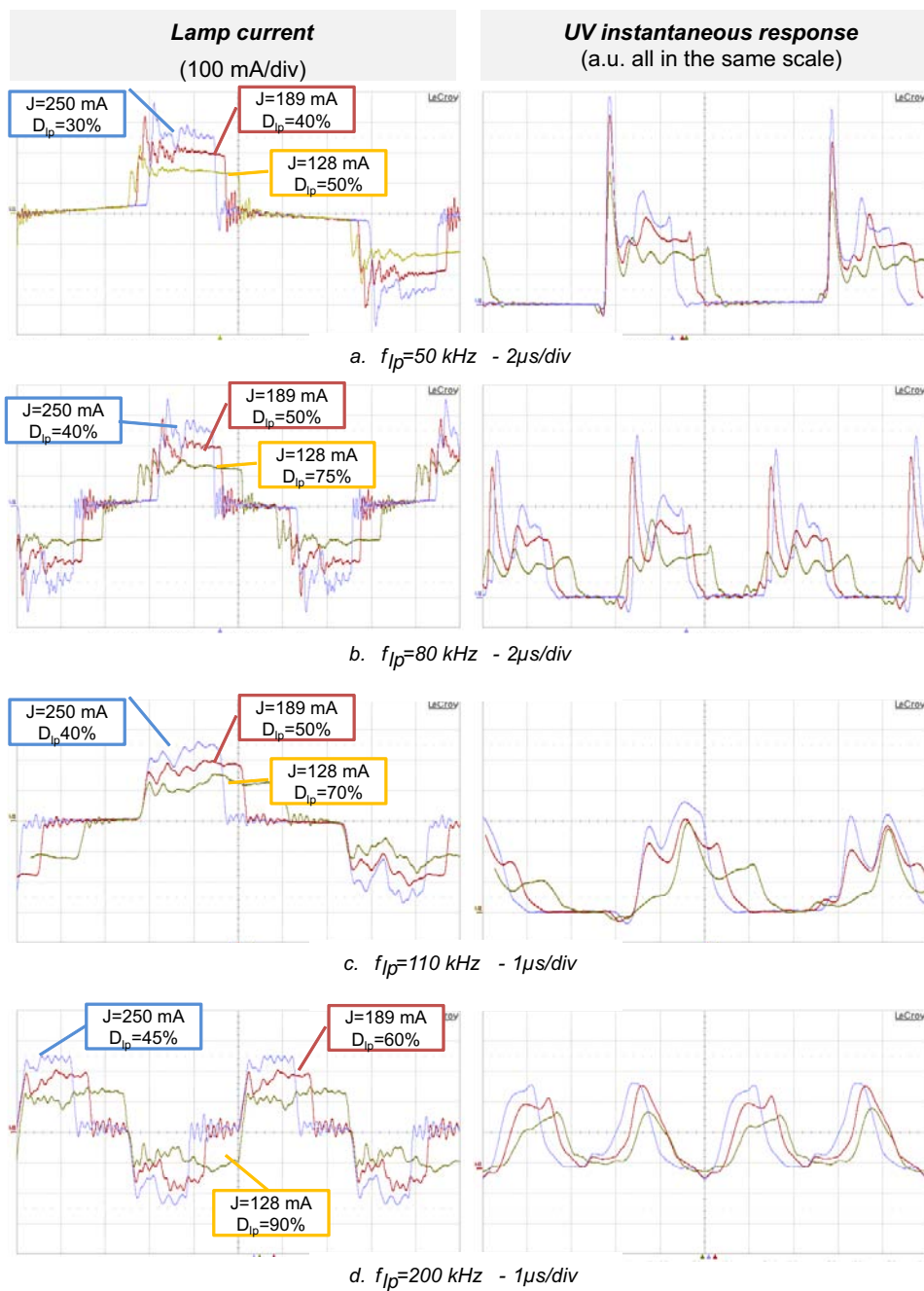
Figure 3.7.: Comparison of the current and UV waveforms for different values of J
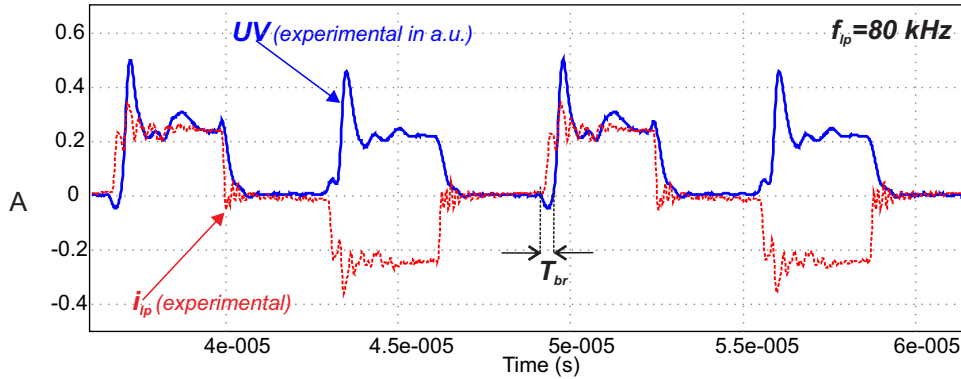
Figure 3.8.: The experimental lamp current and UV (in arbitrary units) waveforms are shown together in order to demonstrate the similarity between both signals. f_{lp}=80 kHz

An interesting fact is that the UV pulse shape is not the same for both current directions; it presents a more continuous shape when the current is negative and a more intense peak value when the current is positive. This can be attributed to the non-symmetrical geometry of the coaxial lamp. Due to the coaxial geometry, the areas of the electrodes are different, thus the surface available for the charges accumulation depends on which of the electrodes act as the anode [3.7, p. 35], and this can affect the efficiency on the creation of the excimers and consequently the UV production. Additionally, the difference in the distance from the photo-detector to each one of the electrodes, can have an impact on the measurement.

3.2.3. Impact of *J* Over the Lamp Model Parameters

As previously explained in Section 1.1.3, the Lissajous figure constructed with the lamp Charge-Voltage trajectory allows a graphical computation of the lamp equivalent electrical parameters [3.8, p. 12]. This method is used here to validate the simplified lamp model. The change of the lamp voltage as a function of the lamp charge Q_{lp}, presented in Fig.3.9, follows a counter-clock wise trajectory.

In the trajectories of Fig.3.9, the slopes of each trajectory (and consequently the values of C_d and C_g) before and after breakdown are not substantially affected by the changes in the lamp current intensity. In the same manner, the V_{th} value does not change significantly with the operating point variation, as observed in Table 3.1, where the equivalent parameter values obtained for each trajectory, are presented. With maximum standard deviation of 15 %, obtained for the C_g parameter, the use of a single equivalent simplified model for a wide lamp operating range is validated. The average values of the obtained parameters, shown in Table 3.1, can be used for the power supplies design.
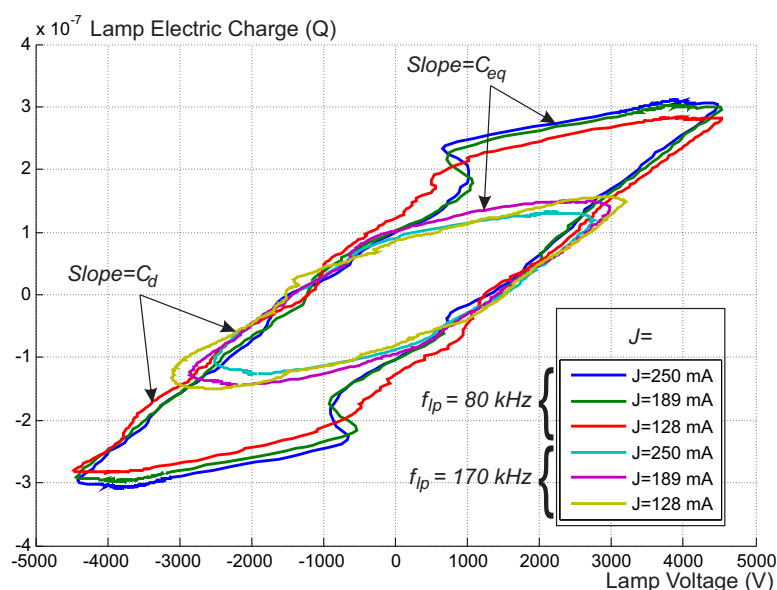
Figure 3.9.: Lamp Charge-Voltage plot for different values of current intensity at constant current frequency and injected power.

$f_{lp}(kHz)$	**80**			**170**			Average	σ
J (mA)	250	189	128	250	189	128		
V_{th} (kV)	1.18	1.25	1.38	1.3	1.32	1.32	1.26	7%
C_d (pF)	91.2	91.2	91.5	86.4	81.4	87.9	87.9	5%
C_g (pF)	29.2	29.2	29.6	27.6	34.5	37.5	31.3	13%

Table 3.1.: Equivalent lamp parameters and standard deviation obtained from the Charge-Voltage Lissajous figures shown in Fig.3.9

3.2.4. Impact of *J* Over the Discharge Regime

For a constant excitation power and frequency, the shape of the discharges becomes more filamentary as the current intensity increases. This can be observed in the pictures of Fig.3.10. As exposed in the precedent Section 3.2.1, higher levels of current intensity are associated to a better performance of the excilamp, thus the existence of well defined filaments can be an indicator of high levels of efficiency in the output radiation power. This result complements the experiments presented in [3.9, p.204] and [3.4, p.59], where the transition from a diffuse channels to clearly defined filaments is studied and associated to a peak in the lamp efficiency.
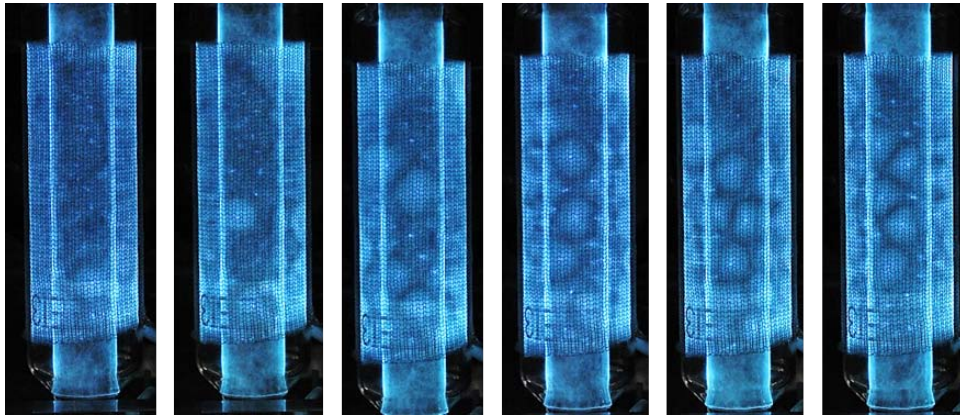
Figure 3.10.: Changes in the visual aspect of the discharges with the increase of the current intensity. $f_{lp} = 70\ kHz$, $P_{lp} = 80\ W$, $J = 95, 116, 133, 154, 171, 186\ mA$ (from left to right)

3.3. Impact of the Lamp Operating Frequency

The effect of the lamp operating frequency is evaluated for f_{lp} equal to 50, 80, 110, 140, 170 and 200 kHz, while keeping constant J. For every f_{lp} value, the lamp electrical power is progressively increased by means of D_{lp} and the trend line of the UV power output vs. the injected electrical power is obtained. Then the curves obtained for each operating frequency are compared. After that, the electrical and UV waveforms, the equivalent lamp model and the appearance of the lamp discharge, obtained for each operating frequency are compared.

3.3.1. Impact of f_{lp} Over the UV Production

At the maximum tested value of J (250 mA) shown in Fig.3.11-left, the impact of the frequency over the UV radiation for the 50-140 kHz range is negligible and the UV output increases linearly with P_{lp}. However, for the 170-200 kHz range, a slope change in the curve is observed; in the first part of the curve ($P_{lp} < 120W$) a reduction of up to 35% in the UV production, compared with the 50-140 kHz range, is evidenced; against a reduction of only 8% for the second curve piece at $P_{lp} = 150W$. A similar effect of f_{lp} is observed for J=189 mA, shown in Fig.3.11-right.
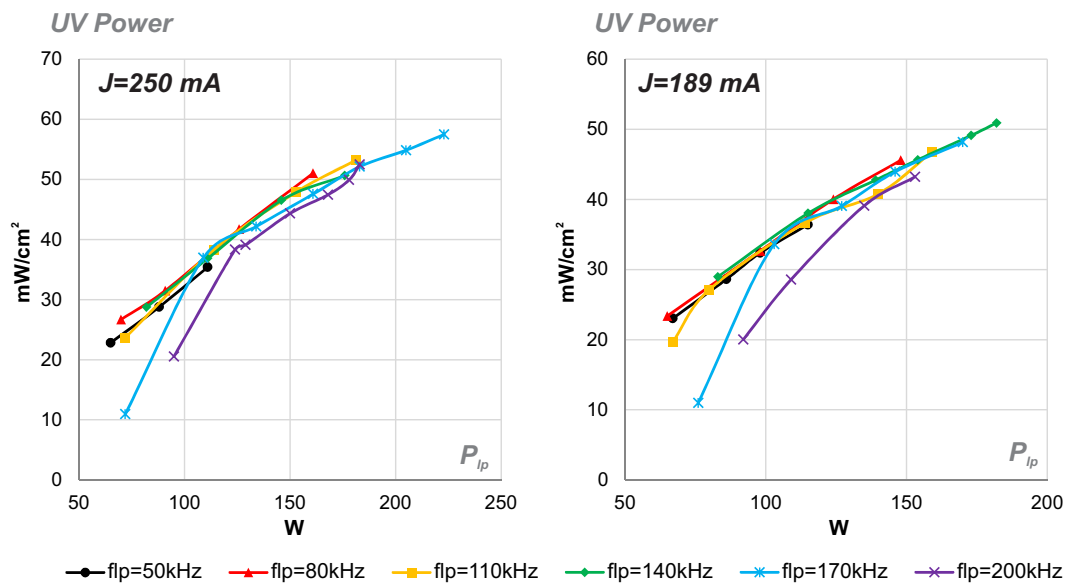
Figure 3.11.: Impact of the operating frequency in the UV output for J=250 mA (left) and for J=189 mA (right)

In this sense, if this DBD excilamp is operated at lower levels of power (below 120 W) the best option is to use a current frequency smaller than 110 kHz to obtain more UV power per Watt injected. However if the objective is to maximize the effective UV output, a higher value of f_{lp} enables the injection of more power into the lamp while respecting

the converter maximum ratings (as expected from (2.3.4)) and thus to maximize the UV radiation production. As observed in Fig.3.11, although the slope of all the curves reduces with the increment of P_{lp}, a saturation point has not been attained, hence it will be possible to produce more UV power.

For J=128 mA, the UV power curves are shown in Fig.3.12-left. In these curves, the abrupt slope change in the curves appears for $f_{lp} \geq 80$ kHz, revealing that the smaller the current intensity, the higher the impact of the frequency on the lamp performance. Finally, for J=67 mA shown in Fig.3.12-right, the duty ratio's limitation at the higher operating frequencies does not allow to supply more than 50 W to the lamp. For this current intensity the fact of increasing f_{lp} from 50 kHz to 110 kHz reduce significantly the UV production, in contrast with the non noticeable effect shown in Fig.3.11 for the same frequency range.
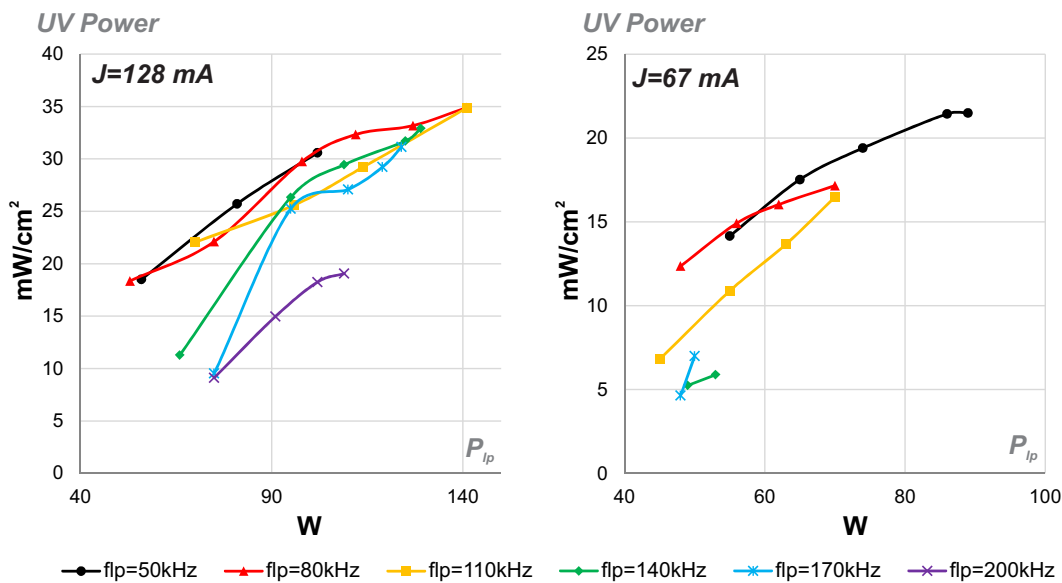
Figure 3.12.: Impact of the operating frequency in the UV output for J=128 mA (left) and for J=67 mA (right)

3.3.2. Impact of f_{lp} Over the Electrical and UV Waveforms

In Fig.3.13, the instantaneous response of the excilamp UV output is presented for different values of P_{lp} at constant values of two D.O.F.: frequency and J. The value of the power is adjusted by means of the D_{lp} duty ratio. An interesting result observed for each operating frequency set, is that the UV peak amplitude decreases when the lamp power increases, even though the current amplitude remains constant. Thus the amplitude of the UV pulses can not be related only to the lamp current intensity.

For f_{lp}=50 kHz and 80 kHz, an overshoot in the UV waveforms is observed. As an hypothesis, a factor that can be associated to this UV overshoot is the reduction in the

a. f_{lp}=50 kHz - 2μs/div

b. f_{lp}=80 kHz - 2μs/div

c. f_{lp}=140 kHz - 1μs/div

d. f_{lp}=200 kHz - 1μs/div
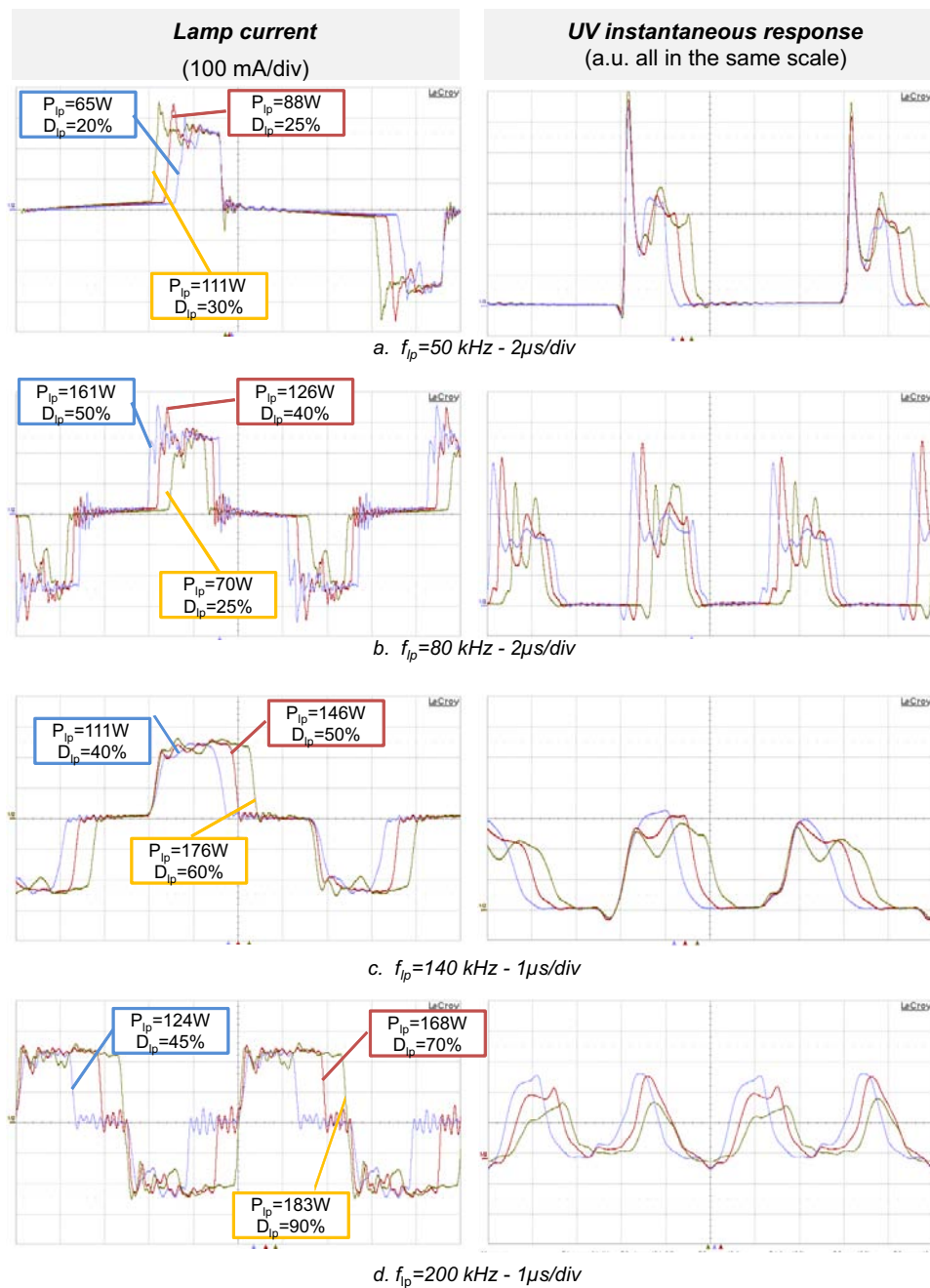
Figure 3.13.: Comparison of the current and UV waveforms for $J = 250mA$

relaxation time of the gas between ignitions as f_{lp} increases. The blanking time between current pulses (equal to $(1 - D_{lp})T_{lp}/2$) is around 6 µs for f_{lp}=50 kHz, J=250 mA and P_{lp}=111 W, and decreases to about 1 µs for f_{lp}=200 kHz at the same lamp power and current intensity. Due to the higher relaxation time, there is more time for the excited molecules to return to the ground state of energy, henceforth a higher gas voltage could be necessary to produce the breakdown. As the breakdown happens the gas voltage returns to its steady state value, called here V_{th}.

Another factor that could be associated to the production of this higher UV peak value, is the higher overshoot in the lamp current, observed at the rise edge of the current pulses in Fig.3.13-a-b. This current overshoot is produced by a higher lamp peak voltage at low frequencies. A higher voltage reflected to the primary side of the transformer produces a faster change in the leakage inductance current and consequently a higher initial lamp peak current (2.3.7). However, this hypothesis is less probable because as can be observed by comparing the lamp current with the UV pulses, the amplitude of the initial peak current does not correspond to the amplitude of the UV overshoot and moreover, this initial lamp peak current does not participate to supply the discharge but to charge C_g. For f_{lp}=200 kHz and D_{lp}=90 % an almost continuous UV radiation is produced. The dead time in the radiation output is determined by T_{br} (2.1.1) and the commutation time of the inverter switches.

3.3.3. Impact of f_{lp} Over the Lamp Model Parameters

For a constant current intensity value, in this case $J = 189\,mA$, the lamp Charge-Voltage trajectory is plotted in Fig.3.14. The slopes of the different operating cases are similar, both before and after gas breakdown. The lamp model parameters, computed for each trajectory as described in 1.1.3, are presented in Table 3.2. Comparing the average of these parameters with the ones obtained in Table 3.1 and the obtained standard deviation, the use of a single electrical equivalent model for the design of power supply independently of the operating frequency, makes sense.

$f_{lp}(kHz)$	50	80	110	140	170	200	Average	σ
V_{th} (kV)	1.30	1.32	1.23	1.33	1.45	1.37	1.33	6%
C_d (pF)	93.4	96.7	86.6	92.8	85.8	83.5	89.8	6%
C_g (pF)	47.3	35.1	35.7	28.0	29.4	39.9	35.9	14%

Table 3.2.: Equivalent lamp parameters and standard deviation obtained from the Charge-Voltage Lissajous figures shown in Fig.3.14. J=250 mA

From these values, no noticeable impact of the frequency increment over the parameters values is observed. However, for f_{lp}=50 kHz, an abrupt change in the sign of the curve slope is observed at the breakdown instant, as indicated in Fig.3.14. As the frequency increases, the transition of the slope from C_{eq} to C_d becomes softer and without negative values. This phenomena is related to the UV overshoot discussed in Section 3.3.2and can be explained in the same manner. This abrupt change observed in the
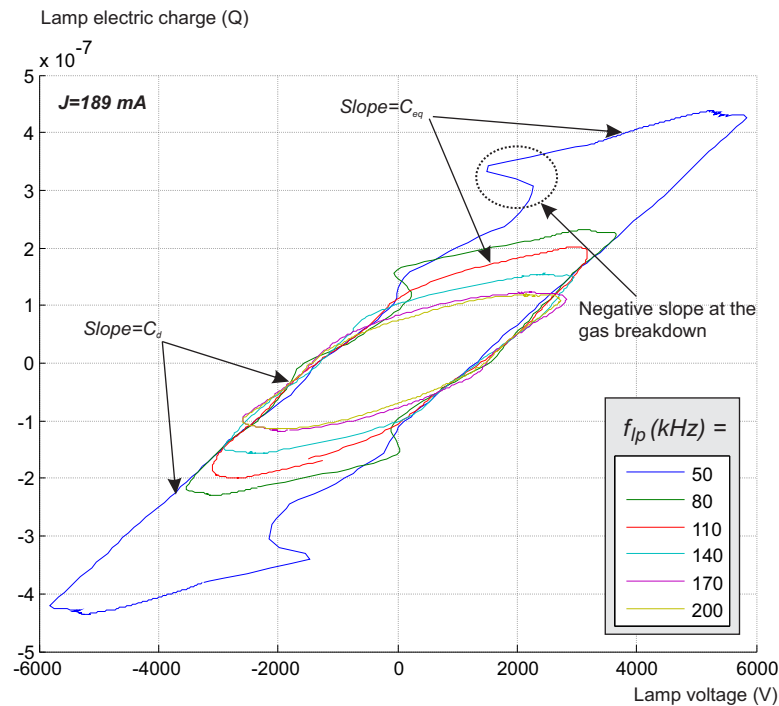
Figure 3.14.: Lamp Charge-Voltage plane for different values of current frequency at constant current intensity and injected power.

Lissajous figure can be observed also in the time domain regarding the v_{lp} waveform shown in Fig.2.27. In this figure it can be observed that, at the gas breakdown instant, a brief oscillation of v_{lp} appears for f_{lp}=50 kHz; for f_{lp}=100 kHz, at the gas breakdown v_{lp} remains almost constant during a short time; and for f_{lp}=50 kHz, there is a soft change in the slope in the transition from before and after the breakdown.

3.3.4. Impact of f_{lp} Over the Discharge Regime

Pictures in Fig.3.15 have been taken for a constant excilamp excitation power, supplied at a constant value of current intensity. Each picture corresponds to a different value of operating frequency. As can be observed, no change in the visual aspect of the discharge is noticed for this operating frequency range (50-100 kHz). The UV power that corresponds to these picture presents a slight decrease of 6 % with the increase of f_{lp}. In conclusion, the visual aspect of the streamers remains diffuse and the UV production does not change significantly. Comparing this behavior with pictures in Fig.3.10 where the change of the discharge from diffuse to filamentary has been accompanied by an increase on the UV power, a relation between the filamentary appearance of the streamers and a high UV production efficiency, can be suggested.
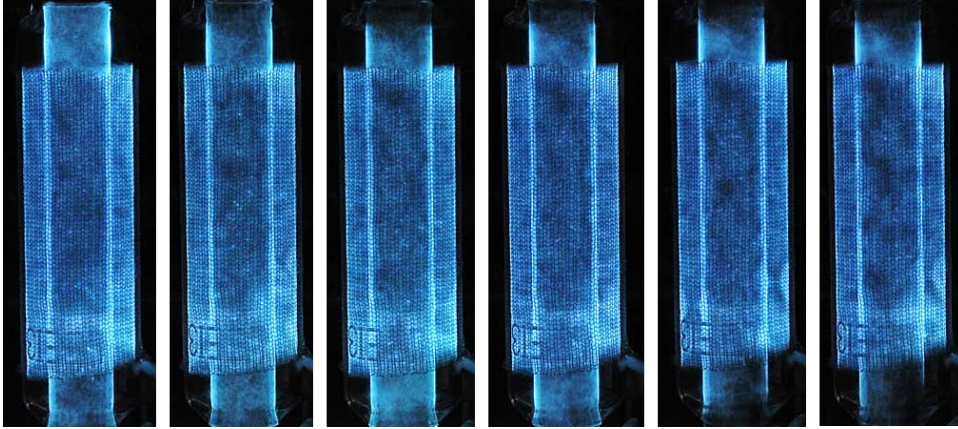
Figure 3.15.: Changes in the visual aspect of the discharges with the increase of the operating frequency. $f_{lp} = 50, 60, 70, 80, 90, 100$ kHz (from left to right), P_{lp}=80 W, J=100 mA

3.4. Best Performance Operating Conditions

From the parametric measurements presented in the precedent section, an optimal excilamp operating condition is suggested. This optimal operating point is found within the studied operating range and for the particular excilamp under study.

In order to evaluate the DBD excilamp performance, a measurement of the lamp energy conversion relative efficiency, defined here as η_{rUV}, is calculated as the conversion ratio from electrical power injected into the lamp (P_{lp}) and the UV output power $P_{UV}(mW/cm^2)$ (3.4.1). This is a relative and not an absolute measurement of the irradiation efficiency because not all the UV power emitted from the lamp is used here, instead, only the irradiation power measurement obtained with the radiometer is used.

$$\eta_{rUV} = \frac{P_{UV}(mW/cm^2)}{P_{lp}(W)} \tag{3.4.1}$$

Inspired by works of [3.10, 3.11] predicting the existence of an optimal range of discharge energy, the excilamp efficiency has been plotted against the energy transferred to the lamp in each current pulse. This pulse energy (E_{lp}) is calculated with (3.4.2).

$$E_{lp} = \frac{P_{lp}}{2f_{lp}} \tag{3.4.2}$$

In Fig.3.16, η_{rUV} is plotted as a function of the supplied pulse energy. In Fig.3.16-left the data points corresponding to the same value of J have the same color in order to evaluate the impact of J over the lamp efficiency. According to this figure, the efficiency for the operating points corresponding to the maximum value of J is slightly higher than the other ones. In Fig.3.16-right, each color means the same operating frequency.

From this figure is found that the maximum efficiency points are obtained for f_{lp}=80 kHz. From both graphics an interesting result from the point of view of the physics of the lamp is found; observe that despite the dispersion of the points, in general the lamp efficiency is very low for $E_{lp} < 300~\mu J$ for the tested values of current frequency and intensity. Note that for f_{lp}=50 kHz no points below 500 µJ are found.
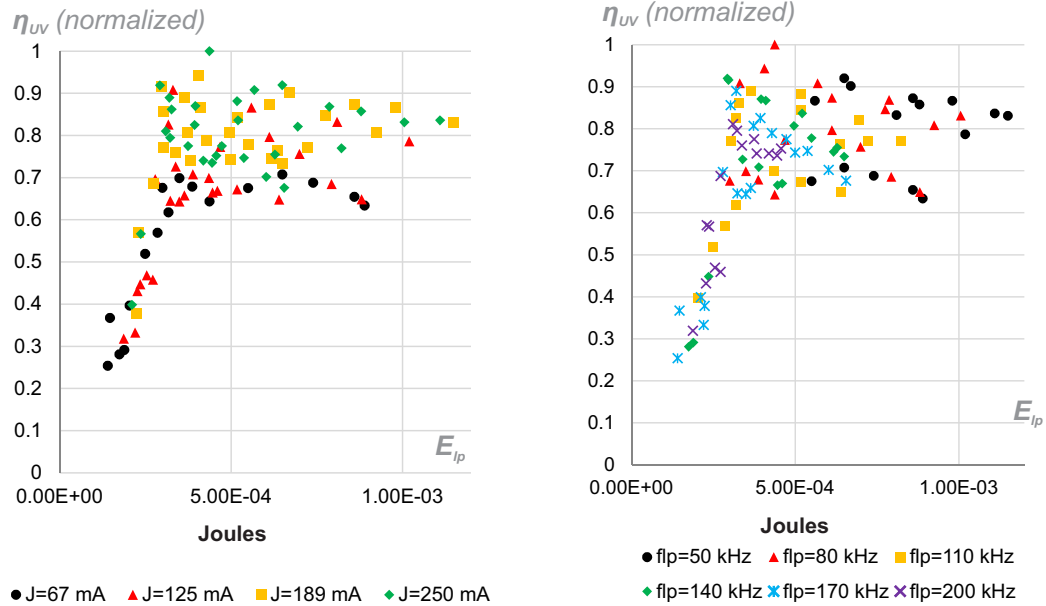
Figure 3.16.: Excilamp relative radiation efficiency as a function of the injected energy, for different values of lamp current intensity (left) and lamp operating frequency (right)

In particular, the maximum lamp efficiency has been obtained for the operating point described in Table 3.3.

$J(mA)$	$f_{lp}(kHz)$	$D_{lp}(\%)$	$P_{UV}(mW/cm^2)$	$P_{lp}(W)$	$E_{lp}(\mu J)$
250	80	25	27	70	438

Table 3.3.: Point of maximum lamp efficiency within the operating range of the experiments

However, the point of maximum lamp efficiency does not guarantee the UV power required in a real application. Henceforth, in order to obtain this desired UV power with high efficiency, Fig.3.17 should be used. This figure shows the UV power as a function of the lamp electrical power. To obtain a given value of UV power, the optimal operating point is the one that requires less electrical power (P_{lp}) (the leftmost data point). For example, if 30 mW/cm^2 of UV power is required, among the operating points highlighted with a circle in Fig.3.17 the leftmost operating point provides 27 % of energy savings when compared with the data point placed at the right limit of the

circle.
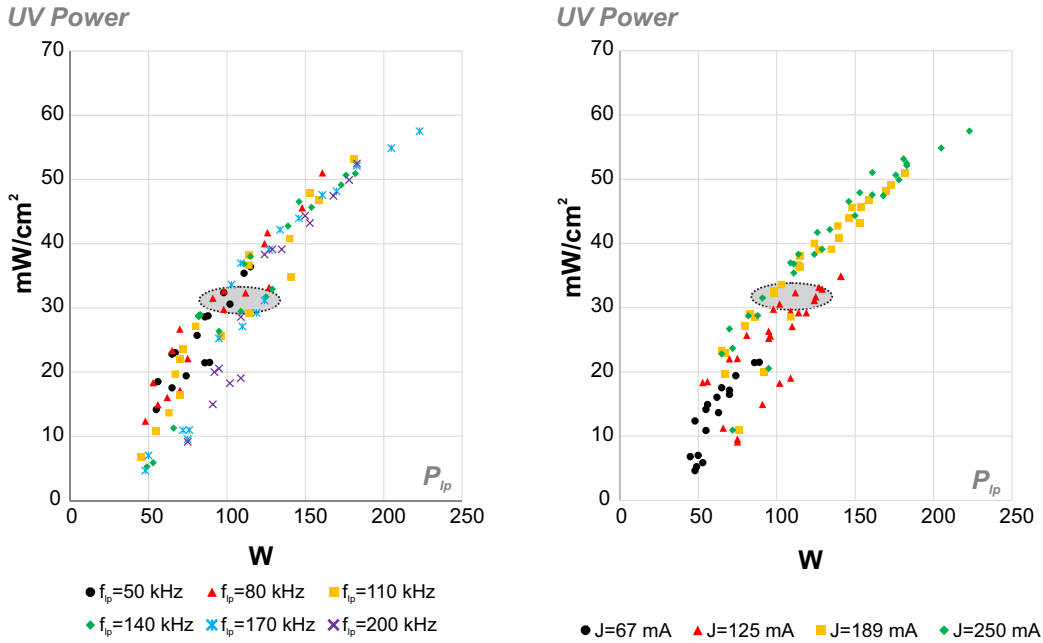
Figure 3.17.: Excilamp UV power as a function of the injected electrical power, with the corresponding lamp current frequency (left) and lamp operating intensity (right)

Previously, in Section 3.2 was shown that for a given lamp electrical power the UV production is enhanced by increasing the current intensity from 67 mA to 189 mA. However, with an additional increase of the current amplitude from 189 mA to 250 mA, a noticeable gain in the lamp efficiency, is not observed. Consequently, to maximize the UV output of the DBD excilamp under test, an operating peak current around 200 mA is suggested.

Depending on the UV radiation power required for a particular application, the optimal operating point must be selected. From the results analyzed in Section 3.3, to maximize the UV production the minimum value of f_{lp}, should be preferred. This minimum value of f_{lp} is determined, from the point of view of the converter by the maximum tolerated output converter voltage, remembering that for a given lamp power, the lamp peak voltage increases inversely with f_{lp}. And from the point of view of the lamp efficiency, for a given value of lamp power, the minimum f_{lp} should be calculated according to (3.4.2) not to produce a pulse energy lower than 300 µJ.

3.5. Conclusions

The lamp heating reduce substantially the UV radiation power, thus the lamp temperature is an operating condition that must be taken into account when evaluating the

DBD excilamp performance. The DBD excilamp UV production is positively affected by the increase of the current intensity. However, for the particular experimental bench studied here, there is no important gain in the lamp performance above 189 mA of current intensity. In contrast, the simplified equivalent electrical model of the lamp is barely affected by the changes in the operating point.

The existence of well defined filaments in the discharge is associated to better levels of UV production efficiency than those measured for non or less filamentary operating points. The amplitude and duration of the UV radiation pulses are governed by the lamp current intensity and the current pulse duration respectively.

The energy injected into the lamp to produce the discharge, seems to has an influence in the lamp performance. For all the tested operating points and for this particular XeCl DBD excilamp, the better performances have been obtained with energy pulses higher than 300 μJ. Additionally it has been demonstrated that by only changing the DBD excilamp operating point, the lamp performance can be drastically improved.

Finally, we point out that the methodology used for the presented study, incorporating the use of the Square-shape current mode supply, has demonstrated to be a valuable tool for the evaluation of DBD excimer lamps. According to [3.4, p. 54] the maximum efficiency conditions can differ depending on the gas mixture of the excilamp, consequently, a comparative study of different types of gas mixtures DBD excilamps, is one of the perspectives of this work.

Bibliography

[3.1] Haruaki Akashi, Akinori Odam, and Yosuke Sakai, "Effect of gas heating on excimer distribution in DBD xe excimer lamp," in *28th ICPIG Conference Records*, (Prague, Czech Republic), July 2007.

[3.2] F. Marchal, N. Sewraj, G. Jabbour, P. R. Akerreta, and G. Ledru, "Temperature dependence of xenon excimer formations using two-photon absorption laser-induced fluorescence," *Journal of Physics B: Atomic, Molecular and Optical Physics*, vol. 43, p. 235210, Dec. 2010.

[3.3] R. J. Carman and R. P. Mildren, "Computer modelling of a short-pulse excited dielectric barrier discharge xenon excimer lamp (172 nm)," *Journal of Physics D: Applied Physics*, vol. 36, pp. 19–33, Jan. 2003.

[3.4] M. I. Lomaev, V. S. Skakun, V. F. Tarasenko, and D. V. Shitts, "Excilamps based on xenon dimers excited by a barrier discharge," *Journal of Optical Technology*, vol. 79, no. 8, pp. 498–502, 2012.

[3.5] S. Bhosle, G. Zissis, J.-J. Damelincourt, A. Capdevila, K. Gupta, F. Dawson, and V. Tarasenko, "Implementation of an efficiency indicator in an electrical modeling of a dielectric barrier discharge lamp," in *Conference Record of the 2006 IEEE Industry Applications Conference, 2006. 41st IAS Annual Meeting*, vol. 4, pp. 1784–1790, 2006.

[3.6] A. Lopez, H. Piquet, D. Patino, R. Diez, and X. Bonnin, "Parameters identification and gas behavior characterization of DBD systems," *IEEE Transactions on Plasma Science*, vol. 41, no. 8, pp. 2335–2342, 2013.

[3.7] Hartnett, James, *Transport Phenomena in Plasma.* Academic Press, Oct. 2007.

[3.8] U. Kogelschatz, "Dielectric-barrier discharges: Their history, discharge physics, and industrial applications," *Plasma Chemistry and Plasma Processing*, vol. 23, no. 1, pp. 1–46, 2003.

[3.9] M. I. Lomaev, V. S. Skakun, E. A. Sosnin, V. F. Tarasenko, D. V. Shitts, and M. V. Erofeev, "Excilamps efficient sources of spontaneous UV and VUV radiation," *Physics-Uspekhi*, vol. 46, pp. 193–209, Feb. 2003.

[3.10] A. M. Razhev and A. A. Zhupikov, "Influence of the specific pump power on the output energy and efficiency of a 223-nm gas-discharge-pumped excimer KrCl laser," *Quantum Electronics*, vol. 38, p. 1005, Nov. 2008.

[3.11] A. M. Boichenko, "The effect of the excitation power on the emission efficiency of barrier- and glow-discharge pumped exciplex and excimer lamps," *Laser Physics*, vol. 14, no. 8, pp. 1036–1044, 2004.

4. High Efficiency DBD Power Supply Working at the Optimal Operating Point

On the basis of the DBD lamp electrical model, it has been proven that the DBD electrical power can be controlled by means of its current instead of using its voltage (Section 1.2). Morevover, by means of the lamp current, the UV temporal response can be also controlled, because, as mentioned in Section 1.1, the fitting between the UV instantaneous response and the lamp current waveform after gas breakdown, has been demonstrated [4.1, 4.2].

Accordingly, in Section 2 a square-waveform current supply with three degrees of freedom, has been designed to study the radiation of DBD lamps. Using this programmable converter, optimal DBD excilamp operating conditions were determined in Chapter 3. However this fully-controlled converter presents hard-switching, diminishing the efficiency and producing EMI.

In order to increase the converter-lamp ensemble efficiency, the present Chapter proposes to supply the lamp at a fixed operating condition employing a Zero Current Switching (ZCS) converter, differing from existing power supplies for DBDs in the following aspects:

- Zero current switching (ZCS) is achieved in all the switches at turn-on and turn-off, also respecting the current mode operation.

- The converter is designed to work at an optimal operating point of the DBD excilamp, based on the parametric study presented in Chapter 3.

This Chapter is organized as follows: Section 4.1 explains the converter operating principle using the simplified lamp model and develops the mathematical relationships for the design of the converter, based on the state plane analysis. The proposed converter design is distinguished from previous developments, by the use of three equivalent electrical parameters of the DBD model (C_d,C_g,V_{th}). Section 4.2 dimensions the components for a specific XeCl excimer lamp and verifies the previous theoretical developments. Experimental results and conclusions are given in Sections 4.3 and 4.4, respectively.

4.1. Topology: SRI Operated in DCM

The classical topology of the series resonant current inverter (SRI), shown in Fig.4.1, combines a current source behavior [4.3], [4.4], [4.5] with the capability of ZCS. For this reason this topology is chosen to implement the proposed DBD current supply.

In this topology the inductance L is connected in series with the DBD lamp through the full-bridge current inverter as shown in Fig.4.1. The lamp current direction is determined by the bridge configuration.
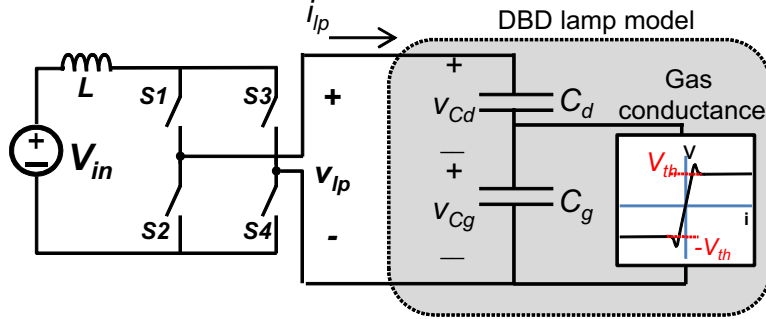
Figure 4.1.: The proposed series-resonant inverter

The converter operating period is divided in six steps, determined by the bridge switches and the gas state. The equivalent circuit for each stage of this operating sequence is presented in Fig.4.2(bottom).

With the switches S1, S4 turned-on, an LC series resonant circuit is obtained, as presented in 4.2 (a), and the lamp current flows in the direction that will be defined as the positive one, henceforth.

Due to the resonance, the lamp current, i_{lp}, grows, as seen in Fig. 4.2 (top), and consequently the gas voltage, v_{Cg}, increases until it reaches the breakdown voltage V_{th}. The breakdown occurs at time t_{br}, and the gas is now represented by the constant voltage source V_{th}, as shown in Fig.4.2 (b); however the dielectric voltage v_{Cd} continues to grow as long as the lamp current remains positive.

In order to obtain the ZCS at turn-off of the switches and maximize the efficiency, when the lamp current falls to zero at the time t_{off} the bridge must turns-off and the lamp is disconnected from the source, as seen in Fig.4.2 (c); consequently, given the capacitive behavior of the lamp, v_{lp} remains constant at its positive peak value, $\hat{V}_{lp}$.

The next half-cycle starts at $T_{lp}/2$ turning-on the switch pair (S3, S2). The equivalent circuit in Fig.4.2 (d) produces a resonant current in the negative direction. In this sequence the gas voltage is taken from V_{th} to $-V_{th}$ to reach again the breakdown condition. When v_{Cg} is equal to $-V_{th}$, the gas capacitance C_g is replaced by the inverted voltage source V_{th} in Fig. 4.2 (e). As done previously for sequence (c), the full-bridge is disconnected from the lamp; starting sequence (f), when the lamp current reaches zero and the lamp voltage reaches its negative peak voltage. This voltage remains constant until the sequence (a) restarts at T_{lp}. In this way, for steady state, the negative lamp peak voltage and zero lamp current (4.1.1), are initial conditions for the equivalent capacitance of the first sequence (a):

$$v_{lp}(t_0) = -\hat{V}_{lp} \ , \ i_{lp}(t_0) = 0A. \qquad (4.1.1)$$
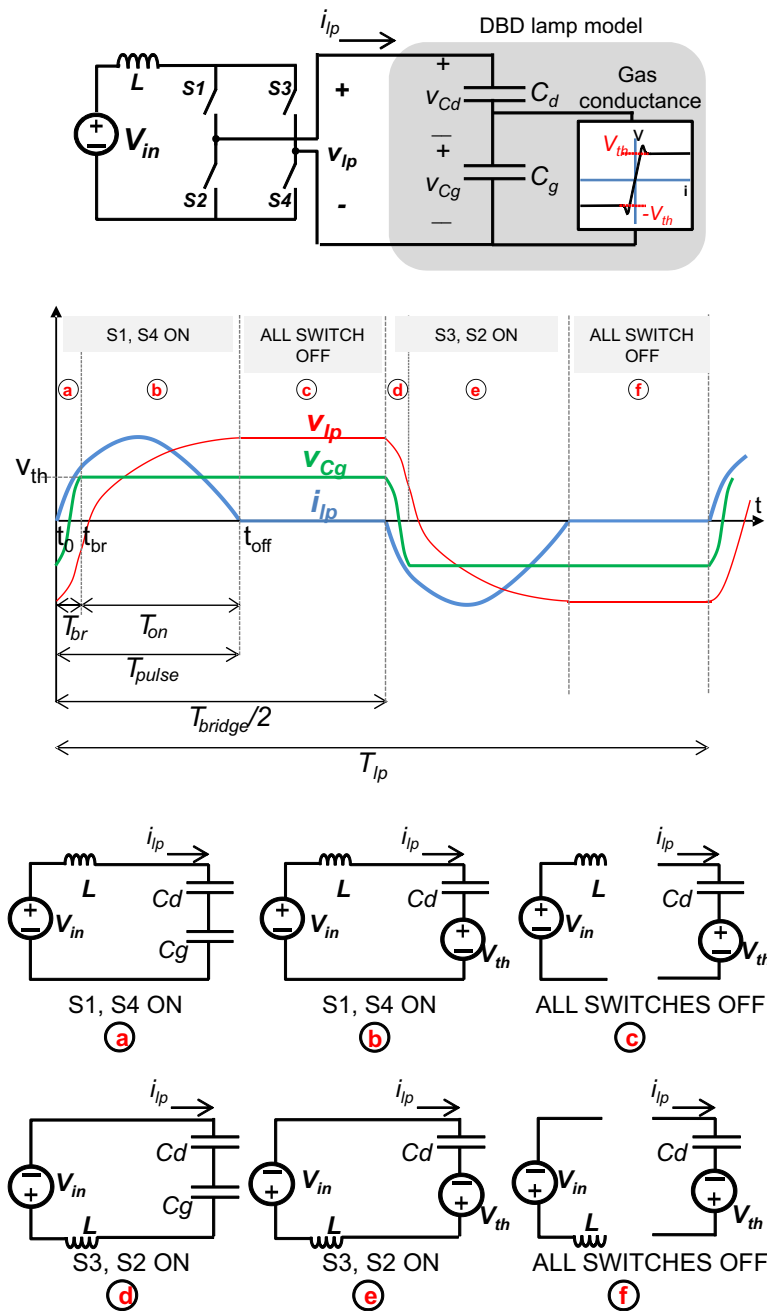
Figure 4.2.: The SRI operating sequences (bottom). Theoretical waveforms for lamp current, lamp voltage and gas voltage (top).

Using the DCM selected in this work, the lamp operating frequency is defined by only the bridge operation, as presented in Fig. 4.2 (top).

The achievement of this DCM mode is implemented thanks to a specific switch, which is presented in Section 4.2. The converter is designed using the state plane analysis [4.3], [4.6]. This method allows the determination of the operating conditions for the converter-lamp system, using the equivalent circuits from Fig. 4.2 (bottom). Despite state plane analysis can be used to find transient response, only the steady-state analytic expressions are presented in this Chapter. Hereafter, the sequences corresponding to the positive current are analyzed; due to symmetry, the study of the negative cycle leads to similar results.

4.1.1. State plane analysis

The state plane analysis is used to plot the current-voltage behavior of a resonant circuit. Fig.4.2 (a) shows the resonant equivalent circuit before gas breakdown occurs. Normalized units are used, leading to the plot of circular clockwise trajectories [4.3] to describe the current-voltage characteristic for the lamp before ignition, as will be presented in Fig. 4.3:

$$u = \frac{v_{lp}}{V_{th}} \tag{4.1.2}$$

$$j = \frac{i_{lp}}{V_{th}} \sqrt{\frac{L}{C_{eq}}} \text{ , with } C_{eq} = \frac{C_d C_g}{C_d + C_g} \tag{4.1.3}$$

After the gas breaks down, the equivalent resonant circuit changes as shown in Fig. 4.2 (b) with v_{Cg} constant and equal to V_{th}. Therefore, a new state plane is used. This new plane shown in Fig.4.4, draws the normalized current-voltage characteristic for the dielectric capacitor, being the dielectric current equal to the lamp current.

As the equivalent capacitance changes from C_{eq} to C_d, normalization is redefined as follows, using * as notation to remember that these variables correspond to the ignited lamp. These variables are used after:

$$u^* = \frac{v_{Cd}}{V_{th}} = \frac{v_{lp} - v_{Cg}}{V_{th}} = \frac{v_{lp}}{V_{th}} - 1 = u - 1 \tag{4.1.4}$$

$$j^* = \frac{i_{lp}}{V_{th}} \sqrt{\frac{L}{C_d}} \tag{4.1.5}$$

Note that j^* does not have the same normalization as j, because the lamp equivalent capacitance change.

4.1.2. State plane: before breakdown trajectory

Two operating cases for the equivalent resonant circuit before lamp ignition, are shown in Fig.4.3: in the state plane of the operating case (A) the lamp peak current is not

reached before the gas breakdown, in the operating case (B) the ignition occurs when the lamp current has already reached its maximum and is decreasing. Depending on the operating case, the expressions describing the converter operating conditions are found differently. Next analytic expressions for these state planes are developed.

As explained in Section 4.1, at the beginning of the positive current cycle, the initial lamp voltage is equal to $-\hat{V}_{lp}$ and the initial lamp current is zero (4.1.1).

Normalizing the initial conditions using (4.1.2) and (4.1.3):

$$U_o = u(t_o) = -\hat{U} \tag{4.1.6}$$

$$J_o = j(t_o) = 0 \tag{4.1.7}$$

The normalized lamp current, j in Fig. 4.3, starts to rise, and the operating point follows a circular path in the plane with center in the normalized DC input voltage U_{in}, as long as this equivalent circuit is valid. That is, while the gas voltage is inverted from $-V_{th}$ to V_{th}. In this way, when the gas breakdown occurs, the total voltage change in the gas is $2V_{th}$. According to the capacitor voltage equation, this net gas voltage change can be expressed as:

$$2V_{th} = \frac{1}{C_g} \int_{t_o}^{t_{br}} i_{lp} \, \mathrm{d}t \tag{4.1.8}$$

The lamp voltage can be calculated in the same manner:

$$v_{lp}(t_{br}) = v_{lp}(t_o) + \frac{1}{C_{eq}} \int_{t_o}^{t_{br}} i_{lp} \, \mathrm{d}t \tag{4.1.9}$$
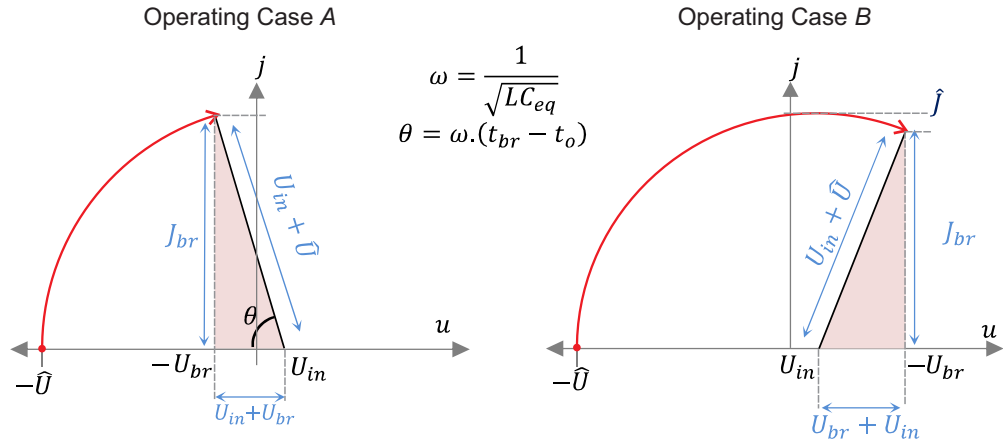
Figure 4.3.: Two operating conditions before breakdown are plotted in the state plane: When the gas breakdown happens before the peak current (left) and after the peak current (right). Only the positive current half-cycle is shown.

Using (4.1.1) and combining (4.1.8) with (4.1.9), this expression can be written after normalization as in (4.1.10), which is the normalized lamp voltage at the breakdown time t_{br}, U_{br}:

$$u(t_{br}) = -U_{br} = -\hat{U} + 2\left(\frac{C_g}{C_{eq}}\right) \tag{4.1.10}$$

At the same instant, the lamp current value is defined as the breakdown current, I_{br}, and in the normalized form as J_{br}. From trigonometric equations for either of the shaded triangles in Fig. 4.3, we obtain:

$$j(t_{br})^2 = J_{br}{}^2 = (U_{in} + \hat{U})^2 - (U_{br} + U_{in})^2 \tag{4.1.11}$$

4.1.3. State plane: after breakdown trajectory

The initial current for the state plane in Fig. 4.4, is equal to the breakdown current I_{br}; However, given that normalization is different from the previous sequence, (4.1.3) and (4.1.5) are used to find the initial normalized current:

$$J_{br}^{*\,2} = J_{br}{}^2 \frac{C_{eq}}{C_d} \tag{4.1.12}$$

From the lamp model the dielectric voltage v_{Cd} is equal to $v_{lp} - v_{C_g}$, hence, at the gas breakdown instant, when $v_{C_g} = V_{th}$, the dielectric voltage is (4.1.13):

$$v_{Cg}(t_{br}) = v_{lp}(t_{br}) - V_{th} \tag{4.1.13}$$

Normalizing (4.1.13) we obtain the dielectric initial normalized voltage for the state
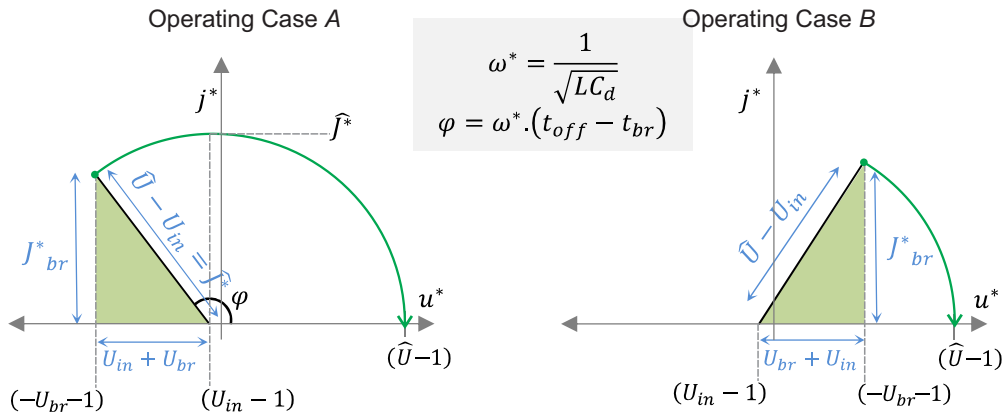
Figure 4.4.: Two operating conditions are plotted in the state plane after breakdown: When the gas breakdown happens before the peak current (left) and after the peak current (right). Only the positive current cycle is shown.

plane in Fig.4.4, $u^*(t_{br})$ (4.1.14):

$$u^*(t_{br}) = -U_{br}^* - 1 \tag{4.1.14}$$

Given that the voltage normalization constant is the same (V_{th}) for both state planes, before and after gas breakdown, we can write (4.1.15):

$$u^*(t_{br}) = -U_{br} - 1 \tag{4.1.15}$$

Now, using geometrical relations for either of the shaded triangles in the state plane of Fig. 4.4, we can write (4.1.16):

$$J_{br}^{*\,2} = (\hat{U} - U_{in})^2 - (U_{br} + U_{in})^2 \tag{4.1.16}$$

In order to find $\hat{U}$ in terms of the normalized input voltage U_{in} we proceed as follows. First, replacing (4.1.12) in (4.1.16), we obtain: (4.1.17)

$$J_{br}^{\,2} \frac{C_{eq}}{C_d} = (\hat{U} - U_{in})^2 - (U_{br} + U_{in})^2 \tag{4.1.17}$$

Now, J_{br} is replaced by the expression given in (4.1.11):(4.1.18)

$$\left[\left(U_{in} + \hat{U} \right)^2 - (U_{br} + U_{in})^2 \right] \cdot \frac{C_{eq}}{C_d} = \left(\hat{U} - U_{in} \right)^2 - (U_{br} + U_{in})^2 \tag{4.1.18}$$

Using (4.1.10), U_{br} is substituted for an expression in terms of $\hat{U}$. Solving the resulting equation, we find the lamp normalized peak voltage value in steady state (4.1.19):

$$\hat{U} = 1 + \frac{C_g}{C_d \left(1 - U_{in} \right)} \tag{4.1.19}$$

and de-normalizing (4.1.19), the lamp peak voltage is found: (4.1.20)

$$\hat{V}_{lp} = V_{th} + \frac{V_{th}^{\,2} C_g}{C_d (V_{th} - V_{in})} \tag{4.1.20}$$

One should point out that the lamp peak voltage depends only on the input voltage and the parameters of the lamp, but not on the inductance value.

4.1.4. Operating conditions

In this Section is shown that the stability of the converter depends on the input voltage value. Once in the stability region, the two operating cases studied before (lamp peak current reached after and before the gas breakdown) are considered for the computation for the operating conditions.

Stability

From (4.1.20) the only variable to control $\hat{V}_{lp}$ is V_{in}. As V_{in} approaches V_{th}, $\hat{V}_{lp}$ tends to infinite, henceforth, a valid solution for (4.1.20) can be found only when condition (4.1.21) is fulfilled:

$$V_{in} < V_{th} \tag{4.1.21}$$

Otherwise, unstable operation occurs. The transient state plane trajectory for stable and unstable operating conditions is plotted from simulation in Fig. 4.5, using the simplified DBD lamp model. This condition of stability can be explained from a physical point of view.

To avoid uncontrolled grown of the lamp energy, the power injected by the voltage supply V_{in} in each semi-cycle must be equal to the power dissipated by the discharge P_{lp}. Because the conduction losses are neglected, the only dissipative element of the load is the equivalent voltage sink V_{th}, whose energy received each half cycle is given by (4.1.22):

$$E_{Vth} = V_{th} \int_{t_{br}}^{t_{off}} i_{lp} \, \mathrm{d}t \tag{4.1.22}$$

The energy stored in L and in C_g in each semi-cycle is always zero because the absolute value of their respective current and voltage does not change (0 A and V_{th} respectively) from the beginning to the end of the semi-cycle. Thus, in unstable operation the only element that causes the lamp voltage to grow is the dielectric voltage v_{C_d}. According to the capacitor energy equation, this C_d voltage increment in each half cycle is due to an energy storage in this capacitance. The energy stored in C_d in each half cycle, $\Delta\xi_{C_d}$, is calculated as (4.1.23):

$$\Delta\xi_{C_d} = \frac{C_d}{2} \left(v_{C_d}^2(t_{off}) - v_{C_d}^2(t_o) \right) \tag{4.1.23}$$

The energy supplied by V_{in} in each semi-cycle (4.1.24), $E_{V_{in}}$, can also be expressed as
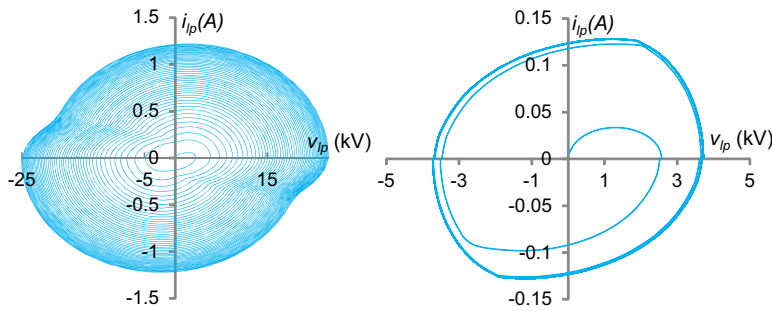
Figure 4.5.: Transient response from simulation. Unstable state plane for $Vin > Vth$ (left), stable state plane for $Vin < Vth$ (right).

$\Delta\xi_{C_d}$ plus E_{Vth} (4.1.22), obtaining: (4.1.25)

$$E_{V_{in}} = V_{in} \int_{t_o}^{t_{off}} i_{lp} \, dt \tag{4.1.24}$$

$$V_{in} \int_{t_o}^{t_{off}} i_{lp} \, dt = \Delta\xi_{Cd} + V_{th} \int_{t_{br}}^{t_{off}} i_{lp} \, dt \tag{4.1.25}$$

According to (4.1.23), to avoid uncontrolled grown of v_{C_d}, the term $\Delta\xi_{C_d}$ in (4.1.25) must be equal to zero: (4.1.26)

$$V_{in} \int_{t_o}^{t_{off}} i_{lp} \, dt = V_{th} \int_{t_{br}}^{t_{off}} i_{lp} \, dt \tag{4.1.26}$$

Spreading the integral at the left hand term of (4.1.26), is found (4.1.27):

$$V_{in} \int_{t_o}^{t_{br}} i_{lp} \, dt + V_{in} \int_{t_{br}}^{t_{off}} i_{lp} \, dt = V_{th} \int_{t_{br}}^{t_{off}} i_{lp} \, dt \tag{4.1.27}$$

And solving (4.1.27), is obtained: (4.1.28)

$$V_{in} \int_{t_o}^{t_{br}} i_{lp} \, dt = (V_{th} - V_{in}) \int_{t_{br}}^{t_{off}} i_{lp} \, dt \tag{4.1.28}$$

Because the integrals in (4.1.28) are always positive terms, this condition implies that $V_{th} - V_{in}$ must be positive too. Consequently $V_{in} < V_{th}$ to ensure stability.

Lamp Peak Current Reached Before and After the Discharge

Within the stability operating range there exist two operating cases: (1) the lamp current reaches its maximum, $\hat{I}_{lp}$, after the gas breakdown and (2) the maximum current is reached before the gas breakdown. Each operating case is described by different state planes, as shown in Fig.4.3 and Fig.4.4, and the lamp peak current $\hat{I}_{lp}$, must be found differently depending on the operating case (Fig.4.4-left) or (Fig.4.3-right). The boundary condition between these two cases is obtained graphically from the state planes in Fig.4.3 for a normalized input voltage U_{in} equal to U_{br} (4.1.10). Using (4.1.10) it is possible to find (4.1.29):

$$U_{in} = -\hat{U} + 2\left(\frac{C_g}{C_{eq}}\right) \tag{4.1.29}$$

Replacing (4.1.19) in (4.1.29) and de-normalizing we find the critical value of the input voltage V_{in_k} that determines the limit between the two operating cases as:

$$V_{in_k} = V_{th}\left(1 + \frac{C_g}{C_d}\left(1 - \sqrt{\frac{C_d}{C_{eq}}}\right)\right) \tag{4.1.30}$$

For an input voltage greater than this critical value V_{in_k}, the normalized peak lamp

current, $\hat{J}_{lp}^*$, is equal to the radius of the semi-circumference traced for the corresponding state plane (Fig.4.4-left) (4.1.31):

$$\hat{J}_{lp}^* = \hat{U}_{lp} - U_{in} \qquad (4.1.31)$$

De-normalizing is found (4.1.32):

$$\hat{I}_{lp} = (\hat{V}_{lp} - V_{in})\sqrt{\frac{C_d}{L}} \qquad (4.1.32)$$

Otherwise, for $U_{in} < U_{in_k}$, the state plane in Fig.4.3-right is used to find (4.1.33):

$$\hat{I}_{lp} = (\hat{V}_{lp} + V_{in})\sqrt{\frac{C_{eq}}{L}} \qquad (4.1.33)$$

The operating case A allows to maximize the current injected into the discharge. Consequently, according to results presented in Section 3.2, this operating case benefits the lamp performance. In this sense, this is the desired operating case. Accordingly, the converter analytic expressions developed hereafter are given for this operating condition.

Output Power

Now that the lamp peak voltage as a function of the converter input variables is known (4.1.20), an expression for the lamp average power, P_{lp}, can be found replacing (4.1.20) in the Manley's power formula (1.2.4). Alternatively P_{lp} can be calculated as twice (positive and negative sequences) the power dissipated by the gas conductance from the time t_{br} until the discharge dies out at t_{off} (Fig. 4.2), obtaining:

$$P_{lp} = 2 f_{lp} V_{th} \int_{t_{br}}^{t_{off}} i_{lp}\, \mathrm{d}t \qquad (4.1.34)$$

Which can be expressed as a function of the charge transferred to C_d (Q_{Cd}) from the breakdown instant until the discharge dies off:

$$P_{lp} = 2 f_{lp} V_{th} Q_{Cd}(t_{br} \to toff) \qquad (4.1.35)$$

Since, the total variation of the lamp voltage in each semi-cycle, ΔV_{lp} can be expressed as the addition of the net voltage change in C_g and C_d:

$$\Delta V_{lp} = \Delta V_{C_g}\left(t_o \to t_{br}\right) + \Delta V_{C_d}\left(t_o \to t_{br}\right) + \Delta V_{C_d}\left(t_{br} \to t_{off}\right) \qquad (4.1.36)$$

$$\Delta V_{lp} = 2V_{th} + \frac{2V_{th}C_g}{C_d} + \frac{1}{2C_d}Q_{Cd}(t_{br} \to t_{off}) = 2\hat{V}_{lp} \qquad (4.1.37)$$

Solving (4.1.37) for $Q_{Cd}(t_{br} \to t_{off})$ and replacing in (4.1.35), P_{lp} is found: (4.1.38)

$$P_{lp} = 4f_{lp}V_{th}C_d \left(\hat{V}_{lp} - \frac{V_{th}C_g}{C_{eq}} \right) \tag{4.1.38}$$

To notice that (4.1.38) is the same Manley's DBD power formula (1.2.3) [4.7].

Replacing (4.1.20) in (4.1.38), an expression of the DBD power as a function of V_{in} is obtained ((4.1.39)):

$$P_{lp} = 4f_{lp}V_{th}{}^2 C_g \times \left(\frac{V_{th}}{V_{th} - V_{in}} - 1 \right) \tag{4.1.39}$$

From (4.1.30) the minimum input voltage to obtain the operating case A is known. Replacing V_{in_k} (4.1.30) in (4.1.39), the minimum lamp power for this operating case is found: (4.1.40)

$$P_{lp_{min}} = 4f_{lp}V_{th}{}^2 \left(\frac{C_d}{\sqrt{\frac{Cd}{Ceq}} - 1} - C_g \right) \tag{4.1.40}$$

Expression (4.1.39) shows that P_{lp} can be adjusted by means of two degrees of freedom: V_{in} and f_{lp}. Because P_{lp} changes linearly with f_{lp}, it is a convenient variable for the power control. P_{lp} as a function of V_{in} is shown in Fig.4.6, calculated using the lamp equivalent model parameters of Table 2.1. From this figure it can be observed that as the function approaches to the asymptote V_t, small perturbations in V_{in} can produce large variations in the output power. Although adjusting f_{lp} a linear control of P_{lp} can be implemented, it has a limit that is calculated next.

Bridge Operating Frequency

For proper operation of the converter, the bridge must be operated at a switching frequency f_{lp} which allows the current to fall to zero before the beginning of a new switching sequence. Thus, considering the lamp current waveforms in Fig. 4.2, condition (4.1.41) should be fulfilled:

$$T_{pulse} < \frac{1}{2f_{lp}} \tag{4.1.41}$$

T_{pulse} is calculated as the time it takes to produce the gas breakdown, T_{br}, plus the duration of the discharge, T_{on}:

$$T_{pulse} = T_{br} + T_{on} \tag{4.1.42}$$

For the operating case A, T_{br} and T_{on} are found using the resonance frequency and angles of their corresponding state planes, shown in Fig.4.3-left and Fig.4.4-left, respectively:

$$T_{pulse} = \frac{\theta}{\omega} + \frac{\varphi}{\omega^*} \tag{4.1.43}$$
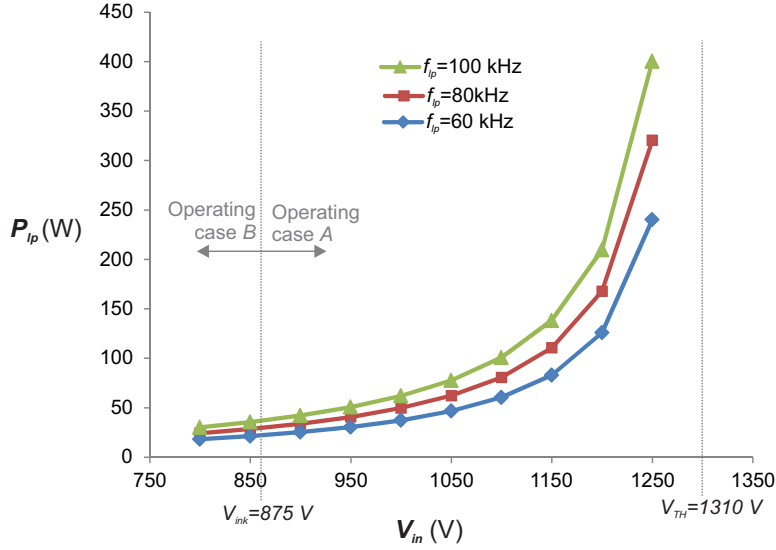
Figure 4.6.: Theoretical lamp power as a function of the converter input voltage, calculated with (4.1.39) (V_{th}=1.31 kV, C_g=28 pF, C_d=85 pF). V_{ink} is the limit between operating cases A and B. V_{th} is the asymptote of the P_{lp} function.

From the trigonometrical equations of the corresponding state planes (Fig.4.3-left and Fig.4.4-left), is found:

$$T_{pulse} = \sqrt{LC_{eq}} \arcsin\left(\frac{I_{br}}{V_{in} - \hat{V}_{lp}}\sqrt{\frac{L}{C_{eq}}}\right) + \sqrt{LC_d}\left(\pi - \arcsin\left(\frac{I_{br}}{V_{in} - \hat{V}_{lp}}\sqrt{\frac{L}{C_d}}\right)\right)$$

(4.1.44)

The lamp current at the breakdown instant, I_{br}, is found replacing (4.1.20) in (4.1.11) and de-normalizing. This expression is valid for both of the operating cases: (4.1.45)

$$I_{br}^2 = \frac{4V_{th}C_g}{L}\left(\hat{V}_{lp} + V_{in} - \frac{V_{th}C_g}{C_{eq}}\right)$$

(4.1.45)

According to condition (4.1.41), the bridge maximum operating frequency, $f_{lp_{max}}$, is found: (4.1.46)

$$f_{lp_{max}} = \frac{1}{2T_{pulse}}$$

(4.1.46)

Accordingly, the maximum lamp power, $P_{lp_{max}}$, that can be obtained for a given input voltage V_{in}, is given by (4.1.39) with f_{lp} equal to the maximum operating frequency:

$$P_{lp_{max}} = \frac{2V_{th}{}^2C_g}{T_{pulse}} \times \left(\frac{V_{th}}{V_{th} - V_{in}} - 1\right)$$

(4.1.47)

The mathematical relationships exposed in this section, have been numerically verified through simulation using the PSIM circuit simulator (Fig. 4.6) and are used for the converter design and the components selection.

4.2. Components Selection and Simulations

The converter is dimensioned to supply a DBD excimer lamp filled with a *XeCl* gas mixture. The equivalent electrical model of this lamp presents a dielectric capacitance C_d=85 pF, a gas capacitance C_g=28 pF and a breakdown voltage V_{th}=1.31 kV. From information provided by the manufacturer, this lamp has been designed for approximately 100 W of electrical power.

4.2.1. Operating Point

Using the results of the parametric study presented in Chapter 3, the SRI operating point to be implemented is selected to maximize the UV production of the DBD excilamp. According to the UV production curves shown in Fig.3.4 and Fig.3.11, a lamp peak current higher than 128 mA and a current pulse rate of $80kHz$ are chosen. For a lamp power of 90W, an operating frequency of 80 kHz corresponds to a pulse energy of $563\mu J$; as shown in Fig.3.16, this pulse energy value is placed in the zone of high UV production efficiency. The theoretical voltages and currents for $P_{lp} = 90W$, at this operating conditions, are presented in Table 4.1.

P_{lp}	f_{lp}	V_{in}	$\hat{V}_{lp}$
90 W	80 kHz	1119 V	4.3 kV

Table 4.1.: Theoretical operating point

In order to validate the converter behavior, the converter control is implemented in open loop, adjusting P_{lp} with V_{in} remaining in the operating case *A* region illustrated in Fig.4.6. Next, the converter switches, the necessary step-up transformer and the inductance, are dimensioned for the chosen operating point.

4.2.2. Switches

For an operating frequency around 80 kHz, high switching speed offered by the MOSFET technology is necessary. Studying the current-voltage characteristic for each switch, unidirectional current switches capable of blocking bipolar voltage should be used in the bridge. This switch characteristic corresponds to a thyristor-like device [4.8] and is implemented as previously done for the Square-shape converter, connecting a diode (GB07SHT12) in series with a MOSFET (P8NK100Z) as shown in the schematic of Fig.4.7. The GB07SHT12 diode is a SiC device chosen due to its negligible reverse recovery current, characteristic that benefits the converter efficiency.

4.2.3. Step-up Transformer

The voltage values at the chosen operating point (Table 4.1) leads to the use of a step-up transformer connecting the DBD lamp to the inverter as explained previously for the Square-wave converter in Section 2.3.3. The implemented step-up transformer has been designed with a transformation ratio of 10 to reduce the peak voltage of the bridge switches to approximately 430 V.

Using the theoretical lamp peak current in Table 4.1 and 10 as transformation ratio, the transformer wires are selected: 38 AWG ($0.00797\,mm^2$) x 81 Strands Litz wire for the primary and 33 AWG ($0.0254\,mm^2$) single copper wire for the secondary.

These transformer requirements are similar to those previously discussed in Section 2.3.3 and 2.4.1 for the square-shape current supply. However, with the aim to reduce further the impact of the transformer parasitic elements over this resonant converter and thus to increase the efficiency, the best solution has been found by using a multi-section transformer developed by Bonnin in [4.9]. The values obtained for the experimental transformer are summarized in the circuit of Fig. 4.7.

4.2.4. Inductance Value

The value of L is solved using (4.1.32), according to the operating point in Table 4.1, assuring that the peak current in the primary side of the transformer respects the current rating of the switches and also respecting condition (4.1.41). An inductance value of 24 mH seen on the secondary, is calculated based on (4.1.44) to obtain a duty cycle of approximately 70% at $f_{lp} = 80kHz$, producing a peak current of 1.9 A on the primary side of the transformer. This duty cycle provides enough dead time for commutation of the switches and for the increase of the switching frequency if necessary. Given a transformation ratio of 10 and taking into account the transformer leakage inductance
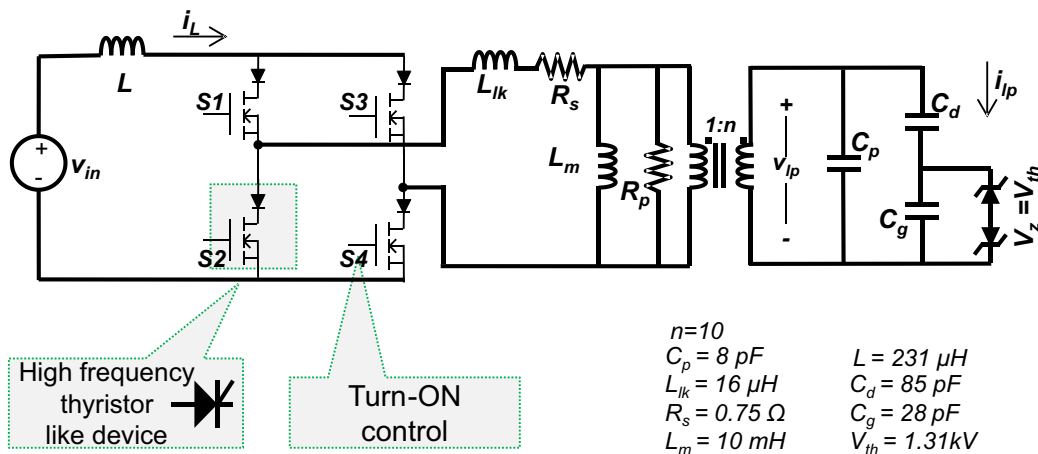
Figure 4.7.: Converter circuit and DBD electrical model used for simulation
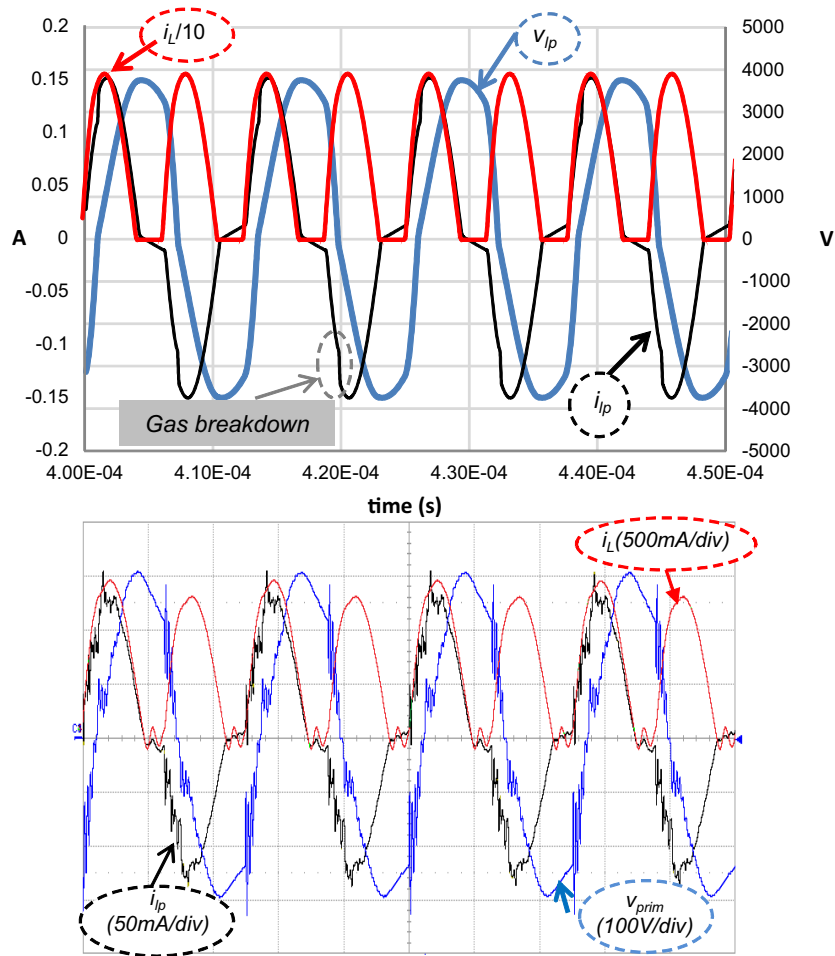
Figure 4.8.: Waveforms comparison from simulation (top) and from the experimental validation (bottom). $f_{lp} = 80kHz$, $V_{in} = 115V$

seen in series with L, an inductance $L = 231\mu H$ is used in the primary side. This inductance is made according to the Wheeler approximation formulas [4.10] with a cylindrical air core of length 80 mm and diameter 30 mm, the winding has 155 turns of 38 AWG ($0.00797\,mm^2$) x 81 Strands Litz wire (ϕ=0.51 mm) wire. The air core is selected taking into account the possible application of the converter for decontamination systems in isolated areas; this type of core is robust, stable with temperature, low cost and avoid saturation problems.

4.2.5. Simulations

The converter, including the transformer parasitic elements (Fig. 4.7), has been simulated using PSIM. The waveforms obtained from this simulation are presented in Fig.
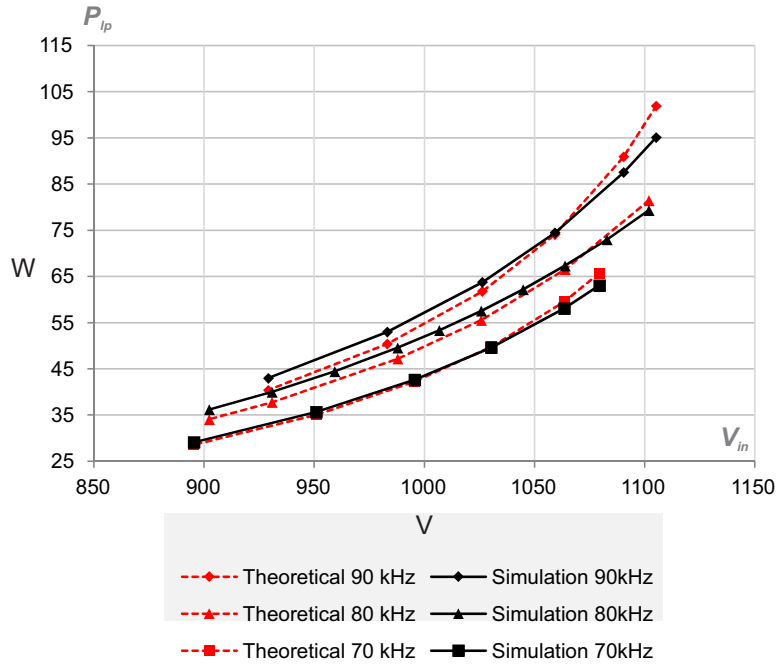
Figure 4.9.: Theoretical lamp power as a function of the converter input voltage calculated with (4.1.39) and simulation results including the transformer parasitic elements (V_{th}=1.31 kV, C_g=28 pF, C_d=85 pF).

4.8-top. The inductance current has been scaled by ten in order to visualize it together with the lamp current. The step observed in the lamp current waveform i_{lp} (marked as "Gas breakdown") is a result of the gas breakdown that changes the current divider between the lamp equivalent capacitance and the transformer parasitic capacitance as previously explained in Section 2.3.3. When i_L becomes zero at the end of each current pulse, i_{lp} does not remains at zero due to the effect of the magnetizing inductance.

The output power P_{lp} obtained in simulation, including the transformer model, is presented in Fig. 4.9 for different values of f_{lp} together with the theoretical power values. The theoretical lamp power is calculated with (4.1.39), excluding the effect of the transformer parasitic elements. Because of the transformer frequency response, the equivalent transformer gain changes with the frequency operation, consequently the equivalent input voltage is reflected to the secondary using the transformer gain measured experimentally: 9.3, 9.5 and 9.7, for 70, 80 and 90 kHz respectively. The difference between the theoretical and the simulated results is due to the impact of the transformer. Despite the differences, this result shows that the deduced equations are sufficiently precise for the converter dimensioning.

4.3. Experimental Results

The experimental validation of the proposed converter has been achieved measuring the electrical signals for the system with a high speed current probe (LeCroy AP015) and a high voltage differential probe (Agilent N2891A). The lamp voltage is measured in the primary side of the transformer (v_{prim}) to reduce the impact of the voltage probe input capacitance (aprox. 7 pF) in the resonant circuit. Given the value of this capacitance, if the voltage probe is connected to the secondary winding its capacitance have the same effect of the transformer stray capacitance C_p; it reduces the lamp current and modifies the equivalent resonant circuit, thus affecting the converter operation. Then, the primary side voltage is multiplied by the transformation ratio to obtain v_{lp}. The transformation ratio has been measured previously at the same operating point, obtaining n=9.5 at a frequency of 80 kHz.

4.3.1. Electrical Waveforms

In Fig. 4.8 a comparison between the simulation and the experimental electrical waveforms is presented. In the experimental waveforms of Fig. 4.8-bottom v_{prim} is shown, instead of v_{lp}, in order to diminish the impact of the probe capacitance on this waveforms. The effect of L_m in the decay of v_{lp} and v_{prim} and the lamp current step at the gas breakdown instant due to C_p, are both observed in simulation and in the experiment. The high frequency oscillation in i_{lp}, produced by L_{lk} and the switches parasitic capacitance, is not observed in simulation because ideal switches were used. In general, the simulated and the experimental waveforms are very similar, demonstrating that simulation of the converter using the schematic shown in 4.7, allows an accurate tuning of the SRI operating point.

Additionally, a second set of experimental waveforms, with the voltage probe connected directly to the lamp, is shown in Fig.4.10. The inductance current, i_L, observed in Fig. 4.8-bottom and Fig.4.10 is, as expected, very similar to the lamp current i_{lp}. Comparing the amplitude of i_L and i_{lp} a transformation ratio around 9.5 is found. Note that the amplitude of the positive lamp current pulses is higher than the negative ones, and accordingly the peak value of the corresponding inductance current pulse is also higher. This change in the current amplitude with the lamp current direction is attributed to the non-symmetrical geometry of this lamp, that produces an excilamp equivalent model that changes slightly with the current direction affecting the equivalent resonant circuit.

The lamp voltage waveform shown in Fig.4.10, acquired directly at the lamp terminals, does not present the HF oscillations that in V_{prim} are observed. Both, v_{lp} and v_{prim} do not remain constant when i_L is zero because the transformer magnetizing inductance is not as large as desired. The transformer parasitic elements also affect the power transfer as shown in Fig. 4.11: simulation results taking into account these parasites are very near to the experimental measurements allowing fine adjust of the design, while theoretical ones are less precise.
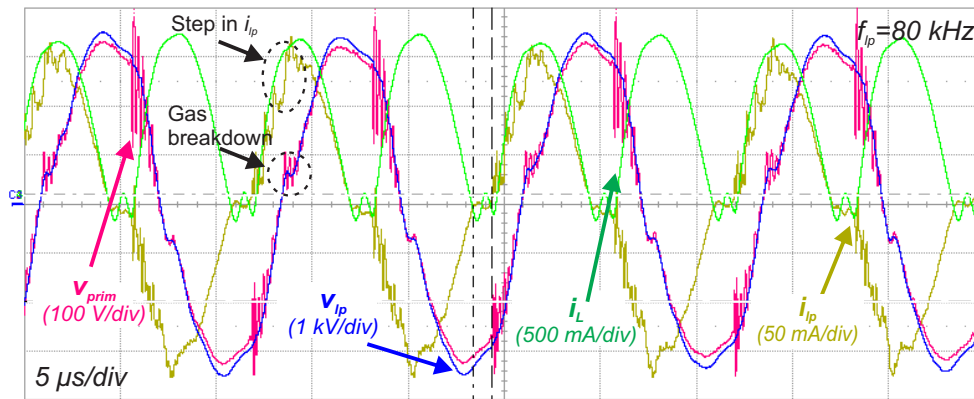
Figure 4.10.: Experimental electrical waveforms of the lamp, the transformer primary side voltage and the inductance current.
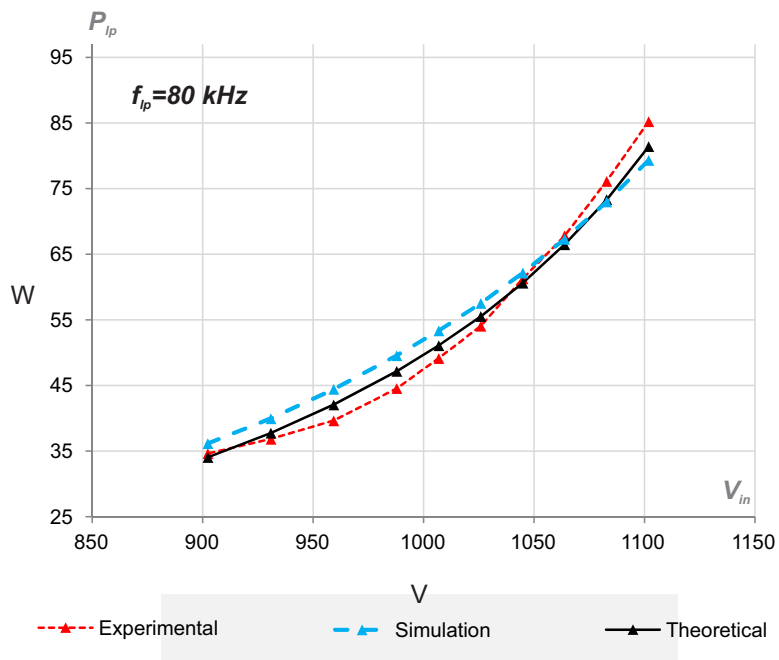
Figure 4.11.: Theoretical, simulated and experimental lamp power as a function of the converter input voltage. The theoretical values are calculated with (4.1.39) (V_{th}=1.31 kV, C_g=28 pF, C_d=85 pF). The schematic used for simulation is presented in Fig.4.7

4.3.2. Performances

The benefits of the SRI are validated experimentally by measuring its efficiency, stability, electromagnetic radiation and the UV radiation obtained from the DBD excilamp.

Efficiency   The measurement of the converter efficiency, in terms of electrical power supplied to the lamp, is obtained as follows: the transformer primary side voltage v_{prim} and i_{lp} output signals are multiplied in the oscilloscope computing the lamp instantaneous power. Then this power signal is averaged (averaging time 1 ms) and multiplied by the transformation ratio obtaining P_{lp}. In a similar manner the power P_{in} supplied by the constant voltage source V_{in} is found, computing the converter efficiency as P_{lp}/P_{in}.

The measurement of P_{lp} obtained for different values of V_{in} at f_{lp}=80 kHz are presented in Fig. 4.11 and the corresponding converter efficiencies are shown in Fig. 4.12. It is found that the transformer is responsible for the most of the converter losses.

Comparing with the efficiency of the supply tested in Section 2.5.4, at the particular operating point of P_{lp}=90 W, f_{lp}=80 kHz, duty cycle of 53% and a current intensity of 125mA, the SRI efficiency was 90.6% against 57% for the square-wave supply.

Stability   For an input voltage slightly higher than 117 V, which corresponds to approximately 1170 V in the secondary, the proximity to the asymptote (V_{th}=1.31 kV in Fig. 4.11) produce an erratic behavior of the system, with intermittent variations of up to 50 W in P_{lp} for a constant value of V_{in}.

As V_{in} approaches to the asymptote, the system is more susceptible to small perturbations caused by the DC voltage supply at the input or by the dynamic behavior of the lamp, which is not included in the lamp simplified model used for this design.
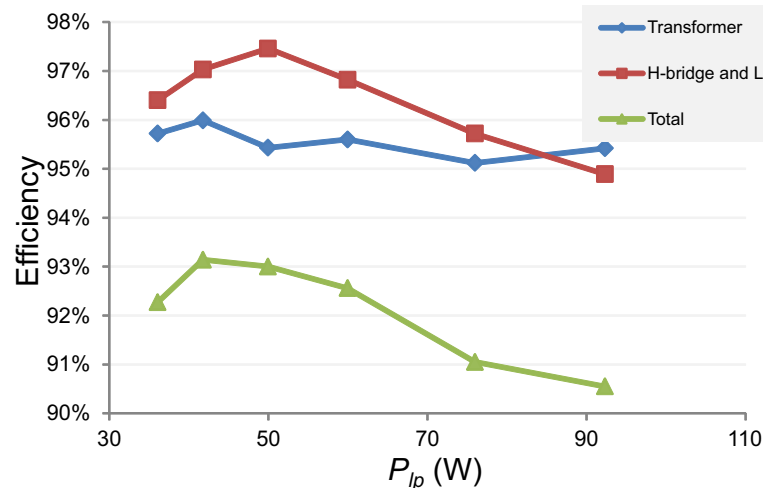
Figure 4.12.: Measured efficiencies of the SRI for different values of output power at f_{lp}=80kHz.
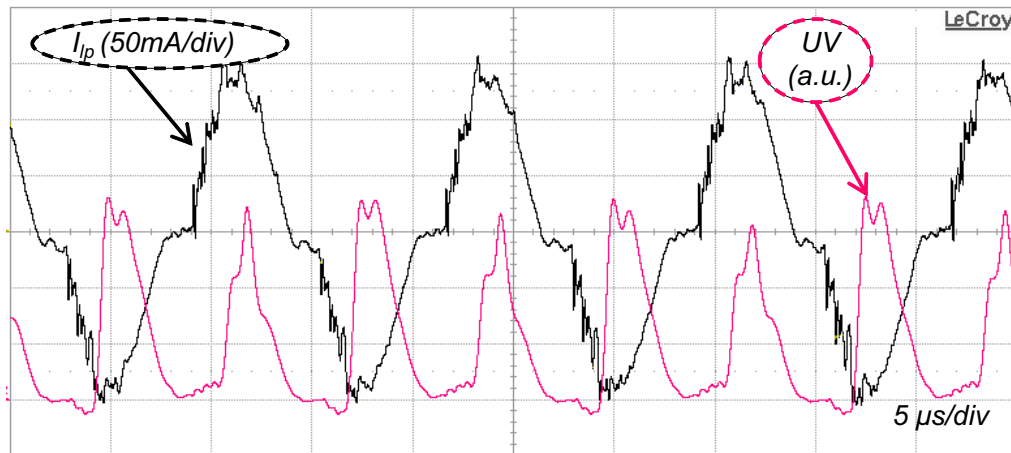
Figure 4.13.: UV waveform and Excilamp current for the SRI.

UV Radiation   For the $XeCl$ excimer lamp used as load, the typical radiation wavelength is 308 nm; the UV radiation power is measured with the optometer OPTIK P-9710 using the UV detector SN5816, installed at 3 mm of the lamp surface. The UV power obtained using the SRI at P_{lp}=90 W and f_{lp}=80 kHz, is 24 mW/cm^2. For the same lamp power, frequency and pulse duration, the UV radiation obtained with the square waveform current is 28 mW/cm^2. This result reveals a decrease of around 10% in the UV power due to the current form factor. This impact of the current form factor in the lamp performance is a work to explore in the future.

The UV waveform is acquired with a Thorlabs PDA-25K photo-detector, installed at 25mm of the lamp surface. As already mentioned in [4.1], and can be observed on Fig.4.13, after the gas breakdown the waveform of the UV radiation (UV) follows the i_{lp} waveform (absolute value).

EMI   The SRI presents advantages in terms of EMI when compared with the hard switching topology. This benefit is evaluated performing a FFT of the lamp current for both topologies under similar operating conditions of f_{lp} and output power (Fig. 4.14).
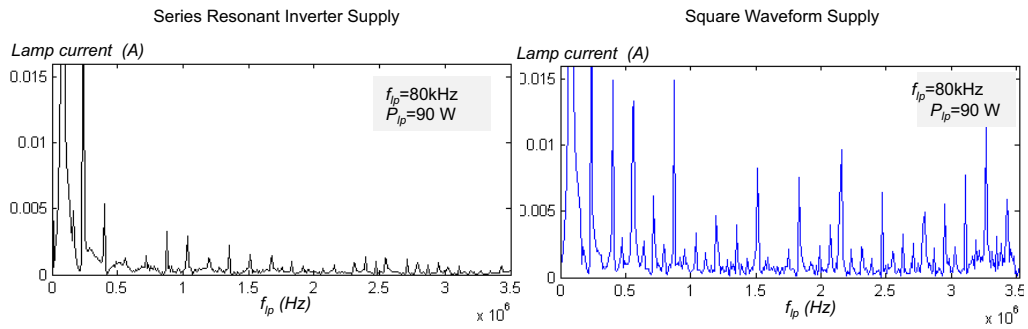
Figure 4.14.: FFT of the lamp current for SRI and Square waveform current-source topologies.

4.4. Conclusions

As presented in section 1.2, among the possible topologies for the supply of DBD devices, resonant topologies offer less switching losses, less EMI, fewer switching devices and additionally can operate in current mode; particularly in the case of the Series Resonant Inverter topology operating in Discontinuous Conduction Mode, proposed in this Chapter, all these benefits are found. With the operating mode selected in this work, the lamp power is imposed with two degrees of freedom and full ZCS is achieved reducing switching losses and EMI.

The use of the lamp electrical model in conjunction with the state plane analysis gives an insight into the process and allows the calculation of the electrical values, including the lamp power, as a function of the input voltage, the inverter frequency, the components and the parameters of the lamp. Analytical study, simulation and experimental results are in accordance, validating the series resonant inverter as an efficient topology for the supply of DBD excimer lamps. Satisfactory efficiency results up to 93% have been obtained for the converter supplying a DBD UV excimer lamp. On the basis of the obtained results, the SRI has been proven to be a good option to supply a DBD excimer lamp.

Bibliography

[4.1] R. Diez, H. Piquet, and S. Bhosle, "Control of the UV emission of an excimer lamp by means of a current-mode power supply," in *Industrial Electronics, 2009. IECON '09. 35th Annual Conference of IEEE*, pp. 3500–3505, IEEE, Nov. 2009.

[4.2] H. Piquet, S. Bhosle, R. Diez, and M. V. Erofeev, "Pulsed current-mode supply of dielectric barrier discharge excilamps for the control of the radiated ultraviolet power," *IEEE Transactions on Plasma Science*, vol. 38, pp. 2531–2538, Oct. 2010.

[4.3] Y. Chéron, C. Goodman, and T. Meynard, *Soft commutation*. London [u.a.: Chapman & Hall, 1992.

[4.4] R. Casanueva, F. J. Azcondo, and S. Bracho, "Series–parallel resonant converter for an EDM power supply," *Journal of Materials Processing Technology*, vol. 149, pp. 172–177, June 2004.

[4.5] R. Casanueva, F. Azcondo, and C. Brañas, "Output current sensitivity analysis of the resonant inverter: Current-source design criteria," *IEEE Transactions on Industrial Electronics*, vol. 54, no. 3, pp. 1560–1568, 2007.

[4.6] R. Oruganti and F. Lee, "Resonant power processors, part I—State plane analysis," *IEEE Transactions on Industry Applications*, vol. IA-21, no. 6, pp. 1453–1460, 1985.

[4.7] T. C. Manley, "The electric characteristics of the ozonator discharge," *Transactions of The Electrochemical Society*, vol. 84, pp. 83–96, Oct. 1943.

[4.8] M. Cousineau, R. Diez, H. Piquet, and O. Durrieu, "Synthesized high-frequency thyristor for dielectric barrier discharge excimer lamps," *IEEE Transactions on Industrial Electronics*, vol. 59, no. 4, pp. 1920–1928, 2012.

[4.9] X. Bonnin, H. Piquet, D. Florez, R. Diez, and X. Bonnin, "Designing the high voltage transformer of power supplies for dbd: windings arrangment to reduce the parasitic capacitive effects," in *Power Electronics and Applications (EPE), 2013 15th European Conference on*, Sept. 2013.

[4.10] Wheeler, H.A., "Simple inductance formulas for radio coils," in *Proc. I.R.E*, vol. 16, p. 1398, Oct. 1928.

5. DBD Supplies comparison

In Chapter 3, some parameters of the UV radiation, like the duration, amplitude and shape of the UV pulses and the radiated power, have been demonstrated to be controlled with the current injected into the lamp by means of a square-shape current mode converter. Also, the capability to control the UV radiation using a soft-switching resonant converter operating in current mode has been established in Chapter 4.

The present Chapter have a view of four different converter structures that comply with the current mode approach and presents a comparison of those structures, made in terms of electric efficiency, waveform of the UV radiation and their impact on the luminous efficacy.

To introduce this comparison, the schematics and operating sequences of the four topologies are developed using the simplified DBD model shown in Fig.1.5. Then, by means of an analytical development the main mathematical expressions describing the converters operating point, are computed. Using these mathematical expressions, the converter design methodology and simulations validating the converter equations, are proposed. As experimental result, a comparison of the UV radiation and the converters efficiency is presented for a particular operating point, under similar conditions of UV pulse duration, lamp power and current frequency, for all the four topologies.

Topologies to be Compared In Fig.5.1 the schematics of the four topologies to be compared, are presented. One of the converters included in this comparison is the rectangular current waveform presented in Chapter 2, shown in Fig.5.1-top with the current inverter replaced by a push-pull inverter, using a two primary winding transformer, reducing the number of switches and the control circuitry. The other three topologies are resonant-based current supplies operating in DCM, assuring the control of the lamp power, including: the SRI inverter proposed in Chapter 4, presented here also with the push-pull inverter instead of the full-bridge; the Boost-based converter found in [5.1] (Fig.1.9) and the Buck-Boost-based supply developed in [5.2] (Fig.1.12).

Accordingly, only the operation of the Boost and the Buck-Boost based supplies are developed in this Section, differing from previous analysis in [5.3] and [5.2] where the time to produce the discharge T_{br} each half-cycle was neglected. The Boost-based and the Buck-Boost based converters are resonant structures differing from the SRI in the current waveform injected into the lamp and the number of switches. In order to simplify the equations and the converters comparison, the transformer turns ratio is assumed as n=1.
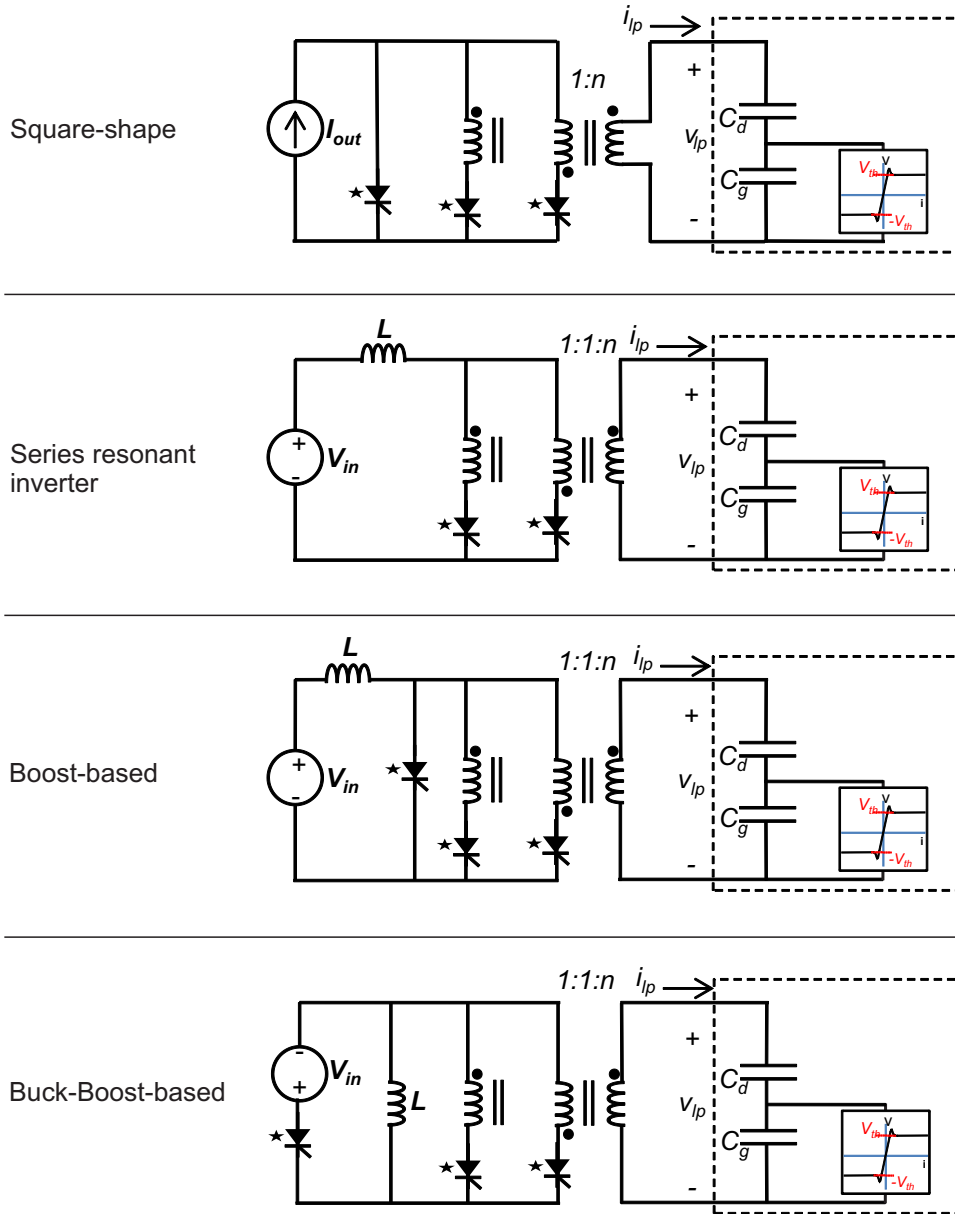
Figure 5.1.: Schematics of the DBD supplies under study

5.1. Analytical Design

As previously done for the SRI, on the basis of the operating sequences and using the state plane analysis, the main equations allowing to find the output power, peak current and voltage, duty cycle and operating frequency of the Boost and Buck-Boost based converters, are found.

5.1.1. Boost Based Converter

This structure, introduced in [5.4], uses a boost-converter working in DCM to replace the two-quadrant chopper from the square-shape current supply configuration. As seen in Fig. 5.2-top, to change the lamp current direction in this converter, instead of the full-bridge inverter, a push-pull inverter is used.

The inductance current presents, for the positive half-cycle, four different sequences shown in Fig.5.2: charge during T_{ch} where the inductance current rises linearly up to I_{Lo}, discharge without ignition during T_{br} (dotted line of i_L in Fig.5.2), discharge with ignition during T_{on} and blanking. Observe that after the time instant t_{br}, i_L and i_{lp} have the same waveform. These sequences are repeated for the negative half-cycle but inverting the current direction, in order to comply with the zero-mean value requirement in the lamp current.

In a similar manner as done for the SRI (4.1.39), for this Boost-based converter the normalized state plane shown in Fig.5.3 is plotted. Note that differing from the SRI, the initial value of the lamp current is not zero, thus there is hard-switching at MOSFETs turn-on.

From the geometrical relations of the case A state plane before gas breakdown, shown in Fig.5.3-left, the normalized breakdown current is computed:

$$J_{br}{}^2 = (r_1)^2 - (U_{in} + U_{br})^2 \tag{5.1.1}$$

With,

$$r_1^2 = \left(U_{in} + \hat{U}\right)^2 + J_{Lo}^2 \tag{5.1.2}$$

Replacing (5.1.2) in (5.1.1):

$$J_{br}{}^2 = \left(U_{in} + \hat{U}\right)^2 + J_{Lo}^2 - (U_{in} + U_{br})^2 \tag{5.1.3}$$

Now, from the shaded triangle of the operating case A state plane after breakdown, shown in Fig.5.3-right, a second equation for the normalized breakdown current, is found:

$$J_{br}^*{}^2 = \left(\hat{U} - U_{in}\right)^2 - (U_{in} + U_{br})^2 \tag{5.1.4}$$

As deduced in (4.1.12), J_{br}^* can be written in terms of J_{br}:

$$J_{br}^*{}^2 = J_{br}{}^2 \frac{C_{eq}}{C_d} \tag{5.1.5}$$
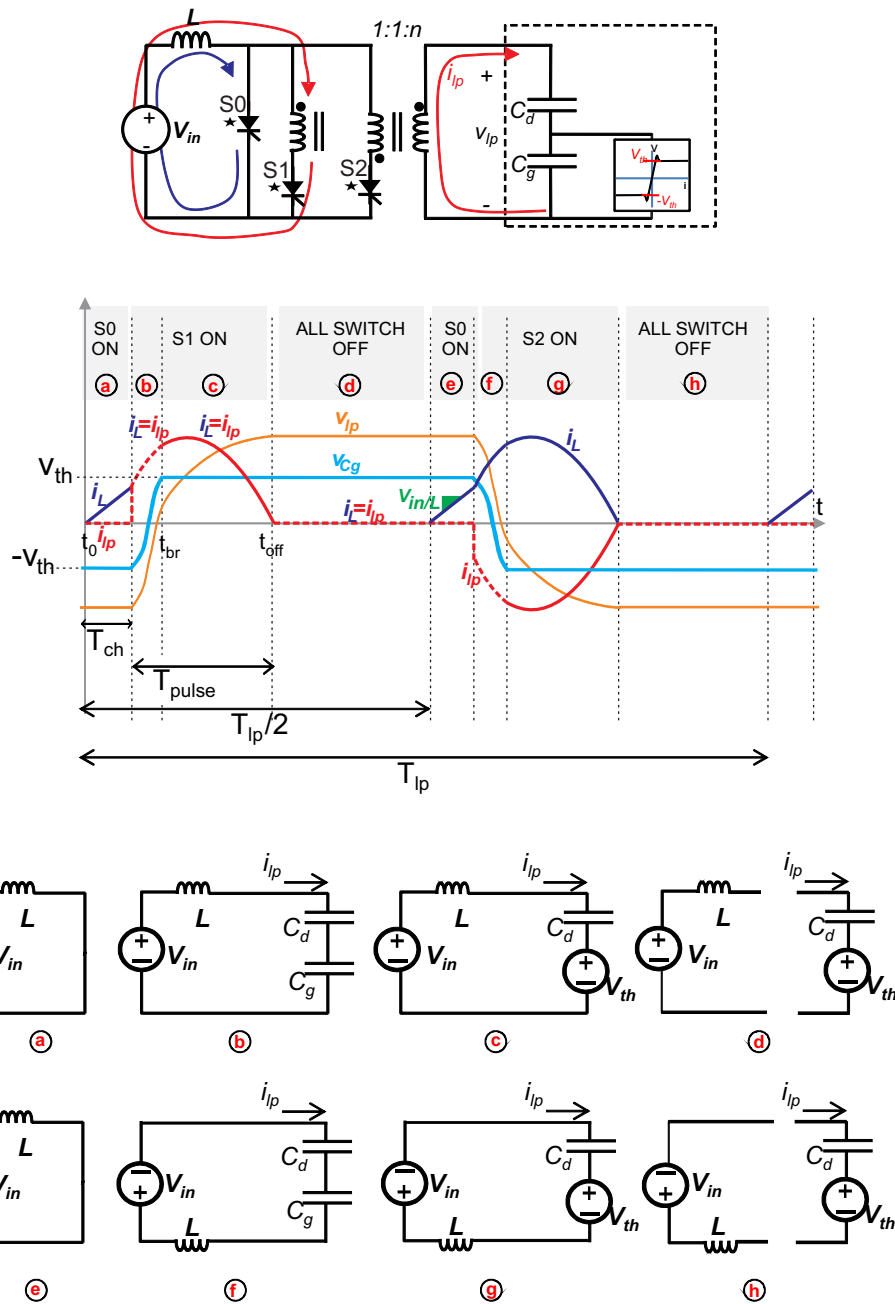
Figure 5.2.: Boost-based converter operating sequences (top) with the output current waveform (bottom).
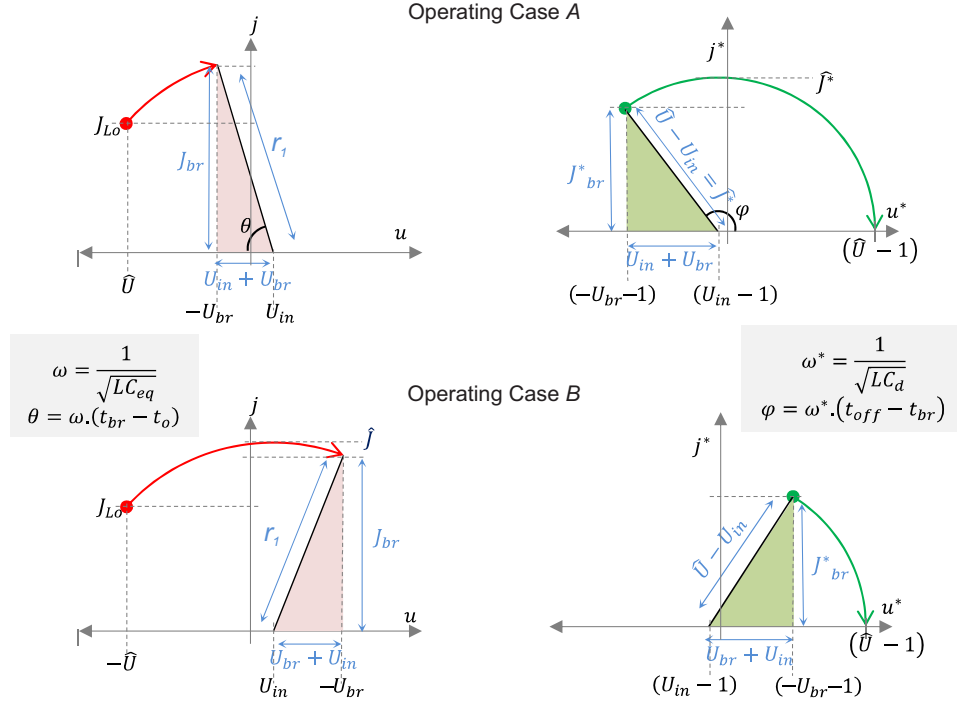
Figure 5.3.: State planes for the Boost-based converter in DCM. Before (left) and after (right) gas breakdown. For two operating cases: When the gas breakdown happens before the peak current (A) and after the peak current (B)

Then, replacing (5.1.3) and (5.1.4) in (5.1.5), we obtain an expression that depends only on the normalized voltages:

$$\hat{U}^2 - U_{br}^2 - 2U_{in}\left(\hat{U} + U_{br}\right) = \frac{C_{eq}}{C_d}\left(\left(U_{in} + \hat{U}\right)^2 + J_{Lo}^2 - (U_{in} + U_{br})^2\right) \qquad (5.1.6)$$

As demonstrated previously (4.1.10), U_{br} is given by :

$$U_{br} = \hat{U} - \frac{2C_g}{C_{eq}} \qquad (5.1.7)$$

Thus, replacing (5.1.7) in (5.1.6), solving for $\hat{U}$ and de-normalizing, the lamp peak voltage is found:

$$\hat{V}_{lp} = \frac{V_{th}C_g}{C_{eq}} + \frac{I_{Lo}^2 L + 4V_{in}V_{th}C_g}{4C_d\left(V_{th} - V_{in}\right)} \qquad (5.1.8)$$

With,

$$I_{Lo} = \frac{V_{in}.T_{ch}}{L} \tag{5.1.9}$$

Replacing (5.1.8) in the Manley's power equation (1.2.4), the power delivered to the lamp is calculated (5.1.10):

$$P_{lp} = \frac{f_{lp}V_{th}\left(LI_{Lo}{}^2 + 4V_{in}V_{th}C_g\right)}{V_{th} - V_{in}} \tag{5.1.10}$$

This expression shows that stability for this converter is assured by maintaining the input voltage V_{in} less than the V_{th} voltage (seen in the primary), which corresponds to the same stability condition demonstrated for the SRI (4.1.20), (4.1.21). Otherwise, divergent development for the voltage and current is found [5.4].

In fact, expression (4.1.39) for the SRI output power, is a special case of the Boost-based converter (5.1.10) where the charge time $T_{ch} = 0$. Additionally to the two D.O.F. of the SRI: V_{in} and f_{lp}, the T_{ch} time appears as an additional D.O.F. for the control of the lamp power. In Fig.5.4 the lamp power curves as function of V_{in} are shown for different values of T_{ch}.
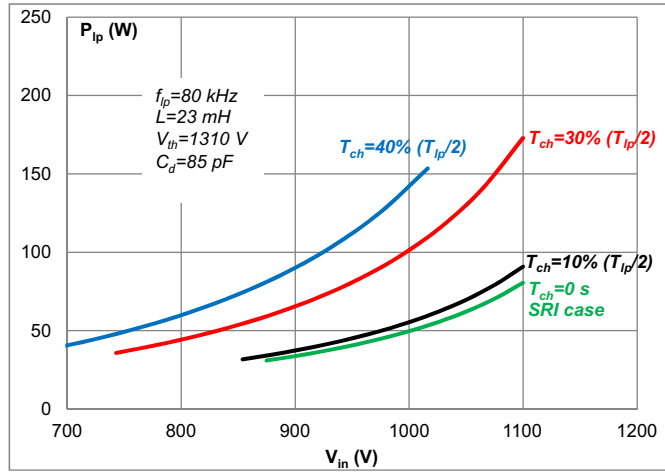
Figure 5.4.: Power delivered to the lamp by the Boost-based converter for different values of inductance charge time.

The end of the discharge phase in this converter is established by the spontaneous turn-off of one of the two inverter switches (ZCS).

The operation of the converter in the case A (Fig.5.3-top) is positive for the lamp performance, because in this case the peak current injected into the discharge is maximized (Section 3.2). According to the state plane shown in Fig.5.3-top, the operating case A is obtained if the condition $U_{br} \leq U_{in}$ is fulfilled. Using (5.1.7) and de-normalizing, this condition is expressed as:

$$\hat{V}_{lp} - \frac{2V_{th}C_g}{C_{eq}} \leq V_{in} \tag{5.1.11}$$

By means of the Manley's equation, $\hat{V}_{lp}$ in (5.1.11) is expressed in terms of P_{lp} in order to find, for a given power and operating frequency, the minimum value V_{in} must have to assure the case A operation:

$$V_{in_A} = \frac{P_{lp}}{4f_{lp}V_{th}C_d} - \frac{V_{th}C_g}{C_{eq}} \tag{5.1.12}$$

And substituting P_{lp} by expression (5.1.10) and solving, we find an expression for V_{in_A} in terms of the inductance and the charge time:

$$V_{in_A} = \frac{V_{th}\left(C_d + C_g - \sqrt{(C_d + C_g)\left(\frac{T_{ch}^2}{4L} + C_g\right)}\right)}{C_d - \frac{T_{ch}^2}{4L}} \tag{5.1.13}$$

In Fig.5.4 the lamp power curves are plotted only for input voltages higher than V_{in_A}.

In the operating case A, the lamp peak current always happens after gas breakdown, thus in the state plane of Fig.5.3-right. Accordingly, in the same manner as deduced for the SRI, $\hat{J}^*$ is equal to the radius of the semi-circumference of this state plane: $r_2 = (\hat{U} - U_{in})$; hence, de-normalizing we obtain:

$$\hat{I}_{lp} = \left(\hat{V}_{lp} - V_{in}\right)\sqrt{\frac{C_d}{L}} \tag{5.1.14}$$

The maximum operating frequency of this Boost-based converter, is determined by T_{pulse} and the inductance charge time T_{ch}:

$$f_{lp} \leq \frac{1}{2\left(T_{ch} + T_{pulse}\right)} \tag{5.1.15}$$

T_{pulse} is the sum the duty time of the discharge, T_{on}, and the time necessary to produce the breakdown, T_{br}. Also from the state plane in Fig.5.3-right, we compute T_{on} as the angle of the semi-circumference, φ, divided by the resonant frequency ω^* and de-normalizing:

$$T_{on} = \sqrt{LC_d}\left[\pi - arcsin\left(\frac{I_{br}}{\hat{I}_{lp}}\right)\right] \tag{5.1.16}$$

In a similar manner, but from the state plane before gas breakdown we compute T_{br}:

$$T_{br} = \sqrt{LC_{eq}}\left[arcsin\left(\frac{I_{br}}{k_{br}}\right) - arcsin\left(\frac{I_{br}}{k_{br}}\right)\right] \tag{5.1.17}$$

with,

$$k_{br} = \sqrt{\frac{\left(\hat{V}_{lp} + V_{in}\right)^2 C_{eq}}{L} + I_{Lo}^2} \qquad (5.1.18)$$

And finally, I_{br} is computed replacing (5.1.8) and (5.1.7) in (5.1.3):

$$I_{br} = \sqrt{\left(I_{Lo}^2 + \frac{4V_{th}V_{in}C_g}{L}\right)\left(1 + \frac{V_{th}C_g}{(V_{th} - V_{in})C - d}\right)} \qquad (5.1.19)$$

In this Section the mathematical expressions describing the operation of the Boost-based converter have been deduced. Comparing the lamp power expression of this converter (5.1.10) with the SRI, is found that the Boost-based can supply more power for the same input voltage. Additionally, using the T_{ch} time as an additional D.O.F., a variety of input voltage values can be used to obtain a desired operating point. The price to pay, compared with the SRI, is the loss of the zero current switching at the switches turn-on and the need for an additional switch.

5.1.2. Buck-Boost based converter

This converter, using a buck-boost in DCM as the unidirectional current source, has the same charge and discharge stages as the Boost-based converter, as shown in Fig.5.5. However the inductance discharge is not sustained by the DC input voltage, as observed in the equivalent circuits (b) and (c) on Fig.5.5-bottom. Accordingly, this converter works as a bidirectional DCM Flyback converter, as detailed in [5.3]. Only the energy stored in the inductance, during the charge phase, is sent to the lamp during each discharge phase.

Because only the energy stored by L is transferred to the lamp, the lamp power can be easily computed as twice the inductance energy, multiplied by the lamp operating frequency:

$$P_{lp} = f_{lp}LI_{Lo}{}^2 = \frac{f_{lp}\left(V_{in}T_{ch}\right)^2}{L} \qquad (5.1.20)$$

As can be observed in (5.1.20), the lamp power is proportional to the square of the DC input voltage and the inductance charge time. Using this expression for P_{lp}, the lamp peak voltage can be found again using the Manley's power equation (1.2.4):

$$\hat{V}_{lp} = \frac{V_{th}C_g}{C_{eq}} + \frac{V_{in}T_{ch}{}^2}{4LC_dV_{th}} \qquad (5.1.21)$$

Differing from the Boost-based topology, the Buck-Boost converter is stable for all the values of the input voltage, as demonstrated in [5.1]. Here, ZCS is assured only at the end of the discharge sequence, as for the Boost-based topology.

In Fig.5.6 the state plane analysis for this Buck-Boost converter is shown. Observe that all the semi-circumferences before breakdown are traced around zero. According to the state plane shown in Fig.5.6-top, the limit between the operating case A and B

is obtained when $-U_{br} \leq 0$. Using this condition and replacing (5.1.21) in (4.1.10), the minimum value of V_{in} necessary to work in the operating case A, V_{in_A} is found (5.1.22):
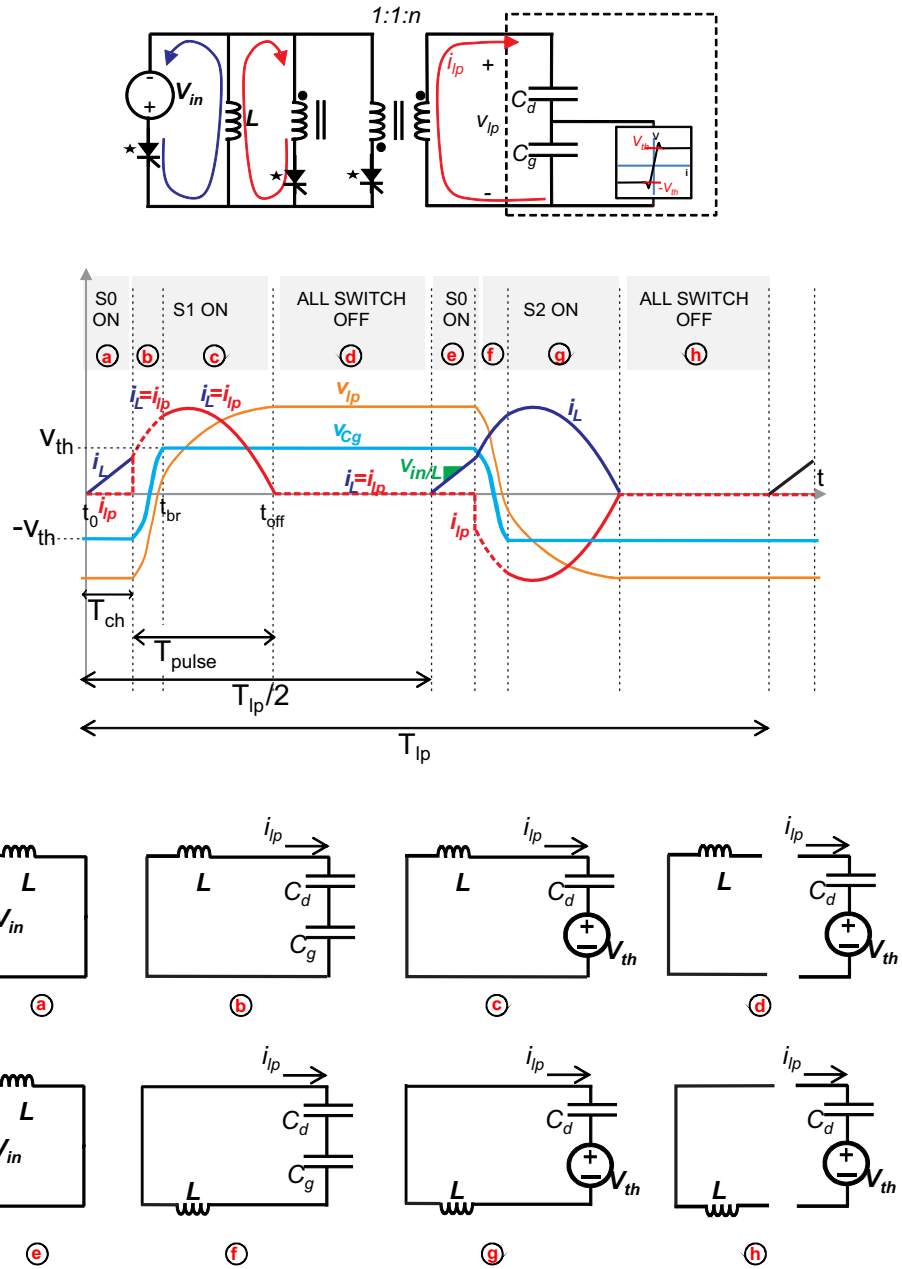
Figure 5.5.: Buck-Boost-based converter output current waveform (bottom) with the corresponding operating sequences (bottom)

$$V_{in_A} = 2V_{th}T_{ch}\sqrt{L\left(C_d + C_g\right)} \tag{5.1.22}$$

The V_{in_A} value decreases linearly with the charge time, as observed in Fig.5.7, where the theoretical output power is traced as a function of V_{in}, with $V_{in} > V_{in_A}$, for different values of inductance charge time. The DBD model and inductance values are the same used to trace the Boost-based curves shown in Fig.(5.1.10). Observe that under this conditions, in the Buck-Boost-based converter a higher input voltage is required to obtain the same lamp power than in the Boost-based

Remembering that the operating case A is more interesting for us because it maximizes the conductance peak current and consequently benefits the lamp performance, next geometrical relations of the case A state planes (Fig.5.6-top) are used to find the equations for $\hat{I}_{lp}$, I_{br}, T_{br} and T_{on}.

The normalized peak current value, J^*, is equal to the normalized lamp peak voltage as observed in the state plane after breakdown (Fig.5.6-right). Thus, de-normalizing we obtain:
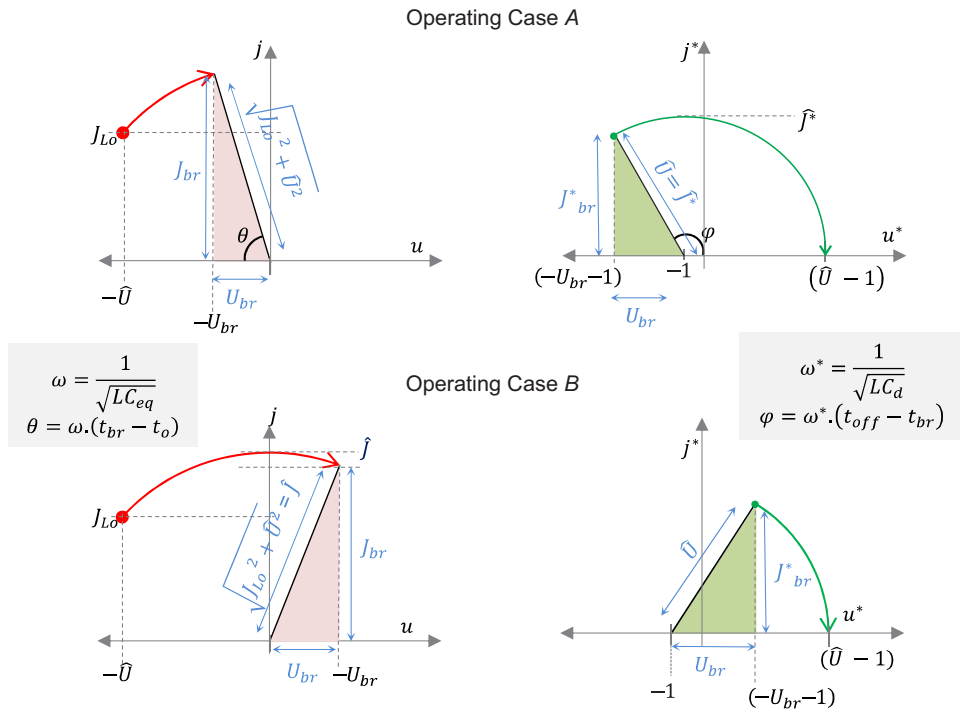
Figure 5.6.: State planes for the Buck-Boost-based converter in DCM. Before (left) and after (right) gas breakdown. For two operating cases: When the gas breakdown happens before the peak current (A) and after the peak current (B)
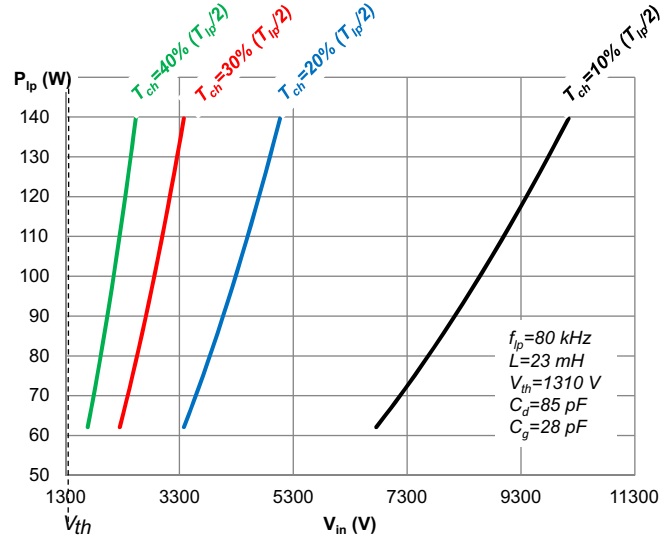
Figure 5.7.: Power delivered to the lamp by the Buck-Boost-based converter for different values of inductance charge time.

$$\hat{I}_{lp} = \hat{V}_{lp}\sqrt{\frac{C_d}{L}} \tag{5.1.23}$$

From (5.1.23), the lamp peak current increases linearly with the lamp peak voltage, therefore, it can be calculated directly with the desired lamp power by means of the Manley's formula (1.2.4).

The maximum operating frequency of this Buck-Boost-based converter, is determined by T_{pulse} and the inductance charge time T_{ch}:

$$f_{lp} \leq \frac{1}{2\left(T_{ch} + T_{pulse}\right)} \tag{5.1.24}$$

T_{pulse} is the sum the duty time of the discharge, T_{on}, and the time necessary to produce the breakdown, T_{br}. Also from the case A state plane in Fig.5.6-right, we compute T_{on} as the angle of the semi-circumference, φ, divided by the resonant frequency ω^* and de-normalizing:

$$T_{on} = \sqrt{LC_d}\left[\pi - arcsin\left(\frac{I_{br}}{\hat{I}_{lp}}\right)\right] \tag{5.1.25}$$

In a similar manner, but from the state plane before gas breakdown we compute T_{br}:

$$T_{br} = \sqrt{LC_{eq}}\left[arcsin\left(\frac{I_{br}}{k_{br}}\right) - arcsin\left(\frac{I_{br}}{k_{br}}\right)\right] \tag{5.1.26}$$

with,

$$k_{br} = \sqrt{\frac{\hat{V}_{lp}^2 C_{eq}}{L} + I_{Lo}^2} \qquad (5.1.27)$$

And finally, I_{br} is computed replacing (5.1.8) and (5.1.7) in (5.1.3):

$$I_{br} = I_{Lo}\sqrt{\frac{C_g}{Ceq}} \qquad (5.1.28)$$

The precedent equations, together with the SRI, Boost-based and Square waveform converter formulas for the operating case A, are presented in Table.5.1. From this comparative table, note that to obtain the same $\hat{V}_{lp}$ value and hence, the same lamp power, the converter that requires the minimum input voltage is the Boost-based. Observe that for the resonant converters, the expression for T_{on} is the same, however this time and also T_{br} can be adjusted by means of T_{ch} in the Boost and Buck-Boost based converters.

5.2. Converters Design and Simulations

Here, on the basis of the best lamp performance conditions identified in Section 3 an operating point is chosen, and accordingly the four different types of converters under comparison are designed. For simplicity, the designs are done assuming a transformation ratio equal to one, thus all the values are computed as seen on the secondary side of the transformer. The operating condition selected for the converters design is: P_{lp}=100 W, f_{lp}=60 kHz and a discharge time $T_{on} = 3.5\,\mu s$.

Using the DBD lamp model in Table.2.1 and the Manley's equation (1.2.4), a lamp peak voltage of 5.48 kV is found.

5.2.1. SRI design

To obtain 100 W of output power from the SRI, a DC input voltage of 1.17 kV is computed with (4.1.39). According to (4.1.30), the minimum value of V_{in} to obtain the operating case A is 875 V, thus the equations of the operating case A can be used.

In the expression of T_{on} for the SRI in Table.5.1, the factor $(I_{br}/\hat{I}_{lp})$ is observed. Solving this factor, the expression (5.2.1) is found:

$$\frac{I_{br}}{\hat{I}_{lp}} = \frac{1}{\hat{V}_{lp} - V_{in}}\sqrt{\frac{4V_{th}C_g}{C_d}\left(\hat{V}_{lp} + V_{in} - \frac{V_{th}C_g}{C_{eq}}\right)} \qquad (5.2.1)$$

Because V_{in} and $\hat{V}_{lp}$ are known, the equation (5.2.1) is a constant. Replacing (5.2.1)

Topology	SRI	Boost-based	Buck-Boost-based	Square waveform
Manley's equation		$P_{lp} = 4f_{lp}C_dV_{th}\left(\hat{V}_{lp} - \dfrac{V_{th}C_g}{C_{eq}}\right)$	$\hat{V}_{lp} = \dfrac{P_{lp}}{4f_{lp}C_dV_{th}} + \dfrac{V_{th}C_g}{C_{eq}}$	
P_{lp}	$P_{lp} = \dfrac{4f_{lp}V_{th}^2C_gV_{in}}{V_{th} - V_{in}}$	$P_{lp} = \dfrac{f_{lp}V_{th}\left(LI_{Lo}^2 + 4V_{in}V_{th}C_g\right)}{V_{th} - V_{in}}$	$P_{lp} = f_{lp}LI_{Lo}^2$	$P_{lp} = JD_{lp}V_{th} - 4f_{lp}C_gV_{th}^2$
$\hat{V}_{lp}$	$\hat{V}_{lp} = \dfrac{V_{th}C_g}{C_{eq}} + \dfrac{V_{th}V_{in}C_g}{C_d(V_{th} - V_{in})}$	$\hat{V}_{lp} = \dfrac{V_{th}C_g}{C_{eq}} + \dfrac{LI_{Lo}^2 + 4V_{in}V_{th}C_g}{4C_d(V_{th} - V_{in})}$	$\hat{V}_{lp} = \dfrac{V_{th}C_g}{C_{eq}} + \dfrac{I_{Lo}^2L}{4C_dV_{th}}$	$\hat{V}_{lp} = V_{th} + \dfrac{JD_{lp}}{4f_{lp}C_d}$
$\hat{I}_{lp}$	$\hat{I}_{lp} = \left(\hat{V}_{lp} - V_{in}\right)\sqrt{\dfrac{C_d}{L}}$		$\hat{I}_{lp} = \left(\hat{V}_{lp}\right)\sqrt{\dfrac{C_d}{L}}$	$\hat{I}_{lp} = J$
I_{br} $\left(\hat{V}_{lp}\right)$	$I_{br}^2 = \dfrac{4V_{th}\hat{V}_{lp}C_g}{L} \cdot \left[1 - \dfrac{V_{th}C_g}{\left(\hat{V}_{lp} - V_{th}\right)C_d}\right]$	$I_{br}^2 = I_{LO}^2 + \dfrac{4V_{th}V_{in}C_g}{L} \cdot \left[\hat{V}_{lp} + V_{in} - \dfrac{V_{th}C_g}{C_{eq}}\right]$	$I_{br}^2 = \dfrac{4V_{th}(C_g + C_d)}{L} \cdot \left(\hat{V}_{lp} - \dfrac{V_{th}C_g}{C_{eq}}\right)$	$I_{br} = J$
I_{br} $\left(V_{in}\right)$	$I_{br}^2 = \dfrac{4V_{th}V_{in}C_g}{L}\left(1 + \dfrac{V_{th}C_g}{C_d(V_{th} - V_{in})}\right)$	$I_{br}^2 = \left(I_{Lo}^2 + \dfrac{4V_{th}V_{in}C_g}{L}\right)\left(1 + \dfrac{V_{th}C_g}{C_d(V_{th} - V_{in})}\right)$	$I_{br} = I_{Lo}\sqrt{\dfrac{C_g}{C_{eq}}}$	$I_{br} = J$
T_{br}	$T_{br} = \sqrt{LC_{eq}} \cdot \arcsin\left(\dfrac{I_{br}}{k}\right)$ $k = \left(\hat{V}_{lp} + V_{in}\right)\sqrt{\dfrac{C_{eq}}{L}}$	$T_{br} = \sqrt{LC_{eq}} \cdot \left[\arcsin\left(\dfrac{I_{br}}{k}\right) - \arcsin\left(\dfrac{I_{Lo}}{k}\right)\right]$ $k = \sqrt{\dfrac{\left(\hat{V}_{lp} + V_{in}\right)^2C_{eq}}{L} + I_{Lo}^2}$	$T_{br} = \dfrac{1}{\sqrt{LC_{eq}}} \cdot \left[\arcsin\left(\dfrac{I_{br}}{k}\right) - \arcsin\left(\dfrac{I_{Lo}}{k}\right)\right]$ $k = \sqrt{\dfrac{\hat{V}_{lp}^2C_{eq}}{L} + I_{Lo}^2}$	$T_{br} = \dfrac{2V_{th}C_g}{J}$
T_{on}		$T_{on} = \sqrt{LC_d}\left[\pi - arcsen\left(\dfrac{I_{br}}{I_{lp}}\right)\right]$		$T_{on} = \dfrac{f_{lp}.D_{lp}}{2} - \dfrac{2V_{th}C_g}{J}$

Table 5.1.: Main equations of the four topologies.

in the expression of T_{on} (Table.5.1-SRI) and solving for L, is found (5.2.2):

$$L = \frac{1}{C_d} \left(\frac{T_{on}}{\pi - arcsin\left(\frac{I_{br}}{\hat{I}_{lp}} \right)} \right)^2 \tag{5.2.2}$$

Using $V_{in} = 1.17\,kV$ and $\hat{V}_{lp} = 5.48\,kV$ in (5.2.2), an inductance value $L = 25\,mH$ is computed. The theoretical operating point of the SRI converter, obtained with the values computed here, are presented in Table 5.2.

	$\hat{I}_{lp}$ (A)	$\hat{V}_{lp}$ (V)	I_{br} (A)	T_{on} (s)	T_{br} (s)	P_{lp} (W)
Theoretical	2.51E-01	5.48E+03	1.7E-01	3.50E-06	7.79E-07	100
Simulation	2.48E-01	5.45E+03	1.6E-01	3.47E-06	7.58E-07	99.1

Table 5.2.: Operating Point for the SRI converter. $V_{in} = 1175V\,V$, $L = 25\,mH$

5.2.2. Boost-based design

For the Boost-based converter, the DC input voltage can have different values to obtain the desired operating point because an additional degree of freedom T_{ch}, is available. Thus, a valid solution among the range of possible combinations of V_{in}, L, and T_{ch} is found.

As can be observed in Table.5.1, T_{on} depends on the term $I_{br}/\hat{I}_{lp}$. Solving this term using the I_{br}, $\hat{I}_{lp}$ and I_{Lo} equations for the Boost-based converter, as a function of V_{in}, is found:

$$\frac{I_{br}}{\hat{I}_{lp}} = \frac{\sqrt{V_{in}^2 \frac{T_{ch}^2}{L} + 4V_{th}C_g \left(\hat{V}_{lp} + V_{in} - \frac{V_{th}C_g}{C_{eq}} \right)}}{\left(\hat{V}_{lp} - V_{in} \right) \sqrt{C_d}} \tag{5.2.3}$$

From the Boost power equation (5.1.10), the term T_{ch}^2/L can also be solved as a function of V_{in}:

$$\frac{T_{ch}^2}{L} = \frac{1}{V_{in}^2} \left(\frac{P_{lp}(V_{th} - V_{in})}{f_{lp}V_{th}} - 4V_{in}V_{th}C_g \right) \tag{5.2.4}$$

Given that the charge time T_{ch} and L are positive values, a solution for (5.2.4) can be found if the right term of this equation is also positive. This condition is fulfilled for:

$$V_{in} \geq \frac{P_{lp}}{P_{lp} + f_{lp}V_{th}^2 C_g} \tag{5.2.5}$$

Replacing P_{lp}=100 W, f_{lp}=60 kHz and using the lamp equivalent parameters, a maximum input voltage V_{in} of 1174 V is calculated.

Now, replacing (5.2.4) in (5.2.3), $I_{br}/\hat{I}_{lp}$ can be simplified (5.2.6):

$$\frac{I_{br}}{\hat{I}_{lp}} = \frac{\sqrt{\frac{P_{lp}}{f_{lp}}\left(\frac{C_g}{C_{eq}} - \frac{V_{in}}{V_{th}}\right)}}{\left(\hat{V}_{lp} - V_{in}\right)\sqrt{C_d}} \tag{5.2.6}$$

Using the T_{on} equation, the inductance value necessary to obtain $T_{on} = 3.5\,\mu s$ can be found as a function of $I_{br}/\hat{I}_{lp}$ (5.2.7):

$$L = \frac{1}{C_d}\left(\frac{T_{on}}{\pi - arcsin\left(\frac{I_{br}}{\hat{I}_{lp}}\right)}\right)^2 \tag{5.2.7}$$

In this way, with (5.2.7), the inductance value to obtain the desired operating point is calculated for different values of V_{in}. With the inductance value, we compute the inductance charge time T_{ch} and the lamp current pulse T_{pulse}. According to condition (5.1.15), T_{pulse} plus T_{ch} must be smaller than $T_{lp}/2$. In order to find the minimum V_{in} value to assure that the D.C.M. is respected, in Fig.5.8 the sum of this two values as a function of V_{in}, is plotted.

With an input voltage of 850 V, using (5.2.7) an inductance value $L_{boost} = 28.3\,mH$ is found. In order to verify that the operating case A is obtained, the constant (5.2.4) is replaced in (5.1.12), finding the minimum value that V_{in} must have, V_{in_A}=611 V. The theoretical operating point calculated here for the Boost-based converter, is summarized in Table 5.3.
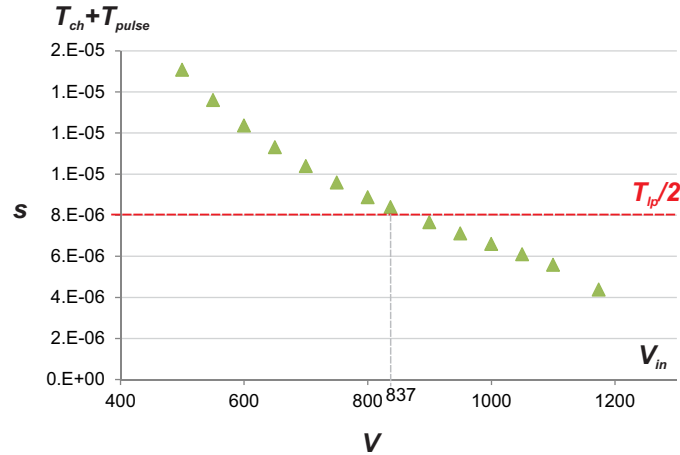
Figure 5.8.: For an operating frequency f_{lp}=60 kHz, the inductance charge time, T_{ch}, plus the lamp current pulse, T_{pulse}, must be smaller than $T_{lp}/2$=8 µs. In this figure, $T_{ch} + T_{pulse}$ is plotted as function of V_{in}.

5.2.3. Buck-Boost-based design

In a similar manner as previously done for the Boost-based converter, the term $I_{br}/\hat{I}_{lp}$ is found using the equations for the Buck-Boost based converter in Table.5.1:

$$\frac{I_{br}}{\hat{I}_{lp}} = \frac{V_{in}}{\hat{V}_{lp}} \sqrt{\frac{C_g}{C_{eq}C_d}} \sqrt{\frac{T_{ch}^2}{L}} \tag{5.2.8}$$

Using the power equation (5.1.20), the value of T_{ch}^2/L as a function of V_{in} is found:

$$\frac{T_{ch}^2}{L} = \frac{P_{lp}}{f_{lp}V_{in}^2} \tag{5.2.9}$$

Replacing (5.2.9) in (5.2.8), is found that $I_{br}/\hat{I}_{lp}$ is independent of V_{in}:

$$\frac{I_{br}}{\hat{I}_{lp}} = \frac{1}{\hat{V}_{lp}} \sqrt{\frac{P_{lp}C_g}{f_{lp}C_{eq}C_d}} \tag{5.2.10}$$

Using expression (5.2.10) in the T_{on} formula (see Table 5.1) and solving for L, an expression to compute the inductance value is found:

$$L = \frac{1}{C_d} \left(\frac{T_{on}}{\pi - arcsin\left(\frac{I_{br}}{\hat{I}_{lp}}\right)} \right)^2 \tag{5.2.11}$$

Solving (5.2.11), an inductance value of $L = 38.1\,mH$ is computed. With L already found, still remain two unknown quantities in (5.2.9) to be determined: V_{in} and T_{ch}. The maximum possible value of T_{ch}, T_{ch-max} is determined with the following expression:

$$T_{ch-max} = \frac{T_{lp}}{2} - T_{on} - T_{br} \tag{5.2.12}$$

Using the equations for the Buck-boost based converter in Table.5.1 and solving for

	$\hat{I}_{lp}$ (A)	$\hat{V}_{lp}$ (V)	I_{br} (A)	T_{on} (s)	T_{br} (s)	P_{lp} (W)
Theoretical	2.54E-01	5.48E+03	1.87E-01	3.50E-06	3.36E-07	100
Simulation	2.53E-01	5.46E+03	1.99E-01	3.43E-06	3.20E-07	99.6

Table 5.3.: Operating Point for the Boost-based converter. $V_{in} = 850\,V$, $L = 28.3\,mH$, $T_{ch} = 4.36\,\mu s$

T_{br}, it can be found that T_{br}, like T_{on}, is independent of V_{in} (5.2.13):

$$T_{br} = \sqrt{LC_{eq}} \left(arcsin \left(\sqrt{\frac{P_{lp}}{f_{lp}\hat{V}_{lp}C_{eq}}} \sqrt{\frac{C_g}{C_{eq}}} \right) - arcsin \left(\sqrt{\frac{P_{lp}}{f_{lp}\hat{V}_{lp}C_{eq}}} \right) \right) \quad (5.2.13)$$

And now the minimum valid value of V_{in}, $V_{in_{min}}$, is determined from (5.2.9) solving for T_{ch-max}:

$$V_{in_{min}} = \sqrt{\frac{P_{lp}L_{bb}}{f_{lp}T_{ch-max}^2}} \quad (5.2.14)$$

Solving (5.2.13), $T_{br} = 0.32\mu s$ is calculated. Replacing this value in (5.2.12), $T_{ch-max} = 4.51\mu s$ is found. Which according to (5.2.14) implies a minimum input voltage of 1.77 kV. This theoretical operating point calculated for the Buck-Boost-based converter, is summarized in Table 5.4.

	$\hat{I}_{lp}$ (A)	$\hat{V}_{lp}$ (V)	I_{br} (A)	T_{on} (s)	T_{br} (s)	P_{lp} (W)
Theoretical	2.59E-01	5.48E+03	2.41E-01	3.50E-06	3.22E-07	100
Simulation	2.58E-01	5.47E+03	2.41E-01	3.51E-06	3.08E-07	99.9

Table 5.4.: Operating Point for the Buck-Boost-based converter. $V_{in} = 2.4\,kV$, $L = 38.1\,mH$, $T_{ch} = 3.32\,\mu s$

5.2.4. Square-shape design

From the Square-shape current equations in Table.5.1 is found that the lamp current intensity J can be expressed as a function on the T_{on} time:

$$J = \frac{2\left(C_d\hat{V}_{lp} - V_{th}\left(C_d + C_g\right)\right)}{T_{on}} \quad (5.2.15)$$

For the desired operating point, using (5.2.15) a value of $J = 181.7\,mA$ is obtained. Replacing this value in the square-shape converter $\hat{V}_{lp}$ equation, and solving for D_{lp}, a duty cycle of 46.8% is computed. In Table 5.5 the theoretical operating point calculated above for the Square-shape converter, is summarized.

	$\hat{I}_{lp}$ (A)	$\hat{V}_{lp}$ (V)	T_{on} (s)	T_{br} (s)	P_{lp} (W)
Theoretical	1.82E-01	5.48E+03	3.50E-06	4.04E-07	100
Simulation	1.82E-01	5.47E+03	3.5E-06	4.07E-07	99.8

Table 5.5.: Operating Point for the Square-shape converter.

5.2.5. Simulations

With the aim to verify the converters equations deduced previously for the simplified DBD mode, the four types of converter have been simulated using the converter design previously presented and using ideal circuits, not including losses nor parasitic elements. In Fig.5.9 the electrical waveforms obtained from these simulation are shown.
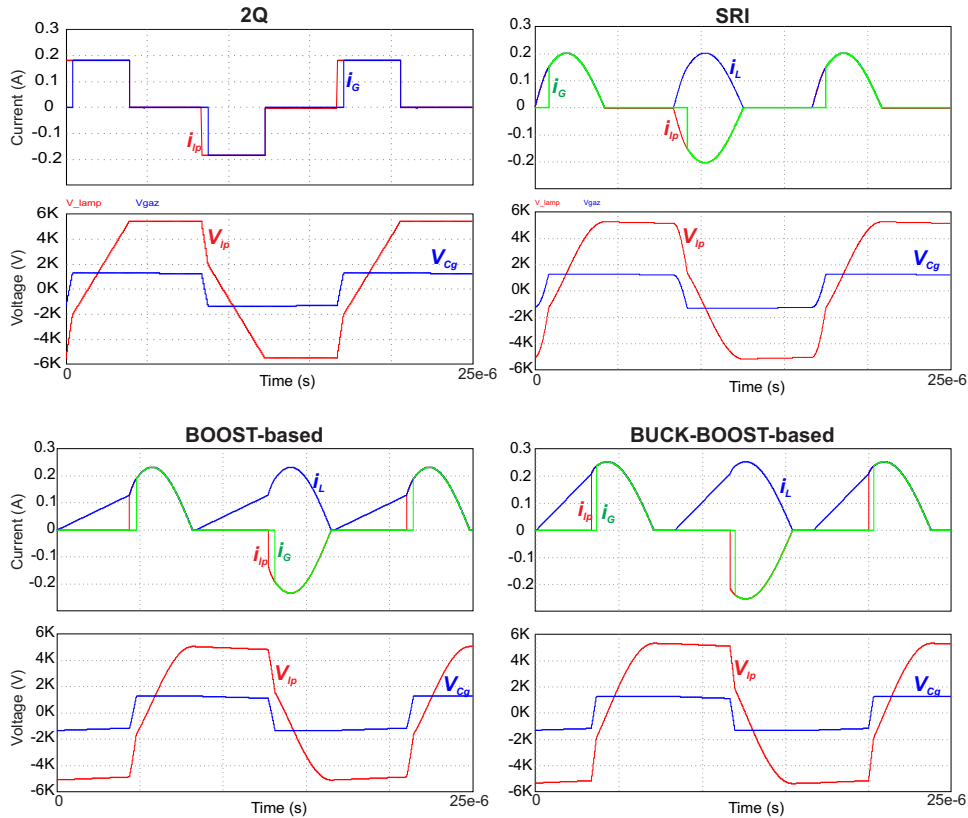
Figure 5.9.: Simulation waveforms of the four topologies.

The main values describing the operating condition for each converter are summarized in Tables 5.2-5.5, comparing the values obtained under simulation and from theoretical calculations. From these results the accuracy of the equations deduced before, is verified. The duration of the lamp ignition T_{on}, the lamp power P_{lp} and the operating frequency f_{lp} is the same for all the tables, 3.5 µs, 100 W and 60 kHz respectively. The $\hat{I}_{lp}$ value obtained for the Buck-Boost-based converter is slightly higher than the other resonant converters and 42 % higher than the Square-shape converter, thus under these operating conditions and according to results found in Section 3.2, for the resonant converters the lamp UV production should be stronger. The highest breakdown current I_{br} is obtained for the Buck-Boost-based converter, condition that could have a positive impact in the lamp performance. The lowest input voltage required for the converters operation is

found for the Boost-based converter; is 30 % of the one required for the Buck-Boost-based.

5.3. Experimental results

In this section the implementation of the four structures is presented, supplying a XeCl DBD excilamp under similar operating conditions. The operating point for the experimental comparison is similar to the one chosen for the converters design example of Section 5.2. However the input voltage of the different converters has been adjusted to obtain exactly the same lamp power.

For all the four converters the lamp peak voltage is around 5000 V. As previously explained in Section 1.2.2, in order to reduce this voltage to the high-frequency semiconductor range, in all the topologies under test a low capacitance step-up transformer with 1:10 ratio is used. The characteristics of this transformer are described in Section 2.4.1.

The experimental waveforms of Fig.5.10 show the different behavior of the four converters, in terms of the current injected into the lamp i_{lp}, also the UV emitted by the lamp. Lamp peak voltage is similar in the four structures, as predicted by (2.3.4). Note that, in the four structures, the lamp voltage waveform is similar and the UV radiation waveform is different. It confirms how difficult would be to control the UV radiation by means of a voltage-mode supply. As expected, the UV instantaneous response is tightly correlated to the lamp current after the gas breakdown. A disparity between the intensities of the UV pulses produced by the positive and negative current pulses, is observed in the four converters waveforms. As explained earlier in Chapter 3, the origin of this disparity is the non-symmetrical geometry of the coaxial DBD excimer lamp.

Table 5.6 details the four structures in terms of losses, in the semiconductors, and in the transformer (the same for all the structures). Efficiency is taken, considering also losses in the passive elements. The UV power measurement is acquired using the same experimental setup described in 3.1.

Converter	V_{in} (V)	I_{in} (A)	P_{in} (W)	P_{prim} (W)	UV ($\frac{mW}{cm^2}$)	$\eta_{circuit}$ (%)	$\eta_{transf.}$ (%)	η_{total} (%)
Square-shape	159.1	1.2	193.5	125	28.3	65	85	55
Boost	79	1.7	131.8	123	25.3	93	86	80
Buck-Boost	246	0.5	134	123	26.8	92	86	79
SRI	136.9	0.9	127.6	124	27.5	97	85	83

Table 5.6.: Converters efficiencies comparison. Electrical power supplied to the lamp: $P_{lp} = 106W$

Regarding semiconductor losses, it is possible to see that the rectangular converter presents the highest, since it is hard-switched; followed by the buck-boost converter, as its initial current during the discharge time is the highest, and so the peak current; the series resonant inverter is the most efficient structure, since it is completely ZCS.
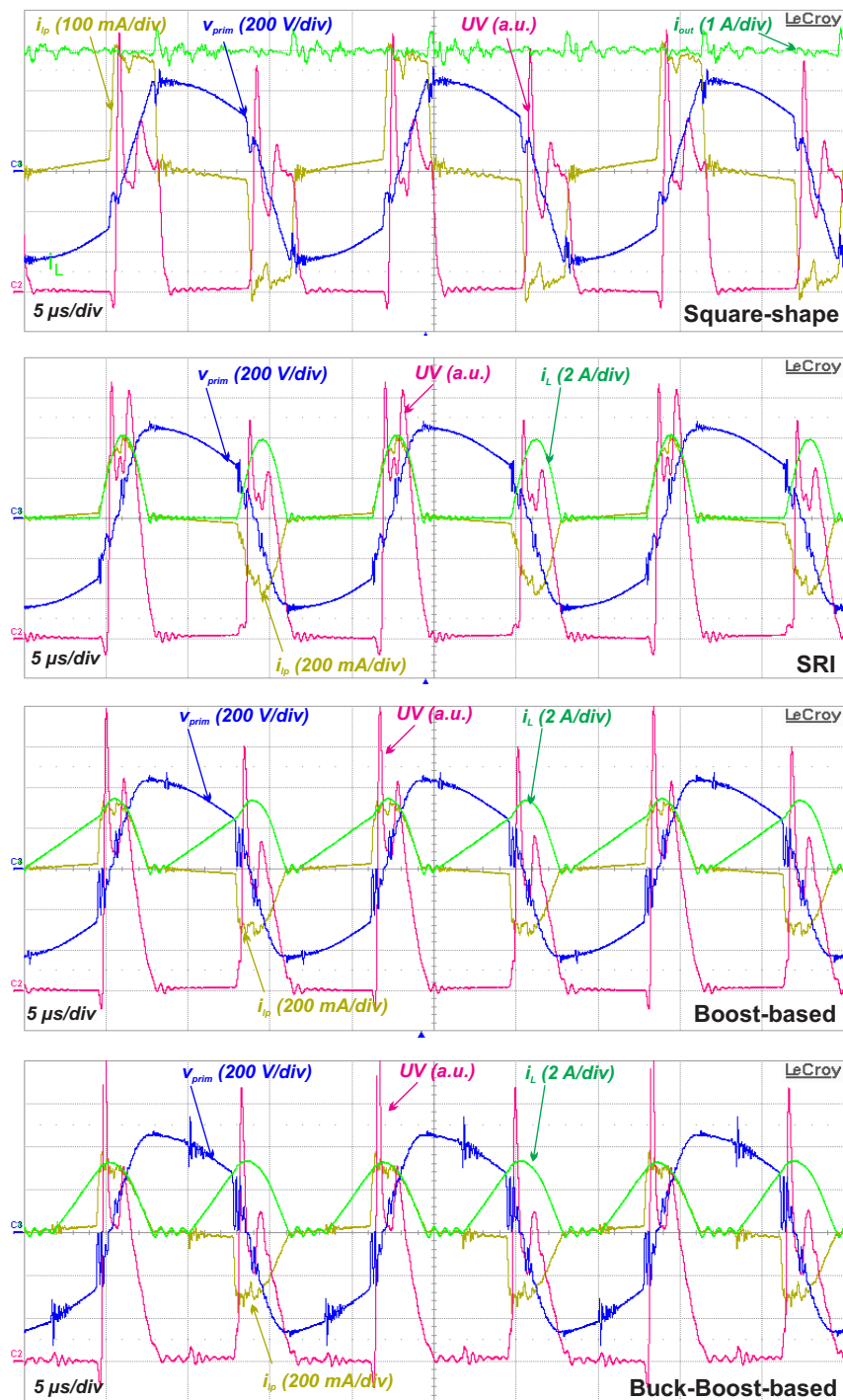
Figure 5.10.: Experimental waveforms of the four topologies. $P_{lp} = 106W$, $f_{lp} = 60kHz$

Since the electrical lamp power is the same for all the structures, as well as the duration and energy of each pulse, the differences in the luminous efficiency of the lamp are determined by the current shape. The lowest UV power was obtained for the Boost-based converter, this UV corresponds to 89 % of the one obtained with the Square-shape supply. Considering the results of the parametric study concerning the impact of the current intensity (Section 3.2), this reduction in the UV production is explained by the lamp current intensity difference between the converters. In this sense, the lowest lamp peak current and luminous power were obtained for the Boost and the Buck-Boost based converters, as can be observed in Fig.5.10. The dissimilarities in the UV production efficiency found in this experimental comparison, can be compensated adjusting the converters operating point in order to increase the peak lamp current for the same injected power.

5.4. Conclusions

By comparing the UV and lamp voltage waveforms obtained with the tested topologies, the difficulty to control the UV radiation from DBD excilamps using voltage mode supplies is experimentally validated. For the compared resonant topologies operating under similar conditions, a similar level of electrical efficiency has been measured. The square-shape current has demonstrated to be slightly more effective in terms of UV production than the resonant current waveforms.

The main analytical expressions of four DBDs current-mode DBD power supplies, three of them resonant topologies, have been obtained on the basis of the DBD simplified model. Those expressions allow to design the presented converters and to evaluate the convenience of these topologies according to the specifications of the intended application.

The Square-shape supply topology offers a large operating range and full control of the operating point with three degrees of freedom; these characteristics are useful for applications requiring a fine adjustment of the UV radiation and lamp operating point, for example in laboratory test and industrial processes.

Among the topologies compared here, the SRI converter features the lowest number of switches. This characteristic make of this converter a good candidate for low cost applications. Also, the SRI is the only of these converters with full Z.C.S., thus is well adapted for EMI sensitive applications and for scenarios where maximum electrical efficiency is required.

In some applications the DC input voltage available to supply the DBD converter is a constraint, e.g. battery operated equipment. In this case the Boost-based converter is a good option because this topology allows to obtain a determined operating condition from a DC input voltage lower than the voltage required for the other evaluated converters. Consequently by using this converter, the required transformer turns ratio is reduced and also the need for a voltage step-up stage can be eliminated.

Finally, the high-stability of the Buck-Boost-based converter is a valuable attribute for open loop operation.

Bibliography

[5.1] R. Diez, H. Piquet, S. Bhosle, and J.-M. Blaquiere, "Current mode converter for dielectric barrier discharge lamp," in *IEEE Power Electronics Specialists Conference, 2008. PESC 2008*, pp. 2485–2491, 2008.

[5.2] H. Piquet, S. Bhosle, R. Diez, and M. V. Erofeev, "Pulsed current-mode supply of dielectric barrier discharge excilamps for the control of the radiated ultraviolet power," *IEEE Transactions on Plasma Science*, vol. 38, pp. 2531–2538, Oct. 2010.

[5.3] R. Diez, H. Piquet, M. Cousineau, and S. Bhosle, "Current-mode power converter for radiation control in DBD excimer lamps," *IEEE Transactions on Industrial Electronics*, vol. 59, no. 4, pp. 1912–1919, 2012.

[5.4] R. Diez, H. Piquet, S. Bhosle, J.-M. Blaquiere, and N. Roux, "Design of a current converter for the study of the UV emission in DBD excilamps," in *IEEE International Symposium on Industrial Electronics, 2008. ISIE 2008*, pp. 62–67, 2008.

6. General Conclusions

The main objective of this thesis was the enhancement of the DBD excimer UV lamp systems efficiency. With this aim, a process covering two main stages has been conceived: The first stage of this process is the study of the lamp best performance operating conditions and the second is the enhancement of the lamp power supply electrical efficiency.

For the first stage, a study of the lamp operating point impact over the lamp performance was proposed. To make possible this performance study, a new scientific tool that provides full control and flexibility to adjust the DBD lamp power has been developed. This tool is a current-mode power supply capable of injecting a square-shape current into the DBD lamp with three degrees of freedom on its current output waveform: current intensity, duty cycle and frequency.

Using this novel equipment with a XeCl DBD UV excilamp, the effect of the lamp current intensity, frequency and pulse energy over the UV radiation and over the lamp efficiency was revealed. From the obtained results (for the tested operating range) the value of the injected pulse energy has been found to be a determinant factor in the lamp efficiency. Pulse energies above $300\,\mu J$, are found to provide the best lamp performance operating conditions. Additionally, for a given value of lamp electrical power, the use of low-frequency and high-intensity currents has demonstrated to benefits the UV radiation output. However a decrease on the lamp performance gain for current intensities above $190\,mA$ has been established.

For the second stage of this optimization process, a high-efficiency converter has been conceived and implemented, designed to work at the optimal lamp operating point found using the square-shape current supply. In order to achieve the high-efficiency requirement for this specific application, a resonant converter that operates on the basis of the series resonant inverter, featuring zero current switching (Z.C.S) at turn-on and turn-off of the switches and Discontinuous Conduction Mode (D.C.M), has been designed. The full Z.C.S minimizes the switching losses; the D.C.M. benefits the system performance ensuring that only the highest current intensity pulse is used to sustain the gas discharge. Using this converter, a maximum electrical efficiency of 94% has been achieved.

After this work, one of the perspectives is the application of the square-shape supply in the performance study of other types of DBD excilamps and DBD reactors. One of the possible applications, already verified in preliminary experiments, is the evaluation of the DBD excimer UV lamp disinfection efficacy as a function of the operating point. With changes in the square-shape converter design and implementing different semiconductor technologies, the DBD excimer lamp studies can be extended to operating ranges different to the one achieved in this thesis, for example supplying the lamp with a current in the range of MHz. Additionally, the development of transformer-less DBD power supplies, profiting the new technologies in HV semiconductors, is an interesting

possibility that could allow to reduce the DBD supplies size while increasing its efficiency and reliability.

Bibliography for Chapter 0

[0.1] United Nations, "Drinking water, sanitation & hygiene. statistics, graphs and maps." `http://www.unwater.org/statistics_san.html`, Nov. 2013.

[0.2] Defensoria del Pueblo - Colombia, *DIAGNOSTICO DE LA CALIDAD DEL AGUA PARA CONSUMO HUMANO ANO 2010*. Defensoria del Pueblo de Colombia, Nov. 2011.

[0.3] Instituto de Hidrologia, Meteorologia y Estudios Ambientales, *Estudio Nacional del Agua 2010*. Bogota D.C.: IDEAM, 2010.

[0.4] United States Environmental Protection Agency, *ULTRAVIOLET DISINFECTION GUIDANCE MANUAL FOR THE FINAL LONG TERM 2 ENHANCED SURFACE WATER TREATMENT RULE*. EPA, Nov. 2006.

[0.5] I. Soloshenko, V. Y. Bazhenov, V. A. Khomich, V. V. Tsiolko, and N. G. Potapchenko, "Comparative research of efficiency of water decontamination by UV radiation of cold hollow cathode discharge plasma versus that of low- and medium-pressure mercury lamps," *IEEE Transactions on Plasma Science*, vol. 34, no. 4, pp. 1365–1369, 2006.

[0.6] C. Dorval Dion and J. Tavares, "Photo-initiated chemical vapor deposition as a scalable particle functionalization technology (a practical review)," *Powder Technology*, vol. 239, pp. 484–491, May 2013.

[0.7] M. Wertheimer, A. Fozza, and A. Holländer, "Industrial processing of polymers by low-pressure plasmas: the role of VUV radiation," *Nuclear Instruments and Methods in Physics Research Section B: Beam Interactions with Materials and Atoms*, vol. 151, pp. 65–75, May 1999.

[0.8] NICHIA CORPORATION, "UV-LED." `http://www.nichia.co.jp/en/product/uvled.html`, 2013.

[0.9] OSRAM GmbH, "PURITEC HNS germicidal ultraviolet lamps." `http://www.osram.com/osram_com/products/lamps/specialty-lamps/ultraviolet-lamps/puritec-hns/index.jsp?productId=ZMP_86446`.

[0.10] Xenon corporation, "About xenon flashlamps." `http://www.xenoncorp.com/lamps.html`, 2013.

[0.11] U. Kogelschatz, "Dielectric-barrier discharges: Their history, discharge physics, and industrial applications," *Plasma Chemistry and Plasma Processing*, vol. 23, no. 1, pp. 1–46, 2003.

[0.12] M. Lomaev, E. Sosnin, and V. Tarasenko, "Excilamps and their applications," *Progress in Quantum Electronics*, vol. 36, pp. 51–97, Jan. 2012.

[0.13] P. G. WILKINSON and Y. TANAKA, "New xenon-light source for the vacuum ultraviolet," *Journal of the Optical Society of America*, vol. 45, pp. 344–349, May 1955.

[0.14] Y. TANAKA, "Continuous emission spectra of rare gases in the vacuum ultraviolet region," *Journal of the Optical Society of America*, vol. 45, pp. 710–713, Sept. 1955.

[0.15] B. Stevens and E. Hutton, "Radiative life-time of the pyrene dimer and the possible role of excited dimers in energy transfer processes," *Nature*, vol. 186, pp. 1045–1046, June 1960.

[0.16] W. C. Ermler, Y. S. Lee, K. S. Pitzer, and N. W. Winter, "Ab initio effective core potentials including relativistic effects. II. potential energy curves for xe2," *The Journal of Chemical Physics*, vol. 69, pp. 976–983, Aug. 1978.

[0.17] R. J. DeYoung and W. R. Weaver, "Spectra from nuclear-excited plasmas," *Journal of the Optical Society of America*, vol. 70, pp. 500–506, May 1980.

[0.18] J. B. Birks, "Excimers," *Reports on Progress in Physics*, vol. 38, p. 903, Aug. 1975.

[0.19] B. Eliasson and U. Kogelschatz, "UV excimer radiation from dielectric-barrier discharges," *Applied Physics B Photophysics and Laser Chemistry*, vol. 46, pp. 299–303, Aug. 1988.

[0.20] J.-Y. Zhang and I. W. Boyd, "Efficient excimer ultraviolet sources from a dielectric barrier discharge in rare-gas/halogen mixtures," *Journal of Applied Physics*, vol. 80, no. 2, p. 633, 1996.

[0.21] E. A. Sosnin, M. I. Lomaev, A. N. Panchenko, V. S. Skakun, and V. F. Tarasenko, "Glow and barrier discharge efficient excilamps," in *Proc. SPIE* (V. F. Tarasenko, G. V. Mayer, and G. G. Petrash, eds.), vol. 3403, pp. 308–313, June 1998.

[0.22] V. Tarasenko, M. Lomaev, A. Panchenko, V. Skakun, E. Sosnin, and A. Fedenev, "High-energy lasers and high-power excilamps," in *, Summaries of papers presented at the Conference on Lasers and Electro-Optics, 1996. CLEO '96*, pp. 375–, 1996.

[0.23] B. Eliasson and U. Kogelschatz, "Modeling and applications of silent discharge plasmas," *IEEE Transactions on Plasma Science*, vol. 19, pp. 309–323, Apr. 1991.

[0.24] B. Turner and J. T. Dolan, "Excimer lamp with high pressure fill," Nov. 1997. U.S. Classification: 313/570; 313/568; 313/571; 313/572; 315/39; 315/246; 315/248; 315/344 International Classification: H01J 6112; H01J 6120.

[0.25] Zoran Falkenstein, USHIO America Inc., "Development of an excimer UV light source system for water treatment." `http://www.revistavirtualpro.com/files/TIE04_200701.pdf`.

[0.26] V. F. Tarasenko, A. V. Krivonosenko, M. I. Lomaev, V. S. Skakun, E. A. Sosnin, and D. V. Shitz, "High-power excilamps with short-pulse duration," in *Proc. SPIE*, vol. 4065, pp. 826–835, 2000.

[0.27] R. Diez-Medina, *Alimentation de puissance d'une lampe exciplexe à décharge à barrière diélectrique, en vue du contrôle du rayonnement.* PhD thesis, INPT, Toulouse, 2008.

[0.28] A. Laroussi, F. C. Dobbs, Z. Wei, A. Doblin, L. Ball, K. Moreira, F. Dyer, and J. Richardson, "Effects of excimer UV radiation on microorganisms," in *Pulsed Power Plasma Science, 2001. IEEE Conference Record - Abstracts*, pp. 321–, 2001.

[0.29] M. I. Lomaev, V. S. Skakun, E. A. Sosnin, V. F. Tarasenko, D. V. Shitts, and M. V. Erofeev, "Excilamps efficient sources of spontaneous UV and VUV radiation," *Physics-Uspekhi*, vol. 46, pp. 193–209, Feb. 2003.

[0.30] Thomas Openlander, "Mercury-free sources of VUV/UV radiation: application of modern excimer lamps (excilamps) for water and air treatment1," *Journal of Environmental Engineering and Science*, vol. 6, pp. 253–264, May 2007.

Bibliography for Chapter 1

[1.1] R. Hippler, H. Kersten, M. Schmidt, and K. H. Schoenbach, eds., *Low Temperature Plasmas: Fundamentals, Technologies and Techniques*. Wiley-VCH, 2 ed., Mar. 2008.

[1.2] Hartnett, James, *Transport Phenomena in Plasma*. Academic Press, Oct. 2007.

[1.3] X. Bonnin, H. Piquet, N. Naude, C. Bouzidi, N. Gherardi, and J.-M. Blaquiere, "Design of a current converter to maximize the power into homogeneous dielectric barrier discharge (DBD) devices," *The European Physical Journal Applied Physics*, July 2013.

[1.4] M. I. Lomaev, V. S. Skakun, E. A. Sosnin, V. F. Tarasenko, D. V. Shitts, and M. V. Erofeev, "Excilamps efficient sources of spontaneous UV and VUV radiation," *Physics-Uspekhi*, vol. 46, pp. 193–209, Feb. 2003.

[1.5] H. Piquet, S. Bhosle, R. Diez, M. Cousineau, M. Djibrillah, D. Le Thanh, A. N. Dagang, and G. Zissis, "Control of the UV flux of a XeCl dielectric barrier discharge excilamp through its current variation," *Quantum Electronics*, vol. 42, pp. 157–164, Feb. 2012.

[1.6] R. Diez, H. Piquet, M. Cousineau, and S. Bhosle, "Current-mode power converter for radiation control in DBD excimer lamps," *IEEE Transactions on Industrial Electronics*, vol. 59, no. 4, pp. 1912–1919, 2012.

[1.7] H. Piquet, S. Bhosle, R. Diez, and M. V. Erofeev, "Pulsed current-mode supply of dielectric barrier discharge excilamps for the control of the radiated ultraviolet power," *IEEE Transactions on Plasma Science*, vol. 38, pp. 2531–2538, Oct. 2010.

[1.8] R. Diez, H. Piquet, and S. Bhosle, "Control of the UV emission of an excimer lamp by means of a current-mode power supply," in *Industrial Electronics, 2009. IECON '09. 35th Annual Conference of IEEE*, pp. 3500–3505, IEEE, Nov. 2009.

[1.9] J. P. Verboncoeur, "Particle simulation of plasmas: review and advances," *Plasma Physics and Controlled Fusion*, vol. 47, p. A231, May 2005.

[1.10] A. Oda, Y. Sakai, H. Akashi, and H. Sugawara, "One-dimensional modelling of low-frequency and high-pressure xe barrier discharges for the design of excimer lamps," *Journal of Physics D: Applied Physics*, vol. 32, p. 2726, Nov. 1999.

[1.11] S. Bhosle, G. Zissis, J.-J. Damelincourt, A. Capdevila, K. Gupta, F. Dawson, and V. Tarasenko, "Implementation of an efficiency indicator in an electrical modeling of a dielectric barrier discharge lamp," in *Conference Record of the 2006 IEEE Industry Applications Conference, 2006. 41st IAS Annual Meeting*, vol. 4, pp. 1784–1790, 2006.

[1.12] L. T. Doanh, S. Bhosle, G. Zissis, and H. Piquet, "Estimation of the light output power and efficiency of a XeCl dielectric barrier discharge exciplex lamp using one-dimensional drift-diffusion model for various voltage waveforms," *IEEE Transactions on Industry Applications*, vol. 49, no. 1, pp. 331–340, 2013.

[1.13] S. Bhosle, G. Zissis, J. Damelincourt, A. Capdevila, K. Gupta, F. Dawson, and V. Tarasenko, "Electrical modeling of an homogeneous dielectric barrier discharge (DBD)," in *Fourtieth IAS Annual Meeting. Conference Record of the 2005*, vol. 4, pp. 2315–2319, IEEE, Oct. 2005.

[1.14] R. Díez, J.-P. Salanne, H. Piquet, S. Bhosle, and G. Zissis, "Predictive model of a DBD lamp for power supply design and method for the automatic identification of its parameters," *The European Physical Journal - Applied Physics*, vol. 37, no. 03, pp. 307–313, 2007.

[1.15] A. El-Deib, *Modeling of and Driver Design for a Dielectric Barrier Discharge Lamp*. Thesis, University of Toronto, Aug. 2010. PhD.

[1.16] A. Flores-Fuentes, R. Pena-Eguiluz, R. Lopez-Callejas, A. Mercado-Cabrera, R. Valencia-Alvarado, S. Barocio-Delgado, and A. de la Piedad-Beneitez, "Electrical model of an atmospheric pressure dielectric barrier discharge cell," *IEEE Transactions on Plasma Science*, vol. 37, pp. 128–134, Jan. 2009.

[1.17] M. A. Djibrillah, *Éléments de conception d'un générateur électrique pour l'alimentation d'un dispositif à décharge à barrière diélectrique (DBD)*. INPT, Apr. 2011.

[1.18] U. Kogelschatz, "Dielectric-barrier discharges: Their history, discharge physics, and industrial applications," *Plasma Chemistry and Plasma Processing*, vol. 23, no. 1, pp. 1–46, 2003.

[1.19] T. C. Manley, "The electric characteristics of the ozonator discharge," *Transactions of The Electrochemical Society*, vol. 84, pp. 83–96, Oct. 1943.

[1.20] W. Sowa and R. Lecheler, "Lamp driver concepts for dielectric barrier discharge lamps and evaluation of a 110 w ballast," in *Industry Applications Conference, 2004. 39th IAS Annual Meeting. Conference Record of the 2004 IEEE*, vol. 2, pp. 1379–1385, IEEE, 2004.

[1.21] R. Diez-Medina, *Alimentation de puissance d'une lampe exciplexe à décharge à barrière diélectrique, en vue du contrôle du rayonnement*. PhD thesis, INPT, Toulouse, 2008.

[1.22] R. Diez, H. Piquet, S. Bhosle, J.-M. Blaquiere, and N. Roux, "Design of a current converter for the study of the UV emission in DBD excilamps," in *IEEE International Symposium on Industrial Electronics, 2008. ISIE 2008*, pp. 62–67, 2008.

[1.23] H.-P. Daub, *Ein adaptives Impuls-EVG zum Betrieb von dielektrisch behinderten Gasentladungslampen*. PhD thesis, KIT Scientific Publishing, Karlsruhe, 2010.

[1.24] A. El-Deib, F. Dawson, G. van Eerden, S. Bhosle, G. Zissis, and T. D. Le, "Analysis and experimental validation of a new current-controlled driver for a dielectric barrier discharge lamp," *IEEE Transactions on Industry Applications*, vol. 47, no. 4, pp. 1971–1982, 2011.

[1.25] M. Cousineau, R. Diez, H. Piquet, and O. Durrieu, "Synthesized high-frequency thyristor for dielectric barrier discharge excimer lamps," *IEEE Transactions on Industrial Electronics*, vol. 59, no. 4, pp. 1920–1928, 2012.

[1.26] M. Meisser, R. Kling, and W. Heering, "Universal resonant topology for high frequency pulsed operation of dielectric barrier discharge light sources," in *2011 Twenty-Sixth Annual IEEE Applied Power Electronics Conference and Exposition (APEC)*, pp. 1180–1187, 2011.

[1.27] M. Meißer, *Resonant Behaviour of Pulse Generators for the Efficient Drive of Optical Radiation Sources Based on Dielectric Barrier Discharges*. PhD thesis, KIT Scientific Publishing, Karlsruhe, 2013.

[1.28] A. El-Deib, F. Dawson, and G. Zissis, "Transformer-less current controlled driver for a dielectric barrier discharge lamp using HV silicon carbide (SiC) switching devices," in *Energy Conversion Congress and Exposition (ECCE), 2011 IEEE*, pp. 1124–1131, IEEE, Sept. 2011.

[1.29] W.-S. Lee, K.-W. Chu, C.-F. Huang, L.-S. Lee, M.-J. Tsai, K.-Y. Lee, and F. Zhao, "Design and fabrication of 4h-sic lateral high-voltage devices on a semi-insulating substrate," *IEEE Transactions on Electron Devices*, vol. 59, no. 3, pp. 754–760, 2012.

[1.30] A. Bolotnikov, P. Losee, K. Matocha, J. Glaser, J. Nasadoski, L. Wang, A. Elasser, S. Arthur, Z. Stum, P. Sandvik, Y. Sui, T. Johnson, J. Sabate, and L. Stevanovic, "3.3kV SiC MOSFETs designed for low on-resistance and fast switching," in *2012 24th International Symposium on Power Semiconductor Devices and ICs (ISPSD)*, pp. 389–392, 2012.

[1.31] J. Alonso, C. Ordiz, M. Dalla-Costa, J. Ribas, and J. Cardesin, "High voltage power supply for ozone generation based on piezoelectric transformer," in *Conference Record of the 2007 IEEE Industry Applications Conference, 2007. 42nd IAS Annual Meeting*, pp. 1901–1908, 2007.

[1.32] M. I. Lomaev, V. S. Skakun, V. F. Tarasenko, and D. V. Shitts, "Excilamps based on xenon dimers excited by a barrier discharge," *Journal of Optical Technology*, vol. 79, no. 8, pp. 498–502, 2012.

[1.33] V. F. Tarasenko, A. V. Krivonosenko, M. I. Lomaev, V. S. Skakun, E. A. Sosnin, and D. V. Shitz, "High-power excilamps with short-pulse duration," in *Proc. SPIE*, vol. 4065, pp. 826–835, 2000.

[1.34] M. Lomaev, E. Sosnin, and V. Tarasenko, "Excilamps and their applications," *Progress in Quantum Electronics*, vol. 36, pp. 51–97, Jan. 2012.

[1.35] M. I. Lomaev, E. A. Sosnin, V. F. Tarasenko, D. V. Shits, V. S. Skakun, M. V. Erofeev, and A. A. Lisenko, "Capacitive and barrier discharge excilamps and their applications (review)," *Instruments and Experimental Techniques*, vol. 49, pp. 595–616, Oct. 2006.

[1.36] A. Shams Taleghani, A. Shadaram, and M. Mirzaei, "Effects of duty cycles of the plasma actuators on improvement of pressure distribution above a NLF0414 airfoil," *IEEE Transactions on Plasma Science*, vol. 40, pp. 1434–1440, May 2012.

[1.37] S. Zhang, W. Wang, L. Jia, Z. Liu, Y. Yang, and L. Dai, "Rotational, vibrational, and excitation temperatures in bipolar nanosecond-pulsed diffuse dielectric-barrier-discharge plasma at atmospheric pressure," *IEEE Transactions on Plasma Science*, vol. 41, pp. 350–354, Feb. 2013.

[1.38] T. Kuroki, T. Oishi, T. Yamamoto, and M. Okubo, "Bromomethane decomposition using a pulsed dielectric barrier discharge," *IEEE Transactions on Industry Applications*, vol. 49, pp. 293–297, Jan. 2013.

[1.39] S. Kalisiak, M. Holub, and T. Jakubowski, "Resonant inverter with output voltage pulse-phase-shift control for DBD plasma reactor supply," in *13th European Conference on Power Electronics and Applications, 2009. EPE '09*, pp. 1–9, 2009.

[1.40] Zoran Falkenstein, USHIO America Inc., "Development of an excimer UV light source system for water treatment." `http://www.revistavirtualpro.com/files/TIE04_200701.pdf`.

[1.41] Z. Falkenstein, "Dielectric barrier discharge-driven (V)UV light source for fluid treatment," July 2002.

[1.42] Heraeus Noblelight LLC., "High power excimer UV system." `http://www.heraeus-noblelight.com/media/webmedia_local/media/pdf/uv/UVP16E_high_power_excimer_system.pdf`.

[1.43] Heraeus Noblelight LLC., "Ultraviolet light for water treatment." `http://www.heraeus-noblelight.com/media/webmedia_local/media/pdf/uv/UVP06_EN_Wasser.pdf`.

[1.44] OSRAM GmbH, "Xeradex excimer lamps." `http://www.osram.com/osram_com/applications/industrial-applications/ozone-production/index.jsp`.

[1.45] A. Voronov, "Mercury free UV-light sources based on excimer lamps," in *17th International Conference on Gas Discharges and Their Applications, 2008. GD 2008*, pp. 501–504, 2008.

[1.46] I. Soloshenko, V. Y. Bazhenov, V. A. Khomich, V. V. Tsiolko, and N. G. Potapchenko, "Comparative research of efficiency of water decontamination by UV radiation of cold hollow cathode discharge plasma versus that of low- and medium-pressure mercury lamps," *IEEE Transactions on Plasma Science*, vol. 34, no. 4, pp. 1365–1369, 2006.

[1.47] WOLFGANG HEERING, "UV SOURCES – basics, properties and applications," *IUVA NEWS*, vol. 6, pp. 7–13, Dec. 2004.

[1.48] S. Schalk, V. Adam, E. Arnold, K. Brieden, A. Voronov, and H. D. Witzke, "UV-lamps for disinfection and advanced oxidation–Lamp types, technologies and applications," *IUVA news*, vol. 8, no. 1, p. 32–37, 2006.

[1.49] Quark Technology Co. Ltd., "Products information - excimer VUV lamp." `http://www.quark-tec.com/english/product/5.html`.

[1.50] USHIO Inc., "Excimer lamps and excimer irradiation unit." `http://www.ushio.co.jp/en/products/list/lamp/lamp_10.html`.

[1.51] Resonance Ltd., "REX4 excimer lamp." `http://www.resonance.on.ca/rex4.htm`.

Bibliography for Chapter 2

[2.1] D. Flórez, R. Díez, A. Hay, G. Perilla, F. Ruiz, and H. Piquet, "Programmable current converter synthesis for the evaluation of UV radiation of excimer lamps," in *2010 IEEE ANDESCON*, pp. 1–6, 2010.

[2.2] D. Florez, R. Diez, K. Hay, and H. Piquet, "DBD excimer lamp power supply with fully controlled operating conditions," in *2012 13th International Conference on Optimization of Electrical and Electronic Equipment (OPTIM)*, pp. 1346–1352, 2012.

[2.3] H. Piquet, S. Bhosle, R. Diez, M. Cousineau, M. Djibrillah, D. Le Thanh, A. N. Dagang, and G. Zissis, "Control of the UV flux of a XeCl dielectric barrier discharge excilamp through its current variation," *Quantum Electronics*, vol. 42, pp. 157–164, Feb. 2012.

[2.4] R. Diez, H. Piquet, M. Cousineau, and S. Bhosle, "Current-mode power converter for radiation control in DBD excimer lamps," *IEEE Transactions on Industrial Electronics*, vol. 59, no. 4, pp. 1912–1919, 2012.

[2.5] R. W. Erickson and D. Maksimovic, *Fundamentals of Power Electronics*. Springer, Jan. 2001.

[2.6] J. M. Alonso, C. Ordiz, D. Gacio, J. Ribas, and A. J. Calleja, "Closed-loop regulated power supply for ozone generation based on buck converter and current-fed push-pull resonant inverter," Sept. 2009.

[2.7] F. Diaz, F. Azcondo, C. Brañas, R. Casanueva, and R. Zane, "Digitally controlled low-frequency square-wave electronic ballast with resonant ignition and power loop," *IEEE Transactions on Industry Applications*, vol. 46, no. 6, pp. 2222–2232, 2010.

[2.8] A. V. Stankovic, L. Nerone, and P. Kulkarni, "Modified synchronous-buck converter for a dimmable HID electronic ballast," *IEEE Transactions on Industrial Electronics*, vol. 59, pp. 1815–1824, Apr. 2012.

[2.9] A. L. Kirsten, M. A. Dalla Costa, C. Rech, R. N. do Prado, and T. B. Marchesan, "Digital control strategy for HID lamp electronic ballasts," *IEEE Transactions on Industrial Electronics*, vol. 60, pp. 608–618, Feb. 2013.

[2.10] M. Cousineau, R. Diez, H. Piquet, and O. Durrieu, "Synthesized high-frequency thyristor for dielectric barrier discharge excimer lamps," *IEEE Transactions on Industrial Electronics*, vol. 59, no. 4, pp. 1920–1928, 2012.

[2.11] X. Bonnin, H. Piquet, N. Naude, C. Bouzidi, N. Gherardi, and J.-M. Blaquiere, "Design of a current converter to maximize the power into homogeneous dielectric barrier discharge (DBD) devices," *The European Physical Journal Applied Physics*, July 2013.

[2.12] D. Gacio, J. Alonso, A. Calleja, J. Garcia, and M. Rico-Secades, "A universal-input single-stag2e high-power-factor power supply for HB-LEDs based on integrated buck-flyback converter," *IEEE Transactions on Industrial Electronics*, vol. 58, no. 2, pp. 589–599, 2011.

[2.13] R. Díez, J.-P. Salanne, H. Piquet, S. Bhosle, and G. Zissis, "Predictive model of a DBD lamp for power supply design and method for the automatic identification of its parameters," *The European Physical Journal - Applied Physics*, vol. 37, no. 03, pp. 307–313, 2007.

[2.14] M. I. Lomaev, V. S. Skakun, E. A. Sosnin, V. F. Tarasenko, D. V. Shitts, and M. V. Erofeev, "Excilamps efficient sources of spontaneous UV and VUV radiation," *Physics-Uspekhi*, vol. 46, pp. 193–209, Feb. 2003.

[2.15] A. El-Deib, F. Dawson, G. van Eerden, S. Bhosle, G. Zissis, and T. D. Le, "Analysis and experimental validation of a new current-controlled driver for a dielectric barrier discharge lamp," *IEEE Transactions on Industry Applications*, vol. 47, no. 4, pp. 1971–1982, 2011.

[2.16] T. C. Manley, "The electric characteristics of the ozonator discharge," *Transactions of The Electrochemical Society*, vol. 84, pp. 83–96, Oct. 1943.

[2.17] R. Diez-Medina, *Alimentation de puissance d'une lampe exciplexe à décharge à barrière diélectrique, en vue du contrôle du rayonnement.* PhD thesis, INPT, Toulouse, 2008.

[2.18] M. A. Djibrillah, *Éléments de conception d'un générateur électrique pour l'alimentation d'un dispositif à décharge à barrière diélectrique (DBD).* INPT, Apr. 2011.

[2.19] X. Bonnin, H. Piquet, D. Florez, R. Diez, and X. Bonnin, "Designing the high voltage transformer of power supplies for dbd: windings arrangment to reduce the parasitic capacitive effects," in *Power Electronics and Applications (EPE), 2013 15th European Conference on*, Sept. 2013.

[2.20] D. Florez, X. Bonnin, H. Piquet, and R. Diez, "Impact of the transformer in the current mode supply of dielectric barrier discharge excimer lamps," (Brazilian Power Electronics Conference (COBEP 2013), Gramaos, Brasil), Oct. 2013.

[2.21] L. Dalessandro, F. da Silveira Cavalcante, and J. W. Kolar, "Self-capacitance of high-voltage transformers," *IEEE Transactions on Power Electronics*, vol. 22, pp. 2081–2092, Sept. 2007.

[2.22] F. Blache, J. P. Keradec, and B. Cogitore, "Stray capacitances of two winding transformers: equivalent circuit, measurements, calculation and lowering," in , *Conference Record of the 1994 IEEE Industry Applications Society Annual Meeting, 1994*, pp. 1211–1217 vol.2, 1994.

[2.23] J. Biela and J. Kolar, "Using transformer parasitics for resonant converters - a review of the calculation of the stray capacitance of transformers," in *Industry Applications Conference, 2005. Fourtieth IAS Annual Meeting. Conference Record of the 2005*, vol. 3, pp. 1868–1875 Vol. 3, 2005.

Bibliography for Chapter 3

[3.1] Haruaki Akashi, Akinori Odam, and Yosuke Sakai, "Effect of gas heating on excimer distribution in DBD xe excimer lamp," in *28th ICPIG Conference Records*, (Prague, Czech Republic), July 2007.

[3.2] F. Marchal, N. Sewraj, G. Jabbour, P. R. Akerreta, and G. Ledru, "Temperature dependence of xenon excimer formations using two-photon absorption laser-induced fluorescence," *Journal of Physics B: Atomic, Molecular and Optical Physics*, vol. 43, p. 235210, Dec. 2010.

[3.3] R. J. Carman and R. P. Mildren, "Computer modelling of a short-pulse excited dielectric barrier discharge xenon excimer lamp (172 nm)," *Journal of Physics D: Applied Physics*, vol. 36, pp. 19–33, Jan. 2003.

[3.4] M. I. Lomaev, V. S. Skakun, V. F. Tarasenko, and D. V. Shitts, "Excilamps based on xenon dimers excited by a barrier discharge," *Journal of Optical Technology*, vol. 79, no. 8, pp. 498–502, 2012.

[3.5] S. Bhosle, G. Zissis, J.-J. Damelincourt, A. Capdevila, K. Gupta, F. Dawson, and V. Tarasenko, "Implementation of an efficiency indicator in an electrical modeling of a dielectric barrier discharge lamp," in *Conference Record of the 2006 IEEE Industry Applications Conference, 2006. 41st IAS Annual Meeting*, vol. 4, pp. 1784–1790, 2006.

[3.6] A. Lopez, H. Piquet, D. Patino, R. Diez, and X. Bonnin, "Parameters identification and gas behavior characterization of DBD systems," *IEEE Transactions on Plasma Science*, vol. 41, no. 8, pp. 2335–2342, 2013.

[3.7] Hartnett, James, *Transport Phenomena in Plasma.* Academic Press, Oct. 2007.

[3.8] U. Kogelschatz, "Dielectric-barrier discharges: Their history, discharge physics, and industrial applications," *Plasma Chemistry and Plasma Processing*, vol. 23, no. 1, pp. 1–46, 2003.

[3.9] M. I. Lomaev, V. S. Skakun, E. A. Sosnin, V. F. Tarasenko, D. V. Shitts, and M. V. Erofeev, "Excilamps efficient sources of spontaneous UV and VUV radiation," *Physics-Uspekhi*, vol. 46, pp. 193–209, Feb. 2003.

[3.10] A. M. Razhev and A. A. Zhupikov, "Influence of the specific pump power on the output energy and efficiency of a 223-nm gas-discharge-pumped excimer KrCl laser," *Quantum Electronics*, vol. 38, p. 1005, Nov. 2008.

[3.11] A. M. Boichenko, "The effect of the excitation power on the emission efficiency of barrier- and glow-discharge pumped exciplex and excimer lamps," *Laser Physics*, vol. 14, no. 8, pp. 1036–1044, 2004.

Bibliography for Chapter 4

[4.1] R. Diez, H. Piquet, and S. Bhosle, "Control of the UV emission of an excimer lamp by means of a current-mode power supply," in *Industrial Electronics, 2009. IECON '09. 35th Annual Conference of IEEE*, pp. 3500–3505, IEEE, Nov. 2009.

[4.2] H. Piquet, S. Bhosle, R. Diez, and M. V. Erofeev, "Pulsed current-mode supply of dielectric barrier discharge excilamps for the control of the radiated ultraviolet power," *IEEE Transactions on Plasma Science*, vol. 38, pp. 2531–2538, Oct. 2010.

[4.3] Y. Chéron, C. Goodman, and T. Meynard, *Soft commutation*. London [u.a.: Chapman & Hall, 1992.

[4.4] R. Casanueva, F. J. Azcondo, and S. Bracho, "Series–parallel resonant converter for an EDM power supply," *Journal of Materials Processing Technology*, vol. 149, pp. 172–177, June 2004.

[4.5] R. Casanueva, F. Azcondo, and C. Brañas, "Output current sensitivity analysis of the resonant inverter: Current-source design criteria," *IEEE Transactions on Industrial Electronics*, vol. 54, no. 3, pp. 1560–1568, 2007.

[4.6] R. Oruganti and F. Lee, "Resonant power processors, part I—State plane analysis," *IEEE Transactions on Industry Applications*, vol. IA-21, no. 6, pp. 1453–1460, 1985.

[4.7] T. C. Manley, "The electric characteristics of the ozonator discharge," *Transactions of The Electrochemical Society*, vol. 84, pp. 83–96, Oct. 1943.

[4.8] M. Cousineau, R. Diez, H. Piquet, and O. Durrieu, "Synthesized high-frequency thyristor for dielectric barrier discharge excimer lamps," *IEEE Transactions on Industrial Electronics*, vol. 59, no. 4, pp. 1920–1928, 2012.

[4.9] X. Bonnin, H. Piquet, D. Florez, R. Diez, and X. Bonnin, "Designing the high voltage transformer of power supplies for dbd: windings arrangment to reduce the parasitic capacitive effects," in *Power Electronics and Applications (EPE), 2013 15th European Conference on*, Sept. 2013.

[4.10] Wheeler, H.A., "Simple inductance formulas for radio coils," in *Proc. I.R.E*, vol. 16, p. 1398, Oct. 1928.

Bibliography for Chapter 5

[5.1] R. Diez, H. Piquet, S. Bhosle, and J.-M. Blaquiere, "Current mode converter for dielectric barrier discharge lamp," in *IEEE Power Electronics Specialists Conference, 2008. PESC 2008*, pp. 2485–2491, 2008.

[5.2] H. Piquet, S. Bhosle, R. Diez, and M. V. Erofeev, "Pulsed current-mode supply of dielectric barrier discharge excilamps for the control of the radiated ultraviolet power," *IEEE Transactions on Plasma Science*, vol. 38, pp. 2531–2538, Oct. 2010.

[5.3] R. Diez, H. Piquet, M. Cousineau, and S. Bhosle, "Current-mode power converter for radiation control in DBD excimer lamps," *IEEE Transactions on Industrial Electronics*, vol. 59, no. 4, pp. 1912–1919, 2012.

[5.4] R. Diez, H. Piquet, S. Bhosle, J.-M. Blaquiere, and N. Roux, "Design of a current converter for the study of the UV emission in DBD excilamps," in *IEEE International Symposium on Industrial Electronics, 2008. ISIE 2008*, pp. 62–67, 2008.

A. Appendix. Résumé de la Thèse en Français

Table des matières

Introduction

Cette thèse est développée dans le cadre d'un projet de recherche qui vise à la conception et la mise en oeuvre d'un prototype du système de désinfection de l'eau, sur la base du rayonnement UV généré par une lampe à excimères à décharge à barrière diélectrique ou "excilampe DBD". Ce projet est soutenu par COLCIENCIAS, ICETEX, et le programme de cooperation Franco-Colombien ECOS-NORD.

Par rapport aux autres sources artificielles de rayonnement UV (Fig.0.1), les excilampes DBD présentent des particularités bien adaptées aux besoins de diverses applications :

- elles sont exemptes de mercure. Par conséquent elles peuvent être utilisées dans des environnements où la présence de mercure est dangereuse, par exemple dans l'industrie alimentaire et la production de médicaments.
- Les électrodes ne sont pas en contact avec le gaz. Par conséquent, à la différence des lampes à décharge classiques, les électrodes ne sont pas altérées par la décharge.
- Allumage instantané. Cela implique une disponibilité immédiate, sans temps préalable de chauffage.
- Elles offrent une surface de rayonnement large du fait de leur géométrie.
- La longueur d'onde du rayonnement est très précise et dépend principalement de la composition du gaz, qui peut être choisie en fonction du micro-organisme à traiter ou des particularités de l'application.

Cependant, aujourd'hui les mécanismes et les phénomènes sur lesquels repose la la technologie des excilamps DBD ne sont pas totalement expliqués et compris, par exemple :

- La corrélation entre l'efficacité de la lampe, du point de vue du rayonnement, et le point de fonctionnement électrique de la lampe n'a pas été clairement établi
- Une connaissance plus approfondie de l'impact des conditions de fonctionnement (de l'intensité du courant , de la tension de fonctionnement , de la fréquence, etc) dans les excilampes existantes et dans leurs modèles électriques équivalents, est

FIGURE 0.1: Sources de rayonnement UV. De gauche à droite : LED [0.1], HID Mercury-vapor lamp [0.2], HID Xenon lamp [0.3] and DBD excimer lamp

nécessaire.
– L'efficacité des alimentations DBD peut être améliorée grâce à l'optimisation du
  bloc d'alimentation qui produit la puissance fournie à la lampe et l'optimisation du
  point de fonctionnement, tenant compte des caractéristiques des excilampes DBD
  et des composants parasites des éléments du système.
On peut attendre de progrès effectués dans ces directions les avantages suivants :
– Plus de rayonnement UV pourrait être obtenu avec moins d'énergie électrique, ce
  qui est particulièrement important pour les applications de décontamination envisa-
  gées, car ceci faciliterait la connexion à une source d'énergie renouvelable de faible
  puissance.
– La puissance de la lampe UV par unité de surface pourrait être augmentée, ce qui
  réduirait la taille de la lampe DBD à excimère.
– Un modèle équivalent de la lampe plus adapté pourrait être mis au point pour une
  conception plus fiable du système et des alimentations plus efficaces.
– cette démarche pourrait aider á une meilleure compréhension des mécanismes physico-
  chimiques des excimères.

Objectives   Dans le contexte du projet de recherche et sur la base des idées exposées
plus haut concernant la technologie des excilampes à DBD, cette thèse de doctorat est
orientée en vue de l'amélioration de la performance des excilampes à DBD en tant que
source UV, à travers l'étude des performances intrinsèques de la lampe, des interactions
alimentation-lampe et le développement d'une nouvelle alimentation à haute efficacité.
Dans ce sens, les objectifs proposés sont les suivants :
– Le développement d'une alimentation électrique adaptée à la lampe excimère UV,
  capable de contrôler la puissance de la lampe et le point de fonctionnement au moyen
  de trois degrés de liberté caractéristiques du courant de la lampe : la fréquence de
  fonctionnement, l'amplitude et le rapport cyclique.
– la détermination du point de fonctionnement optimal de la lampe, en adoptant le
  point de vue de la conversion de l'énergie électrique à la puissance de rayonnement
  UV,.
– Le développement, la mise en œuvre et la validation d'une alimentation destinée à
  maintenir le système au point optimal de fonctionnement de la lampe, et à maximiser
  la performance de l'offre vis-à-vis : - de l'efficacité électrique. - du couplage au
  réseau électrique ou à une source d'énergie renouvelable (photovoltaïque, micro-
  hydroélectrique).

Bibliographie

[0.1] NICHIA CORPORATION, "UV-LED." `http://www.nichia.co.jp/en/product/uvled.html`, 2013.

[0.2] OSRAM GmbH, "PURITEC HNS germicidal ultraviolet lamps." `http://www.osram.com/osram_com/products/lamps/specialty-lamps/ultraviolet-lamps/puritec-hns/index.jsp?productId=ZMP_86446`.

[0.3] Xenon corporation, "About xenon flashlamps." `http://www.xenoncorp.com/lamps.html`, 2013.

1 Contrôle Paramétrique de la Puissance Électrique d'une Excilamp DBD

En conformité avec les objectifs proposés pour cette recherche doctorale, le premier travail est axé sur le développement théorique et la mise en œuvre d'un générateur électrique avec sortie en courant et forme d'onde carrée, capable de contrôler la puissance injectée dans une excilamp DBD.

1.1 Contrôle de la Puissance Avec Trois Dégrées de Liberté

Afin d'approfondir sur les résultats des études antérieures et pour analyser la relation entre le courant injecté dans la lampe et son rayonnement UV, nous proposons d'alimenter la lampe DBD avec un courant en créneaux définis par trois degrés de liberté : amplitude (J), fréquence (f_{lp}) et rapport cyclique (D_{lp}), tel que présenté dans la Fig.1.1.

Ce courant doit avoir une valeur moyenne nulle pour éviter une croissance indéterminée de la tension de la lampe. Dans le même Fig.1.1, les tensions de la lampe (v_{lp}), des barrières diélectriques (v_{Cd}) et du gaz (v_{Cg}) sont calculées à l'aide du modèle présenté à la Fig.1.2. Avec la forme d'onde de courant en créneaux et le modèle équivalent de la lampe, l'expression mathématique pour la puissance électrique de la lampe est déduite :

$$P_{lp} = JD_{lp}V_{th} - 4f_{lp}C_gV_{th}^2 \tag{1.1.1}$$

Cette équation montre que la puissance électrique de la lampe peut être ajustée de manière efficace avec les trois degrés de liberté : J, f_{lp} and D_{lp}.

En plus, en utilisant le modèle électrique équivalent de la lampe, sa tension crête peut être déduite en fonction de la puissance électrique injectée :

$$\hat{V}_{lp} = \frac{P_{lp}}{4f_{lp}V_{th}C_d} + \frac{V_{th}C_g}{C_{eq}} \tag{1.1.2}$$

Pour générer le courant proposé, un convertisseur composé de deux blocs principaux connectés en cascade est utilisé : une source de courant constant et un onduleur à structure en pont complet (Fig.1.3).

1.1.1 Fonctionnement de l'Onduleur de Courant

La sortie de la source de courant DC, *iout*, est reliée directement à cet onduleur (Fig.1.3) et la direction du courant de la lampe, i_{lp}, est déterminée par la séquence de commutation du pont complet. Avec seulement les interrupteurs (S1, S4) allumés,
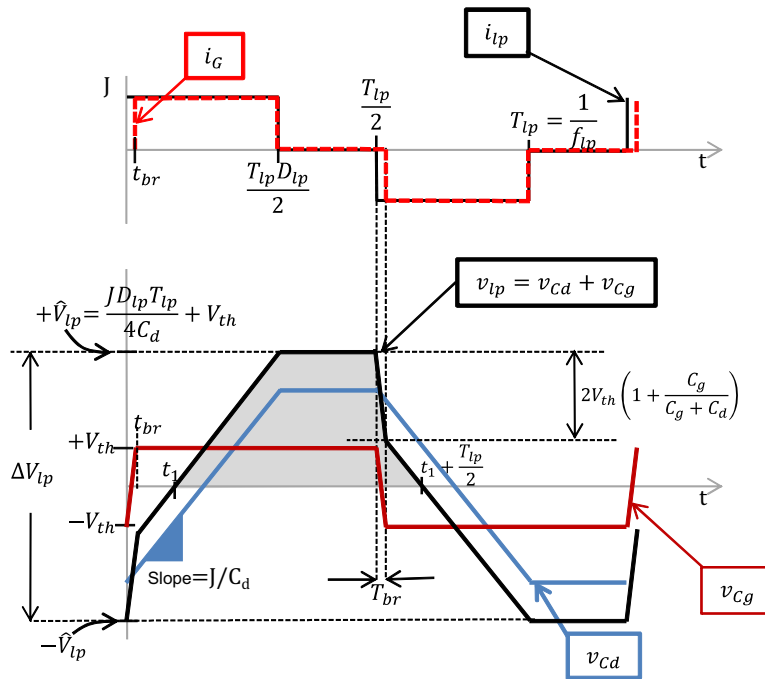
FIGURE 1.1: Forme d'onde du courant injecté dans la lampe i_{lp}, du courant de la conductance i_G (en haut) et de la tension (en bas), calculées sur la base du modèle éclectique de la lampe.

le courant de la lampe circule dans le sens positif ; en mettant en conduction la paire d'interrupteurs (S3, S2), le courant dans la lampe aura la direction opposée. Afin d'avoir un courant nul dans la lampe, sans interrompre le trajet du courant *iout*, l'une des paires suivantes (S1, S2) ou (S3, S4) est mise en conduction. De cette manière f_{lp} est égale à
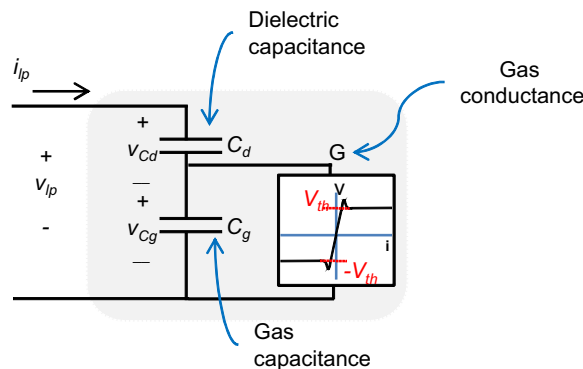

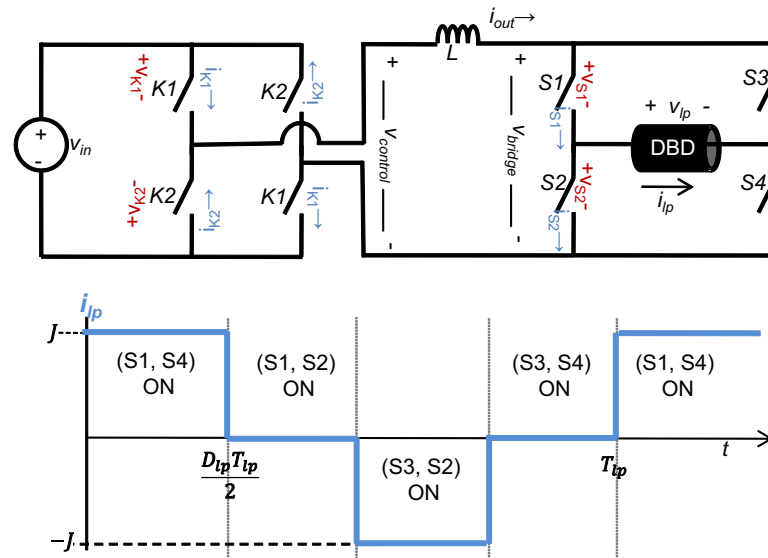FIGURE 1.2: Modelé électrique équivalent de la lampe DBD à excimères

FIGURE 1.3: Topologie du générateur pour DBD, construit sur la base de l'hacheur à deux quadrants

la fréquence de fonctionnement du pont.

À partir de l'analyse des conditions de commutation, on déduit que les interrupteurs ont un amorçage commandé sous tension positive et un blocage spontanée à l'annulation de leur courant. Ces propriétés définissent un dispositif du type thyristor comme décrit en [1.1]. Pour mettre en œuvre ce type d'interrupteur, un dispositif MOSFET en série avec une diode est utilisé.

1.1.2 Source de Courant Continue

En considérant que la tension aux bornes de sortie de la source de courant, v_{bridge}, est une tension bipolaire, une configuration pratique pour mettre en œuvre la source de courant continu est la topologie du hacheur de deux-quadrants [1.2] (Fig.1.3).

Une charge de type DBD présente des transitions rapides de haute tension. Pour cette raison, et à cause de sa robustesse bien connue et de sa réponse rapide, la loi de contrôle par hystérésis est un bon choix pour mettre en œuvre le contrôleur de la source de courant continue.

Compte tenu que la fréquence de fonctionnement typique des excilampes est de l'ordre de centaines de kHz, si f_c est définie supérieur à f_{lp} ceci impliquerait l'utilisation de dispositifs à commutation à des fréquences de l'ordre du MHz causant des pertes par commutation élevées. En conséquence, le fonctionnement de la commande à hystérésis est choisi tel que $f_c < f_{lp}$.

La valeur minimale de L, afin d'obtenir une valeur de f_c toujours inférieure à la fréquence maximale souhaitée du contrôleur hystérésis, f_{cmax} est donnée par :

$$L = \frac{V_{in}}{2 f_{cmax}(\Delta hyst)} \tag{1.1.3}$$

D'autre part, pour trouver la valeur de V_{in} nécessaire pour assurer un contrôle de i_{out}, on considère la valeur maximale de la moyenne de v_{bridge}. Le pire des cas est obtenu pour $\bar{V_{bridge}} = V_{th}$. Donc V_{in} doit être sélectionnée plus grande que V_{th}.

Avec la caractéristique tension-courant pour les interrupteurs K1 et K2, pour K1 on obtient une tenue en tension bidirectionnelle, avec amorçage sous tension positive et une conduction de courant unidirectionnel positif. En conséquence, les fonctions thyristor nécessaires sont réalisées par des associations série de MOSFET et diode.

1.2 Considérations Relatives à la Mise en œuvre

Les paramètres électriques équivalents de l'excilamp DBD utilisée dans cette recherche sont présentés dans le tableau 1.1 Ces valeurs sont utilisées pour dimensionner les composants du générateur et pour établir les limites acceptables des trois degrés de liberté (J, f_{lp}, D_{lp}).

V_{th}	C_d	C_g	P_{lp}
1310 V	85 pF	27 pF	100 W

TABLE 1.1: Paramétrés électriques équivalents pour une excilamp DBD XeCl

f_{lp} varie de 50 kHz à 200 kHz ; cette gamme a été sélectionnée sur la base des résultats antérieurs présentés dans [1.3]pp.203, [1.4]pp.1917 et [1.5]pp.1980.

Selon les caractéristiques de la lampe excimère DBD (tableau 1.1), pour fournir 100 W de puissance électrique à $f_{lp} = 50$kHz et $D_{lp} = 90\%$, un maximum $\hat{V}_{lp}$ de 6,2 kV et un J de 92 mA sont calculés en utilisant (1.1.2) et (1.1.1) respectivement. La Fig.1.4 présente la puissance P_{lp} obtenue pour différentes valeurs de $\hat{V}_{lp}$ en fonction de la fréquence.

Actuellement la technologie MOSFET disponible commercialement ne peut pas tolérer la tension de crête de 6.2 kV, ce qui conduit à l'utilisation d'un transformateur élévateur entre l'onduleur en pont complet et la lampe excimère. Après une évaluation de leur disponibilité et performances, les MOSFET spécifiés pour un 1 kV de tension drain-source, sont pris en compte pour la mise en œuvre du générateur.

Le transformateur, avec ses composants parasites, introduit de nouveaux éléments dans le circuit du générateur. La capacité parasite C_p apparaît en parallèle à la lampe (Fig.1.5). Compte tenu de la nature capacitive de la lampe excimère, si C_p est comparable à la capacité équivalente de la lampe, une quantité importante du courant injecté dans l'enroulement primaire iprim s'écoule à travers C_p, ce qui affecte la forme d'onde et l'amplitude de i_{lp} et même peut empêcher l'allumage de la lampe.

L'inductance de fuite du transformateur, L_{lk}, détermine le temps de montée et de descente des créneaux de courant. En supposant une tension V_{prim} constante au cours de l'intervalle de temps de chevauchement dans laquelle S1, S4 et S2 sont à l'état de conduction, le temps qu'il faut pour i_{out} pour changer sa valeur de J à zéro est T_{lk} :
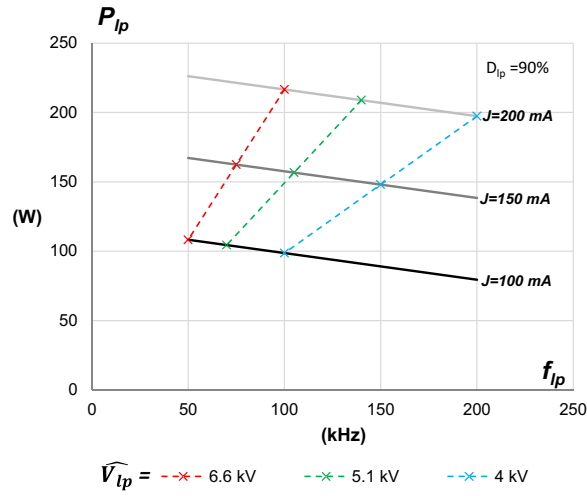
FIGURE 1.4: Puissance de la lampe en fonction de la fréquence du courant de la lampe, pour différentes valeurs de $\hat{V}_{lp}$.

$$T_{lk} = \frac{nI_{out}L_{lk}}{\hat{V}_{lp}} \tag{1.2.1}$$

Où n est le rapport des tours du transformateur.

Comme le montre la figure Fig.1.5, l'inductance magnétisante L_m apparaît comme une branche parallèle qui dérive une partie du courant qui doit être injecté dans la lampe. Ainsi, le courant transféré à l'enroulement primaire du transformateur idéal est égal au courant de sortie de l'onduleur i_{out}, moins le courant de magnétisation i_m. Cette forme d'onde de courant peut être fortement affectée si L_m présente une faible valeur.

D'après les idées exposées avant et comme on peut s'y attendre à partir du modèle du transformateur idéal, L_m doit être maximisé et C_p minimisé afin de réduire leur impact sur le fonctionnement du circuit. Afin d'obtenir des valeurs plus élevées de L_m le nombre
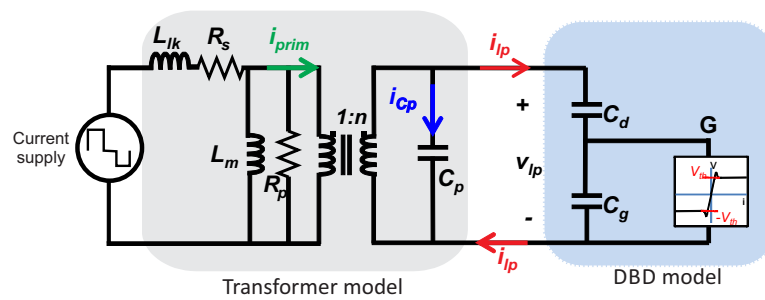

FIGURE 1.5: Modèle du transformateur avec les éléments parasites

de tours du transformateur doit être élevée et en revanche, comme l'a démontré [1.6], [1.7], un nombre élevé de tours augmente la valeur de C_p. Pour obtenir un équilibre entre ces critères opposés, la valeur minimale possible du rapport de transformation doit être sélectionné.

1.3 Sélection des Composants

Pour minimiser C_p, le primaire et les enroulements secondaires sont limités à une seule couche. En raison de sa grande longueur effective, la géométrie choisie est E80/38/20. Cela fait environ 300 tours à être montés en utilisant une seule couche dans l'enroulement secondaire ce qui implique près de 30 tours sur le côté primaire. Les caractéristiques du transformateur sont résumées dans le tableau 1.2.

Parce que la lampe à excimères sous test est destinée à des appareils de décontamination de l'eau, la connexion d'un électrode de la lampe à la terre est nécessaire pour assurer un bon niveau de sécurité. En raison de la connexion de l'une des bornes de l'enroulement secondaire à la masse, la différence de tension entre le secondaire et l'enroulement primaire produit un flux de courant à travers C_1.

Afin de réduire l'impact de la connexion à la masse d'une des bornes du secondaire, la capacité parasite entre les enroulements, C_1, et la capacité parasite C_p doivent être réduites. De cette façon, le diviseur de courant constitué par C_{1p} et C_p dévie moins de courant, et l'allumage de la lampe peut être réalisée (Fig.1.6). Ceci est accompli en augmentant la distance d'isolement entre les enroulements [1.8].
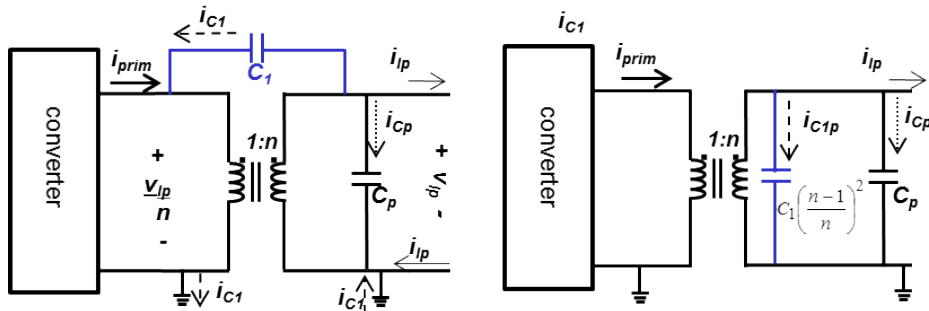

FIGURE 1.6: Modèle du transformateur pour expliquer l'effet de la connection à la masse

En conséquence, la bobine du côté primaire est enroulée en premier lieu, sur une couche d'isolation d'acrylique de 2 mm disposée entre les bobines et le noyau. La couche suivante est un bouclier de 3 mm d'acrylique ($\epsilon = 2.7$ @ 1 MHz). Autour de cette couche, la bobine du côté secondaire est enroulée (Fig.1.7).

Les valeurs des éléments parasites du transformateur ont été obtenues expérimentalement en utilisant un analyseur de réponse en fréquence relié au côté primaire du transformateur. Ces valeurs sont résumés dans la Fig.1.8. Une tension d'entrée DC de
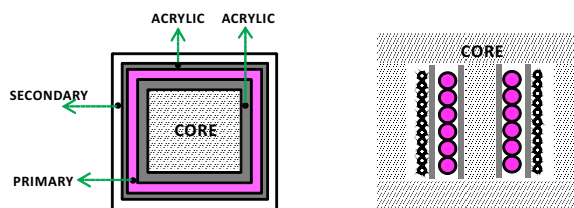
FIGURE 1.7: Vue transversale de la disposition des bobines pour la nouvelle structure de transformateur

170 V a été sélectionné. Avec cette tension d'entrée, pour obtenir une ondulation de courant maximum de 10% et une fréquence maximale de fonctionnement du contrôleur de 40 kHz, une valeur d'inductance de 28 mH a été calculée.

Une inductance de 30 mH a été construite avec deux noyaux de ferrite U référence U93/76/30 3C90 de *Ferroxcube*, avec une longueur d'entrefer de 1 mm et 540 tours. Les interrupteurs K1 sont mis en œuvre avec des MOSFET à haute puissance (P8NK100Z, VDSS 1kV, ID=6.5A) et les interrupteurs K2 avec des diodes de récupération rapide (STTH512D, VRRM=1.2kV, IF=5A). Les commutateurs du type thyristors de l'onduleur sont mis en œuvre avec la connexion d'un diode en série avec un transistor MOSFET. Les références des semiconducteurs utilisés sont les mêmes pour le hacheur deux quadrants.

Primary turns	Primary wire	Secondary turns	Secondary wire	Core
28	LITZ 81 strands x 38 AWG 0.00797 mm2	280	Single copper 33 AWG 0.0254 mm2	Material : 3F3 Size : E80-38-20 (Ferroxcube)

TABLE 1.2: Materiaux utilisés et characteristiques de la construction du transformateur

1.4 Résultats de l'Implémentation

Pour définir le point de fonctionnement souhaité (J, f_{lp}, D_{lp}), une interface utilisateur installée sur ordinateur personnel a été élaboré. Depuis l'ordinateur, les trois paramètres du point de fonctionnement désiré sont communiqués à un processeur de signal numérique (DSP, Fig.1.8). Ce DSP génère les signaux de commande des interrupteurs de l'onduleur et les limites de l'hystérésis du contrôleur de la source de courant.

Dans la figure Fig.1.9 i_{out} est maintenue constante à sa valeur maximale (3A) et le rapport cyclique est ajustée pour atteindre une tension crête de la lampe de 5 kV, pour trois valeurs différentes de f_{lp}. Pour les trois points de fonctionnement, la forme d'onde du courant de lampe est conservée, comme on peut vérifier dans la Fig.1.9. Sur la Fig.1.9 on peut voir que comme prévu selon l'équation (1.1.2), en augmentant la
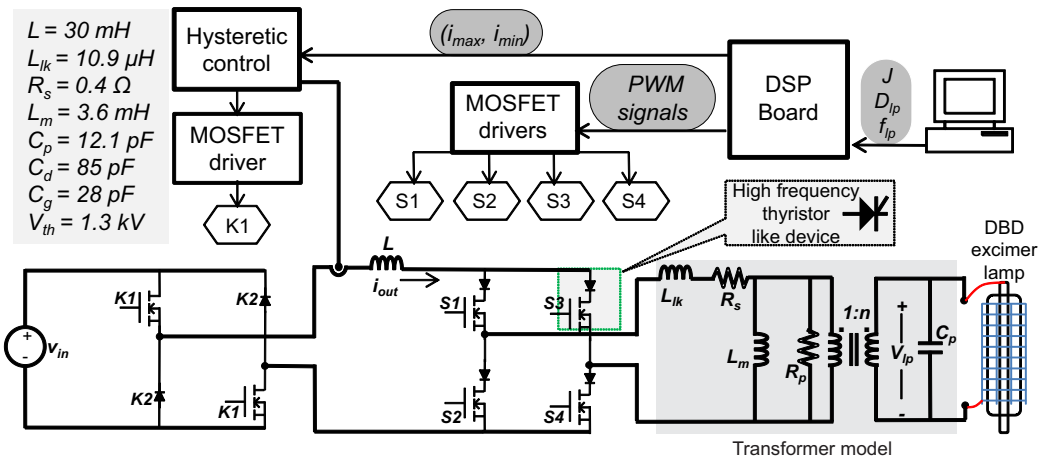
FIGURE 1.8: Diagramme de blocs de l'implémentation de la source d'alimentation pour DBD avec sortie du courant en créneaux.

fréquence de fonctionnement plus de puissance peut être injectée dans la lampe pour la même tension de sortie. La puissance électrique maximale atteinte est de 237 W. Les oscillations à haute fréquence (2,5 MHz) sont expliqués par la résonance entre L_{lk} et les capacités équivalentes des interrupteurs. Les conditions d'exploitation pour chaque point de fonctionnement sont indiquées dans le tableau 1.3.

$f_{lp}(kHz)$	$D_{lp}(\%)$	$P_{UV}(mW/cm^2)$	$P_{lp}(W)$	$P_{in}(W)$	$\eta(\%)$
50	27	32.3	97	215	45
100	60	54.6	180	310	58
150	87	58.6	237	350	68

TABLE 1.3: L'efficacité du convertisseur pour différentes fréquences de fonctionnement de l'onduleur, avec $\hat{V}_{lp}$=5 kV and J=250 mA

La réponse instantanée du rayonnement UV est également présentée sur la figure Fig.1.9. Il est possible de voir que le rayonnement UV instantanée suit la valeur absolue du courant de la lampe. Sur la base de ce test expérimental, on a démontré que la puissance moyenne, l'intensité, la durée et la fréquence des impulsions de rayonnement UV peuvent être contrôlés avec les degrés de liberté du générateur proposée.
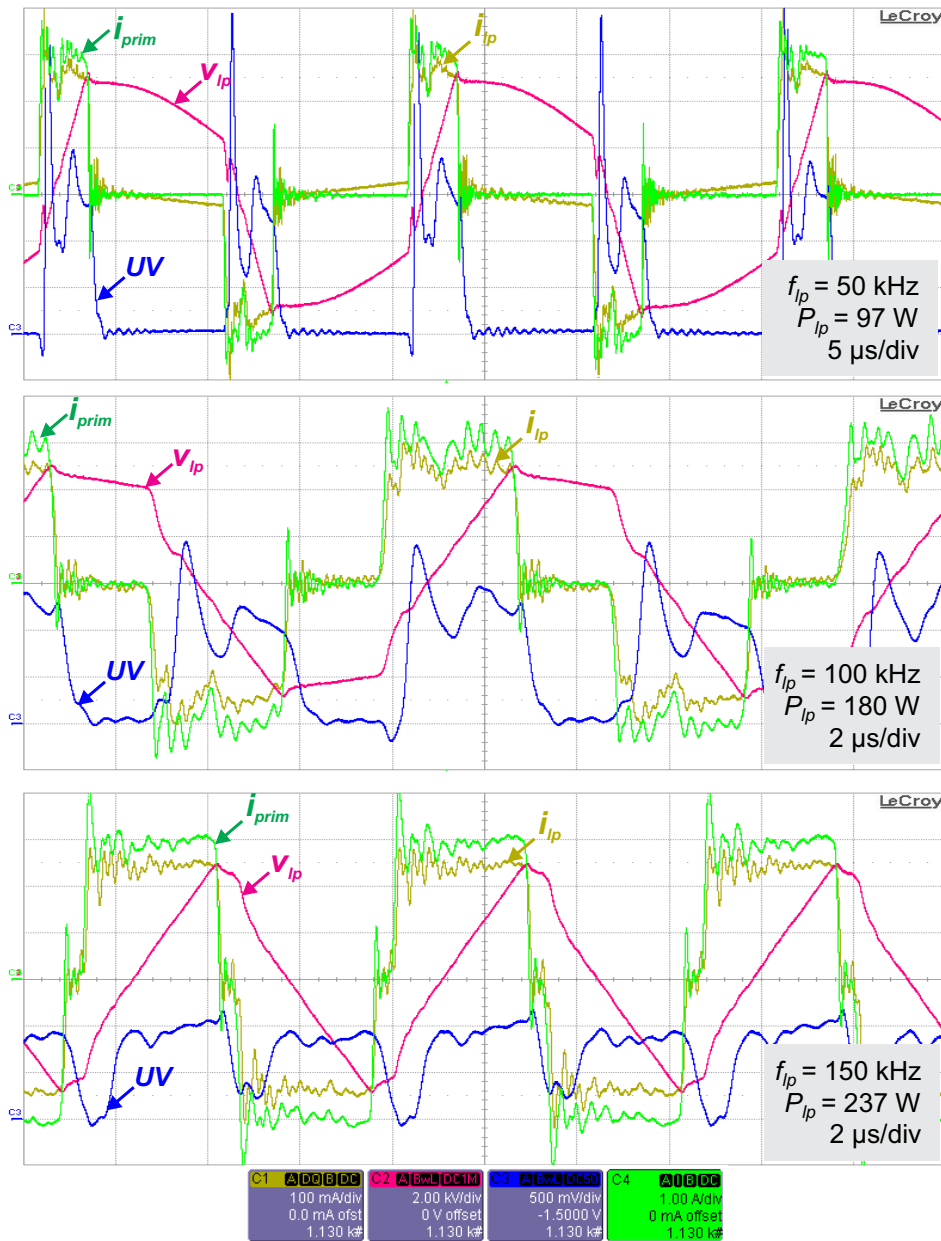
FIGURE 1.9: Lamp voltage, current and UV instantaneous response, for three operating points near to the maximum output voltage and current of the converter.

1.5 Conclusions

Avec l'alimentation en mode courant proposée, la puissance électrique et le rayonnement UV d'une excilamp DBD peuvent être ajustés de manière efficace, en utilisant la commande du courant de la lampe à l'aide de trois degrés de liberté : Amplitude, fréquence et rapport cyclique.

Grâce à l'utilisation de ce générateur, un procédé approprié pour étudier le rayonnement UV des lampes DBD à excimères , est démontrée. Le test expérimental de fonctionnement de ce convertisseur, effectué avec un excilamp DBD XeCl, a montré que le modèle de la lampe utilisée pour la conception convertisseur est approprié.

Bibliographie

[1.1] M. Cousineau, R. Diez, H. Piquet, and O. Durrieu, "Synthesized high-frequency thyristor for dielectric barrier discharge excimer lamps," *IEEE Transactions on Industrial Electronics*, vol. 59, no. 4, pp. 1920–1928, 2012.

[1.2] X. Bonnin, H. Piquet, N. Naude, C. Bouzidi, N. Gherardi, and J.-M. Blaquiere, "Design of a current converter to maximize the power into homogeneous dielectric barrier discharge (DBD) devices," *The European Physical Journal Applied Physics*, July 2013.

[1.3] M. I. Lomaev, V. S. Skakun, E. A. Sosnin, V. F. Tarasenko, D. V. Shitts, and M. V. Erofeev, "Excilamps efficient sources of spontaneous UV and VUV radiation," *Physics-Uspekhi*, vol. 46, pp. 193–209, Feb. 2003.

[1.4] R. Diez, H. Piquet, M. Cousineau, and S. Bhosle, "Current-mode power converter for radiation control in DBD excimer lamps," *IEEE Transactions on Industrial Electronics*, vol. 59, no. 4, pp. 1912–1919, 2012.

[1.5] A. El-Deib, F. Dawson, G. van Eerden, S. Bhosle, G. Zissis, and T. D. Le, "Analysis and experimental validation of a new current-controlled driver for a dielectric barrier discharge lamp," *IEEE Transactions on Industry Applications*, vol. 47, no. 4, pp. 1971–1982, 2011.

[1.6] F. Blache, J. P. Keradec, and B. Cogitore, "Stray capacitances of two winding transformers : equivalent circuit, measurements, calculation and lowering," in , *Conference Record of the 1994 IEEE Industry Applications Society Annual Meeting, 1994*, pp. 1211–1217 vol.2, 1994.

[1.7] J. Biela and J. Kolar, "Using transformer parasitics for resonant converters - a review of the calculation of the stray capacitance of transformers," in *Industry Applications Conference, 2005. Fourtieth IAS Annual Meeting. Conference Record of the 2005*, vol. 3, pp. 1868–1875 Vol. 3, 2005.

[1.8] X. Bonnin, H. Piquet, D. Florez, R. Diez, and X. Bonnin, "Designing the high voltage transformer of power supplies for dbd : windings arrangment to reduce the parasitic capacitive effects," in *Power Electronics and Applications (EPE), 2013 15th European Conference on*, Sept. 2013.

2 Étude Paramétrique de l'Impact du Point de Fonctionnement sur le rendement de l'Excilamp DBD

Dans le chapitre précédent, une alimentation utile pour l'étude des excilampes à DBD a été présentée. L'exploitation de ce convertisseur est couvert ici.

2.1 Conditions de Mesure

L'excilampe UV à DBD en cours de test a une géométrie cylindrique coaxiale et est remplie avec un mélange gazeux XeCl. Le rayonnement UV émis par cette excilamp DBD est mesuré à l'aide du banc expérimental illustré sur la Fig.2.1. La réponse instantanée de l'UV est acquise avec un photo-detecteur THORLABS PDA-25K ; la puissance de radiation UV avec un radiomètre GIGAHERTZ-OPTIK P-9710. Du fait que l'augmentation de la température dans la lampe a un impact négatif sur la production d'UV [3.1], dans nos expériences la température externe de la lampe est toujours la même à l'instant d'allumage.

2.2 Impact de l'Intensité du Courant

Dans la Fig.2.2 lavariation de la puissance de rayonnement UV en fonction de la puissance électrique injectée, est présentée. Chaque ligne de tendance correspond à une
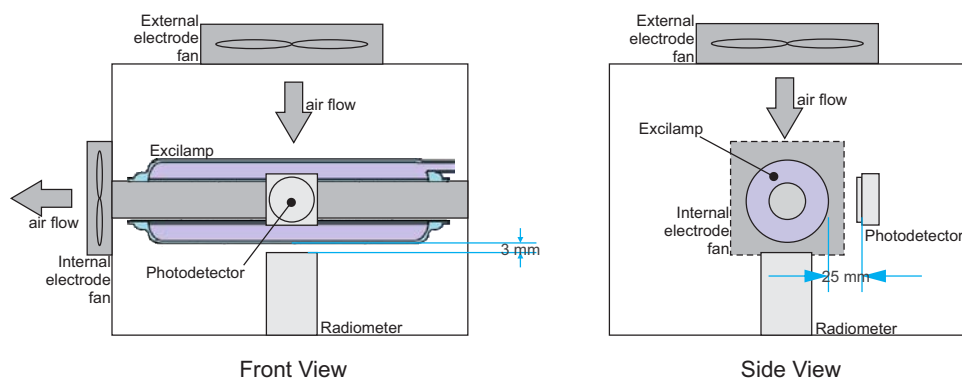

FIGURE 2.1: Illustration du banc d'essais utilisé

intensité différente J : 67, 128, 189 et 250 mA, où la puissance est ajustée avec D_{lp}. Chaque figure montre les courbes pour une fréquence de fonctionnement différent.

Dans la Fig.2.2-gauche la puissance UV obtenue pour le test effectué à $f_{lp} = 50$ kHz est affichée. A partir de ce résultat, une augmentation de la production UV de la lampe, pour une même puissance électrique injectée, est obtenue en augmentant J de 67 mA à 128 mA. Cette augmentation correspond à un gain d'au plus 25 % dans la sortie du rayonnement UV obtenu pour les mêmes valeurs de P_{lp}. Lorsque l'intensité de l'impulsion de courant est augmentée de 129 mA à 189 mA, la tendance à la hausse dans la performance de la lampe est toujours constaté, mais pour J de valeur supérieure à 189 mA le gain diminue. Pour des valeurs supérieures de f_{lp} cet impact positif de l'intensité du courant dans la production d'UV est aussi vérifié.

Á partir de la Fig.2.3 une forte corrélation de l'intensité du courant de la lampe et de l'amplitude des impulsions UV est vérifié. Pour la plage de fonctionnement de l'essai, une fois que l'allumage de la lampe est produit le rayonnement UV est émis sans interruption, tant que le courant continue à être injecté dans la lampe.

En utilisant les figures de Lissajous construits avec la trajectoire Charge-Tension de la lampe, un calcul graphique des paramètres électriques équivalents a été réalisé [3.2, p. 12]. Les valeurs moyennes des paramètres obtenus, présentés dans le tableau 2.1, peuvent être utilisés pour la conception des alimentations.

Pour une excitation à puissance et fréquence constante, les décharges dans la lampe devient plus filamentaires à mesure que l'intensité du courant augmente ; ceci peut être observé dans les images de la Fig.2.4. Ainsi l'existence de filaments bien définis peut être
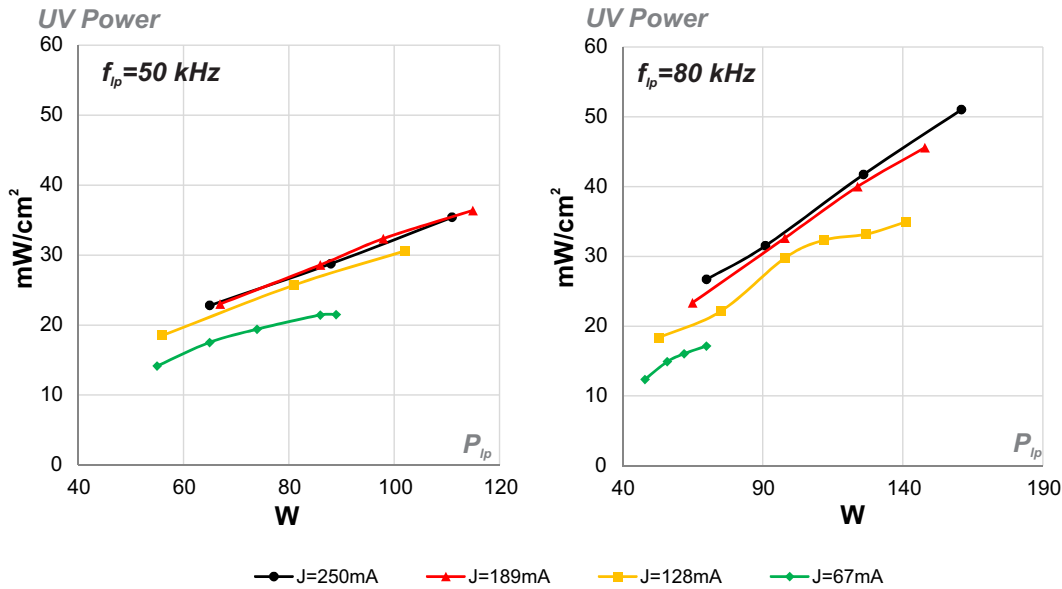

FIGURE 2.2: Impact de l'intensité du courant dans la puissance UV pour f_{lp}=50 kHz (gauche) et f_{lp}=80 kHz (droite)
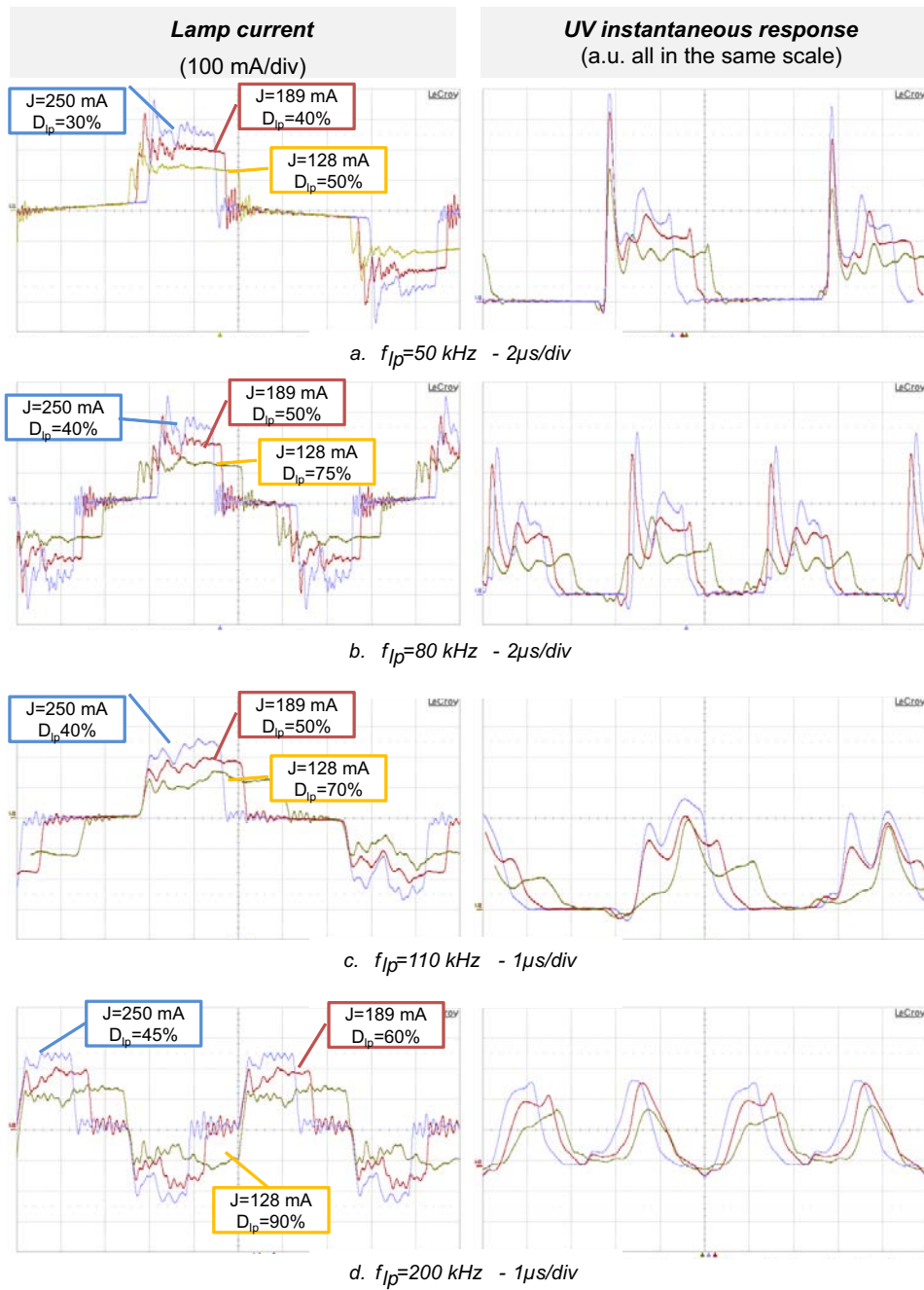
FIGURE 2.3: Comparaison des formes d'onde du courant et de l'UV pour différents valeurs de J

$f_{lp}(kHz)$	**80**			**170**			Average	σ
J (mA)	250	189	128	250	189	128		
V_{th} (kV)	1.18	1.25	1.38	1.3	1.32	1.32	1.26	7%
C_d (pF)	91.2	91.2	91.5	86.4	81.4	87.9	87.9	5%
C_g (pF)	29.2	29.2	29.6	27.6	34.5	37.5	31.3	13%

TABLE 2.1: Paramètres équivalentes de la lampe obtenus à partir des figures de Lissajous charge-tension
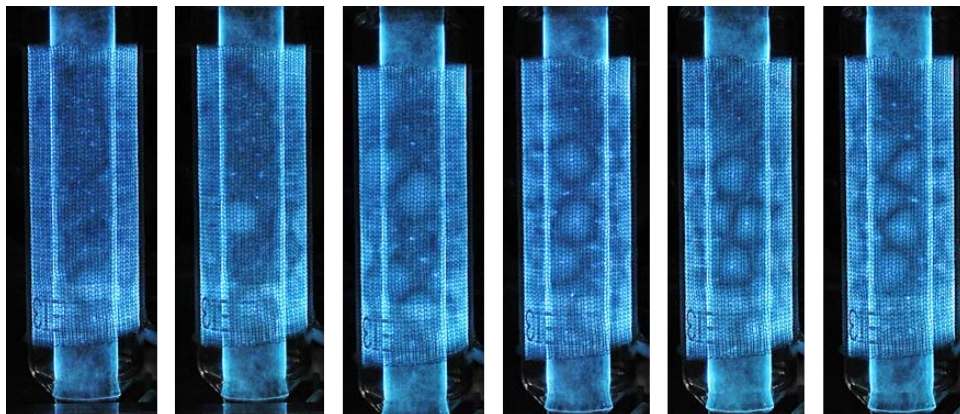

FIGURE 2.4: Variation de l'aspect visuel des décharges avec l'incrément dans l'intensité des pulses de courant. $f_{lp} = 70\,kHz$, $P_{lp} = 80\,W$, $J = 95, 116, 133, 154, 171, 186\,mA$ (de gauche à droite)

un indicateur de hauts niveaux de rendement de la lampe.

2.3 Impact de la Fréquence d'Opération

La puissance UV obtenue est montrée à la Fig.2.5, pour différentes fréquences de fonctionnement. Á partir de cette figure on peut voir que l'impact de la fréquence dans la plage 50-140 kHz est négligeable et qu'à partir de 170 kHz une chute importante dans la production UV est observé.

À partir des formes d'onde de l'UV et du courant de la lampe, montrées dans la Fig.2.6 un résultat intéressant est que l'amplitude des impulsions UV diminue avec l'augmentation de la fréquence de fonctionnement, même si l'intensité du courant reste constante.

Aucune transition du type de celle qui s'opère lors du passage du régime diffus au régime filamentaire dans l'aspect visuel de la décharge, observé quand on augmente l'intensité du courant, n'a été observé pour les changements dans la fréquence de fonctionnement. Aussi les valeurs des paramétres équivalents de la lampe sont similaires aux valeurs obtenues dans la Section 2.2.
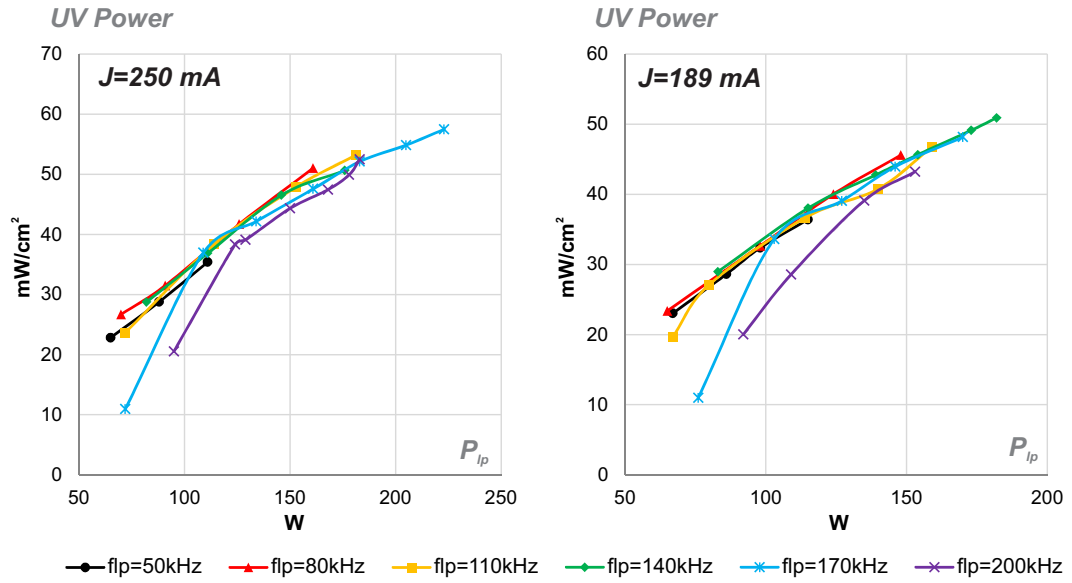
FIGURE 2.5: Impact de la fréquence de fonctionnement dans la puissance UV pour J=250 mA (gauche) et J=189 mA (droite)

2.4 Point Optimal de Fonctionnement

La puissance UV obtenue en fonction de la puissance électrique injectée dans la lampe, pour tous les points de fonctionnement de cette étude, sont présentés à la Fig.2.7. Ce graphique permet de choisir le point de fonctionnement de la lampe pour lequel on obtient une valeur de radiation donnée avec le moins de puissance électrique injectée. En conséquence ce graphique est particulièrement utile pour sélectionner le point de fonctionnement optimal de la lampe.

Par exemple, si pour une application il faut obtenir au moins $30\,mW/cm^2$ de radiation UV, on peut choisir parmi les points d'opération signalés avec un cercle dans la Fig.2.7. Parmi ces points, le point de fonctionnement de puissance électrique minimale est celui qui se trouve plus à gauche. Ce point d'opération est décrit dans le tableau 2.2. Il permet d'obtenir une puissance de radiation de $32\,mW/cm^2$ avec 27 % moins d'énergie que le point qui se trouve le plus à droite.

$J(mA)$	$f_{lp}(kHz)$	$D_{lp}(\%)$	$P_{UV}(mW/cm^2)$	$P_{lp}(W)$	$E_{lp}(\mu J)$
250	80	30	32	91	438

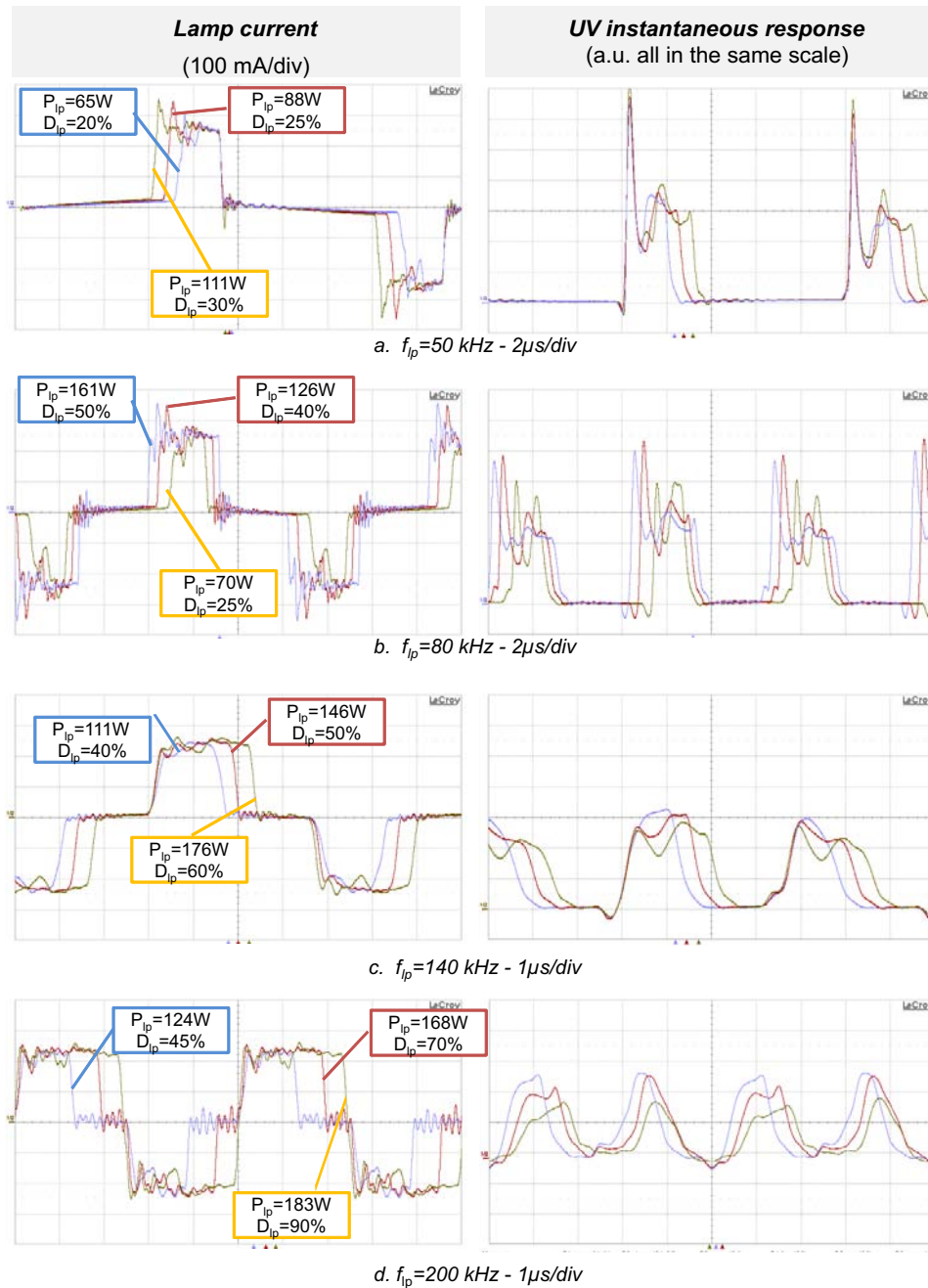TABLE 2.2: Point of maximum lamp efficiency within the operating range of the experiments to obtain $30\,mW/cm^2$

FIGURE 2.6: Comparaison des formes d'onde du courant et de l'UV pour $J = 250mA$
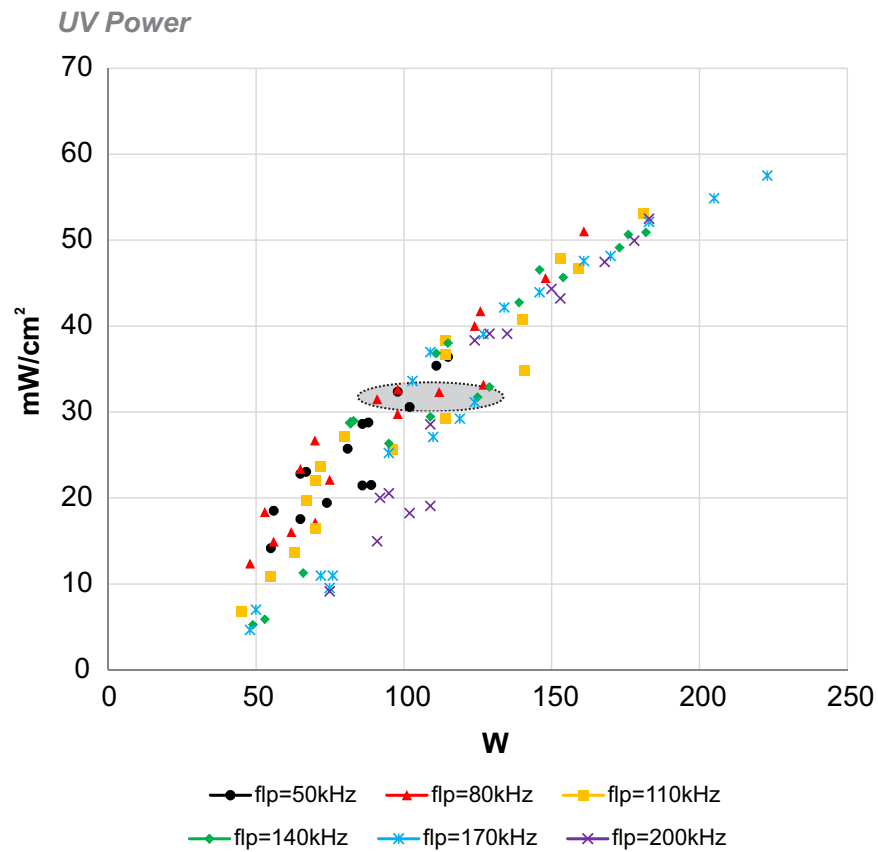
FIGURE 2.7: UV Power obtained for all the tested operating points

2.5 Conclusions

La production de l'UV est positivement influencée par l'augmentation de l'intensité du courant. Cependant, pour la plage expérimental étudiée ici, il n'y a pas de gain important dans la performance de la lampe au-dessus de 189 mA pour l'intensité du courant. En revanche, le modèle électrique équivalent simplifié de la lampe est à peine affecté par les changements dans le point de fonctionnement.

L'existence de filaments bien définis dans la décharge est associée à des niveaux d'efficacité UV meilleurs que ceux mesurés pour des points de fonctionnement non ou moins filamenteux.

L'amplitude et la durée des impulsions de rayonnement UV sont régis par l'intensité du courant de la lampe et la durée de l'impulsion de courant respectivement .

L'énergie injectée dans la lampe pour produire la décharge, semble jouer un rôle déterminant dans le rendement de la lampe. Pour tous les points de fonctionnement testés et pour cette excilampe XeCl DBD en particulier , les meilleures performances ont été obtenues avec des impulsions d'énergie supérieurs à 300 μJ.

Bibliographie

[2.1] Haruaki Akashi, Akinori Odam, and Yosuke Sakai, "Effect of gas heating on excimer distribution in DBD xe excimer lamp," in *28th ICPIG Conference Records*, (Prague, Czech Republic), July 2007.

[2.2] U. Kogelschatz, "Dielectric-barrier discharges : Their history, discharge physics, and industrial applications," *Plasma Chemistry and Plasma Processing*, vol. 23, no. 1, pp. 1–46, 2003.

[2.3] R. Casanueva, F. J. Azcondo, and S. Bracho, "Series–parallel resonant converter for an EDM power supply," *Journal of Materials Processing Technology*, vol. 149, pp. 172–177, June 2004.

[2.4] R. Casanueva, F. Azcondo, and C. Brañas, "Output current sensitivity analysis of the resonant inverter : Current-source design criteria," *IEEE Transactions on Industrial Electronics*, vol. 54, no. 3, pp. 1560–1568, 2007.

[2.5] Y. Chéron, C. Goodman, and T. Meynard, *Soft commutation*. London [u.a. : Chapman & Hall, 1992.

[2.6] R. Oruganti and F. Lee, "Resonant power processors, part I—State plane analysis," *IEEE Transactions on Industry Applications*, vol. IA-21, no. 6, pp. 1453–1460, 1985.

[2.7] X. Bonnin, H. Piquet, D. Florez, R. Diez, and X. Bonnin, "Designing the high voltage transformer of power supplies for dbd : windings arrangment to reduce the parasitic capacitive effects," in *Power Electronics and Applications (EPE), 2013 15th European Conference on*, Sept. 2013.

[2.8] R. Diez, H. Piquet, and S. Bhosle, "Control of the UV emission of an excimer lamp by means of a current-mode power supply," in *Industrial Electronics, 2009. IECON '09. 35th Annual Conference of IEEE*, pp. 3500–3505, IEEE, Nov. 2009.

[2.9] R. Diez, H. Piquet, S. Bhosle, and J.-M. Blaquiere, "Current mode converter for dielectric barrier discharge lamp," in *IEEE Power Electronics Specialists Conference, 2008. PESC 2008*, pp. 2485–2491, 2008.

[2.10] H. Piquet, S. Bhosle, R. Diez, and M. V. Erofeev, "Pulsed current-mode supply of dielectric barrier discharge excilamps for the control of the radiated ultraviolet power," *IEEE Transactions on Plasma Science*, vol. 38, pp. 2531–2538, Oct. 2010.

3 Générateur Électrique à Haut Rendement pour l'Alimentation de la DBD au Point d'Opération Optimal

Afin d'augmenter l'efficacité de l'ensemble convertisseur- lampe, le présent chapitre propose un générateur résonant en mode courant, conçu pour fonctionner à un point d'opération fixe et utilisant un principe de commutation au courant nul.

3.1 Topologie

La topologie classique de l'onduleur résonant série, montrée dans la Fig.3.1 offre une sortie en courant et la possibilité d'obtenir commutation douce au courant nul [3.3], [3.4]. Cette topologie est choisi comme base pour le convertisseur proposé.
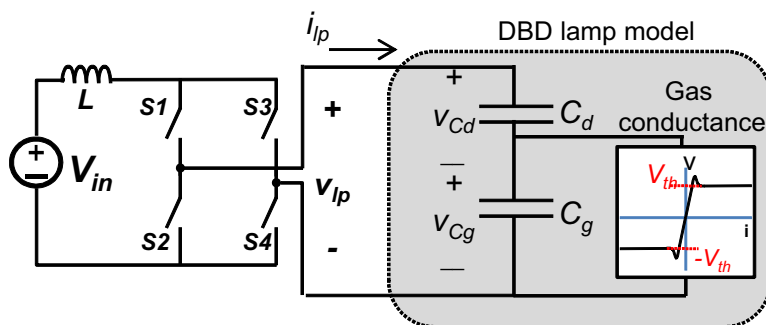

FIGURE 3.1: L'onduleur à resonance serie proposé

La période de fonctionnement du convertisseur est divisée en six étapes, déterminées par l'état des interrupteurs du pont et le modèle équivalent de la lampe. Le circuit équivalent pour chaque étape de cette séquence de fonctionnement est présenté dans la Fig.3.2(bottom).

Comme conséquence de l'utilisation du mode de conduction discontinue (DCM) sélectionné dans le présent travail, la fréquence de fonctionnement de la lampe est définie seulement par la fréquence d'opération du pont inverseur. La réalisation de ce mode DCM est mise en œuvre grâce à l'utilisation d'interrupteurs du type thyristor.

La conception de ce générateur résonant est développée en utilisant l'analyse par diagramme de phase [3.5], [3.6]. En utilisant cette méthodologie les expressions mathé-
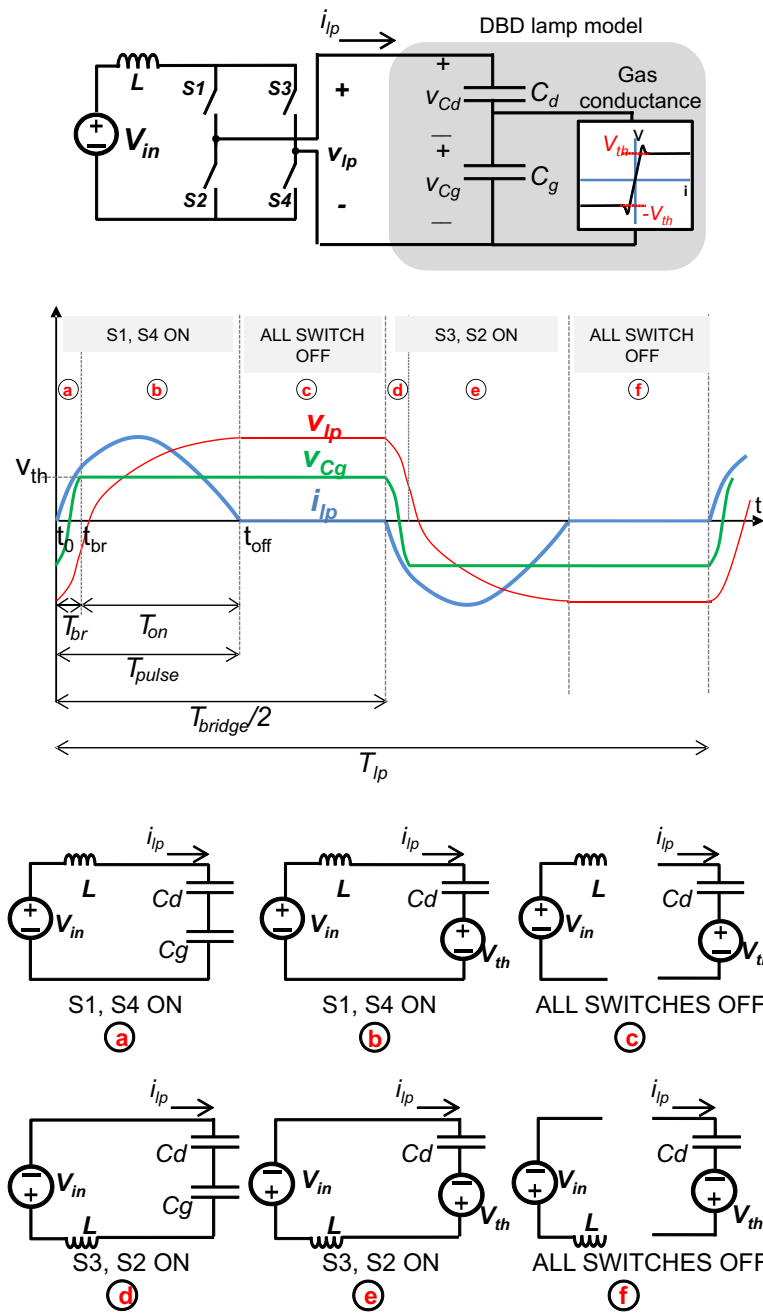
FIGURE 3.2: Sequence de fonctionemment (en bas). Formes d'onde theoriques pour le courant de la lampe, la tension de la lampe et la tension du gaz (en haut).

matiques pour la puissance de sortie, la tension crête, le courant crête et la durée de l'impulsion de courant injecté dans le gaz, ont été déduites.

$$P_{lp} = 4f_{lp}V_{th}{}^2 C_g \times \left(\frac{V_{th}}{V_{th} - V_{in}} - 1 \right) \tag{3.1.1}$$

$$\hat{V}_{lp} = V_{th} + \frac{V_{th}{}^2 C_g}{C_d(V_{th} - V_{in})} \tag{3.1.2}$$

$$\hat{I}_{lp} = (\hat{V}_{lp} - V_{in})\sqrt{\frac{C_d}{L}} \tag{3.1.3}$$

$$T_{pulse} = \sqrt{LC_{eq}}\arcsin\left(\frac{I_{br}}{V_{in} - \hat{V}_{lp}}\sqrt{\frac{L}{C_{eq}}} \right) + \sqrt{LC_d}\left(\pi - \arcsin\left(\frac{I_{br}}{V_{in} - \hat{V}_{lp}}\sqrt{\frac{L}{C_d}} \right) \right) \tag{3.1.4}$$

Où I_{br} est la valeur du courant de lampe au moment du claquage du gaz :

$$I_{br}^2 = \frac{4V_{th}C_g}{L}\left(\hat{V}_{lp} + V_{in} - \frac{V_{th}C_g}{C_{eq}} \right) \tag{3.1.5}$$

Dans la Fig.3.3 la puissance électrique injecté dans la lampe comme fonction de la tension d'entrée peut être observée. L'asymptote de cette courbe de puissance est égale à la tension de claquage V_{th} comme on peut le déduire à partir de (3.1.1).

En conséquence, pour assurer la stabilité du convertisseur la condition $V_{in} < V_{th}$ doit être respectée. Les relations mathématiques exposées dans cette section, ont été vérifiées numériquement par simulation en utilisant le simulateur des circuits PSIM.

3.2 Sélection des Composants et Simulations

Le générateur est dimensionné pour obtenir un point de fonctionnement optimal dans la lampe. En particulier on utilise le point de fonctionnement déduit de la Section 2.4. Ce point correspond à $P_{lp} = 90\,W$, $f_{lp} = 80\,kHz$, $D_{lp} = 35\,k\%$ et $J = 189\,mA$.

Chacun des interrupteurs du type thyristor du pont inverseur a été implémenté avec une diode de technologie Carbure de Silicium (GB07SHT12) en série avec un MOSFET haute tension (P8NK100Z), comme il est montré dans la Fig.3.4. La tension crête de la lampe pour le point d'opération prévu est autour de 4 kV ; en conséquence, un transformateur élévateur entre le pont et la lampe est utilisé.

Le rapport de transformation choisi est égal à 10. Pour réduire encore plus l'effet du condensateur parasite par rapport au transformateur utilisé dans la Section **??**, on utilise la technique de construction à multi-sections proposé dans [3.7].

L'inductance L est calculée avec (3.1.3) pour obtenir un courant crête de 1.9 A au primaire du transformateur. La valeur obtenue est de $L = 231\mu H$.

La puissance électrique de la lampe en fonction de la tension d'entrée, obtenue par

simulation et théoriquement avec (3.1.1) est montrée dans la Fig.3.5. La différence entre la simulation et le calcul théorique est expliqué par l'effet des éléments parasites du transformateurs, pris en compte dans la simulation.
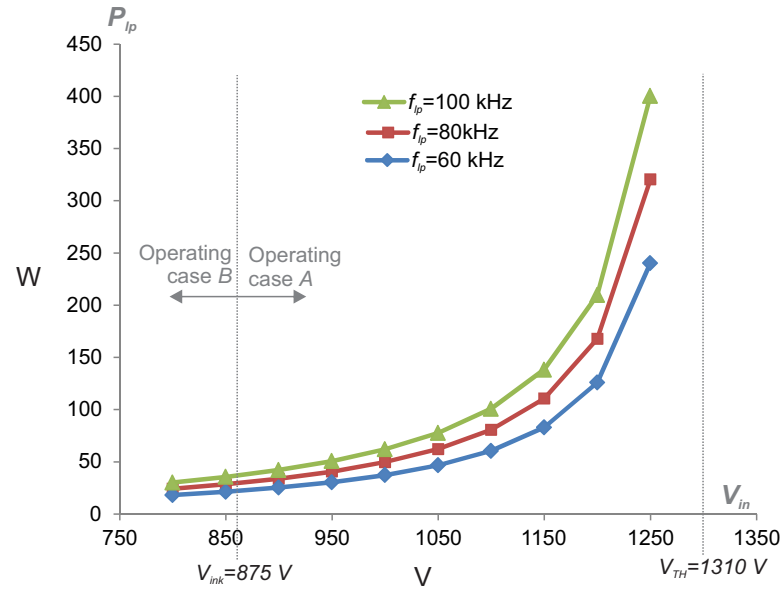

FIGURE 3.3: Puissance théorique de lampe en fonction de la tension d'entrée du convertisseur, calculée avec (3.1.1) (V_{th}=1.31 kV, C_g=28 pF, C_d=85 pF).
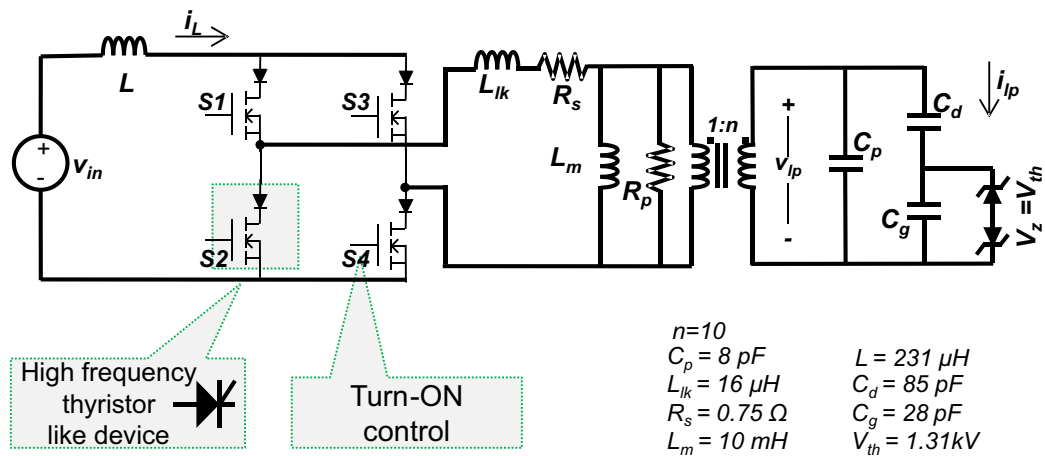

FIGURE 3.4: Circuit du générateur et modele de lampe, utilisé pour les simulations
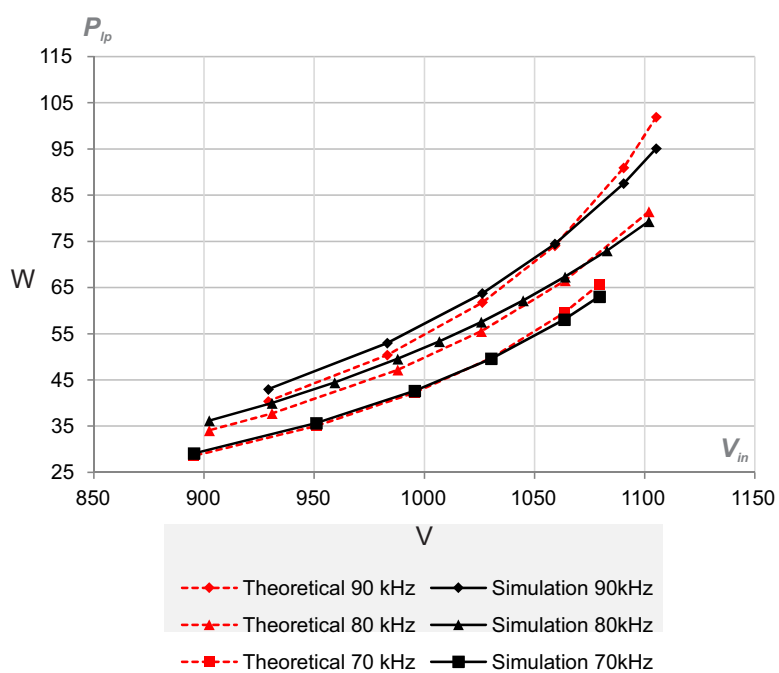
FIGURE 3.5: Puissance théorique de sortie, comme fonction de la tension d-entrée et résultat de simulation (avec les éléments parasites du transformateur inclus) (V_{th}=1.31 kV, C_g=28 pF, C_d=85 pF).

3.3 Résultats Expérimentaux

La puissance électrique obtenue dans la lampe pour différentes valeurs de V_{in} est montrée dans la Fig.3.6. La comparaison entre les courbes de puissance expérimentales, théoriques et de simulation permet d'affirmer que les expressions mathématiques déduites pour cet générateur offrent une précision suffisante pour la conception du convertisseur. Pour une tension d'entrée V_{in} au delà de 117 V, la puissance de sortie est instable à cause de la proximité à l'asymptote V_{th}/n.
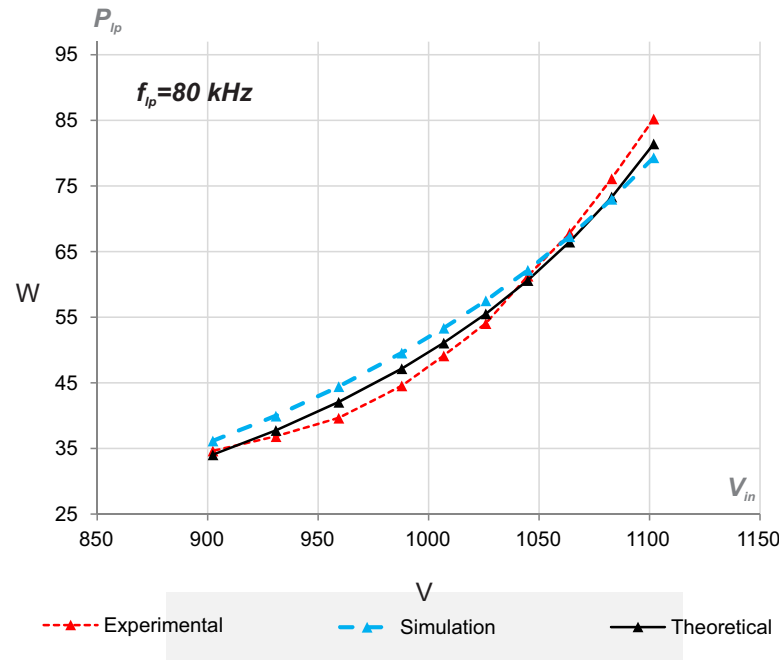

FIGURE 3.6: Puissance de sortie théorique, simulée et expérimental, en fonction de la tension d'entrée.(V_{th}=1.31 kV, C_g=28 pF, C_d=85 pF).

Le courant de l'inductance i_L, montré dans la Fig.3.7 a, comme on s'y attendait, une forme d'onde similaire au courant de la lampe i_{lp}. La tension aux bornes de la lampe v_{lp} ne montre pas les oscillations haute fréquence que l'on trouve sur v_{prim}. Ces deux signaux de tension, ne restent pas constants quand le courant i_L s'annule, à cause de l'inductance de magnétisation. La différence entre les caractéristiques expérimentales, de simulation et théoriques de la puissance de sortie du générateur est expliquée aussi par l'effet des éléments parasites du transformateur sur le circuit résonant et sur le transfert de puissance du primaire au secondaire.

L'efficacité du générateur a été mesurée avec la sonde de tension branchée au primaire du transformateur pour réduire l'impact de la capacité d'entrée de la sonde dans la mesure. Dans la Fig.3.8 on peut voir que le transformateur est responsable de la plupart des pertes du générateur. Pour une puissance de sortie de 90 W l'efficacité obtenue est
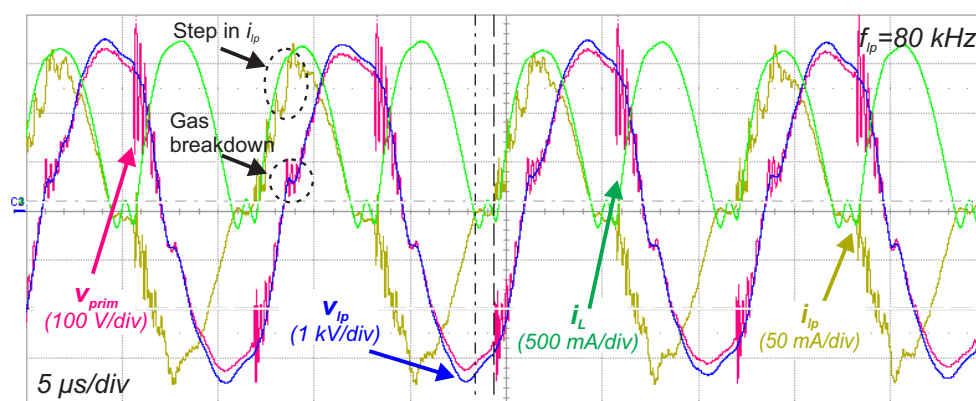
FIGURE 3.7: Formes d'onde expérimentaux avec la sonde de tension connecté au primaire du transformateur

de 90.6% en opposition avec 57% pour la source du courant en crenaux developé dans le Chapitre 1.
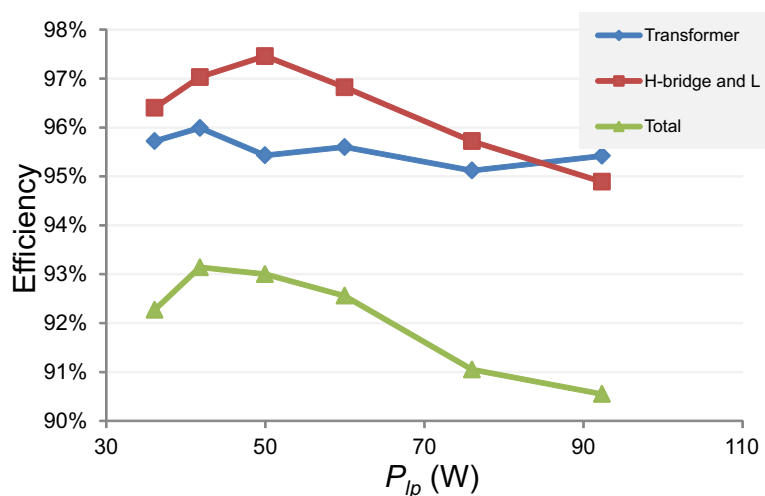

FIGURE 3.8: Rendement du SRI pour différents valeurs de puissance de sortie (f_{lp}=80kHz).

La réponse instantanée du rayonnement UV est acquise avec le photo-détecteur Thorlabs PDA-25K. Comme déjà mentionné dans [3.8], on peut observer sur la Fig.3.9 comment, après le claquage du gaz, la forme d'onde du rayonnement UV (UV) suit la forme d'onde i_{lp} (valeur absolue).
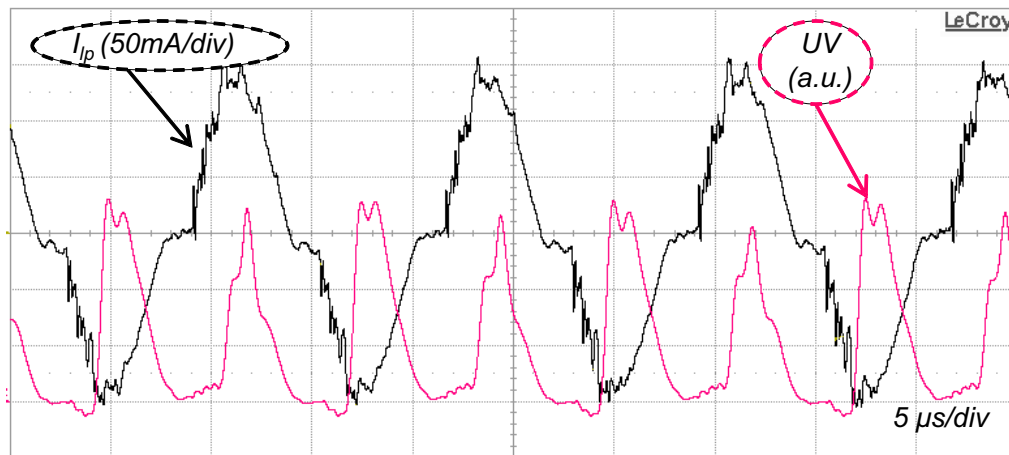
FIGURE 3.9: Forme d'onde de l'UV et du courant injecté dans l'excilamp.

3.4 Comparaison Avec des Autres Topologies

Une comparaison analytique et expérimentale entre le générateur résonant série, la source de courant en créneaux (Chapitre 1), le convertisseur résonant du type Boost [3.9] et du type Buck-Boost [3.10] a été effectuée.

Pour la comparaison, les quatre convertisseurs ont été configurés pour des points de fonctionnement correspondant à la même puissance électrique de sortie (106 W) et même durée des pulses (3.5 µs) de courant. Dans la Fig.3.10 on peut observer les formes d'onde expérimentales pour chacun des générateurs. A partir de ces formes d'ondes on peut voir à nouveau la similitude entre la réponse instantanée de l'UV et la valeur absolue du courant injecté. On peut remarquer aussi que la tension de la lampe v_{lp} a une forme d'onde similaire pour les quatre conditions d'alimentation, même si le courant injecté est différent, ce qui démontre la difficulté de contrôler le rayonnement UV à partir d'une source de tension.

Le tableau 3.1 donne la description du point de fonctionnement pour les quatre générateurs comparés. Par rapport aux pertes par commutation, on peut vérifier que la source de courant en créneaux présente la valeur la plus haute, du fait que l'on utilise la commutation forcée ; ensuite vient la topologie Buck-Boost car son courant au moment de la commutation correspond à la plus grande valeur parmi les convertisseur à résonance du test ; la topologie résonante série (SRI) est la structure avec le meilleur rendement car elle est fonctionne avec commutation au courant zéro pour l'amorçage et blocage des interrupteur.
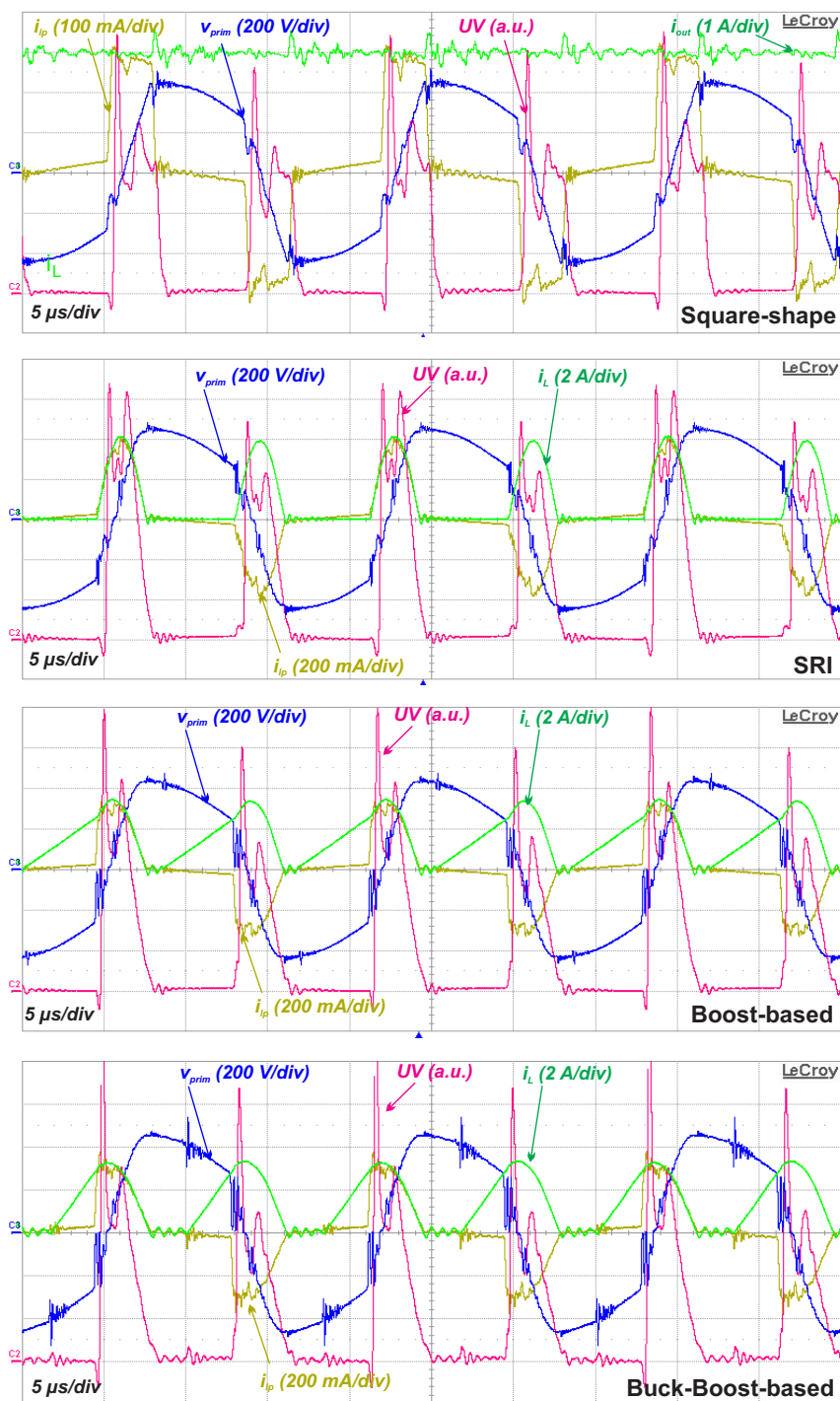
FIGURE 3.10: Formes d'onde expérimentaux pour le quatre topologies comparées. $P_{lp} = 106W$, $f_{lp} = 60kHz$

$Converter$	V_{in} (V)	I_{in} (A)	P_{in} (W)	P_{prim} (W)	UV ($\frac{mW}{cm^2}$)	$\eta_{circuit}$ (%)	$\eta_{transf.}$ (%)	η_{total} (%)
Square-shape	159.1	1.2	193.5	125	28.3	65	85	55
Boost	79	1.7	131.8	123	25.3	93	86	80
Buck-Boost	246	0.5	134	123	26.8	92	86	79
SRI	136.9	0.9	127.6	124	27.5	97	85	83

TABLE 3.1: Comparaison du rendement obtenu ($P_{lp} = 106W$)

3.5 Conclusions

Parmi les topologies possibles pour l'alimentation électrique des dispositifs DBD, les topologies à résonance offrent moins de pertes de commutation, une meilleure compatibilité électromagnétique, moins de dispositifs de commutation et en plus peut fonctionner en mode courant ; en particulier dans le cas du convertisseur résonant série en mode de conduction discontinue, réduisant les pertes par commutation, proposé dans ce chapitre, tous ces avantages sont trouvés. Avec le mode de fonctionnement choisi dans ce travail, la puissance de la lampe est contrôlée à l'aide de deux degrés de liberté.

L'utilisation du modèle électrique de la lampe, en liaison avec l'analyse du plan de phase donne un aperçu du processus et permet le calcul des grandeurs électriques, dont la puissance de la lampe en fonction de la tension d'entrée, la fréquence de l'onduleur, les composants et l' paramètres de la lampe. L'étude analytique, la simulation et les résultats expérimentaux sont conformes, et nous considérons donc que le principe de l'onduleur à résonance série en tant que topologie efficace pour l'alimentation des lampes excimères à DBD a été validé

Bibliographie

[3.1] Haruaki Akashi, Akinori Odam, and Yosuke Sakai, "Effect of gas heating on excimer distribution in DBD xe excimer lamp," in *28th ICPIG Conference Records*, (Prague, Czech Republic), July 2007.

[3.2] U. Kogelschatz, "Dielectric-barrier discharges : Their history, discharge physics, and industrial applications," *Plasma Chemistry and Plasma Processing*, vol. 23, no. 1, pp. 1–46, 2003.

[3.3] R. Casanueva, F. J. Azcondo, and S. Bracho, "Series–parallel resonant converter for an EDM power supply," *Journal of Materials Processing Technology*, vol. 149, pp. 172–177, June 2004.

[3.4] R. Casanueva, F. Azcondo, and C. Brañas, "Output current sensitivity analysis of the resonant inverter : Current-source design criteria," *IEEE Transactions on Industrial Electronics*, vol. 54, no. 3, pp. 1560–1568, 2007.

[3.5] Y. Chéron, C. Goodman, and T. Meynard, *Soft commutation.* London [u.a. : Chapman & Hall, 1992.

[3.6] R. Oruganti and F. Lee, "Resonant power processors, part I—State plane analysis," *IEEE Transactions on Industry Applications*, vol. IA-21, no. 6, pp. 1453–1460, 1985.

[3.7] X. Bonnin, H. Piquet, D. Florez, R. Diez, and X. Bonnin, "Designing the high voltage transformer of power supplies for dbd : windings arrangment to reduce the parasitic capacitive effects," in *Power Electronics and Applications (EPE), 2013 15th European Conference on*, Sept. 2013.

[3.8] R. Diez, H. Piquet, and S. Bhosle, "Control of the UV emission of an excimer lamp by means of a current-mode power supply," in *Industrial Electronics, 2009. IECON '09. 35th Annual Conference of IEEE*, pp. 3500–3505, IEEE, Nov. 2009.

[3.9] R. Diez, H. Piquet, S. Bhosle, and J.-M. Blaquiere, "Current mode converter for dielectric barrier discharge lamp," in *IEEE Power Electronics Specialists Conference, 2008. PESC 2008*, pp. 2485–2491, 2008.

[3.10] H. Piquet, S. Bhosle, R. Diez, and M. V. Erofeev, "Pulsed current-mode supply of dielectric barrier discharge excilamps for the control of the radiated ultraviolet power," *IEEE Transactions on Plasma Science*, vol. 38, pp. 2531–2538, Oct. 2010.

4 Conclusions

L'objectif principal de cette thèse était l'amélioration du rendement des systèmes de lampes UV à excimères DBD. Avec ce but, un processus qui couvre deux grandes étapes a été conçu : La première étape de ce processus est l'étude des meilleures conditions de fonctionnement de la performance de la lampe et la deuxième est l'amélioration du rendement de la source d'alimentation électrique.

Pour la première étape, une étude de l'impact du point de fonctionnement de la lampe sur la performance de la lampe a été proposé. Pour rendre possible cette étude de la performance, un nouvel outil scientifique qui fournit un contrôle complet et la flexibilité pour ajuster la puissance de la lampe DBD a été développé. Cet outil est une alimentation de courant en créneaux avec trois degrés de liberté sur sa forme d'onde de courant de sortie : L'intensité du courant, le rapport cyclique et la fréquence.

En exploitant cet équipement innovateur avec une excilamp UV XeCl DBD, l'impact de l'intensité du courant de la lampe et de la fréquence a été révélé. A partir des résultats obtenus (pour la plage de fonctionnement testée) la valeur de l'énergie de l'impulsion injectée a été trouvée comme étant un facteur important dans le rendement de la lampe. Énergies d'impulsions au dessous de 300 μJ, se trouvent à fournir les meilleures conditions d'exploitation de la performance de la lampe. En outre, on á trové que pour une valeur donnée de puissance électrique, l'utilisation de basse fréquence et de haute intensité des courants augmente la production d' un rayonnement UV. Cependant, une diminution du gain dans le performance de la lampe pour des intensités de courant supérieures 190 mA a été établi. .

Pour la deuxième étape de ce processus d'optimisation, un convertisseur à haut rendement a été conçu et mis en œuvre, conçu pour fonctionner au point de fonctionnement optimale de la lampe, trouvé avec l'étude paramétrique. Afin d'atteindre l'exigence de haute efficacité pour cette application spécifique, un convertisseur résonant qui fonctionne sur la base de l'onduleur résonant série, avec commutation au courante zero (ZCS) et au mode de conduction discontinue (DCM), a été conçu. Le ZCS minimise les pertes de commutation et le DCM bénéficie la performance du système en assurant que seule les pulses de courant avec intensité las plus élevé sont utilisés pour maintenir la décharge du gaz. Avec cet convertisseur, un rendement électrique maximum de 94% a été obtenu.